Al-Farabi Kazakh National University

UDC 539.17   The manuscript

TKACHENKO ALESSYA

Phase shift analysis of nuclear processes with the spin structure 1+1/2, 1+1, 1/2+3/2 and astrophysical applications

6D060500 – Nuclear Physics

Thesis for the degree
of Doctor of Philosophy (PhD)

Local scientific supervisor:
N.A. Burkova, Doctor of Physical and
Mathematical Science, Professor;
Foreign scientific supervisor:
R. Kezerashvili, Ph.D., D.Sc., Professor.

Republic of Kazakhstan
Almaty, 2020

CONTENTS

SYMBOLS AND ABBREVIATIONS

WF	wave function
PCM	potential cluster model
MPCM	modified potential cluster model
BBN	Big Bang Nucleosynthesis
FDM	finite difference method
RGM	resonating group method
ME	matrix element
NN	nucleon-nucleon (interaction, potential, *etc.*)
b	barn, 1b= 10^{-24} sm^2
μb	microbarn, 1 μb = 10^{-6} b
fm	fermi, 1 fm= 10^{-13} sm
MeV	mega-electronvolt
meV	milli-electronvolt
c.m.	center of mass system
l.s.	laboratory system
E_b	binding energy
s	spin of the target or the incident particle
S	Channel spin
$C_{a\alpha b\beta}^{c\gamma}$	Clebsch-Gordan coefficient
$P_n^m(\theta)$	Legendre polynomial
$\begin{Bmatrix} a & b & c \\ d & e & f \end{Bmatrix}$	6j-symbol
$M_{S'\nu'}^{S\nu}$	matrix elements of the transition *M*-matrix
EJ	electrical multipole transitions of rank J
MJ	magnetic multipole transitions of rank J
$d\sigma/d\Omega$	differential cross section
S-factor	astrophysical factor
GS	ground state
FES	first excited state
FS	forbidden state
AS	allowed state
V_{ab}	binary interaction potential
ANC	asymptotic normalizing coefficient
AC	asymptotic constant

INTRODUCTION

One of the fundamental scientific issues of our time sounds like *«How to explain the primordial nucleosynthesis in the Universe and predict its further evolution?»* Once this question arises while reading Nobel monographs and reviews [1-7]. Maybe we have already some answers to this question, but it is no less interesting to continue investigations in this direction while applying modern experimental technique and novel theoretical developments.

Let us first present the scale of events occurring on the macro level, but due to micro-processes. Just take a look around, and imagine for a moment that all of these things have never been – the Earth, planets, stars, constellations, the Milky Way, galaxies, and the Universe. How did it all come into existence? We already have the answer, – the Big Bang.

After the Big Bang the creation of the Universe began. It started with the chain of synthesis of chemical elements, the first of which was the $p(n,\gamma)d$ reaction. All that we see around us, and we ourselves, have come from these elements. Such a clear statement of the problem, «the beginning of everything», was the impetus for the development of the theory of nucleon-nucleon (NN) interaction. At present, several dozens of different NN-potentials have been built (Reid, Bonn, Paris, MSU, Nimegen, Almaty [8], and *etc.*), but the universal one that able to describe any processes does not exist. This *a priori* does not allow the construction of a unified theory of the atomic nucleus more complex than deuterium.

The study of the subsequent synthesis of heavier chemical elements is based on microscopically justified models of the atomic nucleus from the point of view of quantum-mechanical principles, *i.e.* the principle according to which nucleons are combined together in the nucleus (Pauli Exclusion Principle was formulated by Wolfgang Pauli, Nobel laureate, in 1940). It should be note that the Pauli principle reflects the natural fact that all stable nuclear particles produced in the Big Bang are fermions or bosons. However, no one knows why this is the case. In the modern scientific world, one of the most widely recognized is the model known as the "resonant group method" (RGM), see, for example, [9-13].

Thus, in order to solve practical problems in the context of discussing the NN-potential, some approximations are inevitable.

We can consider the solution to the problem from another angle, if we pay attention to the fact that it is possible to design an effective and completely unambiguous *nucleus-nucleus* interaction potential [14]. One of the possible options lies in the fact that relying on the experimental data of elastic scattering, the observed energy spectra and asymptotic constants (ACs) for the bound states of particles, as well as measured geometric characteristics such as charge and mass radii *etc.* one able to reconstruct the interaction potentials in a fixed binary cluster channel. This approach is known today as the potential cluster model (PCM).

In the context of PCM, there are two ways to account for the fundamental Pauli principle. The first one involves the introduction of repulsion in the nuclear potential at small distances, i.e. a low probability of clusters overlapping or, in other words, their

isolation.is simulated. The second method is based on the introduction of a deep attraction potential, which implies the presence of forbidden by the Pauli principle states (FSs) in both discrete and continuous spectra.

The deep or shallow nature of nucleus-nucleus interactions has been a controversial question for a long time, as they can both fit experimental scattering data rather accurately. In Schrodinger quantum mechanics, corresponding Hamiltonians are known as supersymmetric partners. However, their predictions differ in general for the case of radiative capture reactions.

Therefore, our choice was the attractive nuclear potentials deep enough to enlarge the number of solutions, some of which can be identified as FSs [15]. Let us give a simple example. If we want to join to the nucleus of helium (^{4}He) one more nucleon, it can only be placed in the p-shell; that configuration ^{5}s is unphysical and should be forbidden. An allowed configuration is ^{4}s^{1}p. From the point of view of physics, it is necessary to eliminate the forbidden states. From the point of view of mathematics, elimination means that the wave functions of the forbidden states must be orthogonal to those of the allowed states. This is one of the key points used for the modification of PCM, so this option can be called the modified PCM (MPCM).

This very approach has already been used for the description of total cross sections and astrophysical S-factors and, in some cases, the reaction rates of 30 thermonuclear process of radiative capture at astrophysical and thermal energies. The capture processes of nucleons in the following *nucleon-nucleus* channels have been considered: n^2H, p^2H, p^3H, n^6Li, p^6Li, n^7Li, p^7Li, n^8Li, p^9Be, n^9Be, n^{10}Be, p^{10}B, n^{10}B, p^{11}B, n^{11}B, n^{12}C, p^{12}C, n^{13}C, p^{13}C, n^{14}C, p^{14}C, n^{14}N, n^{15}N, p^{15}N, n^{16}O, and p^{16}O. Also the reactions with α-particles and deuterons, such as ^{2}H^{3}He, ^{2}H^{4}He, ^{3}He^{4}He, ^{3}H^{4}He, and ^{4}He^{12}C have been considered [16-21]. This approach allows to explain the experimental data, and in some cases, to predict reliably the behavior of astrophysical S-factors at low and ultralow energies [22, 23].

Some may correctly point out that, every second on the Sun and in stars, hundreds of nuclear reactions occur. Experimenters are trying to replicate many of these in laboratories (LUNA, CERN, etc.) on the most modern high-precision equipment. However, theoretical investigations are able to reproduce, with a certain probability, a primordial nucleosynthesis in the Universe or in the various stellar cycles, determining their *birth* and further *evolution*. They are able not only to explain, but also to predict the behavior of the reaction rates and the S-factors. Further we are going to present a wonderful examples of the possibilities of MPCM, radiative neutron capture processes ^{3}He$(^2$H$, \gamma)^5$Li and ^{10}Be$\left(n, \gamma\right)^{11}$Be (in Sections 3 and 4, respectively).

It is actual to develop and substantiate the mathematical formalism for the construction of the binary intercluster potentials V_{ab}. Their reliability should be checked on the special processes provided by the experimental data. This, in its turn, gives the opportunity to define *the limitation conditions* for the cluster model approach.

Point out our choice of the cluster model approach for the ^{3}He$(^2$H$, \gamma)^5$Li reaction and its role in BBN, the *actual statements* are the following. The interest to the radiative capture reactions in the isobar-analogue channels ^{3}He$(^2$H$, \gamma)^5$Li and ^{3}H$(^2$H$,\gamma)^5$He is

primarily due to the two reasons: these reactions are parts of nucleosynthesis chain of the processes occurring in the early stages of a stable star formation, as well as possible candidates for the overcoming of the well-known problem of the $A = 5$ gap in the synthesis of light elements in the primordial Universe [24] and application of these processes for the diagnostics of nuclear fusion efficiencies of $^2H(^3H, n)^4He$ and $^2H(^3He, p)^4He$ reactions used for experimental studies of tokamak plasmas [25, 26].

It is believed that the $^3He(^2H, \gamma)^5Li$ process is well studied experimentally. Since 1954 [27] a sufficient number of experimental works, see, for example, works [28-32], are devoted to study this process, and the most recent data are presented in scientific publication [33], including compilations of experimental data on cross sections, astrophysical factors and rates of this reaction at energies less than 200 keV [26, p. 2, 34]. However, in our opinion, the experimental and theoretical situation is far from unambiguous and requires systematic analysis, which is implement in this thesis.

There is another «unambiguous» opinion: due to the smallness of the cross section the $^3He(^2H, \gamma)^5Li$ reaction does not contribute to the astrophysical processes [35]. In this research we demonstrate that this statement is disputable, since the rate of this reaction is not negligible.

In addition, a possible scenario for astrophysical processes of ^6Li formation involving a short-lived ^5Li isotope is considered. The two-step process $^2H + ^3He \rightarrow$ $^5Li + \gamma$ and $n + ^5Li + \gamma \rightarrow ^6Li + \gamma$ is considered and discussed as an alternative way of the formation of ^6Li at the BBN.

The purpose of the research in Section 4 is to bring the reliable input in the "round-table" discussion on the relative *boron-beryllium* branching leading to the production of *carbon component* both in the astrophysical processes, and terrestrial reactor constructive problems which may overlap in some temperature ranges. We have been motivated by a set of excellent papers and reviews cited covering the *pre-history* of the rising questions directly in references within the developing research.

The $n + ^{10}Be \rightarrow ^{11}Be + \gamma$ reaction enters into one of the chains of primordial nucleosynthesis in the early Universe [36]

$$\dots ^8Li(n,\gamma)^9Li(\beta^-)^9Be(n,\gamma)^{10}Be(n,\gamma)^{11}Be(\beta^-)^{11}B(n,\gamma)\dots$$
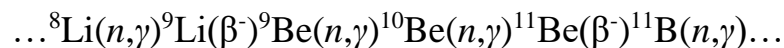
owing to that the elements with $A > 11\text{-}12$ can be synthesized (see for example [37]).

The alternative scenarios concept Fusion Reactions in Supernovae and the Early Universe was suggested in conceptual work [38] where two possible scenarios for *r*-processes conditional on α-induced reactions and competitive (n,γ) neutron radiative capture processes were analyzed in detail. (n,γ) channels possibility justification was given, i.e. when $^{10}Be(\alpha,\gamma)^{14}C$ reaction is excluded,

$$^9Be(n,\gamma)^{10}Be(n,\gamma)^{11}Be(n,\gamma)^{12}Be(\beta^-)^{12}B$$
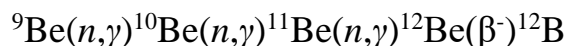
reactions chain is started.

Authors of [38, p. 474] had concluded that taking into account the reactions with light neutron excess nuclei could change an estimation of heavy elements abundance up to order 10!

However, it is clear to realize it we need reliable reaction rate data for many reactions including (n,γ) processes, and some of that are given in [23, p. 35-208]. Therefore, new and more accurate calculations of these reactions rates presented in the current work enable us to specify conclusions given in [38, p. 478].

Another story appeared in works [39, 40] devoted to fusion reactions in Supernovae the chain of reactions with *boron* isotopes

$$^{A}B(n,\gamma)^{A+1}B \ (A = 11,12,13),$$

was accentuated. This chain leads further to one of the variants of carbon isotopes (up to ^{19}C) synthesis initiation. In addition, presented here calculations for $n+^{10}Be \rightarrow ^{11}Be+\gamma$ process will allow clarifying the issues formulated in [40, p. 1173-1189]. The later detailed review suggests the comparative analysis for the reaction rates of 18 reactions providing the *boron* path leading to carbon isotopes abundance as the background for the synthesis of heavier elements. We regard the question o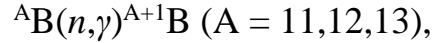n the dominating path is still open. At a time, we are going to analyze various interpretations of [38, p. 474] and [39, p. 301-308, 40, p. 1173-1189].

Purpose of research is a development of the formalism for the phase shift analysis of high-spin scattering processes, as well as approbation and analytical evaluation of methods for constructing interaction potentials in binary cluster channels, applicable for solving astrophysical problems.

Research objectives:

1. To develop a formalism of the phase shift analysis for the systems with spin structures 1+1/2, 1+3/2 and 1+1; To develop a computer program for calculating the scattering phase shifts;

2. To analyze alternative methods for obtaining the scattering phase shifts and building interaction potentials in binary cluster channels;

3. To construct the binary interaction potentials at low and astrophysical energies within the modified potential cluster model approach for the reactions $^{3}He(^{2}H,\gamma)^{5}Li$ and $^{10}Be(n,\gamma)^{11}Be$;

4. To calculate the total cross sections, astrophysical *S*-factors and rates of the reactions $^{3}He(^{2}H,\gamma)^{5}Li$ and $^{10}Be(n,\gamma)^{11}Be$.

Research objects are the binary cluster systems of light nuclei.

Research subjects are the scattering processes of spin particles in binary channels and radiative capture reactions at astrophysical energies.

Research methods: quantum theory of the angular momentum, partial waves method, numerical methods for solving the Schrödinger equation.

Defense Provisions:

1. The differential scattering cross sections for processes with channel spin $S > 1/2$ are *universal* in the framework of the quantum theory of collisions taking into account spin-orbit and spin-spin interactions without restrictions on the number of partial waves and the channel spin value.

2. The two-step mechanism for the synthesis of ^{6}Li nuclei in the Big Bang, which consists of the reactions $^{2}H + ^{3}He \rightarrow ^{5}Li + \gamma$ and $n + ^{5}Li + \gamma \rightarrow ^{6}Li + \gamma$, calculated

on the basis of total cross sections, astrophysical *S*-factor, and $^{3}\text{He}(^{2}\text{H},\gamma)^{5}\text{Li}$ reaction rate for energies up to 5 MeV in the framework of the modified potential cluster model using forbidden states explains the $^{6}\text{Li}/^{7}\text{Li}$ ratio in the Universe.

3. The modified potential cluster model with forbidden states reproduces the available experimental data on the total cross sections for radiation capture of neutrons on a ^{10}Be nucleus in the energy range from 25.3 meV to 10.0 MeV.

Scientific novelty:

1. A universal mathematical formalism is developed for constructing elastic scattering cross sections for multiplet states (from singlet with $2S+1=1$ to sextet with $2S+1=6$), which consider the spin-orbit and spin-spin interactions and allows one to perform the phase shift analysis taking into account any number of partial waves.

2. The experimental total cross sections of the $^{3}\text{He}(^{2}\text{H},\gamma)^{5}\text{Li}$ process at energies up to 5 MeV is reproduced in the framework of the modified potential cluster model. The role of the $^{3}\text{He}(^{2}\text{H},\gamma)^{5}\text{Li}$ process for the formation of ^{6}Li in the Big Bang nucleosynthesis (BBN) via its participation in a two-step mechanism $^{2}\text{H} + {}^{3}\text{He} \rightarrow {}^{5}\text{Li} + \gamma$, $n + {}^{5}\text{Li} + \gamma \rightarrow {}^{6}\text{Li} + \gamma$ has been established.

3. Experimental data for the total cross sections of radiative capture of neutrons on the ^{10}Be nucleus are reproduced in the framework of the modified potential cluster model with forbidden states, and the rate of this reaction was calculated in the energy range from 25.3 meV to 10.0 MeV.

Theoretical and practical significance

The formalism presented for the scattering matrix of particles with a spin structure $\vec{s}_1 + \vec{s}_2 = \vec{1} + \vec{1}/2$, $\vec{s}_1 + \vec{s}_2 = \vec{1}/2 + \vec{3}/2$, and $\vec{s}_1 + \vec{s}_2 = \vec{1} + \vec{1}$ in the form of expansion in partial amplitudes allows one to carry out a sequential phase shift analysis of experimental data both in elastic and inelastic scattering. The same amplitudes are structural elements for calculating polarization characteristics such as asymmetry of the angular distribution, vector and tensor polarizations, and polarization transfer coefficients.

The application area of the obtained mathematical formalism is not limited only to astrophysical problems; it can be used, for example, in the study of low-energy processes in plasma physics, in particular, to take into account quantum-mechanical effects, as well as in problems of hadron and meson scattering in intermediate-energy physics.

The analytical expressions for calculating the elastic scattering cross sections for any integer or half-integer values of the channel spin, due to their universality, open up the possibilities for the most optimal phase shift analysis for cases of one open channel in nuclear reactions. Such calculations are relevant, in particular, for taking into account quantum-mechanical effects in plasma, or molecular systems.

A detailed phase shift analysis further opens up the possibility of constructing binary interaction potentials of varying complexity – central, spin-spin, tensor, etc. In the future, based on the presented analytics, it is possible to create program codes and software for the consistent phase shift analysis based on the modern experimental data.

In the framework of the MPCM, the possibility of extracting the scattering phase shifts in an indirect way was demonstrated, namely, from experimental data on the

spectra of light nuclei – excitation energies E_{cm}, level widths Γ, quantum characteristics J^{π}, and also asymptotic normalization coefficients.

As an illustration of the MPCM capabilities, the process of radiative capture of neutrons $^{10}\mathrm{Be}(n,\gamma)^{11}\mathrm{Be}$ in the energy range $25.3\ \mathrm{meV} \le E \le 10.0\ \mathrm{MeV}$ is studied. The calculation of the total cross sections shows good agreement with the experimental data reconstructed from the measurements of Coulomb dissociation. To date, studies of stellar dynamics have relied on the only modelless calculations of Rauscher, 1993 for the reaction rate [41]. Our $<\sigma \mathrm{v}>$ calculations of the reaction $^{10}\mathrm{Be}(n,\gamma)^{11}\mathrm{Be}$ differ significantly from the Rauscher's data and, thus, can significantly change the idea of the role of the beryllium chain in the overall macroscopic picture of the fractions of the masses of light elements at an early stage of the evolution of the Universe.

In the framework of the MPCM, the cross sections of the $^3\mathrm{H}^3\mathrm{He}$ and $n^5\mathrm{Li}$ processes of radiative capture and their analytical parameterization were calculated. Based on these results, the reaction rates of these processes were calculated, their parameterization was obtained, and a comparison was made with the $^2\mathrm{H}^3\mathrm{He}$ and $^2\mathrm{H}^4\mathrm{He}$ capture reactions rates.

Based on comparisons of the rates of these reactions and the prevalence of light elements, it has been suggested that the two-step process $^2\mathrm{H} + {}^3\mathrm{He} \to {}^5\mathrm{Li} + \gamma$ and $n + {}^5\mathrm{Li} + \gamma \to {}^6\mathrm{Li} + \gamma$ can make a certain contribution to the formation of $^6\mathrm{Li}$ at BBN, especially at temperatures T_9 of the order of unity. In this temperature range, the number of neutrons has not yet begun to decrease, and the number of $^2\mathrm{H}$ deuterium nuclei and $^3\mathrm{He}$ isotope is already reaching its maximum, which leads to an increase in the yield of the $^2\mathrm{H} + {}^3\mathrm{He} \to {}^5\mathrm{Li} + \gamma$ reaction. Thus, additional quantitative calculations of the contribution of this reactions to the accumulation of the $^6\mathrm{Li}$ nucleus at BBN, in stars, and other astrophysical processes are required.

Personal contribution of the author. Alessya Tkachenko took part in all stages of research, including the development of a formalism for phase shift analysis and the MPCM implementation for studying astrophysical processes $^3\mathrm{He}(^2\mathrm{H},\gamma)^5\mathrm{Li}$ and $^{10}\mathrm{Be}(n,\gamma)^{11}\mathrm{Be}$. Research work was carried out at Al-Farabi Kazakh National University, as well as during a foreign internship held at the City University of New York (CUNY, New York, USA).

Research approbation and publications. The main results from the dissertation were published in local and Russian journals: *International Journal of Mathematics and Physics* [42], *Russian Physics Journal* [43-44], *News of NAS RK* [45]; in foreign scientific journals with impact-factor: *Nuclear Physics A* [46, 47] and *Astroparticle Physics* [48]; and also were reported and discussed at the following conferences: the 9th International Scientific Conference "*Modern Achievements of Physics and Fundamental Physical Education*" (October 12-14, 2016, Kazakhstan, Almaty) [49], the International Conference of Students and Young Scientists "*Farabi Alemy*" (April 10-13, 2017 and April 9-12, 2018, Almaty, Kazakhstan) [50-53], the International Scientific Forum "*Nuclear Science and Technology*" (September 12-15, 2017, Almaty, Kazakhstan) [54], the *International Conference on Few-Body Problems in Physics* (FB22) (July 9-13, 2018, Caen, France) [55].

The reliability of the results, first of all, is due to the fact that the calculations use the algebraic methods of the quantum theory of angular momentum. Moreover, the construction of interaction potentials and calculations of the characteristics of radiative capture reactions based on modern experimental data on level spectra, their width, asymptotic constants (ACs), cross sections and astrophysical S-factors. The reliability and validity of the results is also confirmed by publications in journals recommended by the Committee for Control of Education and Science of the Ministry of Education and Science of the Republic of Kazakhstan, as well as in the proceedings of international scientific conferences.

The connection of the thesis with research programs. The research work is carried out in accordance with the following programs:

1. "Study of the thermonuclear processes in the Universe" (0073-8/ПЦФ-15-МОН/1-16-ОТ, 2015-2017);

2. "Study of thermonuclear processes in stars and the primordial nucleosynthesis in the universe" (IRN: BR05236322-OT-19, 2018-2020);

Thesis structure and volume. The thesis consists of Introduction, four Sections, Conclusion, References and two Appendixes. It contains 19 figures and 14 tables. References consists of 146 items. The thesis is set out on 129 pages of printed text.

1 CONSTRUCTION OF A SCATTERING MATRIX IN CHANNELS WITH A SPIN STRUCTURE 1/2+1, 1/2+3/2 AND 1+1

Phase shift analysis is usually performed on the basis of expressions for the elastic scattering cross sections of nuclear particles, namely, on the basis of the representation of the differential cross sections for the elastic scattering through the phase shifts of elastic scattering [56-57].

Many of these expressions can be found in the scientific literature, and were subsequently collected in books [58] and [57, p. 120-136]. For example, the scattering of spinless particles on a zero spin target and a system of non-identical particles with a channel spin $S = 1/2$, such as $N-^4\text{He}$, is described in detail in works [57 P. 120-136, 59]. However, a particular difficulty is the calculation of differential cross sections for high-spin states (channel spin $S > 1$) of a system of particles. Results for a high channel spin, in particular, for a particle system with the spin structure $1/2 + 1$ and $1/2+3/2$ were given in Refs. [60] and [61], respectively.

However, we still lack fully analytical expressions for calculations of the differential elastic scattering cross sections for half-integer channel spins $S = 3/2$ and $S = 5/2$ and integer channel spins $S = 1$ and $S = 2$.

This Section covers the scattering phase shift formalism for the high-spin nuclear processes. In other words, one can find here the analytical expressions for the partial and total differential cross sections for the processes with the spin structures $1+1/2$, $1+3/2$ and $1+1$ to extract the scattering phase shifts, and under the high-spin processes are meant states with the channel spin $S \geq 1$. The corresponding independent partial amplitudes for each channel spin are obtained. These expressions are presented for *arbitrary* orbital angular momentum ℓ and taking into account spin-orbit splitting.

In addition, one can find in this Section the relation of parameters in the laboratory system and in the center of mass system, which can be useful in the available experimental data processing.

1.1 Theoretical formalism for particles with spins

Begin our discussion by considering a collision of two particles with spins. Only one of the particles can be a nucleon (in this case, the second particle is a proton or neutron) or both collision participants can be nuclei. When the two colliding particles have spins, these spins may be reoriented by the scattering process even if internal excitations of nuclei do not occur. The total angular momentum and its projection are conserved so that flipping one spin, which is related to changing the value of its projection on the z-axis, is compensated by a flip of the other or by an exchange of angular momentum with the relative orbital motion. In the latter case, the plane of the orbits is tilted [46, p. 3].

For the elastic scattering channel, the *differential cross section* can be written as [58, p. 171]

$$\frac{d\sigma}{d\Omega} = \sum_{S\nu\nu'} g(S) \frac{d\sigma(S)}{d\Omega}, \tag{1.1}$$

where $g(S)$ is the *statistical weight* for channel spin S

$$g(S) = \frac{2S+1}{(2s_1+1)(2s_2+1)}.$$ (1.2)

The spin of the scattering reaction channel is the result of the vector addition of the spins s_1 and s_2 of the incident and target particles and is

$$\mathbf{S} = \mathbf{s_1} + \mathbf{s_2}, \quad |s_1 - s_2| \le S \le s_1 + s_2.$$ (1.3)

In the general case, *the partial differential cross sections* can be written as

$$\frac{d\sigma(S)}{d\Omega} = \sum_{SS'vv'} g(S) M_{S'v'}^{Sv\,*} M_{S'v'}^{Sv},$$ (1.4)

where $M_{S'v'}^{Sv}$ are the matrix elements of the transition M-matrix [46, p. 3].

Here we consider the general case where the spins of both particles are coupled via the interaction potential (interaction potentials is described in more detail in Subsection 1.5). For an elastic scattering, when $S = S'$, equation (1.4) describes the partial cross section in equation (1.1).

In the channel spin representation, the relationship between the transition M-matrix and the scattering or collision matrix U is described by the expansion of the scattering amplitude in terms of the Legendre polynomials $P_n^m(\theta)$ as [62]:

$$M_{S'v'}^{Sv}(\theta) = f_c(\theta)\delta_{SS'}\delta_{vv'} + \frac{i}{2k}\left[\sum_{J\ell\ell'} \sqrt{\frac{(\ell'-m')!}{(\ell'+m')!}} C_{sv\ell0}^{Jv} C_{s'v'\ell'm'}^{Jv} \times \right.$$
$$\left. \times \exp\left[i(\omega_\ell + \omega_{\ell'})\right]\left(\delta_{SS'}\delta_{\ell\ell'} - U_{S'\ell'S\ell}^{J^\pi}\right)P_{\ell'}^{m'}(\theta)\right].$$ (1.5)

In this case the initial and final channel spins S and S' may take any possible values.

In equation (1.5) the following notations are used: S and S' are the spins of the initial and final channels, respectively, v and v' are their projections on the z-axis, ℓ and ℓ' are the orbital quantum numbers of the initial and final channels, $C_{a\alpha b\beta}^{c\gamma}$ are the Clebsch-Gordan coefficients, ω_ℓ are the Coulomb scattering phase shifts, and $U_{S'\ell'S\ell}^{J^\pi}$ is the scattering matrix. The *primes* hereinafter indicate the characteristics of the final state. The Coulomb amplitude is defined as follows

$$f_c(\theta) = -\left(\frac{\gamma}{2k\sin^2(\theta/2)}\right)\exp\left(i\gamma\ln\left[\sin^{-2}(\theta/2)\right] + 2i\omega_0\right).$$ (1.6)

In equation (1.6) θ is the scattering angle, k is the wave number of the relative motion of the colliding particles, $k^2 = 2\mu E / \hbar^2$, where μ is the reduced mass of the particles and E is the energy of colliding particles in the center of mass system (the relation between parameters in different reference systems is covered by Subsection 1.6), and $\gamma = \dfrac{\mu Z_1 Z_2 e^2}{k\hbar^2}$ is the Coulomb parameter, where Z is the particle's charge in units of the elementary charge.

For a proper description of the scattering cross section, it is sufficient to take into account only elastic channels. Then the collision U-matrix takes the form:

$$U_{S\ell} = \exp\left(2i\delta_{S\ell}\right). \tag{1.7}$$

The description of partial differential cross sections requires only those amplitudes for which $S = S'$. The matrix elements with $S \neq S'$ can be used for calculations of polarization effects, which require the consideration of spin-mixing states. For analytical calculations of elastic scattering cross sections i.e. for the case when the spins of the initial and final channels have the same value ($S = S'$) it is convenient to present the partial amplitudes of the M-matrix in a more succinct form [46, p. 4].

For this case the expression (1.5) could be written in the following form

$$M_{\nu'}^{S\nu}(\theta) \equiv M_{S\nu'}^{S\nu}(\theta) = \sum_{J\ell m} C_{S\nu\ell 0}^{J\nu} C_{S\nu'\ell m}^{J\nu} A_{J\ell}^{S} Y_{\ell m}(\theta, 0), \tag{1.8}$$

where

$$A_{J\ell}^{s}(\theta) = \frac{\sqrt{\pi}}{k}\begin{cases} f_c(\theta) + i(2\ell+1)^{1/2} \cdot \exp(2i\omega_\ell)(1 - U_{S\ell}^{J}), & \text{if} \quad \nu = \nu'; \\ i(2\ell+1)^{1/2} \cdot \exp(2i\omega_\ell)(1 - U_{S\ell}^{J}), & \text{if} \quad \nu \neq \nu'. \end{cases} \tag{1.9}$$

In the next step we perform the recoupling procedure for the Clebsch-Gordan coefficients in equation (1.8) using the relevant expression from [63]

$$C_{a\alpha f\varphi}^{d\delta} C_{b-\beta e\varepsilon}^{d\delta} = \sum_{c\gamma}(-1)^{c+d-\beta-\varphi}(2d+1)C_{a\alpha b\beta}^{c\gamma} C_{f-\varphi e\varepsilon}^{c\gamma}\begin{Bmatrix} a & b & c \\ e & f & d \end{Bmatrix}, \tag{1.10}$$

where $\begin{Bmatrix} \cdots \\ \cdots \end{Bmatrix}$ are Wigner $6j$-symbols. Therefore, using one-to-one correspondence for the $\{a \quad f \quad d\} \rightarrow \{S \quad \ell \quad J\}$ and $\{b \quad e \quad d\} \rightarrow \{S \quad \ell \quad J\}$ we can transform the product of the Clebsch-Gordan coefficients as

$$C_{Sv\ell0}^{Jv}C_{Sv'\ell m}^{Jv} = \sum_{\kappa m}(-1)^{\kappa+J-v'}(2J+1)C_{SvS-v'}^{\kappa m}C_{\ell0\ell m}^{\kappa m}\begin{Bmatrix} S & S & \kappa \\ \ell & \ell & J \end{Bmatrix}. \tag{1.11}$$

According to the rules of addition of angular momenta, the summation by κ in equation (1.11) includes the integers in the intervals $0 \le \kappa \le 2S$ and $0 \le \kappa \le 2\ell$ [46, p. 5].

Using the following symmetry properties of the Clebsch-Gordan coefficients [63, p. 207-210]

$$C_{a\alpha b\beta}^{c\gamma} = (-1)^{a+b-c}C_{b\beta a\alpha}^{c\gamma},$$

$$C_{a\alpha b\beta}^{c\gamma} = (-1)^{a+b}\sqrt{\frac{2c+1}{2a+1}}C_{c-\gamma b\beta}^{a-\alpha}, \tag{1.12}$$

$$C_{a\alpha b\beta}^{c\gamma} = (-1)^{a+b-c}C_{a-\alpha b-\beta}^{c-\gamma},$$

the first coefficient $C_{SvS-v'}^{\kappa m}$ in equation (1.11) can be rewritten as

$$C_{SvS-v'}^{\kappa m} = (-1)^{S+\kappa-v'}\sqrt{\frac{2\kappa+1}{2S+1}}C_{\kappa m Sv'}^{Sv}. \tag{1.13}$$

Thus, equations (1.9), (1.11) and (1.13) allow one to obtain the following form of the matrix elements $M_{v'}^{Sv}(\theta)$ [46, p. 5]:

$$M_{v'}^{Sv}(\theta) = \sum_{\kappa J \ell m}(-1)^{J+S}(2J+1)\sqrt{\frac{2\kappa+1}{2S+1}}C_{\kappa m Sv}^{Sv}C_{\ell0\ell m}^{\kappa m}\begin{Bmatrix} S & S & \kappa \\ \ell & \ell & J \end{Bmatrix}A_{J\ell}^{S}Y_{\ell m}(\theta,0). \tag{1.14}$$

Let us turn now to the construction of the differential cross section based on the $M_{v'}^{Sv}(\theta)$ matrix elements. According to equation (1.1) the differential cross section can be written as

$$\frac{d\sigma}{d\Omega} = \sum_{Svv'}g(S)M_{v'}^{Sv*}M_{v'}^{Sv}. \tag{1.15}$$

Substituting equation (1.14) into (1.15) we can perform the external summation over v and v' using the well-known relation for the Clebsch-Gordan coefficients [63, p. 219]

$$\sum_{a\alpha}C_{a\alpha b\beta}^{c\gamma}C_{a\alpha b\beta'}^{c\gamma'} = \frac{\Pi_c^2}{\Pi_b^2}\delta_{bb'}\delta_{\beta\beta'}, \text{ where}$$

$$\Pi_{ab...c} = \sqrt{(2a+1)(2b+1)...(2c+1)}. \tag{1.16}$$

14

The application of (1.16) leads to

$$\sum_{\nu\nu'} C_{\kappa m S\nu'}^{S\nu} C_{\kappa'm'S\nu'}^{S\nu} = \delta_{\kappa\kappa'}\delta_{mm'}\frac{2S+1}{2\kappa+1}. \tag{1.17}$$

Thus, considering (1.14) and (1.17) in equation (1.15), we obtain the final expression for the differential cross section as follows [46, p. 5]:

$$\frac{d\sigma}{d\Omega} = \sum_{S\kappa} g(S) \sum_{J\ell m} \left| (-1^J)(2J+1) C_{\ell 0\ell m}^{\kappa m} \begin{Bmatrix} S & S & \kappa \\ \ell & \ell & J \end{Bmatrix} A_{J\ell}^S Y_{\ell m}(\theta,0) \right|^2. \tag{1.18}$$

It should be noted that this expression for the differential cross section has a universal form and can be applied to any processes of elastic scattering, regardless of whether the channel spins are integer or half-integer.

In Table 1.1 [46, p. 6] the particles and light nuclei with the spins 1/2, 1, 3/2 and 2 relevant to the nucleosynthesis chain of light elements in the primordial Universe are listed.

Table 1.1. Possible incident particles and targets. J^{π} is the angular momentum and parity.

Z	Particle	J^{π}	Half-life	Z	Particle	J^{π}	Half-life
0	n	$1/2^+$	$880{,}0 \pm 0{,}9$ s	5	^{9}B	$3/2^-$	$8{,}00(300)\times10^{-16}$ s
1	p	$1/2^+$	Stable	5	^{11}B	$3/2^-$	Stable
1	d	1^+	Stable	5	^{12}B	1^+	$20{,}20(2)\times10^{-3}$ s
1	^{3}H	$1/2^+$	$12{,}32(2)$ years	5	^{14}B	$3/2^-$	$12{,}5(5)\times10^{-3}$ s
1	^{4}H	2^-	$1{,}39(10)\times10^{-22}$ s	5	^{15}B	2^-	$9{,}93(7)\times10^{-3}$ s
2	^{3}He	$1/2^+$	Stable	5	^{17}B	$3/2^-$	$5{,}08(5)\times10^{-3}$ s
3	^{4}Li	2^-	$91(9)\times10^{-24}$ s	6	^{9}C	$3/2^-$	$126{,}5(9)\times10^{-6}$ s
3	^{5}Li	$3/2^-$	$370(30)\times10^{-24}$ s	6	^{11}C	$3/2^-$	$20{,}334(24)$ min
3	^{6}Li	1^+	Stable	6	^{13}C	$1/2^-$	Stable
3	^{7}Li	$3/2^-$	Stable	6	^{15}C	$1/2^+$	$2{,}449(5)$ s
3	^{9}Li	$3/2^-$	$178{,}3(4)\times10^{-3}$ s	6	^{17}C	$3/2^+$	$193(5)\times10^{-6}$ s
3	^{10}Li	1^-	$2{,}0(5)\times10^{-21}$ s	6	^{19}C	$1/2^+$	$46{,}2(23)\times10^{-6}$ s
4	^{7}Be	$3/2^-$	$53{,}22(6)$ days	7	^{10}N	2^-	200×10^{-24} s
4	^{9}Be	$3/2^-$	Stable	7	^{13}N	$1/2^-$	$9{,}965$ min
4	^{11}Be	$1/2^+$	$13{,}81(8)$ s	7	^{15}N	$1/2^-$	Stable
5	^{7}B	$3/2^-$	$3{,}50(50)\times10^{-20}$ s	7	^{16}N	2^-	$7{,}13$ s
5	^{8}B	2^+	$770(3)\times10^{-3}$ s				

Table 1.1 clearly demonstrates possible participants of the scattering processes with the spin structure 1/2+1, 1/2+3/2 and 1+1.

1.2 Processes with spin-1/2 – spin-3/2

Let us consider the spin states for the collision of two particles with spin 1/2 and 3/2. In this case the collision of the following particles according to Table 1.1 can be considered: n, p, $^3\mathrm{H}(1/2^+)$, or $^3\mathrm{He}(1/2^+)$ as the first particle and $^5\mathrm{Li}(3/2^-)$, $^7\mathrm{Li}(3/2^-)$, $^9\mathrm{Li}(3/2^-)$, $^7\mathrm{Be}(3/2^-)$, $^9\mathrm{Be}(3/2^-)$, $^7\mathrm{B}(3/2^-)$, $^9\mathrm{B}(3/2^-)$, $^{11}\mathrm{B}(3/2^-)$, $^{13}\mathrm{B}(3/2^-)$, $^{15}\mathrm{B}(3/2^-)$, $^9\mathrm{C}(3/2^-)$, $^{11}\mathrm{C}(3/2^-)$, $^{17}\mathrm{C}(3/2^+)$, or $^{13}\mathrm{O}(3/2^-)$ as the second one [44, p. 1041, 46, p. 6].

In this case, according to the vector addition rule (1.3), the channel spin can be $S=1$ and $S=2$. For the channel with the integer spin values 1 and 2, the M-matrix, similar to scientific paper [60, p. 254], is represented as [46, p. 6]

$S\nu$ / $S'\nu'$	2 2	2 1	2 0	2 −1	2 −2	1 1	1 0	1 −1
2 2	Q_2^{22}	Q_2^{21}	Q_2^{20}	$-Q_{-2}^{22}$	Q_2^{2-2}	$\mathfrak{M}_{22}^{11}$	$\mathfrak{M}_{22}^{10}$	$\mathfrak{M}_{22}^{1-1}$
2 1	Q_1^{22}	Q_1^{21}	Q_1^{20}	Q_1^{2-1}	$-Q_{-1}^{22}$	$\mathfrak{M}_{21}^{11}$	$\mathfrak{M}_{21}^{10}$	$\mathfrak{M}_{21}^{1-1}$
2 0	Q_0^{22}	Q_0^{21}	Q_0^{20}	$-Q_0^{21}$	Q_0^{22}	$\mathfrak{M}_{20}^{11}$	0	$\mathfrak{M}_{20}^{11}$
2 −1	Q_{-1}^{22}	Q_1^{2-1}	$-Q_1^{20}$	Q_1^{21}	$-Q_1^{22}$	$-\mathfrak{M}_{21}^{1-1}$	$\mathfrak{M}_{21}^{10}$	$-\mathfrak{M}_{21}^{11}$
2 −2	Q_2^{2-2}	Q_{-2}^{21}	Q_2^{20}	$-Q_2^{21}$	Q_2^{22}	$\mathfrak{M}_{22}^{1-1}$	$-\mathfrak{M}_{22}^{10}$	$\mathfrak{M}_{22}^{11}$
1 1	$\mathfrak{M}_{11}^{22}$	$\mathfrak{M}_{11}^{21}$	$\mathfrak{M}_{11}^{20}$	$\mathfrak{M}_{11}^{2-1}$	$\mathfrak{M}_{11}^{2-2}$	T_1^{11}	T_1^{10}	T_1^{1-1}
1 0	$\mathfrak{M}_{10}^{22}$	$\mathfrak{M}_{10}^{21}$	0	$\mathfrak{M}_{10}^{21}$	$-\mathfrak{M}_{10}^{22}$	T_0^{11}	T_0^{10}	$-T_0^{11}$
1 −1	$\mathfrak{M}_{11}^{2-2}$	$-\mathfrak{M}_{11}^{2-1}$	$\mathfrak{M}_{11}^{20}$	$-\mathfrak{M}_{11}^{21}$	$\mathfrak{M}_{11}^{22}$	T_1^{1-1}	$-T_1^{10}$	T_1^{11}

$$M = \qquad (1.19)$$

In matrix (1.19) we use the letters T and Q for the notation of triplet and quintet spin states for partial amplitudes and the Fraktur letter $\mathfrak{M}$ denotes the and spin-mixing states partial amplitudes, respectively. We especially labeled spin-mixing states by the letter $\mathfrak{M}$ to avoid later confusion with the general labeling of matrix elements of the M-matrix [46, p. 6].

The matrix (1.19) has in total 64 partial amplitudes. Using parity conservation [63, p. 207-210], which restricts the sum $\ell + \ell'$ to being even, it is easy to show that

$$M_{S'-\nu'}^{S-\nu} = \begin{cases} (-1)^{S'-S+\nu'-\nu} M_{S'\nu'}^{S\nu}, & if \ S \neq S', \\ (-1)^{\nu'-\nu} M_{\nu'}^{S\nu}, & if \ S = S'. \end{cases} \qquad (1.20)$$

Thus, it is possible to reduce the number of independent partial amplitudes from 64 to 34. Considering that 2 of the 16 spin-mixing partial amplitudes equal to 0, finally 32 independent M-matrix elements remain.

The deferential cross section for the elastic scattering in a system of two particles with spin-1/2 – spin-3/2, taking into account the spin-orbit interaction, can be written as [46, p. 7]:

$$\frac{d\sigma}{d\Omega}(\theta) = \frac{3}{8}\frac{d\sigma_T}{d\Omega} + \frac{5}{8}\frac{d\sigma_Q}{d\Omega} \qquad (1.21)$$

The deferential cross section $d\sigma_T/d\Omega$ corresponds to the triplet state with channel spin $S = S' = 1$ and can be constructed as a combination of independent partial amplitudes from matrix (1.19). The deferential cross section for the elastic scattering in the triplet channel is determined only by five independent partial amplitudes T^{10}_0, T^{11}_1, T^{10}_1, T^{11}_0, and T^{1-1}_1 given by the 3×3 matrix in the lower right corner of matrix (1.19) and can be written as

$$\frac{d\sigma_T}{d\Omega} = \frac{1}{3}\left[\left|T^{10}_0\right|^2 + 2\left(\left|T^{11}_1\right|^2 + \left|T^{10}_1\right|^2 + \left|T^{11}_0\right|^2 + \left|T^{1-1}_1\right|^2\right)\right]. \qquad (1.22)$$

The analytical expressions obtained for the independent partial amplitudes $T^{1\nu}_{\nu'}$ for the scattering triplet state are:

$$T^{10}_0 = f_c(\theta) + \frac{1}{2ik}\sum_{\ell=0}\left[(\ell+1)\alpha^{\ell+1} + \ell\alpha^{\ell-1}\right]\exp(2i\omega_\ell)P_\ell(\cos\theta), \qquad (1.23)$$

$$T^{11}_1 = f_c(\theta) + \frac{1}{4ik}\sum_{\ell=0}\left[(\ell+2)\alpha^{\ell+1} + (2\ell+1)\alpha^\ell + (\ell-1)\alpha^{\ell-1}\right]\times$$
$$\times\exp(2i\omega_\ell)P_\ell(\cos\theta), \qquad (1.24)$$

$$T^{10}_1 = \frac{1}{2ik\sqrt{2}}\sum_{\ell=1}\left[\alpha^{\ell+1} - \alpha^{\ell-1}\right]\exp(2i\omega_\ell)P^1_\ell(\cos\theta), \qquad (1.25)$$

$$T^{11}_0 = \frac{1}{2ik\sqrt{2}}\sum_{\ell=1}\frac{1}{\ell(\ell+1)}\left[\ell(\ell+2)\alpha^{\ell+1} - (2\ell+1)\alpha^\ell - (\ell-1)(\ell+1)\alpha^{\ell-1}\right]\times$$
$$\times\exp(2i\omega_\ell)P^1_\ell(\cos\theta), \qquad (1.26)$$

$$T^{1-1}{}_1 = \frac{1}{4ik} \sum_{\ell=2} \frac{1}{\ell(\ell+1)} \left[\alpha^{\ell+1} - (2\ell+1)\alpha^{\ell} + (\ell+1)\alpha^{\ell-1} \right] \times$$

$$\times \exp(2i\omega_\ell) P_\ell^2 (\cos\theta). \tag{1.27}$$

The value $\alpha^J = \left(U_{S\ell}^{J^\pi} - 1 \right)$ for each state with full momentum J is entered here [46, p. 11].

   To describe *quintet* spin states with channel spin $S = S' = 2$, 13 independent amplitudes are required. The differential cross section $d\sigma_Q / d\Omega$ for the elastic scattering for a quintet spin state is described by the expression

$$\frac{d\sigma_Q}{d\Omega} = \frac{1}{3}\left[\left| Q^{20}_0 \right|^2 + 2\left(\left| Q^{21}_1 \right|^2 + \left| Q^{22}_2 \right|^2 + \left| Q^{20}_1 \right|^2 + \left| Q^{21}_0 \right|^2 + \left| Q^{22}_1 \right|^2 + \right. \right.$$

$$\left. \left. + \left| Q^{21}_2 \right|^2 + \left| Q^{2-1}_1 \right|^2 + \left| Q^{20}_2 \right|^2 + \left| Q^{22}_0 \right|^2 + \left| Q^{21}_{-2} \right|^2 \left| Q^{22}_{-1} \right|^2 + \left| Q^{2-2}_2 \right|^2 \right) \right]. \tag{1.28}$$

   The independent partial amplitudes Q^{20}_0, Q^{21}_1, Q^{22}_2, Q^{20}_1, Q^{21}_0, Q^{22}_1, Q^{21}_2, Q^{2-1}_1, Q^{20}_2, Q^{22}_0, Q^{21}_{-2}, Q^{22}_{-1}, Q^{2-2}_2 correspond to the case where the total spin in the incoming and outgoing channels are equal [46, p. 7]. We obtained the analytical expressions for $Q^{2\nu}_{\nu'}$ independent partial amplitudes:

$$Q^{20}_0 = f_c(\theta) + \frac{1}{4ik} \sum_{\ell=0} \left[\frac{3(\ell+1)(\ell+2)}{2\ell+3} \alpha^{\ell+2} + \frac{2\ell(\ell+1)(2\ell+1)}{(2\ell+3)(2\ell-1)} \alpha^{\ell} + \right.$$

$$\left. + \frac{3\ell(\ell-1)}{2\ell-1} \alpha^{\ell-2} \right] \exp(2i\omega_\ell) P_\ell (\cos\theta), \tag{1.29}$$

$$Q^{21}_1 = f_c(\theta) + \frac{1}{4ik} \sum_{\ell=0} \left[\frac{2(\ell+1)(\ell+3)}{2\ell+3} \alpha^{\ell+2} + \ell\alpha^{\ell+1} + \frac{3(2\ell+1)}{(2\ell+3)(2\ell-1)} \alpha^{\ell} + \right.$$

$$\left. + (\ell+1)\alpha^{\ell-1} + \frac{2\ell(\ell-2)}{2\ell-1} \alpha^{\ell-2} \right] \exp(2i\omega_\ell) P_\ell (\cos\theta), \tag{1.30}$$

$$Q^{22}_2 = f_c(\theta) + \frac{1}{8ik} \sum_{\ell=0} \left[\frac{(\ell+3)(\ell+4)}{2\ell+3} \alpha^{\ell+2} + 2(\ell+3)\alpha^{\ell+1} + \right.$$

$$\left. + \frac{6(\ell+2)(2\ell+1)(\ell-1)}{(2\ell-1)(2\ell+3)} \alpha^{\ell} + 2(\ell-2)\alpha^{\ell-1} + \frac{(\ell-2)(\ell-3)}{2\ell-1} \alpha^{\ell-2} \right] \times \tag{1.31}$$

$$\times \exp(2i\omega_\ell) P_\ell (\cos\theta),$$

$$Q^{20}_{1} = -\frac{\sqrt{6}}{4ik} \sum_{\ell=2} \frac{1}{(2\ell+3)(2\ell-1)} \Big[(\ell+2)(2\ell-1)\alpha^{\ell+2} - (2\ell+1)\alpha^{\ell} -$$
$$- (2\ell+3)(\ell-1)\alpha^{\ell-2} \Big] \exp(2i\omega_\ell) P^2_\ell(\cos\theta), \tag{1.32}$$

$$Q^{21}_{0} = -\frac{\sqrt{6}}{4ik} \sum_{\ell=1} \Big[\frac{\ell+3}{2\ell+3}\alpha^{\ell+2} - \frac{1}{\ell+1}\alpha^{\ell+1} - \frac{(2\ell+1)(3-\ell(\ell+1))}{\ell(\ell+1)(2\ell+3)(2\ell-1)}\alpha^{\ell} -$$
$$- \frac{1}{\ell}\alpha^{\ell-1} - \frac{\ell-2}{2\ell-1}\alpha^{\ell-2} \Big] \exp(2i\omega_\ell) P^1_\ell(\cos\theta), \tag{1.33}$$

$$Q^{22}_{1} = -\frac{1}{4ik} \sum_{\ell=1} \Big[\frac{(\ell+3)(\ell+4)}{(2\ell+3)(\ell+1)}\alpha^{\ell+2} + \frac{(\ell+3)(\ell-2)}{\ell(\ell+1)}\alpha^{\ell+1} -$$
$$- \frac{9(\ell+2)(2\ell+1)(\ell-1)}{\ell(2\ell-1)(2\ell+3)(\ell+1)}\alpha^{\ell} - \frac{(\ell+3)(\ell-2)}{\ell(\ell+1)}\alpha^{\ell-1} - \frac{(\ell-2)(\ell-3)}{\ell(2\ell-1)}\alpha^{\ell-2} \Big] \times \tag{1.34}$$
$$\times \exp(2i\omega_\ell) P^1_\ell(\cos\theta),$$

$$Q^{21}_{2} = -\frac{1}{4ik} \sum_{\ell=1} \Big[\frac{\ell+3}{2\ell+3}\alpha^{\ell+2} + \alpha^{\ell+1} - \frac{3(2\ell+1)}{(2\ell+3)(2\ell-1)}\alpha^{\ell} - \alpha^{\ell-1} -$$
$$- \frac{\ell-2}{2\ell-1}\alpha^{\ell-2} \Big] \exp(2i\omega_\ell) P^1_\ell(\cos\theta), \tag{1.35}$$

$$Q^{2-1}_{1} = \frac{1}{4ik} \sum_{\ell=2} \Big[\frac{2(\ell+3)}{(2\ell+3)(\ell+2)}\alpha^{\ell+2} - \frac{\ell+4}{(\ell+1)(\ell+2)}\alpha^{\ell+1} -$$
$$- \frac{9(2\ell+1)}{\ell(2\ell-1)(2\ell+3)(\ell+1)}\alpha^{\ell} - \frac{\ell-3}{\ell(\ell-1)}\alpha^{\ell-1} + \frac{\ell-2}{(2\ell-1)(\ell-1)}\alpha^{\ell-2} \Big] \times \tag{1.36}$$
$$\times \exp(2i\omega_\ell) P^2_\ell(\cos\theta),$$

$$Q^{20}_{2} = -\frac{\sqrt{6}}{8ik} \sum_{\ell=2} \frac{1}{(2\ell+3)(\ell-1)} \Big[(2\ell-1)\alpha^{\ell+2} - 2(2\ell+1)\alpha^{\ell} + (2\ell+3)\alpha^{\ell-2} \Big] \times \tag{1.37}$$
$$\times \exp(2i\omega_\ell) P^2_\ell(\cos\theta),$$

$$Q^{22}_{0} = \frac{\sqrt{6}}{8ik} \sum_{\ell=2} \Big[\frac{(\ell+3)(\ell+4)}{(2\ell+3)(\ell+1)(\ell+2)}\alpha^{\ell+2} - \frac{4(\ell+3)}{\ell(\ell+1)(\ell+2)}\alpha^{\ell+1} - \tag{1.38}$$

$$-\frac{4(2\ell+1)(\ell+4)(\ell-1)}{\ell(\ell+1)(2\ell+3)(2\ell-1)}\alpha^{\ell}+\frac{4(\ell-2)}{\ell(\ell+1)(\ell-1)}\alpha^{\ell-1}+\frac{(\ell-2)(\ell-3)}{\ell(2\ell-1)(\ell-1)}\alpha^{\ell-2}\Bigg]\times$$

$$\times\exp(2i\omega_\ell)P_\ell^2(\cos\theta),$$

$$Q^{21}_{-2}=-\frac{1}{4ik}\sum_{\ell=3}\Bigg[\frac{1}{(2\ell+3)(\ell+2)}\alpha^{\ell+2}-\frac{1}{(\ell+1)(\ell+2)}\alpha^{\ell+1}-$$

$$-\frac{3(2\ell+1)}{\ell(\ell+1)(2\ell+3)(2\ell-1)}\alpha^{\ell}+\frac{1}{\ell(\ell-1)}\alpha^{\ell-1}-\frac{1}{(2\ell-1)(\ell-1)}\alpha^{\ell-2}\Bigg]\times \qquad (1.39)$$

$$\times\exp(2i\omega_\ell)P_\ell^3(\cos\theta),$$

$$Q^{22}_{-1}=-\frac{1}{4ik}\sum_{\ell=3}\Bigg[\frac{\ell+4}{(2\ell+3)(\ell+1)(\ell+2)}\alpha^{\ell+2}-\frac{\ell+6}{\ell(\ell+1)(\ell+2)}\alpha^{\ell+1}+$$

$$+\frac{15(2\ell+1)}{\ell(2\ell-1)(2\ell+3)(\ell+1)}\alpha^{\ell}+\frac{\ell-5}{\ell(\ell-1)(\ell+1)}\alpha^{\ell-1}-\frac{\ell-3}{\ell(2\ell-1)(\ell-1)}\alpha^{\ell-2}\Bigg]\times \qquad (1.40)$$

$$\times\exp(2i\omega_\ell)P_\ell^3(\cos\theta),$$

$$Q^{2-2}_{2}=\frac{1}{8ik}\sum_{\ell=4}\Bigg[\frac{1}{(\ell+1)(\ell+2)(2\ell+3)}\alpha^{\ell+2}-\frac{2}{\ell(\ell+1)(\ell+2)}\alpha^{\ell+1}+$$

$$+\frac{6(2\ell+1)}{\ell(\ell+1)(2\ell+3)(2\ell-1)}\alpha^{\ell}-\frac{2}{\ell(\ell+1)(\ell-1)}\alpha^{\ell-1}+\frac{1}{\ell(\ell-1)(2\ell-1)}\alpha^{\ell-2}\Bigg]\times \qquad (1.41)$$

$$\times\exp(2i\omega_\ell)P_\ell^4(\cos\theta).$$

Independent amplitudes (1.29 – 1.41) are listed as the elements of 5×5 diagonal matrix in the upper left corner of matrix (1.19) [46, p. 11-13].

There are 30 amplitudes $\mathfrak{M}^{1\nu}_{2\nu'}$ and $\mathfrak{M}^{2\nu}_{1\nu'}$ for the spin-mixing states for the collision of particles with spins 1/2 and 3/2. The number of these amplitudes can be reduced to 14 due to parity conservation (1.20) and considering that 2 spin-mixing partial amplitudes equal to 0. The analytical expressions for 7 independent $\mathfrak{M}^{1\nu}_{2\nu'}$ and 7 independent $\mathfrak{M}^{2\nu}_{1\nu'}$ partial spin-mixing amplitudes are obtained and the results are given in Appendix A, equations (A.1) – (A.14).

1.3 Processes with spin-1/2 – spin-1

In this case, according to (1.3), channel spin can be $S=1/2$ and $S=3/2$. For the channel with half-integer spin values 1/2 and 3/2 the M-matrix, just as it is in [61, p. 370], can be represented as [46, p. 8]

$$
M = \begin{array}{c|cccccc}
\begin{array}{c} S\nu \\ S'\nu' \end{array} & \frac{3}{2}\ \frac{3}{2} & \frac{3}{2}\ \frac{1}{2} & \frac{3}{2}\ -\frac{1}{2} & \frac{3}{2}\ -\frac{3}{2} & \frac{1}{2}\ \frac{1}{2} & \frac{1}{2}\ -\frac{1}{2} \\
\hline
\frac{3}{2}\ \frac{3}{2} & Q^{3/2\ 3/2}_{3/2} & Q^{3/2\ 1/2}_{3/2} & Q^{3/2\ -1/2}_{3/2} & -Q^{3/2\ 3/2}_{-3/2} & \mathfrak{M}^{1/2\ 1/2}_{3/2\ 3/2} & \mathfrak{M}^{1/2\ -1/2}_{3/2\ 3/2} \\[4pt]
\frac{3}{2}\ \frac{1}{2} & Q^{3/2\ 3/2}_{1/2} & Q^{3/2\ 1/2}_{1/2} & Q^{3/2\ -1/2}_{1/2} & Q^{3/2\ 3/2}_{-1/2} & \mathfrak{M}^{1/2\ 1/2}_{3/2\ 1/2} & \mathfrak{M}^{1/2\ -1/2}_{3/2\ 1/2} \\[4pt]
\frac{3}{2}\ -\frac{1}{2} & Q^{3/2\ 3/2}_{-1/2} & -Q^{3/2\ -1/2}_{-1/2} & Q^{3/2\ 1/2}_{1/2} & -Q^{3/2\ 3/2}_{1/2} & \mathfrak{M}^{1/2\ -1/2}_{3/2\ 1/2} & -\mathfrak{M}^{1/2\ 1/2}_{3/2\ 1/2} \\[4pt]
\frac{3}{2}\ -\frac{3}{2} & Q^{3/2\ 3/2}_{-3/2} & Q^{3/2\ -1/2}_{3/2} & -Q^{3/2\ 1/2}_{3/2} & Q^{3/2\ 3/2}_{3/2} & -\mathfrak{M}^{1/2\ -1/2}_{3/2\ 3/2} & \mathfrak{M}^{1/2\ 1/2}_{3/2\ 3/2} \\[4pt]
\frac{1}{2}\ \frac{1}{2} & \mathfrak{M}^{3/2\ 3/2}_{1/2\ 1/2} & \mathfrak{M}^{3/2\ 1/2}_{1/2\ 1/2} & \mathfrak{M}^{3/2\ -1/2}_{1/2\ 1/2} & \mathfrak{M}^{3/2\ -3/2}_{1/2\ 1/2} & D^{1/2\ 1/2}_{1/2} & D^{1/2\ -1/2}_{1/2} \\[4pt]
\frac{1}{2}\ -\frac{1}{2} & -\mathfrak{M}^{3/2\ -3/2}_{1/2\ 1/2} & \mathfrak{M}^{3/2\ -1/2}_{1/2\ 1/2} & -\mathfrak{M}^{3/2\ 1/2}_{1/2\ 1/2} & \mathfrak{M}^{3/2\ 3/2}_{1/2\ 1/2} & D^{1/2\ -1/2}_{1/2} & D^{1/2\ 1/2}_{1/2}
\end{array}
\qquad (1.42)
$$

In matrix (1.42) we use the Fraktur letter $\mathfrak{M}$ for spin-mixing states, while the letters D and Q denote doublet and quintet spin states. The matrix (1.42) is defined by 36 partial amplitudes. However, according to (1.20) the number of partial amplitudes of this *M*-matrix can be reduced from 36 to 18 independent partial amplitudes.

The differential cross section for elastic scattering in a system of two particles with spin-1/2 – spin-1, taking into account the spin-orbit interaction, takes the form:

$$
\frac{d\sigma(\theta)}{d\Omega} = \frac{1}{3}\frac{d\sigma_D}{d\Omega} + \frac{2}{3}\frac{d\sigma_Q}{d\Omega}. \qquad (1.43)
$$

The channel spin S can take values 1/2 (doublet) and 3/2 (quartet) [46, p. 8].

In this case according to Table 1.1 n, p, ^{3}H(1/2$^+$), ^{3}He(1/2$^+$) and ^{2}H(1$^+$), ^{6}Li(1$^+$), ^{10}Li(1$^-$), ^{12}B(1$^+$) can be considered as colliding particles [43, p. 239, 46, p. 8].

The doublet state, which corresponds to the channel spin $S = S' = 1/2$, is described by two independent amplitudes $D^{1/2\ 1/2}_{1/2}$ and $D^{1/2\ -1/2}_{1/2}$ of matrix (1.42), which are presented by the 2×2 matrix in (1.42). The differential cross section for the elastic scattering in the *doublet* channel is well known and can be written as

$$
\frac{d\sigma_D}{d\Omega} = \left| D^{1/2\ 1/2}_{1/2} \right|^2 + \left| D^{1/2\ -1/2}_{1/2} \right|^2 \qquad (1.44)
$$

The cross section for the doublet spin channel is defined by two independent partial amplitudes. In equation (1.44) the expressions for the independent partial amplitudes $D^{1/2\ 1/2}_{1/2}$ and $D^{1/2\ -1/2}_{1/2}$ are [62, p. 272-274]

$$D^{1/2}\,{}^{1/2}_{1/2} = f_c(\theta) + \frac{1}{2ik}\sum_{\ell=0}\left[(\ell+1)\alpha^{\ell+1/2} + \ell\alpha^{\ell-1/2}\right]\exp(2i\omega_\ell)P_\ell(\cos\theta), \quad (1.45)$$

$$D^{1/2\,-1/2}_{1/2} = -\frac{1}{2ik}\sum_{\ell=1}\sqrt{\ell(\ell+1)}\left(\alpha^{\ell+1/2} - \alpha^{\ell-1/2}\right)\exp(2i\omega_\ell)P_\ell^1(\cos\theta). \quad (1.46)$$

The description of the *quartet* spin channel, $S = S' = 3/2$, is given by 16 partial amplitudes. However, as it follows from (1.20), only 8 independent $Q^{3/2}\,{}^{\nu}_{\nu'}$ amplitudes of matrix (1.42) are needed to describe the quartet spin channel. The differential cross section for the elastic scattering for a quartet state is defined as [46, p. 25]

$$\frac{d\sigma_Q}{d\Omega} = \frac{1}{2}\left(\left|Q^{3/2\,1/2}_{1/2}\right|^2 + \left|Q^{3/2\,3/2}_{3/2}\right|^2 + \left|Q^{3/2\,-1/2}_{1/2}\right|^2 + \left|Q^{3/2\,1/2}_{3/2}\right|^2 + \right.$$
$$\left. + \left|Q^{3/2\,-1/2}_{3/2}\right|^2 + \left|Q^{3/2\,3/2}_{1/2}\right|^2 + \left|Q^{3/2\,3/2}_{-1/2}\right|^2 + \left|Q^{3/2\,3/2}_{-3/2}\right|^2\right). \quad (1.47)$$

We obtained the analytical expressions for the independent partial quartet amplitudes $Q^{3/2\,1/2}_{1/2}$, $Q^{3/2\,3/2}_{3/2}$, $Q^{3/2\,-1/2}_{1/2}$, $Q^{3/2\,1/2}_{3/2}$, $Q^{3/2\,-1/2}_{3/2}$, $Q^{3/2\,3/2}_{1/2}$, $Q^{3/2\,3/2}_{-1/2}$, $Q^{3/2\,3/2}_{-3/2}$ in equation (1.42). They are:

$$Q^{3/2\,1/2}_{1/2} = f_c(\theta) + \frac{1}{4ik}\sum_{\ell=0}\left[\frac{3(\ell+1)(\ell+2)}{2\ell+3}\alpha^{\ell+3/2} + \frac{\ell(\ell+1)}{2\ell+3}\alpha^{\ell+1/2} + \right.$$
$$\left. + \frac{\ell(\ell+1)}{2\ell-1}\alpha^{\ell-1/2} + \frac{3\ell(\ell-1)}{2\ell-1}\alpha^{\ell-3/2}\right]\exp(2i\omega_\ell)P_\ell(\cos\theta), \quad (1.48)$$

$$Q^{3/2\,3/2}_{3/2} = f_c(\theta) + \frac{1}{4ik}\sum_{\ell=0}\left[\frac{(\ell+2)(\ell+3)}{2\ell+3}\alpha^{\ell+3/2} + \frac{3(\ell+1)(\ell+2)}{2\ell+3}\alpha^{\ell+1/2} + \right.$$
$$\left. + \frac{3\ell(\ell-1)}{2\ell-1}\alpha^{\ell-1/2} + \frac{(\ell-1)(\ell-2)}{2\ell-1}\alpha^{\ell-3/2}\right]\exp(2i\omega_\ell)P_\ell(\cos\theta), \quad (1.49)$$

$$Q^{3/2\,-1/2}_{1/2} = -\frac{1}{4ik}\sum_{\ell=1}\left[\frac{3(\ell+2)}{2\ell+3}\alpha^{\ell+3/2} - \frac{\ell+3}{2\ell+3}\alpha^{\ell+1/2} + \frac{\ell-2}{2\ell-1}\alpha^{\ell-1/2}\right.$$
$$\left. - \frac{3(\ell-1)}{2\ell-1}\alpha^{\ell-3/2}\right]\exp(2i\omega_\ell)P_\ell^1(\cos\theta), \quad (1.50)$$

22

$$Q^{3/2\ 1/2}_{\ \ \ 3/2} = -\frac{\sqrt{3}}{4ik}\sum_{\ell=1}\left[\frac{\ell+2}{2\ell+3}\alpha^{\ell+3/2} + \frac{\ell+1}{2\ell+3}\alpha^{\ell+1/2} - \frac{\ell}{2\ell-1}\alpha^{\ell-1/2} - \right.$$
$$\left. -\frac{\ell-1}{2\ell-1}\alpha^{\ell-3/2}\right]\times\exp(2i\omega_\ell)P_\ell^1(\cos\theta),\tag{1.51}$$

$$Q^{3/2\ -1/2}_{\ \ \ \ 3/2} = -\frac{\sqrt{3}}{4ik}\sum_{\ell=1}\left[\frac{(\ell+2)(\ell+3)}{(\ell+1)(2\ell+3)}\alpha^{\ell+3/2} + \frac{(\ell+2)(\ell-3)}{\ell(2\ell+3)}\alpha^{\ell+1/2} - \right.$$
$$\left. -\frac{(\ell+4)(\ell-1)}{(\ell+1)(2\ell-1)}\alpha^{\ell-1/2} - \frac{(\ell-1)(\ell-2)}{\ell(2\ell-1)}\alpha^{\ell-3/2}\right]\exp(2i\omega_\ell)P_\ell^1(\cos\theta),\tag{1.52}$$

$$Q^{3/2\ 3/2}_{\ \ \ 1/2} = \frac{\sqrt{3}}{4ik}\sum_{\ell=2}\left[\frac{1}{2\ell+3}\alpha^{\ell+3/2} - \frac{1}{2\ell+3}\alpha^{\ell+1/2} - \frac{1}{2\ell-1}\alpha^{\ell-1/2} + \right.$$
$$\left. +\frac{1}{2\ell-1}\alpha^{\ell-3/2}\right]\exp(2i\omega_\ell)P_\ell^2(\cos\theta),\tag{1.53}$$

$$Q^{3/2\ 3/2}_{\ \ \ -1/2} = \frac{\sqrt{3}}{4ik}\sum_{\ell=2}\left[\frac{\ell+3}{(\ell+1)(2\ell+3)}\alpha^{\ell+3/2} - \frac{\ell+6}{\ell(2\ell+3)}\alpha^{\ell+1/2} - \right.$$
$$\left. -\frac{\ell-5}{(\ell+1)(2\ell-1)}\alpha^{\ell-1/2} + \frac{\ell-2}{\ell(2\ell-1)}\alpha^{\ell-3/2}\right]\exp(2i\omega_\ell)P_\ell^2(\cos\theta),\tag{1.54}$$

$$Q^{3/2\ 3/2}_{\ \ \ -3/2} = -\frac{1}{4ik}\sum_{\ell=3}\left[\frac{1}{(\ell+1)(2\ell+3)}\alpha^{\ell+3/2} - \frac{3}{\ell(2\ell+3)}\alpha^{\ell+1/2} + \right.$$
$$\left. +\frac{3}{(\ell+1)(2\ell-1)}\alpha^{\ell-1/2} - \frac{1}{\ell(2\ell-1)}\alpha^{\ell-3/2}\right]\exp(2i\omega_\ell)P_\ell^3(\cos\theta).\tag{1.55}$$

There are 16 partial amplitudes that determine the spin-mixing states. According to equation (1.20) this number can be reduced to 8. The analytical expression for the spin-mixing independent partial $\mathfrak{M}^{1/2\ \nu}_{3/2\ \nu'}$ and $\mathfrak{M}^{3/2\ \nu}_{1/2\ \nu'}$ amplitudes of the M-matrix for the half-integer channel spin $S=1/2$ and $S=3/2$ are obtained and the corresponding amplitudes are presented in Appendix A, equations (A.15) – (A.22) [46, p. 9].

1.4 Processes with spin-1/2 – spin-2 and spin-1 – spin-3/2

These additional systems are considered in order to confirm the universality of the obtained analytical expressions (1.45) – (1.46) for a doublet state with S=1/2 and (1.48) – (1.55) for a quartet state with S=3/2 for partial cross sections.

For the processes with the spin structure 1/2 + 2 the channel spin can take the values S=3/2 and S=5/2. For a system with spin-1/2–spin-2 channel spin S can be 1/2, 3/2 and 5/2.

For the channel with the spin value $S = S' = 5/2$ of the incoming and outgoing channel, the part of M-matrix corresponding to the sextet spin channel is represented as

$$
M =
\begin{array}{c}
\begin{array}{c} Sv \\ S'v' \end{array}
\end{array}
\begin{array}{cccccc}
\frac{5}{2}\frac{5}{2} & \frac{5}{2}\frac{3}{2} & \frac{5}{2}\frac{1}{2} & \frac{5}{2}-\frac{1}{2} & \frac{5}{2}-\frac{3}{2} & \frac{5}{2}-\frac{5}{2}
\end{array}
$$

$$
M =
\begin{array}{c}
\frac{5}{2}\frac{5}{2} \\[4pt]
\frac{5}{2}\frac{3}{2} \\[4pt]
\frac{5}{2}\frac{1}{2} \\[4pt]
\frac{5}{2}-\frac{1}{2} \\[4pt]
\frac{5}{2}-\frac{3}{2} \\[4pt]
\frac{5}{2}-\frac{5}{2}
\end{array}
\left|
\begin{array}{cccccc}
S^{5/2\ 5/2}_{\ \ \ 5/2} & S^{5/2\ 3/2}_{\ \ \ 5/2} & S^{5/2\ 1/2}_{\ \ \ 5/2} & -S^{5/2\ 1/2}_{\ \ -5/2} & S^{5/2-3/2}_{\ \ \ 5/2} & -S^{5/2\ 5/2}_{\ \ -5/2} \\[6pt]
S^{5/2\ 5/2}_{\ \ \ 3/2} & S^{5/2\ 3/2}_{\ \ \ 3/2} & S^{5/2\ 1/2}_{\ \ \ 3/2} & S^{5/2-1/2}_{\ \ \ 3/2} & -S^{5/2\ 3/2}_{\ \ -3/2} & S^{5/2-5/2}_{\ \ \ 3/2} \\[6pt]
S^{5/2\ 5/2}_{\ \ \ 1/2} & S^{5/2\ 3/2}_{\ \ \ 1/2} & S^{5/2\ 1/2}_{\ \ \ 1/2} & -S^{5/2\ 1/2}_{\ \ -1/2} & S^{5/2-3/2}_{\ \ \ 1/2} & -S^{5/2\ 5/2}_{\ \ -1/2} \\[6pt]
S^{5/2\ 5/2}_{\ \ -1/2} & S^{5/2-3/2}_{\ \ \ 1/2} & S^{5/2\ 1/2}_{\ \ -1/2} & S^{5/2\ 1/2}_{\ \ \ 1/2} & -S^{5/2\ 3/2}_{\ \ \ 1/2} & S^{5/2\ 5/2}_{\ \ \ 1/2} \\[6pt]
S^{5/2-5/2}_{\ \ \ 3/2} & S^{5/2\ 3/2}_{\ \ -3/2} & S^{5/2-1/2}_{\ \ \ 3/2} & -S^{5/2\ 1/2}_{\ \ \ 3/2} & S^{5/2\ 3/2}_{\ \ \ 3/2} & -S^{5/2\ 5/2}_{\ \ \ 3/2} \\[6pt]
S^{5/2\ 5/2}_{\ \ -5/2} & S^{5/2-3/2}_{\ \ \ 5/2} & S^{5/2\ 1/2}_{\ \ -5/2} & S^{5/2\ 1/2}_{\ \ \ 5/2} & -S^{5/2\ 3/2}_{\ \ \ 5/2} & S^{5/2\ 5/2}_{\ \ \ 5/2}
\end{array}
\right|
\qquad (1.56)
$$

In the interaction of particles with spins 1/2 and 2, the channel spin can take the values $S=3/2$ (quartet state, $d\sigma_Q / d\Omega$) and $S = 5/2$ (sextet state, $d\sigma_S / d\Omega$). In this case the following particles from Table 1.1, which gives the quartet and sextet channel spin, can be involved in the collision process: n, p, ^{3}H(1/2$^+$), ^{3}He(1/2$^+$) and ^{4}H(2$^-$), ^{3}Li(2$^+$), ^{4}Li(2$^-$) ^{8}B(2$^+$), ^{14}B(2$^-$), ^{10}N(2$^-$), ^{16}N(2$^-$) [43 P. 239, 46, p. 9]. The corresponding differential cross section for the elastic scattering is

$$
\frac{d\sigma(\theta)}{d\Omega} = \frac{2}{5}\frac{d\sigma_Q}{d\Omega} + \frac{3}{5}\frac{d\sigma_S}{d\Omega}. \qquad (1.57)
$$

The partial differential cross section for the channel's spin $S = 5/2$ is represented by the following combination of amplitudes of matrix (1.56) [46, p. 9]

$$
\begin{aligned}
\frac{d\sigma_S}{d\Omega} = \frac{1}{2}\Bigg(& \left| S^{5/2\ 1/2}_{\ \ \ 1/2} \right|^2 + \left| S^{5/2\ 3/2}_{\ \ \ 3/2} \right|^2 + \left| S^{5/2\ 5/2}_{\ \ \ 5/2} \right|^2 + \left| S^{5/2\ 1/2}_{\ \ -1/2} \right|^2 + \\
& + \left| S^{5/2\ 1/2}_{\ \ \ 3/2} \right|^2 + \left| S^{5/2\ 3/2}_{\ \ \ 1/2} \right|^2 + \left| S^{5/2\ 3/2}_{\ \ \ 5/2} \right|^2 + \left| S^{5/2\ 5/2}_{\ \ \ 3/2} \right|^2 + \\
& + \left| S^{5/2-1/2}_{\ \ \ 3/2} \right|^2 + \left| S^{5/2\ 1/2}_{\ \ \ 5/2} \right|^2 + \left| S^{5/2-3/2}_{\ \ \ 1/2} \right|^2 + \left| S^{5/2\ 5/2}_{\ \ \ 1/2} \right|^2 + \\
& + \left| S^{5/2\ 1/2}_{\ \ -5/2} \right|^2 + \left| S^{5/2\ 3/2}_{\ \ -3/2} \right|^2 + \left| S^{5/2\ 5/2}_{\ \ -1/2} \right|^2 + \left| S^{5/2-3/2}_{\ \ \ 5/2} \right|^2 + \\
& + \left| S^{5/2-5/2}_{\ \ \ 3/2} \right|^2 + \left| S^{5/2\ 5/2}_{\ \ -5/2} \right|^2 \Bigg).
\end{aligned}
\qquad (1.58)
$$

where $S^{5/2}_{\ \ \nu'}^{\ \nu}$ are 18 independent partial amplitudes: $S^{5/2\ 1/2}_{\ \ \ 1/2}$, $S^{5/2\ 3/2}_{\ \ \ 3/2}$, $S^{5/2\ 5/2}_{\ \ \ 5/2}$, $S^{5/2\ 1/2}_{\ \ -1/2}$, $S^{5/2\ 1/2}_{\ \ \ 3/2}$, $S^{5/2\ 3/2}_{\ \ \ 1/2}$, $S^{5/2\ 3/2}_{\ \ \ 5/2}$, $S^{5/2\ 5/2}_{\ \ \ 3/2}$, $S^{5/2-1/2}_{\ \ \ \ 3/2}$, $S^{5/2\ 1/2}_{\ \ \ 5/2}$, $S^{5/2-3/2}_{\ \ \ \ 1/2}$, $S^{5/2\ 5/2}_{\ \ \ 1/2}$, $S^{5/2\ 1/2}_{\ \ -5/2}$, $S^{5/2\ 3/2}_{\ \ -3/2}$, $S^{5/2\ 5/2}_{\ \ -1/2}$, $S^{5/2-3/2}_{\ \ \ \ 5/2}$, $S^{5/2-5/2}_{\ \ \ \ 3/2}$, and $S^{5/2\ 5/2}_{\ \ -5/2}$. Results of our calculations for the 18 independent partial amplitudes $S^{5/2}_{\ \ \nu'}^{\ \nu}$ are [46, p. 29-32]:

$$S^{5/2\ 1/2}_{\ \ \ 1/2}= f_c(\theta)+\frac{1}{4ik}\sum_{\ell=0}\left[\frac{5(\ell+1)(\ell+2)(\ell+3)}{(2\ell+3)(2\ell+5)}\alpha^{\ell+5/2}+\frac{\ell(\ell+1)(\ell+2)}{(2\ell+3)(2\ell+5)}\alpha^{\ell+3/2}+\right.$$
$$+\frac{2\ell(\ell+1)(\ell+2)}{(2\ell+3)(2\ell-1)}\alpha^{\ell+1/2}+\frac{2\ell(\ell+1)(\ell-1)}{(2\ell+3)(2\ell-1)}\alpha^{\ell-1/2}+\frac{\ell(\ell+1)(\ell-1)}{(2\ell-1)(2\ell-3)}\alpha^{\ell-3/2}+ \qquad (1.59)$$
$$\left.+\frac{5\ell(\ell-1)(\ell-2)}{(2\ell-1)(2\ell-3)}\alpha^{\ell-5/2}\right]\exp(2i\omega_\ell)P_\ell(\cos\theta),$$

$$S^{5/2\ 3/2}_{\ \ \ 3/2}= f_c(\theta)+\frac{1}{8ik}\sum_{\ell=0}\left[\frac{5(\ell+1)(\ell+3)(\ell+4)}{(2\ell+3)(2\ell+5)}\alpha^{\ell+5/2}+\right.$$
$$+\frac{9\ell(\ell+2)(\ell+3)}{(2\ell+3)(2\ell+5)}\alpha^{\ell+3/2}+\frac{2(\ell+1)(\ell-3)^2}{(2\ell+3)(2\ell-1)}\alpha^{\ell+1/2}+\frac{2\ell(\ell+4)^2}{(2\ell+3)(2\ell-1)}\alpha^{\ell-1/2}+ \quad (1.60)$$
$$\left.+\frac{9(\ell+1)(\ell-1)(\ell-2)}{(2\ell-1)(2\ell-3)}\alpha^{\ell-3/2}+\frac{5\ell(\ell-2)(\ell-3)}{(2\ell-1)(2\ell-3)}\alpha^{\ell-5/2}\right]\exp(2i\omega_\ell)P_\ell(\cos\theta),$$

$$S^{5/2\ 5/2}_{\ \ \ 5/2}= f_c(\theta)+\frac{1}{8ik}\sum_{\ell=0}\left[\frac{(\ell+3)(\ell+4)(\ell+5)}{(2\ell+3)(2\ell+5)}\alpha^{\ell+5/2}+\right.$$
$$+\frac{5(\ell+2)(\ell+3)(\ell+4)}{(2\ell+3)(2\ell+5)}\alpha^{\ell+3/2}+\frac{10(\ell+3)(\ell+1)(\ell-1)}{(2\ell+3)(2\ell-1)}\alpha^{\ell+1/2}+$$
$$+\frac{10\ell(\ell+2)(\ell-2)}{(2\ell+3)(2\ell-1)}\alpha^{\ell-1/2}+\frac{5(\ell-1)(\ell-2)(\ell-3)}{(2\ell-1)(2\ell-3)}\alpha^{\ell-3/2}+ \qquad (1.61)$$
$$\left.+\frac{(\ell-2)(\ell-3)(\ell-4)}{(2\ell-1)(2\ell-3)}\alpha^{\ell-5/2}\right]\exp(2i\omega_\ell)P_\ell(\cos\theta),$$

$$S^{5/2\ 1/2}_{\ \ -1/2}= -\frac{1}{4ik}\sum_{\ell=1}\left[\frac{5(\ell+2)(\ell+3)}{(2\ell+3)(2\ell+5)}\alpha^{\ell+5/2}-\frac{(\ell+2)(\ell+5)}{(\ell+3)(2\ell+5)}\alpha^{\ell+3/2}+\right.$$
$$+\frac{2(\ell+2)(\ell-2)}{(2\ell+3)(2\ell-1)}\alpha^{\ell+1/2}-\frac{2(\ell+3)(\ell-1)}{(2\ell+3)(2\ell-1)}\alpha^{\ell-1/2}+\frac{(\ell-1)(\ell-4)}{(2\ell-1)(2\ell-3)}\alpha^{\ell-3/2}- \quad (1.62)$$
$$\left.-\frac{5(\ell-1)(\ell-2)}{(2\ell-1)(2\ell-3)}\alpha^{\ell-5/2}\right]\exp(2i\omega_\ell)P_\ell^1(\cos\theta),$$

$$S^{5/2\ 1/2}_{\quad\ 3/2}=-\frac{\sqrt{2}}{8ik}\sum_{\ell=1}\left[\frac{5(\ell+2)(\ell+3)}{(2\ell+3)(2\ell+5)}\alpha^{\ell+5/2}+\frac{(\ell+2)(3\ell+5)}{(2\ell+3)(2\ell+5)}\alpha^{\ell+3/2}-\right.$$

$$-\frac{2(\ell+1)(\ell+2)}{(2\ell+3)(2\ell-1)}\alpha^{\ell+1/2}+\frac{2\ell(\ell-1)}{(2\ell+3)(2\ell-1)}\alpha^{\ell-1/2}-\frac{(\ell-1)(3\ell-2)}{(2\ell-1)(2\ell-3)}\alpha^{\ell-3/2}- \quad (1.63)$$

$$\left.-\frac{5(\ell-1)(\ell-2)}{(2\ell-1)(2\ell-3)}\alpha^{\ell-5/2}\right]\exp(2i\omega_\ell)P_\ell^1(\cos\theta),$$

$$S^{5/2\ 3/2}_{\quad\ 1/2}=-\frac{\sqrt{2}}{8ik}\sum_{\ell=1}\left[\frac{5(\ell+3)(\ell+4)}{(2\ell+3)(2\ell+5)}\alpha^{\ell+5/2}+\frac{3(\ell+2)(\ell+3)(\ell-5)}{(\ell+1)(2\ell+3)(2\ell+5)}\alpha^{\ell+3/2}-\right.$$

$$-\frac{2(\ell^2+4\ell-6)(\ell-3)}{\ell(2\ell+3)(2\ell-1)}\alpha^{\ell+1/2}+\frac{2(\ell+4)(\ell^2-2\ell-9)}{(\ell+1)(2\ell+3)(2\ell-1)}\alpha^{\ell-1/2}- \quad (1,64)$$

$$-\frac{3(\ell+6)(\ell-1)(\ell-2)}{\ell(2\ell-1)(2\ell-3)}\alpha^{\ell-3/2}-\frac{5(\ell-2)(\ell-3)}{(2\ell-1)(2\ell-3)}\alpha^{\ell-5/2}\left.\right]\exp(2i\omega_\ell)P_\ell^1(\cos\theta),$$

$$S^{5/2\ 3/2}_{\quad\ 5/2}=-\frac{\sqrt{5}}{8ik}\sum_{\ell=1}\left[\frac{(\ell+3)(\ell+4)}{(2\ell+3)(2\ell+5)}\alpha^{\ell+5/2}+\frac{3(\ell+2)(\ell+3)}{(2\ell+3)(2\ell+5)}\alpha^{\ell+3/2}+\right.$$

$$+\frac{2(\ell+1)(\ell-3)}{(2\ell+3)(2\ell-1)}\alpha^{\ell+1/2}-\frac{2\ell(\ell+4)}{(2\ell+3)(2\ell-1)}\alpha^{\ell-1/2}-\frac{3(\ell-1)(\ell-2)}{(2\ell-1)(2\ell-3)}\alpha^{\ell-3/2}- \quad (1.65)$$

$$\left.-\frac{(\ell-2)(\ell-3)}{(2\ell-1)(2\ell-3)}\alpha^{\ell-5/2}\right]\exp(2i\omega_\ell)P_\ell^1(\cos\theta),$$

$$S^{5/2\ 5/2}_{\quad\ 3/2}=-\frac{\sqrt{5}}{8ik}\sum_{\ell=1}\left[\frac{(\ell+3)(\ell+4)(\ell+5)}{(\ell+1)(2\ell+3)(2\ell+5)}\alpha^{\ell+5/2}+\right.$$

$$+\frac{(\ell+2)(\ell+3)(\ell+4)(3\ell-5)}{\ell(\ell+1)(2\ell+3)(2\ell+5)}\alpha^{\ell+3/2}+\frac{2(\ell+3)(\ell-1)(\ell-8)}{\ell(2\ell+3)(2\ell-1)}\alpha^{\ell+1/2}-$$

$$-\frac{2(\ell+9)(\ell+2)(\ell-2)}{(\ell+1)(2\ell+3)(2\ell-1)}\alpha^{\ell-1/2}-\frac{(3\ell+8)(\ell-1)(\ell-2)(\ell-3)}{\ell(\ell+1)(2\ell-1)(2\ell-3)}\alpha^{\ell-3/2}- \quad (1.66)$$

$$\left.-\frac{(\ell-2)(\ell-3)(\ell-4)}{\ell(2\ell-1)(2\ell-3)}\alpha^{\ell-5/2}\right]\exp(2i\omega_\ell)P_\ell^1(\cos\theta),$$

$$S^{5/2\ -1/2}_{\quad\ 3/2}=\frac{\sqrt{2}}{8ik}\sum_{\ell=2}\left[\frac{5(\ell+3)}{(2\ell+3)(2\ell+5)}\alpha^{\ell+5/2}-\frac{(3\ell+10)}{(2\ell+3)(2\ell+5)}\alpha^{\ell+3/2}-\right.$$

$$-\frac{2(\ell+7)}{(2\ell+3)(2\ell-1)}\alpha^{\ell+1/2}-\frac{2(\ell-6)}{(2\ell+3)(2\ell-1)}\alpha^{\ell-1/2}-\frac{3\ell-7}{(2\ell-1)(2\ell-3)}\alpha^{\ell-3/2}+ \quad (1.67)$$

$$+\frac{5(\ell-2)}{(2\ell-1)(2\ell-3)}\alpha^{\ell-5/2}\Bigg]\exp(2i\omega_\ell)P_\ell^2(\cos\theta),$$

$$S^{5/2\ \ 1/2}_{\quad 5/2}=\frac{\sqrt{10}}{8ik}\sum_{\ell=2}\Bigg[\frac{\ell+3}{(2\ell+3)(2\ell+5)}\alpha^{\ell+5/2}+\frac{\ell+2}{(2\ell+3)(2\ell+5)}\alpha^{\ell+3/2}-$$

$$-\frac{2(\ell+1)}{(2\ell+3)(2\ell-1)}\alpha^{\ell+1/2}-\frac{2\ell}{(2\ell+3)(2\ell-1)}\alpha^{\ell-1/2}+\frac{\ell-1}{(2\ell-1)(2\ell-3)}\alpha^{\ell-3/2}+ \quad (1.68)$$

$$+\frac{\ell-2}{(2\ell-1)(2\ell-3)}\alpha^{\ell-5/2}\Bigg]\exp(2i\omega_\ell)P_\ell^2(\cos\theta),$$

$$S^{5/2-3/2}_{\quad 1/2}=\frac{1}{4\sqrt{2}ik}\sum_{\ell=2}\Bigg[\frac{5(\ell+3)(\ell+4)}{(\ell+2)(2\ell+3)(2\ell+5)}\alpha^{\ell+5/2}-$$

$$-\frac{3(\ell+3)(\ell+10)}{(\ell+1)(2\ell+3)(2\ell+5)}\alpha^{\ell+3/2}-\frac{2(\ell-3)\,(\ell^2-2\ell-18)}{\ell(\ell+2)(2\ell+3)(2\ell-1)}\alpha^{\ell+1/2}-$$

$$-\frac{2(\ell+4)\,(\ell^2+4\ell-15)}{(\ell+1)(\ell-1)(2\ell+3)(2\ell-1)}\alpha^{\ell-1/2}-\frac{3(\ell-2)(\ell-9)}{\ell(2\ell-1)(2\ell-3)}\alpha^{\ell-3/2}+ \quad (1.69)$$

$$+\frac{5(\ell-2)(\ell-3)}{(\ell-1)(2\ell-1)(2\ell-3)}\alpha^{\ell-5/2}\Bigg]\exp(2i\sigma_\ell)P_\ell^2(\cos\theta),$$

$$S^{5/2\ \ 5/2}_{\quad 1/2}=\frac{\sqrt{10}}{8ik}\sum_{\ell=2}\Bigg[\frac{(\ell+3)(\ell+4)(\ell+5)}{(\ell+1)(\ell+2)(2\ell+3)(2\ell+5)}\alpha^{\ell+5/2}+$$

$$+\frac{(\ell+3)(\ell+4)(\ell-10)}{\ell(\ell+1)(2\ell+3)(2\ell+5)}\alpha^{\ell+3/2}-\frac{2(\ell+3)\,(\ell^2+6\ell-22)}{\ell(\ell+2)(2\ell+3)(2\ell-1)}\alpha^{\ell+1/2}-$$

$$-\frac{2(\ell-2)\,(\ell^2-4\ell-27)}{(\ell+1)(\ell-1)(2\ell+3)(2\ell-1)}\alpha^{\ell-1/2}+\frac{(\ell-2)(\ell-3)(\ell+11)}{\ell(\ell+1)(2\ell-1)(2\ell-3)}\alpha^{\ell-3/2}+ \quad (1.70)$$

$$+\frac{(\ell-2)(\ell-3)(\ell-4)}{\ell(\ell-1)(2\ell-1)(2\ell-3)}\alpha^{\ell-5/2}\Bigg]\exp(2i\omega_\ell)P_\ell^2(\cos\theta),$$

$$S^{5/2\ 1/2}_{\quad -5/2}=-\frac{\sqrt{10}}{8ik}\sum_{\ell=3}\Bigg[\frac{1}{(2\ell+3)(2\ell+5)}\alpha^{\ell+5/2}-\frac{1}{(2\ell+3)(2\ell+5)}\alpha^{\ell+3/2}-$$

$$-\frac{2}{(2\ell+3)(2\ell-1)}\alpha^{\ell+1/2}+\frac{2}{(2\ell+3)(2\ell-1)}\alpha^{\ell-1/2}+\frac{1}{(2\ell-1)(2\ell-3)}\alpha^{\ell-3/2}- \quad (1.71)$$

$$-\frac{1}{(2\ell-1)(2\ell-3)}\alpha^{\ell-5/2}\Bigg]\exp(2i\omega_\ell)P_\ell^3(\cos\theta),$$

$$S^{5/2\ 3/2}_{\ \ -3/2} = -\frac{1}{8ik}\sum_{\ell=3}\left[\frac{5(\ell+4)}{(\ell+2)(2\ell+3)(2\ell+5)}\alpha^{\ell+5/2} - \right.$$

$$-\frac{9(\ell+5)}{(\ell+1)(2\ell+3)(2\ell+5)}\alpha^{\ell+3/2} + \frac{2(\ell+12)(\ell-3)}{\ell(\ell+2)(2\ell+3)(2\ell-1)}\alpha^{\ell+1/2} -$$

$$-\frac{2(\ell+4)(\ell-11)}{(\ell+1)(\ell-1)(2\ell+3)(2\ell-1)}\alpha^{\ell-1/2} + \frac{9(\ell-4)}{\ell(2\ell-1)(2\ell-3)}\alpha^{\ell-3/2} -$$

$$\left. -\frac{5(\ell-3)}{(\ell-1)(2\ell-1)(2\ell-3)}\alpha^{\ell-5/2}\right]\exp(2i\omega_\ell)P_\ell^3(\cos\theta),$$

(1.72)

$$S^{5/2\ 5/2}_{\ \ -1/2} = -\frac{\sqrt{10}}{8ik}\sum_{\ell=3}\left[\frac{(\ell+4)(\ell+5)}{(\ell+1)(\ell+2)(2\ell+3)(2\ell+5)}\alpha^{\ell+5/2} - \right.$$

$$-\frac{(\ell+15)(\ell+4)}{\ell(\ell+1)(2\ell+3)(2\ell+5)}\alpha^{\ell+3/2} - \frac{2(\ell^2-4\ell-42)}{\ell(\ell+2)(2\ell+3)(2\ell-1)}\alpha^{\ell+1/2} +$$

$$+\frac{2(\ell^2+6\ell-37)}{(\ell+1)(\ell-1)(2\ell+3)(2\ell-1)}\alpha^{\ell-1/2} + \frac{(\ell-3)(\ell-14)}{\ell(\ell+1)(2\ell-1)(2\ell-3)}\alpha^{\ell-3/2} -$$

$$\left. -\frac{(\ell-3)(\ell-4)}{\ell(\ell-1)(2\ell-1)(2\ell-3)}\alpha^{\ell-5/2}\right]\exp(2i\omega_\ell)P_\ell^3(\cos\theta),$$

(1.73)

$$S^{5/2-3/2}_{\ \ 5/2} = \frac{5}{8ik}\sum_{\ell=4}\left[\frac{1}{(\ell+2)(2\ell+3)(2\ell+5)}\alpha^{\ell+5/2} - \right.$$

$$-\frac{3}{(\ell+1)(2\ell+3)(2\ell+5)}\alpha^{\ell+3/2} + \frac{2(\ell-3)}{\ell(\ell+2)(2\ell+3)(2\ell-1)}\alpha^{\ell+1/2} +$$

$$+\frac{2(\ell+4)}{(\ell+1)(\ell-1)(2\ell+3)(2\ell-1)}\alpha^{\ell-1/2} - \frac{3}{\ell(2\ell-1)(2\ell-3)}\alpha^{\ell-3/2} +$$

$$\left. +\frac{1}{(\ell-1)(2\ell-1)(2\ell-3)}\alpha^{\ell-5/2}\right]\exp(2i\omega_\ell)P_\ell^4(\cos\theta),$$

(1.74)

$$S^{5/2-5/2}_{\ \ 3/2} = \frac{5}{8ik}\sum_{\ell=4}\left[\frac{\ell+5}{(\ell+1)(\ell+2)(2\ell+3)(2\ell+5)}\alpha^{\ell+5/2} - \right.$$

$$-\frac{3\ell+20}{\ell(\ell+1)(2\ell+3)(2\ell+5)}\alpha^{\ell+3/2} + \frac{2(\ell+17)}{\ell(\ell+2)(2\ell+3)(2\ell-1)}\alpha^{\ell+1/2} +$$

$$+\frac{2(\ell-16)}{(\ell+1)(\ell-1)(2\ell+3)(2\ell-1)}\alpha^{\ell-1/2} - \frac{3\ell-17}{\ell(\ell+1)(2\ell-1)(2\ell-3)}\alpha^{\ell-3/2} +$$

$$\left. +\frac{\ell-4}{\ell(\ell-1)(2\ell-1)(2\ell-3)}\alpha^{\ell-5/2}\right]\exp(2i\omega_\ell)P_\ell^4(\cos\theta),$$

(1.75)

$$S^{5/2\;5/2}_{\;\;\;-5/2} = -\frac{1}{2ik}\sum_{\ell=5}\sqrt{\frac{(\ell-5)!}{(\ell+5)!}}\left[\alpha^{\ell+5/2}-5\alpha^{\ell+3/2}+10\alpha^{\ell+1/2}-10\alpha^{\ell-1/2}+\right.$$

$$\left.+5\alpha^{\ell-3/2}-\alpha^{\ell-5/2}\right]\exp(2i\omega_\ell)P_\ell^{\,5}(\cos\theta). \tag{1.76}$$

For a system with spin-1/2–spin-2 channel spin S and S' can be 1/2, 3/2 and 5/2. In this case, the differential cross section for elastic scattering is determined by the expression [46, p. 10]

$$\frac{d\sigma(\theta)}{d\Omega}=\frac{1}{6}\frac{d\sigma_D}{d\Omega}+\frac{1}{3}\frac{d\sigma_Q}{d\Omega}+\frac{1}{2}\frac{d\sigma_S}{d\Omega}. \tag{1.77}$$

The collision of particles n, p, ^{3}H($1/2^+$), ^{3}He($1/2^+$) and ^{4}H(2^-), ^{3}Li(2^+), ^{4}Li(2^-) ^{8}B(2^+), ^{14}B(2^-), ^{10}N(2^-), ^{16}N(2^-) from Table 1.1, which leads to the channel spin 1/2, 3/2 and 5/2, can be considered. The corresponding independent partial amplitudes for $d\sigma_D/d\Omega$, $d\sigma_Q/d\Omega$ and $d\sigma_S/d\Omega$ cross sections are given by Equations (1.45) – (1.46), (1.48) – (1.55) and (1.58) – (1.76), respectively. The general form of the 12×12 matrix for the processes with spin-1/2 – spin-2 and spin-1 – spin-3/2 is presented in [43, p. 239]. The number of independent matrix elements can be reduced from 144 to 72. The doublet spin state with the channel spin $S = 1/2$ is described by only 2 partial amplitudes, while for the description of the quartet channel with spin $S = 3/2$ and the sextet spin state with $S = 5/2$, 8 and 18 independent matrix elements, respectively, are required.

This matrix also contains 8 independent spin-mixing amplitudes for the mixing doublet and quartet states. However, in the general case of the 12×12 matrix there are also 12 independent spin-mixing amplitudes $\mathfrak{M}^{1/2\;\nu}_{5/2\;\nu'}$ and $\mathfrak{M}^{5/2\;\nu}_{1/2\;\nu'}$ for the mixing doublet and sextet states, and 24 independent spin-mixing amplitudes $\mathfrak{M}^{3/2\;\nu}_{5/2\;\nu'}$ and $\mathfrak{M}^{5/2\;\nu}_{3/2\;\nu'}$ for the mixing quartet and sextet states. The spin-mixing amplitudes for the latter two cases can be obtained [46, p. 10].

To summarize, we can say that to describe the triplet state with the channel spin $S = 1$, 5 independent amplitudes $T^{1\nu}_{\;\nu'}$ required. To describe the quintet ($S = 2$), the number of independent amplitudes $Q^{3/2\;\nu}_{\;\;\;\nu'}$ increases to 13. The number of independent spin-mixing amplitudes $\mathfrak{M}^{1\nu}_{2\nu'}$ and $\mathfrak{M}^{2\nu}_{1\nu'}$ in this case is 14.

For the description of the half-integer doublet ($S = 1/2$) channel spin state only 2 independent partial amplitudes $D^{1/2\;\nu}_{\;\;\;\nu'}$ are required, while for the quartet state with the channel spin $S = 3/2$ the number of independent amplitudes $Q^{3/2\;\nu}_{\;\;\;\nu'}$ equals 8. There are 18 independent partial amplitudes $S^{5/2\;\nu}_{\;\;\;\nu'}$ for the sextet state with the channel spin S

= 5/2. In the case of mixing doublet and quartet states 8 independent spin-mixing amplitudes $\mathfrak{M}^{1/2\ \nu}_{3/2\ \nu'}$ and $\mathfrak{M}^{3/2\ \nu}_{1/2\ \nu'}$ are required [46, p. 10-11] .

Obviously, with an increase of the channel spin, the number of required independent amplitudes for a correct description of scattering processes increases. For low energy processes, whose description requires a small number of partial waves, general expressions for the partial amplitudes can be reduced to simple algebraic expressions.

The obtained expressions for the differential cross sections and independent partial amplitudes enable phase shift analyses for different integer and half-integer channel spins and allow one to find corresponding phase shifts using experimental data for a nucleon-nucleus and nuclear-nuclear reaction cross sections.

The results from Subsections 1.1 – 1.4 were previously presented in the scientific publications [42, p. 141-146, 43, p. 232-241, 44, p. 1036-1042, 46, p. 1-33, 49, p. 38, 51, p. 11, 54, p. 154].

The computer program was developed on the basis of the formulas from Subsections 1.1 – 1.4. As mentioned earlier, when experimental differential cross sections are known, one can usually find a set of parameters, so-called nuclear phase shifts. The set of nuclear phase shifts can reproduce properly the form of the experimental cross section. In this case, the quality of the description of the experimental data can be estimated by the χ^2-method. Obtaining the set of nuclear phase shifts is the multiparameter variation problem. Methods and frameworks that can be used for this problem solving are described in detail in the book [57, P.91-275].

It shows good results for simple cases, for example, for the 1/2 + 1 system (p-^{2}H system was used for a test program). However, when moving to a higher channel spin, significant deviations from the expected results are observed. Obviously, further clarification for the developed software is required. The text of the computer program is given in Appendix B.

In case of insufficient amount of experimental data on total cross sections alternative indirect methods for obtaining phase shifts and constructing interaction potentials can be used.

As mentioned above, relying on the experimental data of elastic scattering, such as the observed energy spectra and ACs for the bound states, as well as measured geometric characteristics such as charge and mass radii, one able to reconstruct the interaction potentials in a fixed binary cluster channel. This approach is known today as the potential cluster model (PCM). Section 2 discusses this method with allowance for forbidden states in more detail (so-called MPCM). Sections 3 and 4 show the specific results of using this method for solving astrophysical problems on the example of radiative capture reactions $^3\mathrm{He}(^2\mathrm{H},\gamma)^5\mathrm{Li}$ and $^{10}\mathrm{Be}(n,\gamma)^{11}\mathrm{Be}$.

1.5 Relationship of parameters in the laboratory and center of mass systems

To make the processing and calculations of the differential cross sections and corresponding scattering amplitudes independent on the choice of experimental performance we are presenting here the brand new convenient relationship for the

kinematic characteristics of the scattering processes, analogues of which we have not found in any other sources.

In studying various scattering phenomena of two particles two coordinate systems are usually used. The first system is the laboratory system (l.s.), in which one of the particles, called the target, is at rest before scattering, and the second one moves relative to it (this particle is called the incident particle or projectile). The second reference system is the center-of-mass (or inertia) system (c.m.), in which the common center of inertia of both colliding particles rests. In the center of inertia system, both particles move before the scattering towards each other and moves apart in opposite directions after the scattering. In experiments, all quantities are measured in a laboratory system, while a theoretical study of scattering processes is more convenient to carry out in a center of inertia system [64, p. 193-197].

Obtain the formulas that allow us to transfer the values obtained during the experiment from the laboratory system to the center-of-mass system. The following notations are introduced: m_1, υ_0 is mass and velocity of the first particle (incident particle), m_2 is a mass of the target at rest in the laboratory system, υ_1, υ_2 are the velocities of both particles before the collision in the cms, and υ'_1, υ'_2 are the velocities of the particles after scattering in the center of mass system. Figure 1.1 shows the scattering process of two particles in different systems.

We denote the angle of departure of the particle after scattering in the laboratory system as Θ_{LS}. The angle of momentum of the relative motion of particles in the center of mass system is denoted by Θ_{CM}.

The relationship between the angles Θ_{LS} and Θ_{CM} may be expressed by the following relation:

$$\cos\Theta_{CM} = \frac{m_1}{m_2}\left[\cos\Theta_{LS}\sqrt{\left(\frac{m_2}{m_1}\right)^2 - \sin^2\Theta_{LS}} - \sin^2\Theta_{LS}\right], \qquad (1.47)$$

or

$$\cos\Theta_{CM} = \cos\Theta_{LS}\sqrt{1 - \left(\frac{m_1}{m_2}\right)^2\sin^2\Theta_{LS}} - \frac{m_1}{m_2}\sin^2\Theta_{LS}. \qquad (1.48)$$
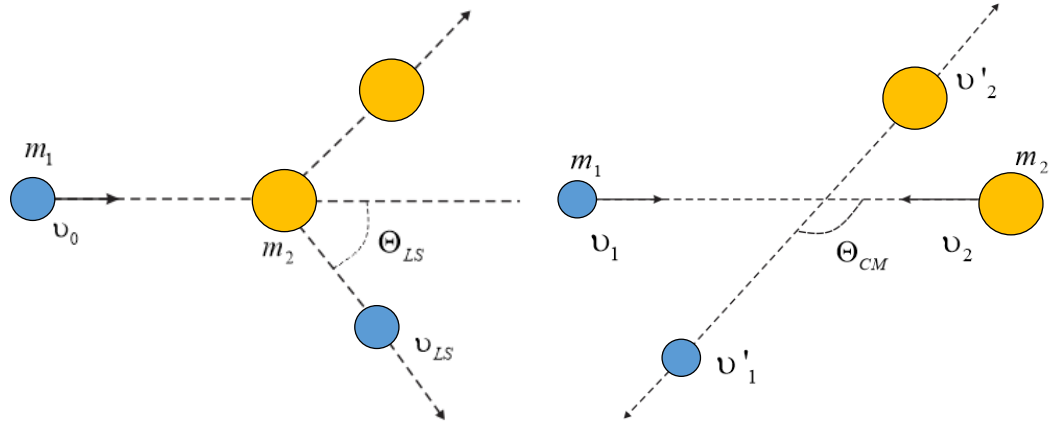
Scattering of two particles m₁ and m₂ in a laboratory system (left) and in the center-of-mass system (right)

Figure 1.1 – Scattering of two particles

We introduce the notation $\gamma = m_1 / m_2$ and as a result, we obtain the relation:

$$\cos \Theta_{CM} = \cos \Theta_{LS} \sqrt{1 - \gamma^2 \sin^2 \Theta_{LS}} - \gamma \sin^2 \Theta_{LS}. \tag{1.49}$$

Expression (1.49) gives the relation between the parameters in the laboratory system and the center-of-mass system.

This relation is used in Sections 3 and 4 in the processing of experimental data.

2 MPCM FRAMEWORK FOR THE DESCRIPTION OF CLUSTER-CLUSTER SYSTEMS RELEVANT FOR ASTROPHYSICAL APPLICATIONS

Analytical estimates of the reduction of the exact method of phase shifts analysis in the framework of the modified potential cluster model are presented in this Section, *e.g.* the problem of reconstructing the interaction potentials from the experimental observables is considered.

The principles for constructing the potentials of discrete and continuous spectra within the framework of MPCM, developed and substantiated in monographs and original works [8, p. 5-46 22, p. 40-94, 57, p. 10-69, 65, 66], are presented below.

Further in Sections 3 and 4, the results of calculations of the total cross sections and reaction rates based on the obtained interaction potentials for $^3\text{He}(^2\text{H},\gamma)^5\text{Li}$ and $^{10}\text{Be}(n,\gamma)^{11}\text{Be}$ processes are presented.

2.1 Model and methods

For calculating the astrophysical *S*-factors (for charged projectiles) and reaction rates, it is necessary at first to calculate the total cross sections.

Further, the necessary formulas and formalism elements for calculations of the radiative capture reactions characteristics are provided.

In this Subsection the basic methods of the radiative capture total cross-sections calculations, cluster states classification according to Young diagrams, and principles of intercluster interaction potential constructing in the used MPCM are considered in general.

2.1.1 Elements of formalism for radiative capture reactions

Consider the basic formulas for the calculation of the total cross sections for the electric *EJ* and magnetic *MJ* transitions.

The total cross-sections of radiative capture $\sigma(NJ,J_f)$ for the *EJ* and *MJ* transitions in the PCM are presented, for example, in [22, p. 59, 23, p. 29] and [67] and have the form

$$\sigma_c(NJ,J_{\mathrm{f}}) = \frac{8\pi Ke^2}{\hbar^2 q^3} \frac{\mu}{(2S_1+1)(2S_2+1)} \frac{J+1}{J[(2J+1)!!]^2} A_{\mathrm{J}}^2(NJ,K) \times$$
$$\times \sum_{\mathrm{L_i},\mathrm{J_i}} P_{\mathrm{J}}^2(NJ,J_{\mathrm{f}},J_{\mathrm{i}}) I_{\mathrm{J}}^2(J_{\mathrm{f}},J_{\mathrm{i}}), \tag{2.1}$$

where σ corresponds the radiative capture total cross-section, μ designates the reduced mass of initial channel particles in atomic mass unites, q is the wave number of initial channel particles, S_1 and S_2 denote the initial channel particles spins, K and J are the wave number and an angular moment of γ-quantum in the final channel respectively, and N corresponds to E or M transitions of J multipolarity from J_i initial to J_f final nucleus state [48, p. 93-94].

For *EJ(L)* electric orbital transitions ($S_i = S_f = S$) quantity P_J has the form [23, p. 29-30]

$$P_J^2(EJ, J_f, J_i) = \delta_{S_i S_f}[(2J+1)(2L_i+1)(2J_i+1)(2J_f+1)] \times$$

$$\times (L_i 0 J 0 | L_f 0)^2 \begin{Bmatrix} L_i & S & J_i \\ J_f & J & L_f \end{Bmatrix}^2, \qquad (2.2)$$

$$A_J(EJ, K) = K^J \mu^J \left(\frac{Z_1}{m^J_1} + (-1)^J \frac{Z_2}{m^J_2} \right), \quad I_J(J_f, J_i) = \langle \chi_f | r^J | \chi_i \rangle.$$

Here S_i, S_f, L_f, L_i, J_f, J_i denote the total spins and the moments of initial (i) and final (f) channels particles, m_1, m_2, Z_1, Z_2 correspond the masses (in amu) and charges (in "e" units) of the initial channel particles, I_J is the integral of the wave functions of χ_i initial and χ_f final state, as functions of relative motion of clusters with the intercluster distance r [48, p. 94].

For the spin part of $M1(S)$ magnetic process at $J = 1$ in the model used the following expression was obtained ($S_i = S_f = S$, $L_i = L_f = L$) [22, p. 59-61, 23, p. 30-32]:

$$P_1^2(M1, J_f, J_i) = \delta_{S_i S_f} \delta_{L_i L_f} \left[S(S+1)(2S+1)(2J_i+1)(2J_f+1) \right] \begin{Bmatrix} S & L & J_i \\ J_f & 1 & S \end{Bmatrix}^2,$$

$$(2.3)$$

$$A_1(M1, K) = i \frac{\hbar K}{m_0 c} \sqrt{3} \left(\mu_1 \frac{m_2}{m} - \mu_2 \frac{m_1}{m} \right), \quad I_J(J_f, J_i) = \langle \chi_f | r^{J-1} | \chi_i \rangle.$$

Here m is the nucleus mass in amu, μ_1, μ_2 are the clusters magnetic moments, and the remaining notation is the same as in the previous expression. The constant $\hbar^2 / m_0$ is equal to 41.4686 MeV·fm^2 [48, p. 94].

2.1.2 Principles for construction of interaction potentials

Earlier in the framework of the modified potential cluster model with the forbidden states the possibility of describing the astrophysical S-factors of radiative capture reactions on many light and the lightest atomic nuclei was shown. Such model takes into account the supermultiplet symmetry of the clusters system wave function (WF) with separation of orbital states according to Young diagrams [48, p. 94].

The used orbital state classification enables to analyze the intercluster interactions structure, to determine the presence and quantity of the allowed states (ASs) and forbidden states (FSs) in the intercluster wave functions, and therefore gives an opportunity to find number of nodes of the cluster relative motion WF. For any cluster system the task many-particle character and antisymmetrization effects are qualitatively taken into account by separation of one-particle bound levels of such potential into the states which are allowed or forbidden by the Pauli exclusion principle [68].

In the approach used the intercluster interaction potentials for scattering processes are constructed on the basis of the elastic scattering phase shifts description taking into

account their resonance behavior. These phase shifts come from the experimental data for differential cross-sections by applying the phase shift analysis [48, p. 94-95].

For the bound states (BSs) of light nuclei in the cluster channels the potentials are constructed not only on the basis of the scattering phase shifts description but also by using the certain additional requirements. For example, one of these requirements is the reproduction of binding energy and some other basic characteristics of the nuclei bound states, and in some cases this requirement is essential. In addition, it is assumed that a nucleus ground bound state is relevant to the cluster channel which consists of initial particles participating in the capture reaction [48, p. 95, 69, 70].

The choice of the modified potential cluster model for the description of such cluster systems in nuclei, nuclear and thermonuclear processes at astrophysical energies [71] is caused by that the possibility of forming the nucleon associations, i.e. clusters, in many light atomic nuclei, and the degree of their isolation from each other are comparatively high. It is confirmed by many experimental measurements and different theoretical calculations obtained by different authors during the last 50-60 years [72]. Such assumption, of course, is a certain idealization of situation really existing in the nucleus, because it assumes that there is 100% clusterization of the nucleus in the bound state (BS) for the initial channel particles [48, p. 95].

If one cluster channel is dominated in the nucleus structure, then the used one-channel cluster model allows us to identify this dominant cluster channel and describe the nuclear system properties caused by him [73].

Now let us consider in detail the procedure of construction of the partial intercluster potentials at the given orbital moment L and other quantum numbers by defining the criteria and sequence of finding parameters, and specifying their possible varieties and possible ambiguities [48, p. 95]. First the parameters of the ground states (GS) potentials are found. These parameters at the given number of the allowed and forbidden in the certain partial wave bound states are fixed quite uniquely by the binding energy, nucleus radius and an asymptotic constant in the considered channel.

The accuracy of the BS potential parameters calculation in such a way, is connected with the asymptotic constants (AC) accuracy which is equal to $10 \div 20\%$. Other ambiguities are absent in this potential because the classification of states according to Young diagrams allows to fix uniquely the number of the BSs which are forbidden or allowed in the given partial wave. This number determines completely the depth of the potential, while the potential width depends completely on the AC value [48, p. 95]. The principles for the FSs and ASs number determination in the given partial wave are presented below.

It should be noted here the charge radius calculations in any model contain the model varieties, i.e. the varieties caused by the model accuracy. In any model such radius values depend on the integral of the model WF, i.e. the model varieties of such functions are simply summarized. At the same time the AC values are determined by the model WFs in one point of their asymptotics and seemingly contain the appreciably small variety. Therefore, hereinafter the BSs potentials are constructed so that to be agreed with the AC values obtained by independent methods which allow determining the AC from the experimental data [74].

The intercluster potential of the nonresonance capture process is also constructed quite uniquely by using the scattering phase shifts at the given number of the BSs allowed and forbidden states in the considered partial wave. This potential parameters determination accuracy is connected mainly with the accuracy of determination of scattering phase shifts from the experimental data and may reach 20÷30%. As in the previous case such potential does not have any ambiguities because the states classification according to Young diagrams allows us to fix uniquely the BSs number which determines completely its depth. This potential width at the given depth is determined completely by a form of the elastic scattering phase shift [48, p. 95].

Upon construction of the nonresonance scattering potential by using the data for nuclei spectra in the definite channel, it is difficult to evaluate its parameters calculation accuracy even at the given number of the BSs, though one may seemingly hope this accuracy does not exceed the variety in the previous case. As it usually assumed for the energy region up to 1 MeV the same potential must lead to near-zero value of the scattering phase shift, or to the smoothly dropping form of the phase shift, if there are not any resonance levels in the nucleus spectra.

In the case of the resonance scattering analysis the potential is constructed uniquely, because at the given BSs number and energies up to 1 MeV there is a comparatively narrow resonance in the considered partial wave, the width of that is of the order of 10÷50 keV. At the given BSs number, the potential depth is fixed uniquely by the resonance level energy, and its width is determined completely by this resonance width. Its parameters variety as a rule does not exceed the variety of this resonance width determination and is equal to about 3 ÷ 5% [48, p. 95]. Moreover, it is also concerned to construction of the partial potential by using the scattering phase shifts, and its parameters determination on the basis of the resonance in the nucleus spectra.

As a result, all the potentials do not have any ambiguities that are common to the optical model, and, as one can see later, they allow us to describe correctly the radiative capture total cross-sections. The BSs potentials must describe correctly the known values of the AC which is connected with an asymptotic normalizing coefficient (ANC) determined from the experiment and denoted as A_{NC}, by the following expression [74, p. 3419-3424, 75]

$$A_{NC}^2 = S_f \cdot C^2, \tag{2.4}$$

where S_f is the spectroscopic factor, and C is the dimensional asymptotic constant expressed in $\mathrm{fm}^{-1/2}$

$$\chi_L(r) = C W_{-\eta L+1/2}(2k_0 r), \tag{2.5}$$

which is connected with the non-dimensional AC C_w [76] used by us

$$\chi_L(r) = \sqrt{2k_0} C_w W_{-\eta L+1/2}(2k_0 r), \tag{2.6}$$

in the following way:

$$C = \sqrt{2k_0}\,C_w \qquad\qquad (2.7)$$

In conclusion, it should be stressed that upon construction of the partial interaction potentials it is assumed they depend not only on the orbital moment *L,* but also on the total spin *S*, and the total moment *J* of the clusters system. In other words, for the different moments *JLS* we have different parameters' values. Since the *E*1 and *M*1 transitions between the different $^{(2S+1)}L_J$ states in the continuous and discrete spectra are usually considered, so the potentials of these states will be different [48, p. 95].

In addition, one of the modifications of the model used here is an assumption that the intercluster potentials dependent explicitly on the Young diagrams {*f*}. In other words, if two diagrams are allowed in the states of continuous spectrum and only one is allowed in the discrete spectrum, so such potentials can have different parameters at the same *JLS*, i.e. in the same partial wave.

2.2 Radiative ^{3}He(^{2}H, γ)^{5}Li capture

Let us now examine in more detail the various aspects of the ^{3}He(^{2}H, γ)^{5}Li reaction, including the experimental data presented in the data base of EXFOR [77] and the original papers cited therein.

Parametrization of the experimental data for ^{2}H capture in ^{3}He [30, p. 52-58] for the *S*-factor at energies from 0.2 to 1.0 MeV according to Breit-Wigner and its further extrapolation to zero energy leads to a value of 0.24 keV·b [47, p. 48].

Let us give for comparison several known values of the *S*-factors at zero energy for some radiative capture reactions. For example, the latest data for the astrophysical factor of the proton capture on ^{2}H give the value $S(0) = 0.216(11)\cdot10^{-3}$ keV·b [78], while in the scientific paper [79] is reported $S(0) = 0.166(14)\cdot10^{-3}$ keV·b. At the same time, for the proton capture on ^{3}H, $S(0) = 2.0(2)\cdot10^{-3}$ keV·b [80], *i.e.* an order of magnitude greater. Measurements in the research [81] lead to $S(0) =1.3(3)$ keV·b and $S(0) =6.0(1.2)\cdot10^{-6}$ keV·b for ^{3}H(^{2}H, γ)^{5}He and ^{2}H(^{2}H, γ)^{4}He capture, respectively. The *S*-factor for ^{2}H(^{2}H, γ)^{4}He capture is smaller due to the strong *E*1 transition in this process, which is forbidden due to equal masses of the particles in the initial channel [26, p. 112021].

In [81, p. 181-183], 0.36(9) keV·b is given for the astrophysical factor of the ^{3}He(^{2}H, γ)^{5}Li capture. At the same time, more recent results [34, p. R64] for the ^{3}He(^{2}H, γ)^{5}Li capture, the *S*-factor is $S(0) = 0.26(7)$ keV·b, which is in a good agreement with the value of 0.24 keV·b, which we report below. Although the error bands of these data [34, p. R64] and [81, p. 181-183] overlap, in fact, the values of the astrophysical factor of this reaction can be in the range 0.19–0.45 keV·b [47, p. 48]. This is a very large uncertainty for its values, which leads, despite the relatively low abundance of ^{3}He, to the rather large uncertainty of the contribution of the reaction under consideration to the primordial nucleosynthesis in the Universe and the processes of initial star formation.

Therefore, a more detailed study of this process will allow to obtain the results for the reaction rate and to compare it with the rates of other reactions of thermonuclear

fusion, given, for example, by [35, p. 283-294]. This work contains analytical parameterizations of rates for dozens of thermonuclear reactions, but there are no data for ^{3}He(^{2}H, γ)^{5}Li capture. Perhaps this is due to the fact that the rate of the reaction under study was considered to be negligible. However, below we show that the rate of this reaction at certain temperatures is larger than the rate of proton capture on ^{2}H and is comparable with the rate of proton capture on ^{3}H. Thus, the ^{3}He(^{2}H, γ)^{5}Li reaction rate among the rates of the processes of radiative capture in the considered temperature range of 0.01–10.0 T_9 is actually of the similar magnitude to the other processes which are considered as an important [47, p. 48].

2.2.1 Nuclear physics aspects and modern experimental results of the ^{3}He(^{2}H,γ)^{5}Li capture reaction

Let us present a survey of experimental measurements of the total cross sections of the ^{3}He(^{2}H,γ)^{5}Li capture as well as our estimation of the total cross section obtained from the measurements of differential cross sections and the polarization characteristics. From the point of view of nuclear physics, practically all experimental studies of the total cross sections of ^{3}He(^{2}H, γ)^{5}Li reaction for capturing to the ground state of ^{5}Li from the 1960s to the present are limited to two works published in late 1960s and early 1970s: [30, p. 52-58] and [31, p. 234-243]. Only in these works the total cross sections of the radiative ^{3}He(^{2}H, γ)^{5}Li capture at the astrophysical energy range are shown in an explicit form.

In paper [30, p. 47-64] measurements were made at a deuteron energy of 200–1360 keV in the laboratory system (l.s.). For the ^{3}He(^{2}H,γ)^{5}Li reaction separation of the transitions into the GS and the first excited state (FES) of ^{5}Li (see Figure 2.1) have been studied. However, as a result of the poor quality of the experimental data for the transition to the FES of ^{5}Li, the integral cross sections are presented only for the transition to the ground state with a value of 21(4) μb for $\sigma_{\gamma0,cm}$ at $E_R = E_{cm} = 0.27$ MeV [30].

The angular distributions measured in [30, p. 58] at $E_{cm} = 0.288$ and 0.615 MeV for the transition to the ground state of ^{5}Li was consistent with isotropy to within 10%. The total cross-sections obtained in [30, p. 56-58] with an accuracy of 20% are shown below in Figure 2.2 [47, p. 49].

In research [31, p. 234-243] the total cross sections were measured at excitation energy E_x from 17.4 to 21.1 MeV. If we use the binding energy for the ^{2}H^{3}He channel of 16.66 MeV [82, p. 27-29], we obtain capture energy of 0.74–4.44 MeV in the c.m. In paper [31, p. 235] the value of the binding energy of 16.4 MeV was used, which is close to 16.39 MeV given in [83, p. 18-19]. Using energy of 16.4 MeV, we obtain capture energy of 1.0–4.7 MeV in the c.m. These values will be used throughout the thesis.

The capture total cross sections obtained in work [31, p. 238-239] have a wide maximum (the width of 3–4 MeV) with the value of 59(3.0) μb at the energy $E_x = 19.7$ MeV, *i.e.* at 3.3 MeV in the c.m. This maximum points at the existing group of broad levels in this energy range. This group of levels at energies 19.28–22.06 MeV is clearly visible in the spectra of ^{5}Li [82, p. 27-29], shown in Figure 2.1 [47, p. 49].

22.06 (5/2⁻,1/2)

20.53 (1/2⁺,1/2)

19.96(3/2⁻,1/2)

19.71 (5/2⁺,1/2)

19.45 (7/2⁺,1/2)

19.31 (7/2⁺,1/2)

19.26 (3/2⁺,1/2)

19.28 (3/2⁻,1/2)

19.14 (5/2⁺,1/2)   ²H³H

16.87 (3/2⁺,1/2)   ²H³He   16.84 (3/2⁺,1/2)   16.70

16.388

1.27 (1/2⁻,1/2)

1.49 (1/2⁻,1/2)   [-0,51]

n⁴He

⁵He (3/2⁻,1/2)

⁵Li (3/2⁻,1/2)   p⁴He   -0.798

-1.69

Data is provided with a binding energy of ^{5}Li in the ^{3}He^{2}H channel of 16.39 MeV and a binding energy of ^{5}He in the ^{3}H^{2}H channel of 16.70 MeV [83].

Figure 2.1 – Experimental energy levels for ^{5}Li and ^{5}He from [82, p. 30-31]

The total cross sections for capture into the GS obtained in [31, p. 238-239] are shown in Figure 2.2. The angular distributions at angles $\theta_{\gamma,lab} = 0°–130°$ obtained in research [82, p. 30-31] for the transition to the GS of ^{5}Li were close to isotropic up to the energy of 4 MeV in c.m. The statistical error of the data obtained in [31, p. 234-243] was 5%, but due to the high uncertainty of the procedure of separating the peaks from the transitions to the ground and first excited states of ^{5}Li the error in the determination of the absolute values of the cross sections can reach up to 40% [47, p. 50].

Once again we note that the most complete databases of nuclear data such as EXFOR [77], as well as well-known atomic characteristics databases, for example, PHYSICS, CDFE, NASA DATA [85, 86], contain only these data for total cross sections of ^{3}He(^{2}H,γ)^{5}Li capture at low energies. Besides them, however, there are several publications [27, p. 1023-1029, 28, p. 593-602, 29, p. 1585-1587, 32, p. 429-431, 33, p. 921-922, 84, p. 345] in which measurements of the number of events observed in experiments with a polarized beam and differential capture cross sections are realized. Therefore, we perform a recalculation of some of the experimental

measurements of these studies with the extraction of the total cross sections from them [47, p. 50].
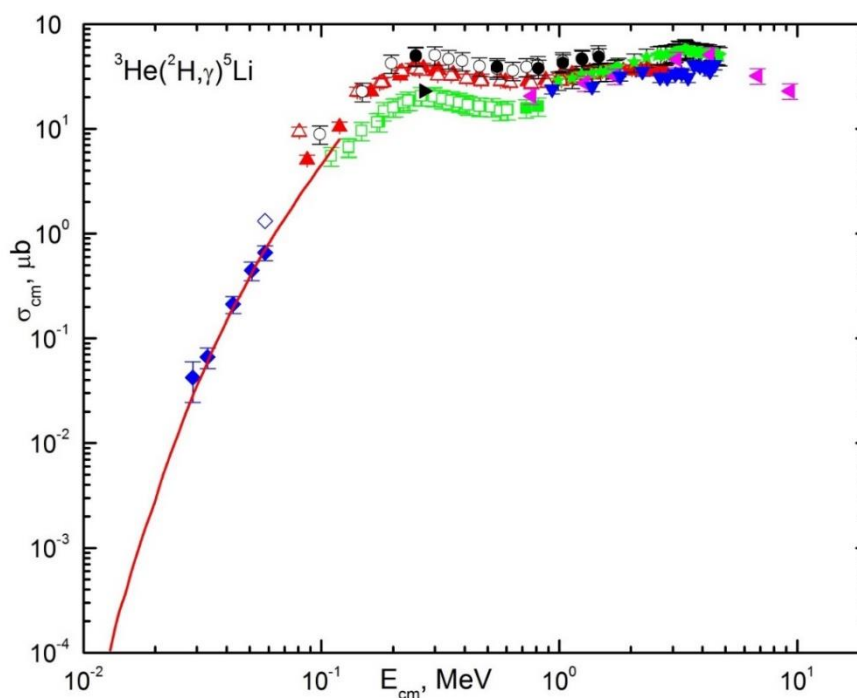
Experimental data: □ and ■ are from [30, p. 56-58] for γ_0, ★ are from [31, p. 238-239]. The other data are recounted by us: ○ and ● are from [27, p. 1023-1029] for $\gamma_0+\gamma_1$, △ and ▲ – from [28, p. 593-602] for γ_0, ▼ – from [29, p. 1585-1587] for $\gamma_0+\gamma_1$, for γ_0, ◄ – from [84, p. 345] for γ_0, ♦ for γ_0, ◊ for γ_1 – from [88, 89], ► – from [32, p. 429-431, 33, p. 921-922] for γ_0, and the solid curve is from [34, p. R63] for γ_0.

Figure 2.2 – The total cross sections of the ^{3}He(^{2}H,γ)^{5}Li capture

Let us now explore in more detail on the experimental aspects of above mentioned studies and make a comparison of the total cross sections obtained with their help.

Probably, for the first time, the yields of the ^{3}He(^{2}H,γ)^{5}Li reaction at low energies were measured by Blair et al. [27, p. 1023-1029] back in 1954. It was assumed that the reaction proceeds with capture to the ground and first excited states of the nucleus. However, due to the insufficient energy resolution, the peaks from these transitions could not be separated and as a result the total yield from all possible transitions was presented [47, p. 50].

The excitation function obtained for $\theta_{\gamma,\text{lab}} = 90°$ and $E_{\text{cm}} = 0.1–1.5$ MeV showed a wide resonance at $E_{\text{cm}} = 0.27$ MeV with a total cross section in the peak equal to 50(10) μb. Also authors of [27, p. 1023-1029], measured the angular distribution of the total yield of the reaction at $E_{\text{cm}} = 0.35$ MeV, which turned out to be isotropic with an accuracy of 10%. To obtain the integral cross sections from the data of [27, p. 1023-1029] the yield of this reaction, shown in Figure 4 in this work was normalized to the total cross section measured at $E_R = E_{cm} = 0.27$ MeV. In Figure 2.2 are presented the

integral cross sections, which we recalculated from the yield of the ^{3}He(^{2}H,γ)^{5}Li reaction given in [27, p. 1023-1029].

Subsequently, in [28, p. 593-602], the differential cross sections of the ^{3}He(^{2}H,γ)^{5}Li reaction for $\theta_{\gamma,\text{lab}} = 90^\circ$ were measured in the energy range $E_{\text{cm}} = 0.08$–2.76 MeV. Authors of Ref. [28, p. 593-602] could not find any indications of the presence of a peak from the transition to the first excited state of ^{5}Li in the spectra of the ^{3}He(^{2}H,γ)^{5}Li reaction, and the single broad peak in the spectra was interpreted as the peak from the transition to the ground state of ^{5}Li [47, p. 50-51]. However, it is possible that this broad peak contained also the transition to the first excited state of ^{5}Li but the accuracy of the experiment did not allow one to distinguish it [47, p. 50].

The measurement of the angular distributions at $E_{\text{cm}} = 0.3$ and 1.66 MeV with 7% error reported in scientific paper [28, p. 593-602] also turned out to be isotropic. The integral cross section obtained in [28, p. 593-602] for ^{3}He(^{2}H,γ)^{5}Li at the resonance energy $E_R = E_{\text{cm}} = 0.27$ MeV is 38(4) µb.

Furthermore, in work [29, p. 1585-1587] the sum of the differential cross sections of the reaction ^{2}H(^{3}He,γ)^{5}Li for the transitions to the ground and first excited states of ^{5}Li at $\theta_{\gamma,\text{lab.}} = 90^\circ$ in the energy range of $E_{\text{cm}} = 0.93$–4.5 MeV were measured. The obtained excitation function, accurate to within 10% of the measurement demonstrates a smooth growth with increasing energy without a clear indication of the presence of any resonances of the reaction ^{2}H(^{3}He,γ)^{5}Li in the considered energy range.

When we obtained the integral cross sections from the data of [28, P.593-602, 29, p. 1585-1587], the differential cross sections shown in Figure 5 of [28, p. 593-602] and Figure 2 of [29, p. 1587] were simply multiplied by 4π (here we assume the isotropy in the angular distributions that was shown in all works listed above) and these results are shown in Figure 2.2 [47, p. 51].

It can be seen from Figure 2.2 that the data of [28, p. 593-602] differ quite strongly from the measurements of [30, p. 56-58], although in both cases it is said that capture is only to the GS of ^{5}Li. In addition, the results of [29, p. 1585-1587] for capture to the GS and FES lie below the cross sections of research [31, p. 238-239] obtained for the capture to the GS [47, p. 51].

Somewhat later in work [84, p. 344-345] the excitation functions of the reaction ^{2}H(^{3}He, γ)^{5}Li at $\theta_{\gamma,\text{lab}} = 90^\circ$ and $E_{\text{cm}} = 0.76$–10.1 MeV for transitions to the ground and first excited states of ^{5}Li were obtained. Moreover, in scientific paper [84, p. 344-345] the sum of the differential cross sections for the transitions to the ground and first excited states of ^{5}Li at $\theta_{\gamma,\text{lab.}} = 90^\circ$ is given. For five energies, the angular distributions for these transitions were measured.

Work [84, p. 346] presented a table with the ratios of the coefficients of the Legendre functions of A_2/A_0 and A_1/A_0 for the cases when the first two and first three terms of the expansion in describing these angular distributions are taking into account [47, p. 51].

The error in determining the absolute values of the cross sections without taking into account the error in the procedure of separating of the peaks from the two transitions was 17%.

A change of the angular distributions with the energy and the form of the excitation functions of the ^{2}H(^{3}He,γ)^{5}Li reaction allowed the authors of work [84, p. 346-349] to make a conclusion about the existence of a broad resonance structure with the width of 3–4 MeV in the range of $E_{cm} = 0.76$–10.1 MeV and the maximum $\sigma_{\gamma 0} = 51(8)$ μb located at $E_{cm} \approx 4.3$ MeV. Using data [84, p. 344-345], we obtained the values of the integral cross section for $E_{cm} = 0.764$, 1.282, 1.712, 3.112, 4.312, 6.812, 9.312 MeV only for capture to the ground state of ^{5}Li, since the data of [84, p. 346-349] for the first excited state of ^{5}Li are unreadable due to the error of the order of 100% [47, P.51].

We obtain the cross section for the energy $E_{cm} = 0.764$, 1.282, and 1.712 MeV, by simply multiplying the differential cross sections [84, p. 345], taken from Figure 8 of this work by 4π, since at these energies the angular distributions are isotropic. We obtain the integral cross sections at $E_{cm} = 3.112$, 4.312, 6.812, 9.312 MeV, using data presented in Figure 8 and Table 1 from scientific paper [84, p. 345-346].

As a first step we find the coefficients A_0, and then these coefficients are multiplied by 4π. The calculated integral cross sections for the two cases from Table 1 of [84, p. 346] agree within their respective margins of error. These results are shown in Figure 2.2, which lie somewhat lower than the data given in [31, p. 238-239] for capture to the GS, but higher than the results reported in [29, p. 1585-1587], where the sum of the cross sections for transitions to the GS and FES of ^{5}Li were measured [47, P.51].

Using the polarized deuteron beam with $E_{cm} = 0.48$ MeV, a thick target of ^{3}He, which completely absorbed the beam energy, the angular distribution of the products of the reaction of deuteron capture by the ^{3}He to the ground state of ^{5}Li was measured [33, p. 921-922]. The obtained angular distribution of γ quanta was isotropic within the error of 10% [47, p. 52].

In a similar work [32, p. 429-431] data for a polarized deuteron beam with $E_{lab} = 0.6$ MeV and a ^{3}He target in which the deuterons lost 0.3 MeV were presented. Within the experimental error, the differential cross sections reported in researches [32, p. 429-431] and [33, p. 921-922] coincide. The total cross section, obtained from these differential cross sections is 23 μb and depicted in Figure 2.2 in position of the first resonance of the reaction, *i.e.* at $E_R = E_{cm} = 0.27$ MeV [47, p. 52].

To conclude this review, we note that the aforementioned difference in the energy of the channel reported by [82, p. 27-29] and [83, p. 16-18] force us to recalculate this energy. We used data for the masses of ^{2}H and ^{3}He 1875.613 MeV and 2808.392 MeV, respectively, from [85], and the mass of ^{5}Li (4667.617 MeV) was taken from the database of [86]. Then, for the binding energy of the ^{3}He^{2}H channel of ^{5}Li, a value of 16.388 MeV is obtained, which, within precision of rounding errors, coincides with 16.39 MeV given in [83, p. 16].

As we have already mentioned, a value of 16.66 MeV presented in [82, p. 27-29] differs significantly from the results and the data of the survey of [83, p. 16-18]. For ^{5}He in the ^{3}H^{2}H channel with $m(^3$H$) = 2808.921$ MeV [85] and $m(^5$He$) = 4667.838$ MeV [86], we have obtained $E_{bin.} = 16.696$ MeV, which is in good agreement with 16.70 MeV reported in [83, p. 16-18]. At the same time, the value of 16.792 MeV

given by Tilley *et al.* (2002) [82, p. 27-29] also differs noticeably from our results and the data of [83, p. 16-18].

2.2.2 Application of ^{2}H(^{3}He,γ)^{5}Li reaction to plasma problems

Now let us consider other experimental studies related to the plasma of synthesis reactors performed in references [81, p. 181-183, 87, 88, p. 691-692], which are applicable when considering the plasma of synthesis reactors. Work [81, p. 181-183] presented an astrophysical *S*-factor at zero energy and the total cross section of the ^{2}H(^{3}He,γ)^{5}Li reaction for the capture to the GS at 40 keV in c.m. [47, p. 52].

In [87, p. 412-413], the reaction rate of the ^{2}H(^{3}He,γ)^{5}Li capture to the GS is given and we use the latter rate further to compare with our results. The results for the total cross sections and the astrophysical *S*-factor for the capture to the GS at the energy range *13–120* keV in c.m. are given and the reaction rate at temperatures up to 1.0 T_9 is presented in [34, p. R63]. These results are also obtained for their application and use in the study of thermonuclear processes in the plasma of artificial thermonuclear fusion reactors. In Figure 2.2 the corresponding integral cross sections from scientific paper [34 P. R63-R64] for nuclei not screened by the electron shells of atoms are depicted by the solid curve [47, P.52].

All these results are based on the experimental work of [88, p. 691-692], in which the ^{3}He(^{2}H,γ)^{5}Li reaction was studied at $E_{cm} = 0.025$–0.06 MeV. In [88, p. 691-692] the branching ratios for the ^{3}He(^{2}H,γ_0)^{5}Li/^{3}He(^{2}H,p)^{4}He at five energies within the aforementioned range and for the ^{3}He(^{2}H,γ_1)^{5}Li/ ^{3}He(^{2}H,p)^{4}He at $E_{cm} \approx 0.06$ MeV were measured within the errors range 12% to 40%.

It is shown in [88, p. 691-692], that the ratio of the branching of ^{3}He(^{2}H,γ_0)^{5}Li/ ^{3}He(^{2}H,p)^{4}He in the range of $E_{cm} = 0.025$–0.06 MeV is practically constant and equal to $(4.5\pm1.2)\cdot10^{-5}$, and for the case of ^{3}He(^{2}H,γ_1)^{5}Li/ ^{3}He(^{2}H,p)^{4}He at $E_{cm} \approx 0.06$ MeV the value of $(8 \pm 3)\cdot10^{-5}$ is obtained. Moreover, the authors of [88, p. 691-692] carried out a simple extrapolation of the branching ratio for the ^{3}He(^{2}H,γ_0)^{5}Li/ ^{3}He(^{2}H,p)^{4}He to the point of 0 keV and the value of $(8 \pm 2)\cdot10^{-5}$ was obtained [47, p. 52].

However, it is possible that the increased value of the branching ratio for the transition to the ground state obtained at the lowest energy in work [88, p. 691-692] can be explained by the large error of about 40%, and that in fact the ratio of the branching for the ^{3}He(^{2}H,γ_0)^{5}Li/^{3}He(^{2}H,p)^{4}He is constant up to 0 keV and equal to $(4.5 \pm 1.2)\cdot10^{-5}$.

To obtain the integral cross sections of the reaction ^{3}He(^{2}H,$\gamma_{0,1}$)^{5}Li in the region $E_{cm} = 0.025$–0.06 MeV, presented in Figure 2.2, we use data from research [88, p. 691-692] and [89, p. 797] given in Figure 4 and Table 1 respectively. Work [89, p. 797-798] presented the astrophysical *S*-factor of the ^{3}He(^{2}H,p)^{4}He reaction for $E_{cm} = 0.008$–0.06 MeV with an error of about 3% [47, p. 52]. First, from the *S*-factors given in [89, p. 797-798] we obtain the integral cross sections for the energies considered in [88, 691-692], and then these cross sections we multiply by the values of the branching ratios for the ^{3}He(^{2}H,$\gamma_{0,1}$)^{5}Li/ ^{3}He(^{2}H,p)^{4}He from [88, p. 691-692].

Moreover, it can be seen from Figure 4 in scientific paper [89, p. 797-798] that in the range of $E_{cm} = 0.025$–0.06 MeV, the *S*-factors of the ^{3}He(^{2}H,p)^{4}He reaction for screened by the electron shells of the target atoms nuclei differ from *S*-factors for bare nuclei by no more than 5%. Therefore, in constructing the experimental bare integrated

cross sections for the ^{3}He(^{2}H,$\gamma_{0,1}$)^{5}Li reactions with an accuracy of 13–41%, we do not take into account the screening effects [47, p. 53].

There are theoretical studies [90-93], which provide based on various approaches descriptions of either the differential cross sections and the polarization characteristics, or the spectral levels and their widths. Modern "*ab initio*" microscopic calculations for systems with $A = 5$, as well as the reactions ^{3}H(^{2}H,n)^{4}He and ^{3}He(^{2}H,p)^{4}H in the context of applications to thermonuclear processes in the Big Bang and laboratory fusion are presented in scientific paper [94]. However, the processes of radiation capture, for example, ^{3}He(^{2}H,γ)^{5}Li the authors of did not consider.

Theoretical calculations that would include the main static and dynamic characteristics of the reaction ^{3}He(^{2}H,γ)^{5}Li and the final nucleus ^{5}Li could not be found, at least in the sources available to us. As a result one can conclude that consideration of all the experimental and theoretical works presented above, the capture reaction ^{3}He(^{2}H,γ)^{5}Li does not seem to be sufficiently studied both in the experimental and theoretical senses [47, p. 53].

The single-channel MPCM with forbidden states and the classification of cluster states according to Young diagrams are applied to study the radiative ^{3}He(^{2}H,γ)^{5}Li capture. This model is much simpler than the known Resonating Group Method (RGM) [95] and its modifications [96, 97], but in many cases it allows one to obtain quite reliable numerical results for many reactions such as radiative capture.

2.2.3 Scattering phase shifts, interaction potentials for elastic ^{2}H^{3}He scattering, and potentials for ^{2}H^{3}He bound states

We present the classification by orbital symmetries of the ^{2}H^{3}He and ^{2}H^{3}H systems, *i.e.* a configuration of 2+3 nucleons. The doublet channel spin ($S = 1/2$) scattering states depend on the two allowed orbital Young diagrams {41} and {32}, and these are regarded as mixed in terms of the orbital symmetries. The quartet channel spin ($S = 3/2$) allows only one symmetry {32}, so these states are pure according to the Young diagrams. Therefore, it is assumed that states with a minimal spin in some lightest cluster systems scattering processes, including those considered here, can turn out to be mixed in Young orbital diagrams, as was shown in [98].

The classification of states according to Young diagrams for these systems is given in Table 2.1 and was obtained in [98, p. 1513-1514, 99] on the basis of general tables of Young diagrams products from [100]. In Table 2.1 T, S and L are isospin, spin and the orbital angular momentum of the particle system, $\{f\}_S$, $\{f\}_T$, $\{f\}_{ST}$ and $\{f\}_L$ are spin, isospin, spin-isospin, and possible orbital Young diagrams, respectively and $\{f\}_{AS}$, $\{f\}_{FS}$ are Young diagrams of allowed and forbidden orbital states [47, p. 55].

Table 2.1 shows the forbidden state with the Young diagram {5} for the *S*-waves of doublet and quartet channels, while in the *P*-wave the forbidden state with the Young diagram {41} is present only for the quartet channel, in the doublet channel this state is allowed [47, p. 55].

At the same time, the states of clusters in the discrete spectrum, for example, the ground states of ^{5}He and ^{5}Li nuclei are assumed to be pure with the Young diagram {41} [98, p. 1513-1514]. Furthermore, it is assumed that since the scattering

states and the discrete spectrum depend on different Young diagrams, it is possible to juxtapose them different interaction potentials. In other words, explicit dependence of the potentials on the orbital symmetries {f} is allowed, and not only on the quantum numbers *JLS* – total angular momentum, orbital angular momentum and spin of the nuclear particles system [98, p. 1513-1514].

Table 2.1 – Classifications of ASs and FSs in cluster systems with $A = 5$.

System	T	S	$\{f\}_S$	$\{f\}_T$	$\{f\}_{ST}$	$\{f\}_L$	L	$\{f\}_{AS}$	$\{f\}_{FS}$
^{2}H^{3}He ^{2}H^{3}H	1/2	1/2	{32}	{32}	{5}+{41}+{32}+ {311}+{221}+{2111}	{5} {41} {32}	0 1 0,2	– {41} {32}	{5} – –
		3/2	{41}	{32}	{41}+{32}+{311} +{221}	{5} {41} {32}	0 1 0,2	– – {32}	{5} {41} –

We note that the total angular momentum $J = 3/2^-$ for the GS or $J = 1/2^-$ for the FES in *P* waves of ^{5}He or ^{5}Li nuclei can also be obtained in the doublet spin channel of ^{2}H^{3}He (^{2}H^{3}H) clusters with total spin $S = 1/2$ and in the quartet channel with $S = 3/2$. Therefore, the GS and FES of these systems are actually ^{2+4}P mixtures of such channels. These spin-mixed ^{2+4}P states turn out to be mixed also according to Young diagrams, since the doublet pure channel corresponds to the {41} diagram, and the quartet channel to the {32} one [47, p. 55].

However, now only one Young diagram corresponds to each spin channel, but not two, as it was in the previous case with mixing one spin channel in terms of orbital symmetries. Therefore, the potentials obtained below with $J = 3/2^-$ and $1/2^-$ for GS and FES are called pure, although in reality they are mixed along the spin, and, hence, along the Young diagrams.

In the present calculations of the nuclear characteristics of the reaction under consideration, the interaction potentials of particles have the form of a Gaussian attraction

$$V(r, JLS\{f\}) = V_{0,JLS\{f\}} \exp(-\alpha_{JLS\{f\}} r^2) + V_c(r) \qquad (2.8)$$

with the Coulomb potential $V_c(r)$ of two point particles for the zero Coulomb radius that has the form which was given above [47, p. 56].

Follow the reference [101] we considered the ^{2}H^{3}He scattering phase shifts in the energy range up to 3 MeV in the c.m., which are sufficient for solving various astrophysical problems, in particular, for calculating the total cross sections for the capture reaction.

Parameters of partial, *i.e.* depending on $^{2S+1}L_J$, potentials of the continuous spectrum, given in Table 2.2, including the resonance states potentials, which will be

described in detail later. The characteristics of these states are given in the last column of Table 2.2 [82, p. 27-29, 83, p. 16-18].

Table 2.2 – Parameters of the partial potentials of elastic ^{2}H^{3}He scattering. The characteristics of the potentials of the resonance states are given in the last column

$^{2S+1}L_J$	V_0, MeV	α, fm^{-2}	The resonance energy E_{cm}, MeV	The angular momentum and parity J^π
$^2S_{1/2}$, $^{2+4}D_{3/2}$	-30.0	0.15	–	–
$^{2+4}D_{5/2}$	-31.29	0.09	3.35	5/2$^+$
$^2P_{1/2}$	-48.0	0.1	–	–
$^{2+4}P_{3/2}$	-2412.2	4.0	2.89	3/2$^-$
$^4S_{3/2}$	-34.5 (-34.85)	0.1	0.48	3/2$^+$
$^4D_{1/2}$	-39.88	0.115	4.14	1/2$^+$
$^4D_{7/2}$	31.99	0.09	3.06	7/2$^+$
$^4P_{1/2}$	-30.0	0.1	–	–
$^4P_{5/2}$	- 456.7	0.8	5.67	5/2$^-$

The phase shifts of the *non-resonance doublet potentials* from Table 2.2, given in ordinary type, are shown by the solid curves in Figure 2.3a. For the potential of the $^2D_{3/2}$ wave the parameters of the $^2S_{1/2}$ potential at $L = 2$ were used. In $P_{3/2}$ and $D_{5/2}$ scattering waves that are mixed along the spin channel, there are resonances that follow from the nuclear spectra shown in Figure 2.1 [82, p. 27-29, 83, p. 16-18]. Parameters of such potentials are given in bold face in Table 2.2 and the corresponding phase shifts are shown in Figure 2.3a by the dashed curves [47, p. 56].

Let us further consider the potentials for quartet scattering states whose phase shifts are shown by the solid curves in Figure 2.3b. If we plot the $^4S_{3/2}$ potential over the scattering phase shifts, the parameters from Table 2.2 can be used. The phase shift of this potential is shown in Figure 3b by the solid curve 1. Using this potential at $L = 2$ the $^4D_{3/2}$ phase shift is obtained. It is shown in Figure 2.3b by the solid curve 2 [47, p. 57].

At 3.7 MeV in the c.m. the potential leads to a resonance with a width of 4.3 MeV in the c.m. It should be noted that in the spectra shown in Figure 2.1 such a resonance is not observed. Therefore, for $^4D_{3/2}$ waves we will use the $^2D_{3/2}$ scattering potential, since these states are spin-mixed with the same total momentum [47, p. 58].

Now we recall that we use a single-channel $d + {}^3$He model in which the influence of other channels is not taken into account. To substantiate the using of a single-channel model in this case, we provide interesting results from [94, p. 2-4], where they considered $d + {}^3$He elastic scattering in the framework of the *ab initio* method.
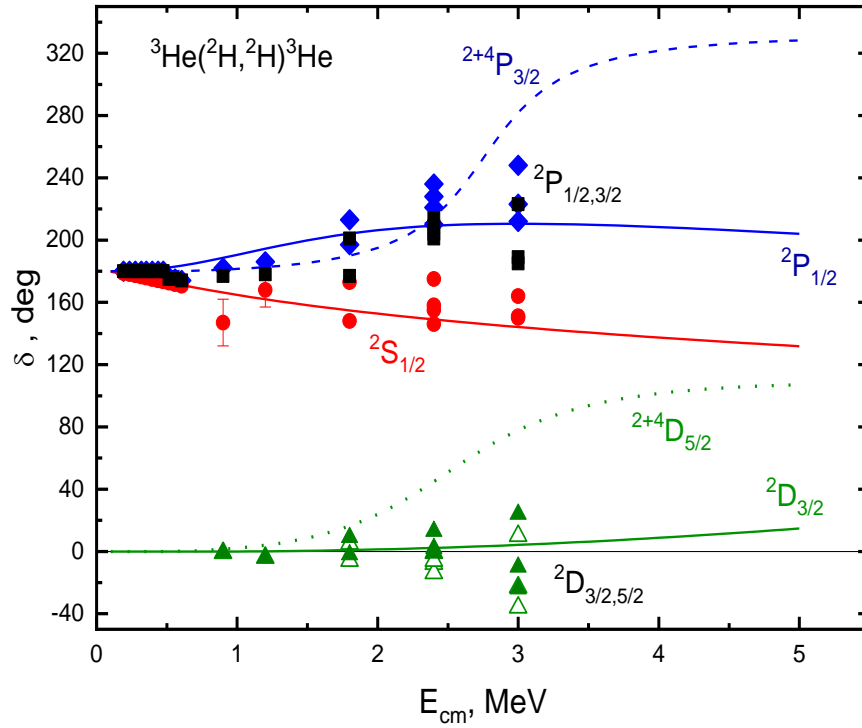
Symbols ■ and ◆ describes the results from [101, p. 98-99] for the $^2P_{1/2}$ and $^2P_{3/2}$ waves, ▲ and △ triangles – for the $^2D_{3/2}$ and $^2D_{5/2}$ waves, respectively, ● – for the $^2S_{1/2}$ wave. The notation for several total momentums $^2P_{1/2,3/2}$ refers to the results of [101, p. 98-99].

Figure 2.3a – Comparison of the $^2H+^3He$ doublet phase shifts mixed by orbital diagrams calculated using the potentials from Table 2.2 with results from [101, p. 98-99]

In Figure 2.3c we compare our theoretical calculations of the doublet and quartet S scattering phase shifts performed within the framework of the MPCM with to *ab initio* calculations [94, p. 2-4] and the experimental data. From the figure one can see that for the $^2S_{1/2}$ phase shift all variations of the calculations for a different number of channels yield very close results, *i.e.* the influence of other channels is almost negligible. For the *ab initio* $^4S_{3/2}$ phase shift channel coupling accounting (black dashed and dotted curves) also appears very slightly [47, p. 59].

The real agreement of the scattering phase shifts extracted from the experiment [101, p. 98-99], the present calculations, and *ab initio* is observed only when the channel $p + {}^4He$ and channel $^2H^* + {}^3He$ with the excited deuteron coupling is used in [94, p. 2-4]. In our opinion, this is a rather unexpected result, which, apparently, requires physical substantiation and interpretation. At the same time, for the purposes of our work, we can assume that the presented comparison makes it possible to draw a conclusion that the single-channel approximation employed in the present work is justified, since taking into account the two channels $p + {}^4He$ and $^2H^* + {}^3He$ in the *ab initio* method practically does not change the results for the scattering phase shifts in the single-channel case. It is well known that at low energies the asymptotic part of wave function plays a significant role in the most of nuclear processes, but at high energy the internal part of the wave function is very important due the strong *NN*

interaction at small distances, while the latter one has a slight influence on low energy characteristics of reactions [47, p. 57].
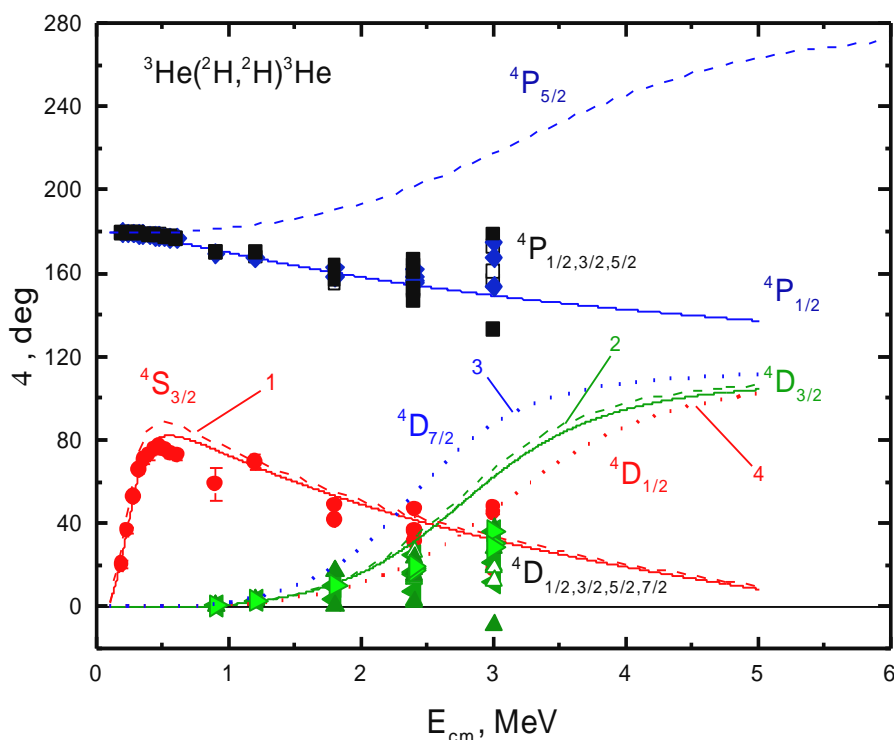
Symbols ■, ♦, and □ describes results from [101, p. 98-99] for the $^4P_{1/2}$, $^4P_{3/2}$ and $^4P_{5/2}$ waves, ▲ – for the $^4D_{1/2}$, △ – for the $^4D_{3/2}$, ◄ – for the $^4D_{5/2}$, and ► – for the $^4D_{7/2}$ waves, dots – for the $^4S_{3/2}$ wave. The notation for several total momentums $^4P_{1/2,3/2,5/2}$ is explained in Figure 2.3a.

Figure 2.3b – Comparison of the $^2H+^3He$ quartet phase shifts (solid curve), which pure by orbital diagrams calculated using the potentials from Table 2.2 with results from [101, p. 98-99]

Let us now consider in more detail the potentials for partial waves with resonances. Figure 2.1 clearly shows the first resonance of ^5Li, which is 0.482 MeV above the $^2H^3He$ channel threshold. The excitation energy, momentum and width in c.m are 16.87 MeV, $J^\pi = 3/2^+$, 0.267 MeV, respectively. This state can be attributed to a $^4S_{3/2}$ wave of the continuous spectrum, and its description requires a potential with FS for the diagram {5} and parameters

$$V_{S3/2} = -34.85 \text{ MeV and } \alpha = 0.1 \text{ fm}^{-2} \qquad (2.9)$$

which lead to a resonance energy of 0.480 (1) MeV in c.m [47, p. 57].
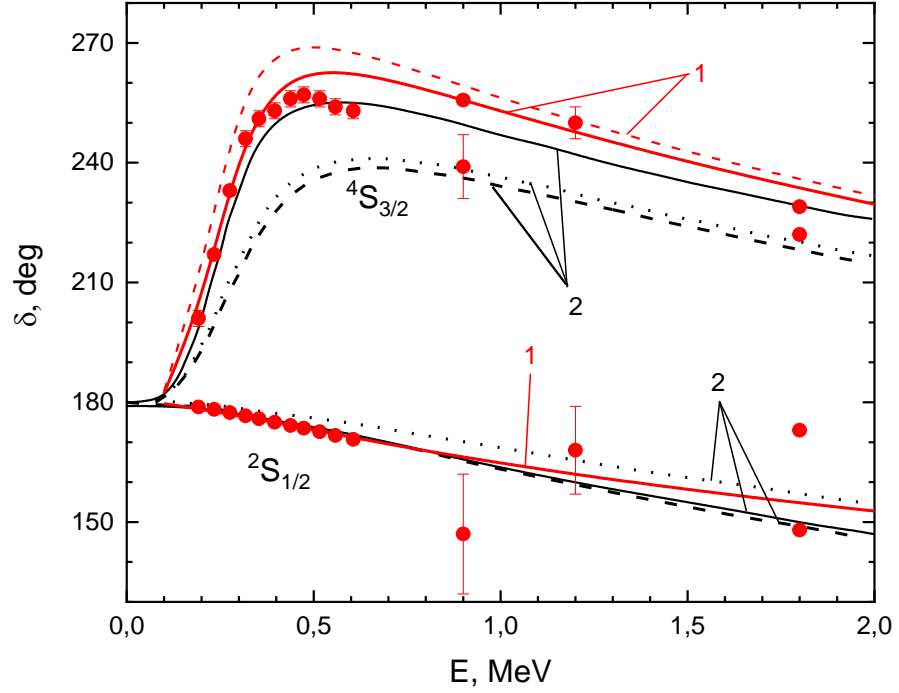
Potentials in MPCM are represented by group 1 (red curves), and *ab initio* [94, p. 2-4] corresponds the group 2 (black curves). The dashed curve – calculation taking into account the coupling of the $p + {}^4\text{He}$ and $d + {}^3\text{He}$ channels; dotted curve – calculation without regard to channel coupling; solid curve – calculation taking into account the channel $p + {}^4\text{He}$ and the excited deuteron in the $d^* + {}^3\text{He}$ channel coupling.

Figure 2.3c – Comparison of the calculations of the scattering S phase shifts for potentials in MPCM and in *ab initio* [94, p. 2-4]

The corresponding phase shift is shown in Figure 2.3b with the red dashed curve 1. For $L = 2$, the potential gives a ${}^4D_{3/2}$ phase shift resonance at 3.6(1) MeV in c.m. with a width of 4.1(1) MeV in c.m. Its phase shift is shown in Figure 2.3b with the dashed curve 2. The potential with parameters (2.9) differs little from the one given in Table 2.2, but more accurately describes the resonance energy. At a resonance energy of 0.480 MeV, it leads to the scattering phase shift equal to 89.45°.

The second resonance in the ${}^2\text{H}{}^3\text{He}$ system appears at 19.28 MeV with the angular momentum $J^\pi = 3/2^-$ and width of 0.959 MeV [82, p. 27-29] is laying at 19.28 MeV relative to the GS (2.892 MeV towards the channel threshold). The $P_{3/2}$ wave may match this state in doublet or quartet spin channel. The phase shift analysis presented in [101, p. 98-99] shows no any resonance behavior of the $P_{3/2}$ waves. While, the ${}^2P$ phase shift illuminates the smooth rising in the doublet channel, its quartet partner ${}^4P$ is clearly slowly decreasing.

For properly reproducing this ${}^{2+4}P_{3/2}$ resonance we need a potential with the FS and the following parameters [47, p. 59]:

$$V_{P3/2} = -2412.2 \text{ MeV and } \alpha = 4.0 \text{ fm}^{-2}. \tag{2.10}$$

The potential (2.10) provides the following resonance parameters: the position is fitted at the energy of 2.890(1) MeV in the c.m., and the corresponding width is 0.962(1) MeV in c.m. Its $P_{3/2}$ phase shift is shown in Figure 2.3a with a dashed curve, and at the resonance energy it has a value of 90.0(1)°.

In Figure 2.1 the first column shows the higher laying levels for $J^{\pi} = 7/2^+$ and $J^{\pi} = 5/2^+$ with the following corresponding parameters: the energy position of 19.45 and 19.71 MeV relative to the GS (or 3.06 and 3.32 MeV in c.m. relative to the channel threshold), the level width of 3.28 and 4.31 MeV in c.m. (see Table 5.3 in [82, p. 27]).

The strong $E1$ transitions to the GS are conditioned by direct capture from the doublet and quartet channels corresponding to the second $5/2^+$ resonance. For a correct description of the $^{2+4}D_{5/2}$ resonance a potential without the FS and with the following parameters [47, p. 59]

$$V_{D5/2} = -31.29 \text{ MeV and } \alpha = 0.09 \text{ fm}^{-2} \qquad (2.11)$$

is needed.

The calculated $D_{5/2}$ scattering phase shift is shown in Figure 2.3a with the dotted curve. At the resonance energy the value of this phase shift is 90.0(1)°. The calculated resonance parameters are the following: the energy position of 3.32 (1) MeV in c.m., and the width of 4.09(1) MeV in c.m. There is no resonance for the $D_{5/2}$ phases shift at such energies in Ref. [101, p. 98-99]. The ^4D phase shifts have a slight tendency to rise at 3.0 MeV in c.m [47, p. 59].

The level with $J^{\pi} = 7/2^+$ at 3.06 MeV in c.m. and a width of 3.28 MeV in c.m. can be attributed to the $^4D_{7/2}$ state. In this case the $M2$ transition to the GS is possible, the total cross sections for which will be noticeably smaller than the cross sections for the $E1$ processes [47, p. 59]. However, we give the potential without the FS for this resonance the following parameters

$$V_{D7/2} = -31.99 \text{ MeV and } \alpha = 0.09 \text{ fm}^{-2}. \qquad (2.12)$$

This potential leads to resonance at energy of 3.06(1) MeV in c.m. with a width of 3.18(1) MeV in c.m., its $D_{7/2}$ scattering phase shift is shown in Figure 2.3b with the dotted curve 3. At the resonance energy the phase shift has a value of 90.0(1)°.

The next level can be detected at the excitation energy of 20.53 MeV or at 4.14 MeV in c.m. with a momentum $J^{\pi} = 1/2^+$ and a width of 5.0 MeV in c.m., so it can be attributed to the $^4D_{1/2}$ resonance. A correct description of such resonance requires a potential with the following parameters [47, p. 59]:

$$V_{D1/2} = -39.88 \text{ MeV and } \alpha = 0.115 \text{ fm}^{-2} \qquad (2.13)$$

This potential leads to the resonance at energy of 4.14(1) MeV in c.m. with a width of 5.1(1) MeV in c.m., and its scattering phase shift is shown in Figure 2.3b by the dotted curve 4. At resonance energy the phase shift has a value of 90.0(1)°.

Let us consider one more level, which lies at an excitation energy of 22.06 MeV or 5.67 MeV in c.m. with a momentum $J^\pi = 5/2^-$ and a width of 15.5 MeV in c.m. This resonance can be attributed to the $^4P_{5/2}$ state. A potential with the FS and parameters

$$V_{P5/2} = -456.7 \text{ MeV and } \alpha = 0.8 \text{ fm}^{-2} \qquad (2.14)$$

is required to correctly describe the $^4P_{5/2}$ state.

The potential leads to resonance at the energy of 5.67(1) MeV in c.m. with a width of 15.7(1) MeV in c.m., and its scattering phase shift is shown in Figure 2.3b with a dotted curve 3; at the resonance energy the phase shift has a value of 90.0(1)°.

The detailed study of these levels shows that the phase shift analysis performed in Ref. [101, p. 98-99] does not take into account the position of the resonances under consideration with large widths [47, p. 60].

The phase shift analysis is a subject to further refinement with the expansion of the energy region to 5–7 MeV in c.m. However, in order to make a detailed phase shift analysis the measurements of differential cross sections in the energy region of interest in steps of 0.3–0.5 MeV (in the region of narrow resonances the energy step should be even smaller) is required.

In order to properly depict the phase shift resonance, it is required to have a step of measuring cross sections in the resonance region of not less than $\Gamma/5$. In other words, within the width of the resonance there must be at least five points of the cross sections measurement. Only in this case the resonance form of the phase shift appears quite accurately [47, p. 60].

For example, for a resonance of the potential (2.10) described with a width of about $\Gamma \sim 1$ MeV, a step of ~0.2 MeV is needed. For the potential (2.9) with resonance in the ^4S wave, the energy step should be of the order of 0.05–0.06 MeV.

Now consider the potential of the GS of ^{5}Li in the ^{2}H^{3}He channel [47, p. 60]. The P states with potentials from Table 2.2 allowed in the doublet and quartet channels have an energy that does not agree with the binding energy of the $P_{3/2}$ and $P_{1/2}$ levels of the ground and first excited states of ^{5}Li, whose spectrum is shown in Figure 2.1 [82, p. 27-29, 83, p. 16-18].
These potentials depend on two Young orbital diagrams, and the BS potential should depend only on one orbital diagram {41} [98, p. 1513-1514]. In addition, the channel energies for the GS and FES of ^{5}Li were specified above. Therefore, we carried out a refinement of the potentials of these BSs and the results are given in Table 2.3, where the width parameter α is equal to 0.18 fm^{-2}. The binding energy of the FES is obtained from [82, p. 27-29], where 1.49 MeV above the GS is given.

In the calculations of the BS energy the exact masses of the particles were used, and the relative accuracy of the calculations for binding energy is at a level of 10^{-6} MeV [47, p. 60].

In Table 2.3, in the third column, the experimental energy values of the levels [82, p. 27-29] are given in parenthesis. The dimensionless asymptotic normalizing coefficients (ANC) C_w are given in the last column in Table 2.3. They are defined according to scientific paper [102]

$$\chi_L(R) = \sqrt{2k_0}\, C_W W_{-\eta L + 1/2}(2k_0 R). \qquad (2.15)$$

In Equation (2.15) $\chi_L(R)$ is the numerical GS radial WF, viz. the solution of the Schrödinger equation normalized to unit, $W_{-\eta L + 1/2}(2k_0 R)$ is Whittaker function, k_0 is a wave number related to the channel binding energy, η is the Coulomb parameter, L is the orbital angular momentum of the bound state [22, p. 63].

Table 2.3 – Potential parameters for the $^2H^3He$ system in pure state by Young diagrams for the GS and FES

L_J	V_0, MeV	E_{bs} (E_{exp} ([18]), MeV	C_w	R_{rms}, fm
$P_{3/2}$ (GS)	-83.505593	-16.388000 (-16.388)	6.30(1)	2.25
$P_{1/2}$ (FES)	-80.485333	-14.898000 (-14.898)	5.74(1)	2.26

The pointed ANC error is determined by its averaging over the interval from 5–6 up to 8–10 fm and shown in parenthesis. The charge root mean square radii (R_{rms}) for the BSs of ^5Li in the $^2H^3He$ channel were also calculated and are given in Table 2.3 [47, p. 61].

Since the ground $P_{3/2}$ state is spin-mixed, it is necessary to consider the $E1$ transitions from the doublet and quartet states of S and D scattering. In the framework of the MPCM, it is impossible to explicitly isolate the $^2P_{3/2}$ and $^4P_{3/2}$ parts in the WF of the GS. So, for the calculations we will use the spin-mixed function of the $P_{3/2}$ state, which is obtained when solving the Schrödinger equation with a given GS potential from Table 2.3. For the scattering states quartet and mixed over the Young diagrams doublet potentials from Table 2.2 are used and also the resonance potentials (2.9) – (2.14) [47, p. 61].

2.2.4 Multipole transitions for the radiative $^3He(^2H,\gamma)^5Li$ capture

The complete set of $E1$ and $M1$ transition amplitudes accounted in our calculations is given in Table 2.4 [47, p. 61]. Transitions from the resonance state with the main input to the total cross sections are № 2, 4, 6, 9, 10, 12. Transitions from non-resonance scattering states give a noticeably smaller contribution at low energies. The last column contains the values of the coefficient P^2 in expressions (2.2) and (2.3).

The interaction potentials have been corroborated by the experimental data on the elastic scattering phase shifts and energy levels spectra [47, p. 61], so, the WFs obtained as the solutions of the Schrödinger equation with those potentials account effectively the cluster system states, in particular, of the mixing by channel spin.

Therefore, the total cross section of the $E1$ transition from the mixed continuous states to the spin mixed GS may be taken as simple doubling of the partial cross section as each is calculated with the same functions. However, spin algebraic factors are specified for every matrix element (2.2) [23, p. 29-31]:

$$\sigma_0(E1) = {}^2\sigma({}^2D_{3/2} \rightarrow {}^2P_{3/2}) + {}^4\sigma({}^4D_{3/2} \rightarrow {}^4P_{3/2}). \qquad (2.16)$$

Table 2.4 – Transitions accounted for calculations the total radiative ^{3}He(^{2}H,γ)^{5}Li capture cross section

№	$(^{2S+1}L_J)_i$	The resonance energy in MeV	The angular momentum and parity J^π	Transition	$(^{2S+1}L_J)_f$	P^2
1	$^2S_{1/2}$	–		E1	$^2P_{3/2}$	4
2	$^4S_{3/2}$	16.87	$3/2^+$	E1	$^4P_{3/2}$	4
3	$^2P_{1/2}$	–		M1	$^2P_{3/2}$	4/3
4	$^2P_{3/2}$	19.28	$3/2^-$	M1	$^2P_{3/2}$	5/3
5	$^4P_{1/2}$	–		M1	$^4P_{3/2}$	10/3
6	$^4P_{3/2}$	19.28	$3/2^-$	M1	$^4P_{3/2}$	22/15
7	$^4P_{5/2}$	22.06	$5/2^-$	M1	$^4P_{3/2}$	18/5
8	$^2D_{3/2}$	–		E1	$^2P_{3/2}$	4/5
9	$^2D_{5/2}$	19.71	$5/2^+$	E1	$^2P_{3/2}$	36/5
10	$^4D_{1/2}$	20.53	$1/2^+$	E1	$^4P_{3/2}$	2/5
11	$^4D_{3/2}$	–		E1	$^4P_{3/2}$	64/25
12	$^4D_{5/2}$	19.71	$5/2^+$	E1	$^4P_{3/2}$	126/25

In reality, there is only one transition from the scattering state to the GS, rather than two different $E1(^2\sigma + {}^4\sigma)$ processes. The averaging procedure concerns the transitions from the $D_{5/2}$ and $D_{3/2}$ scattering states to the $P_{3/2}$ GS of ^{5}Li in the ^{2}H^{3}He channel [47, p. 61].

Thus, the total cross section of the capture process on the GS for electromagnetic $E1$ transitions is represented as the following combination of partial cross sections

$$\sigma_0(E1) = \sigma(^2S_{1/2} \rightarrow {}^2P_{3/2}) + \sigma(^4S_{3/2} \rightarrow {}^4P_{3/2}) + \sigma(^4D_{1/2} \rightarrow {}^4P_{3/2}) +$$
$$+ [\sigma(^2D_{3/2} \rightarrow {}^2P_{3/2}) + \sigma(^4D_{3/2} \rightarrow {}^4P_{3/2})]/2 + [\sigma(^2D_{5/2} \rightarrow {}^2P_{3/2}) + \qquad (2.17)$$
$$+ \sigma(^4D_{5/2} \rightarrow {}^4P_{3/2})]/2.$$

Since for the $M1$ transitions there is also spin mixing for some P scattering waves, the total cross section is written in the same way as $E1$ transitions to the GS:

$$\sigma_0(M1) = \sigma(^4P_{5/2} \rightarrow {}^4P_{3/2}) + [\sigma(^2P_{1/2} \rightarrow {}^2P_{3/2}) + \sigma(^4P_{1/2} \rightarrow {}^4P_{3/2})]/2 +$$
$$+ [\sigma(^2P_{3/2} \rightarrow {}^2P_{3/2}) + \sigma(^4P_{3/2} \rightarrow {}^4P_{3/2})]/2. \qquad (2.18)$$

It should be noted that $M1$ transitions from non-resonance P scattering states exert a noticeable effect on the total cross sections only at energies above 300-400 keV in c.m. Thus, we have identified all the major transitions that may contribute to the total cross sections of the ^{3}He(^{2}H,γ)^{5}Li capture process at low energies, which are treated

here. Of course, the $M2$ transition is also possible, but we do not consider it because of the smallness of its cross sections [47, p. 62].

2.3 Radiative n^{10}Be capture process

The data [103] have been obtained from recalculation of experimental measurements of dB/dE_γ Coulomb dissociation probability for ^{11}Be [104].

However, the new results for ^{11}Be Coulomb dissociation have subsequently been obtained and presented in [105, 106]. Moreover, the results obtained by T. Nakamura and Y. Kondo in [106, p. 67-119] should be considered as an improvement of previous data presented in [104, p. 298-300]. We finally got an opportunity to compare the total cross-sections from different experimental data [104, p. 298-300, 105, p. 4-10, 106, p. 67-119] between each other and with previous data [103, p. 326c].

Such a sequential analysis of different experimental data is presented further in Subsection 2.3.2.

The theoretical calculations of the radiative capture total cross-sections, reaction rates, and analytical parameterizations actual for astrophysical calculations of ^{11}Be isotope synthesis balance are presented in Section 4.

2.3.1 Structure of n^{10}Be discrete states

For ^{10}Be as for ^{10}B [23, p. 152] the orbital Young tableau {442} is used, so for n^{10}Be system we have {1} × {442} = {542} + {443} + {4421} [107, 108]. The first of the obtained diagrams is compatible with the orbital moment $L = 0, 2, 3, 4$, and it is forbidden because five nucleons cannot be in the s-shell. The second tableau is allowed and compatible with the orbital moment $L = 1, 2, 3, 4$, and the third one is also allowed and compatible with $L = 1, 2, 3$ [48, p. 95].

Due to the lack of Young diagrams' product tables for number of particles, that is equal to 10 and 11, it is impossible to classify accurately the cluster states in the considered particles system.

However, even so accurate assessment of the orbital symmetries enables the determination of the presence of the FSs in the S and D-waves and the lack of the FSs for P states. These very structures of FSs and ASs in the different partial waves enables to construct further the intercluster interaction potentials required for the calculation of the radiative capture total cross-sections [48, p. 95-96].

Thus, taking into account only the lowest partial waves with the orbital moment $L = 0, 1, 2$ we can say that for n^{10}Be system (it is known that for ^{10}Be $J^\pi, T = 0^+, 1$ [109]) there is only the allowed state (AS) in the potentials of ^2P wave, while ^2S-, ^2D-waves have the forbidden state (FS). The state in the $^2S_{1/2}$ wave with the FS corresponds to the ^{11}Be ground state with $J^\pi, T = 1/2^+, 3/2$ and corresponds to the n^{10}Be system binding energy of, that is equal to -0.5016 MeV [110, p. 99-102].

Let us note that the ^2P waves correspond to two allowed Young diagrams {443} and {4421}. This situation is, seemingly, the same as in N^2H or N^{10}B systems [111-113], when the scattering potentials depend on two Young diagrams, while the BSs potentials are defined by the only one [114].

Therefore, such potentials for one partial wave in the scattering states and discrete spectrum can be different. Here it is also assumed that the potential of the $^2P_{1/2}$ bound state (see Figure 2.4) corresponds to one tableau {443} that is the first excited state (FES) of ^{11}Be at the energy 0.32004 MeV relative to the GS [48, p. 96].

To fix the idea we will consider that for the discrete spectrum the allowed state in the $^2P_{1/2}$ wave is bound, while for the scattering processes it is unbound. Therefore, the depth of such potential can be set equal to zero.

Let us turn again our attention to that these potentials can be different because they correspond to the states with different Young diagrams. For the potential of $^2S_{1/2}$ scattering wave or the discrete spectrum in the n^{10}B system the FSs and ASs are bound [48, P.96].

$\Gamma_{cm} = 45(10)$ keV

5.255 (5/2⁻,?)

$\Gamma_{cm} = 10(5)$ keV

3.955 (3/2⁻,?)

$\Gamma_{cm} = < 8$ keV

3.889 (5/2⁻,?)

$\Gamma_{cm} = 122(8)$ keV

3.40 (3/2⁻ or 3/2⁺,?)

$\Gamma_{cm} = 206(8)$ keV

2.654 (3/2⁻,?)

$\Gamma_{cm} = 100(10)$ keV

1.783 (5/2⁺,?)

n^{10}Be

0.5016

$T_{1/2} = 115(10)$ fs

0.32004 (1/2⁻,?)

$T_{1/2} = 13.76(7)$ s

^{11}Be (1/2⁺,3/2)
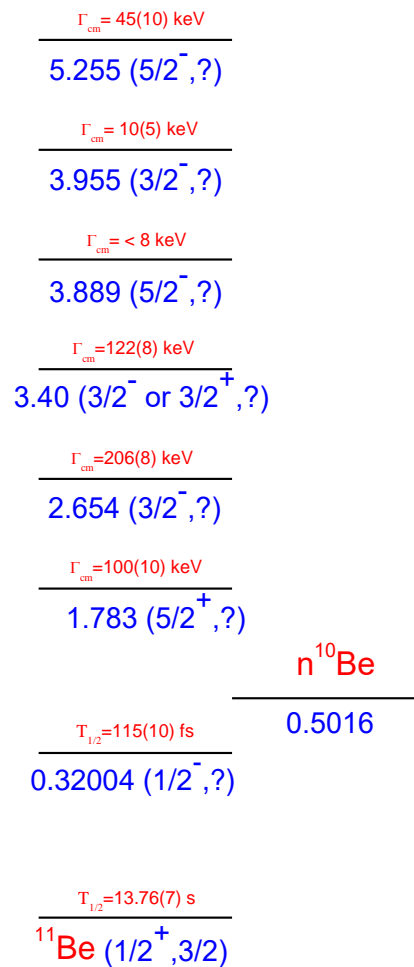
Figure 2.4 – ^{11}Be energy levels in MeV (c.m.) and their widths

Now let us consider the FES that is bound in the n^{10}Be channel, and several resonance states of ^{11}Be [110, p. 99-102], which are unbound in the n^{10}Be channel and correspond to the resonances in the n^{10}Be scattering:

1. The first excited state (ES) of ^{11}Be is found at the energy that is equal to 0.32004 MeV relative to the GS with the moment $J^\pi = 1/2^-$ or -0.18156 MeV relative to the threshold of n^{10}Be channel. This state can be related to the doublet $^2P_{1/2}$ level with the bound AS but without the bound FSs (see Figure 2.4).

2. The first resonance state has the excitation energy equal to 1.783 MeV relative to the GS or 1.2814 MeV (c.m.) relative to the threshold of the n^{10}Be channel. For this level J^π is equal to $5/2^+$, that leads to $L=2$ and enables to consider it as the $^2D_{5/2}$ resonance in the n^{10}Be system at 1.41 MeV in the laboratory system (l.s.). The potential of this resonance has the bound FS. This resonance width is equal to 100(10) keV in the center-of-mass system [48, p. 96].

3. The second resonance state energy is equal to 2.654 MeV relative to the GS or 2.1524 MeV (c.m.) relative to the channel threshold with the width equal to 206(8) keV (c.m.). Its moment J^π is equal to $3/2^-$ [110, p. 101]. These characteristics enable to consider it as $^2P_{3/2}$ resonance in n^{10}Be system at 2.37 MeV (l.s.), and its potential does not have any bound FSs or ASs [48, p. 96].

4. The third resonance state at the excitation energy equal to 3.400(6) MeV (c.m.) with the width 122(8) keV (c.m.) has the moment $J^\pi = 3/2^+$ (or $3/2^-$) [110, p. 101] that leads to $L = 2$ and enables to consider it as the $^2D_{3/2}$ resonance in the n^{10}Be system at 3.19 MeV (l.s.). However, the ambiguity in parity of this level enables to assume $^2P_{3/2}$ state for it also. Due to such ambiguity we will not consider this resonance [48, p. 96].

5. We did not consider the next two resonances shown in Figure 2.4 because its width is of the order of 10 keV and less.

6. The resonance at 5.255(3) MeV has the width equal to 45(10) keV, the moment $J^\pi = 5/2^-$ and can be corresponded with $^2P_{5/2}$ wave. However, its width is rather less than the low resonances width, and we will not consider it [48, p. 96].

For higher energies there are only two resonances. The first one has the energy equal to 8.020(20) MeV with the width equal to 230(55) keV and the moment $J^\pi = 3/2$, and the second one with the energy equal to 10.59(50) MeV, the width equal to 210(40) keV, and $J^\pi = 5/2^-$.

These two resonances have the totally determined characteristics [110, p. 101]. The first of them may be correlated with $^2P_{3/2}$ state, and in this case the $E1$ transition to the GS can be considered. However, its width relative to the excitation energy is comparatively small, so the contribution of this potential into the total cross-sections at such energy will be relatively small [48, p. 96].

For the second level only $M2$ transition is possible, so we will not consider it. As the result we will take into account only the second resonance at 2.654 MeV, which has the larger width and well determined quantum numbers, though the neutron radiative capture on ^{10}Be total cross-section will be calculated up to 10 MeV [48, p. 96].

2.3.2 The phase shifts and potentials for n^{10}Be scattering states

As n^{10}Be interaction in each partial wave with the given orbital moment L and other quantum numbers including $\{f\}$ we usually use the potential in the Gauss type form with the point Coulomb term which is simply absent for the neutron processes [48, p. 97]

$$V(r,JLS\{f\}) = V_0(JLS\{f\})\exp\{-\gamma(JLS\{f\})r^2\}. \qquad (2.19)$$

^{11}Be GS in the n^{10}Be channel is $^2S_{1/2}$ level, and such potential should describe correctly the binding energy and the AC of this channel. To determine this constant from the available experimental data let's treat data for the spectroscopic factors S_f and asymptotic normalizing coefficients A_{NC}, connected with the AC. The results for A_{NC} given in [37, p. 108] are presented in Table 2.5, also in this table we added some results from [36, p. 1545-1446].

Table 2.5 – Data for A_{NC} of ^{11}Be in the n^{10}Be channel

The reaction which the A_{NC} was obtained from	The A_{NC} in fm$^{-1/2}$ for the GS	The A_{NC} in fm$^{-1/2}$ for the FES	Reference
(d,p_0) at 12 MeV	0.723(16)	0.133(4)	[37, p. 108]
(d,p_0) at 25 MeV	0.715(35)	0.128(6)	[37, p. 108]
(d,p_0) at 25 MeV	0.81(5)	0.18(1)	[36, p. 1545-1446]
	0.68–0.86	*0.122–0.19*	*Present* (Range)
	0.749	*0.147*	*Present* (Average $\overline{A_{NC}}$)

Furthermore, we succeeded in finding a lot of data for the spectroscopic factors of ^{11}Be in the n^{10}Be channel [110, p. 101], so let's present their values in the separate Table 2.6 [48, p. 97].

Table 2.6 – Data for the spectroscopic S-factors of ^{11}Be in the n^{10}Be channel

S for the GS	S for the FES	Reference
0.87(13)	–	[115]
0.72(4)	–	[116]
0.61(5)	–	[105, p. 9]
0.73(6)	0.6(2)	[117]
0.73(6)	0.63(15)	[118]
0.77	0.96	[119]
0.56–1.0	*0.4–0.96*	*Present* (Range)
0.74	*0.73*	*Present* (Average $\overline{S}$)

Next on the basis of the given above expressions for the GS we obtain the value of $\overline{A_{NC}}/\sqrt{\overline{S}} = \overline{C} = 0.87\,\text{fm}^{-1/2}$, and as $\sqrt{2k_0} = 0.546$, so the dimensionless AC determined as $\overline{C_W} = \overline{C}/\sqrt{2k_0}$ is equal to 1.59.

However, the range of the spectroscopic S-factor values is so wide that the C_W values for the average ANC can be in the region 1.37–1.83. If we take into account the A_{NC} varieties, this range may be expanded up to 1.25–2.10 [48, p. 97].

Similarly to the GS, for the first excited state at $\sqrt{2k_0} = 0.423$ we obtain $\overline{C_W} = 0.41$, and the range of C_W values for the average ANC is from 0.35 to 0.55.

If we take into account the A_{NC} varieties, the range of the dimensionless AC values can be increased up to 0.29–0.71. These results are used further for the construction of the GS and FES potentials which should be agreed with the binding energy of these levels and their AC values [48, p. 97].

Specifically, for the potential of $^2S_{1/2}$ GS with the FS the following parameters may be used

$$V_{S1/2} = 174.15483 \text{ MeV and } \gamma_{1/2} = 0.4 \text{ fm}^{-2}. \tag{2.20}$$

It leads to the binding energy that is equal to -0.501600 MeV at the used here finite-difference method (FDM) accuracy equals 10^{-6} MeV [120], the AC is equal to $C_w = 1.32(1)$ in the range 7–30 fm, the mass radius is equal to 2.88 fm, the charge radius is equal to 2.43 fm. The AC varieties are determined by its averaging over the pointed range of distances [48, p. 97].

Such potential of the GS with the FS is in total accordance with the classification of states according to Young diagrams, given above, and leads to the ^{11}Be charge radius being in a good agreement with data [110, p. 101].

The potential parameters (2.20) enable to obtain the AC value at its lower limit. The potential phase shift is shown in Figure 2.5 by the red solid line. This potential at the orbital moment $L = 2$ leads to the nonresonance ^2D scattering phase shift without the spin-orbit splitting, that is shown in Figure 2.5 by the red dotted line.

The n^{10}Be scattering $^2S_{1/2}$ phase shifts obtained in [121] are presented in the same figure by the black points [48, p. 97].

For the potential of the resonance $^2D_{5/2}$ wave with the FS, which is used further for consideration of the $E2$ transitions, the following parameters have been obtained

$$V_{D5/2} = 474.505 \text{ MeV and } \gamma_{5/2} = 0.37 \text{ fm}^{-2}. \tag{2.21}$$

The potential leads to the resonance at 1.41(1) MeV (l.s.) and the width $\Gamma_{\text{c.m.}}$ equal to 100(1) keV, that is in a complete agreement with data [110, p. 101]. Its phase shift is shown in Figure 2.5 by the red dashed line [48, p. 97].

The potential of the $^2P_{3/2}$ resonance state at the energy equal to 2.654 MeV (c.m.) with the width equal to 206(8) keV (c.m.) relative to the GS or 2.37 MeV (l.s.) above the threshold of the n^{10}Be channel without the FS, can have parameters

$$V_{P3/2} = 10935.65 \text{ MeV and } \gamma_{1/2} = 40.0 \text{ fm}^{-2}. \tag{2.22}$$

It leads to the resonance energy equal to 2.37(1) MeV (l.s.) at the width equal to 204(1) keV (c.m.), and its phase shift is presented in Figure 2.5 by the blue dashed line. The potential of $^2P_{1/2}$ first excited state of ^{11}Be without the FS has the parameters

$$V_{P1/2} = 192.799497 \text{ MeV and } \gamma_{1/2} = 0.7 \text{ fm}^{-2}. \tag{2.23}$$

58

The potential leads to the binding energy equal to -0.181560 MeV at the FDM accuracy equal to 10^{-6} MeV [120], the AC is equal to 0.27(1) in the range of 10 – 30 fm, the mass radius is equal to 2.61 fm, and the charge radius is equal to 2.40 fm [48, p. 97-98].

This potential phase shift is shown in Figure 2.5 by the red dotted-dashed line. The parameters of potential (2.23) have been optimized to describe correctly the total cross-sections of the neutron capture on ^{10}Be at the thermal energy equal to 25.3 meV, which were obtained in [36, 1546-1547], and the value of its dimensionless AC is approximately near the lower limit 0.29 – 0.71 [48, p. 98].

In this work the matrix elements (ME) for the total cross-sections computation were calculated at the distances up to 30 fm, and the parameters of this potential were also selected from [36, 1546-1547] to describe correctly the neutron capture on ^{10}Be total cross-sections at the thermal energy equals 25.3 meV.

Subsequently it was ascertained that due to extremely small value of the binding energy for the GS and, particularly, for the FES the ME calculation should be performed at large distances. Table 2.7 shows the values of the total cross-sections for the GS and FES capture, and their convergence depending on the upper integration limit R_{max} in ME [48, p. 98].

As one can see from Table 2.7, the ME have the correct values only at the distances equal to 100-150 fm. Therefore, in all present calculations of the total cross-sections of the given system we used the ME integration distance equal to 150 fm. As a result, new parameters of potential (2.23) have been obtained [48, p. 98].

The GS potential was also changed that is caused by changing the capture total cross-sections presented in Section 4, so the parameters of this potential were selected for the correct description of new data in energy region of the order of 1 MeV.

The results of [122] may be considered as taking into account only the core effects in ^{11}Be. But in the present work we have taken into account the halo effects caused by the odd neutron of this nucleus. These effects appear generally in the cross-sections of capture to the FES [48, p. 98].

As it can be seen from the tables given above, the R_{max} increasing from 30 to 150 fm leads to the total cross-section increasing by about 2,5 times in the case of the capture to the GS, and by almost 6 times for the capture to the FES. As the $^2P_{1/2}$ potential of ^{11}Be FES is constructed so that to describe correctly the thermal cross-sections, so the difference between the given results and results [122, p. 6-9] at low energies is only in its parameters.

The results for the total cross-sections obtained in the present work by using new parameters (2.23) insignificantly differ from the results [122, p. 9-12] obtained by using the previous parameters. Furthermore, the capture cross-section for the transitions to the GS is increased by two times at low energies because in this case the ME is calculated up to 150 fm [48, p. 98].

Let us return to the consideration of criteria for construction of the $^2P_{1/2}$ scattering wave potential that may differ from the FES potential due to the difference between the Young diagrams for these states.
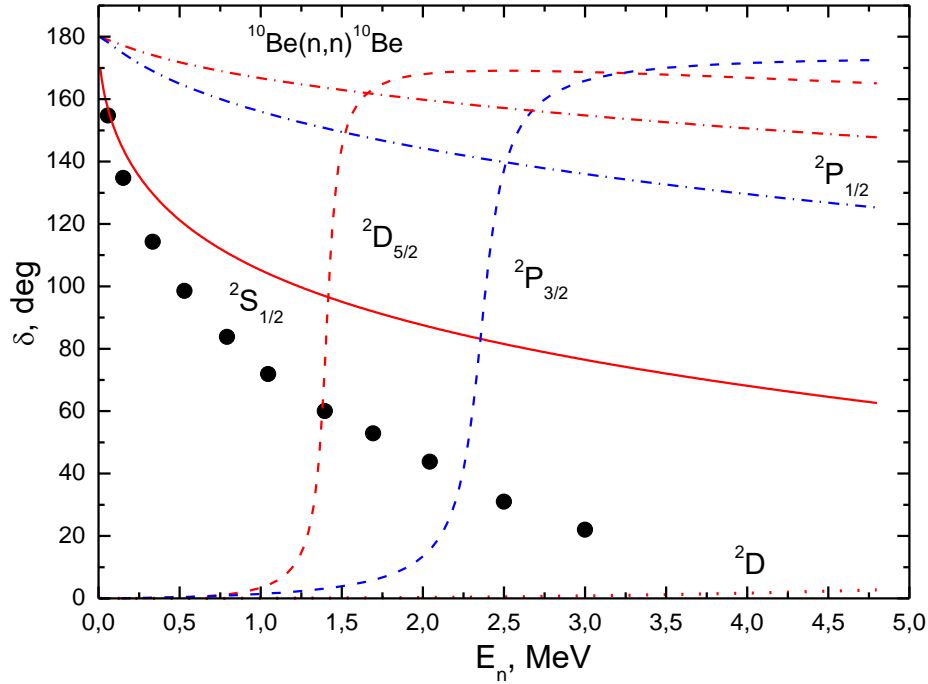
Red solid line shows the phase shift of potential (2.20); red dashed line shows the phase shift of potential (2.21); blue dashed line shows the phase shift of potential (2.22); red dotted-dashed line shows the phase shift of potential (2.23); blue dotted-dashed line shows the phase shift of potential (2.24); red dotted line shows the nonresonance ^2D scattering phase shift without the spin-orbit splitting. Black points show n^{10}Be scattering $^2S_{1/2}$ phase shifts obtained in [121].

Figure 2.5 – n^{10}Be elastic scattering phase shifts in $^2S_{1/2}$ and ^2D waves

Table 2.7 – The value of the neutron capture on ^{10}Be total cross-section for the transition to the GS for potential (2.20) and to the FES for potential (2.23) calculated at 1 keV

R_{max}, fm	GS	FES
	σ_{tot}, μb	σ_{tot}, μb
30	0.27	0.21
50	0.56	0.92
100	0.64	1.50
150	0.64	1.52
200	0.64	1.52

First, as it was shown above, such potential should not have the forbidden state. As we have not the results of the phase shift analysis for the n^{10}Be elastic scattering and in ^{11}Be spectra there is not the resonance with the accurately determined moment $J^\pi = 1/2^-$ and the known width [110, p. 101] at energy lower than 10.0 MeV, we will assume that $^2P_{1/2}$ potential must lead to practically zero scattering phase shifts in this

energy region, therefore its parameters can have zero width. For $^2S_{1/2}$ scattering potential the interaction between $^2S_{1/2}$ GS and the FS, i.e. the parameters of potential (2.20), will be used [48, p. 98].

3 ASTROPHYSICAL d³He PROCESS AT LOW ENERGIES

In this Section we present the results obtained with the potentials from Section 2 for the total cross section, the astrophysical S-factor, the S-factor screening effects, and the rate of the ^{3}He(^{2}H,γ)^{5}Li radiative capture reaction.

In addition, a possible scenario for the formation of ^{6}Li in astrophysical processes involving the short-lived ^{5}Li isotope was considered. The two-step process ^{2}H + ^{3}He $\rightarrow$ ^{5}Li + γ and n + ^{5}Li + $\gamma \rightarrow$ ^{6}Li + γ is proposed as an alternative way of ^{6}Li formation at the BBN.

3.1 Results for total cross sections, astrophysical *S*-factor and reaction rate
3.1.1 Total cross section

The results of the calculated $E1$ and $M1$ radiative capture in ^{2}H^{3}He cluster channel at the energies up to 5.0–6.0 MeV are presented in Figure 3.1. The solid curve 1 denotes the cross section for the $E1$ transition from the ^2S and ^4S scattering states to the GS $^{2+4}P_{3/2}$ defined by the interaction potential parameters from Table 2.3, while for the scattering potentials, the data from Table 2.2 are used. Cross sections for the $E1$ transitions from the ^2S wave are of few orders suppressed as it is of non-resonance behavior [47, p. 62].
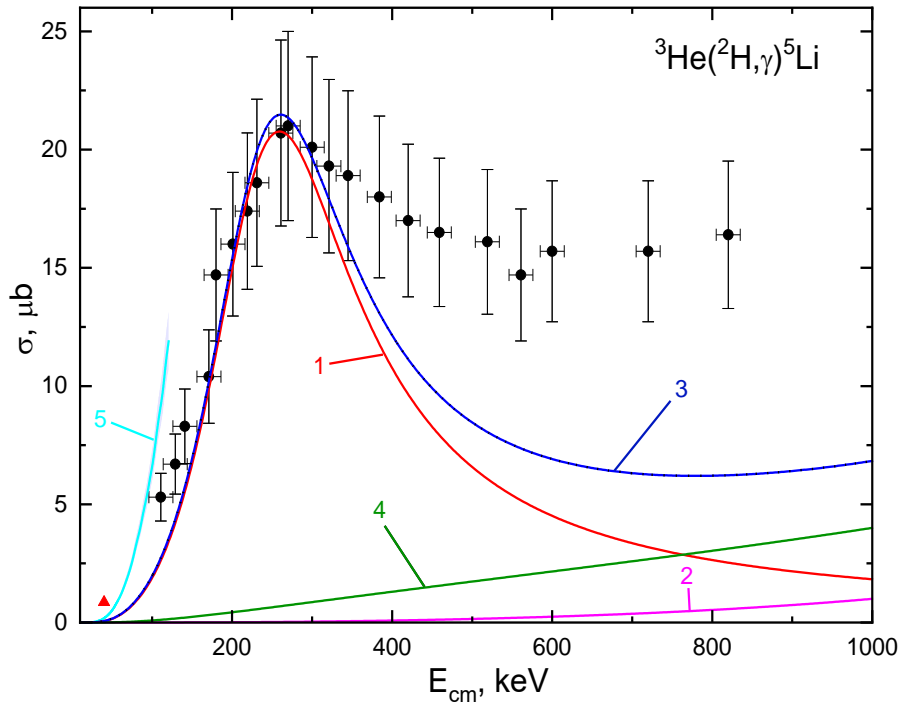
Experimental data: ● are from [30, p. 56-58] and ▲ is from [81, p. 181-183], band 5 – results from [34, R63-R64]. Calculated curves correspond to the potential parameters of Tables 2 and 3 and text. Two last black dots are taken from Figure 9 of the work [30, p. 63].

Figure 3.1a – Total cross section for ^{3}He(^{2}H,γ)^{5}Li bellow 1.0 MeV.
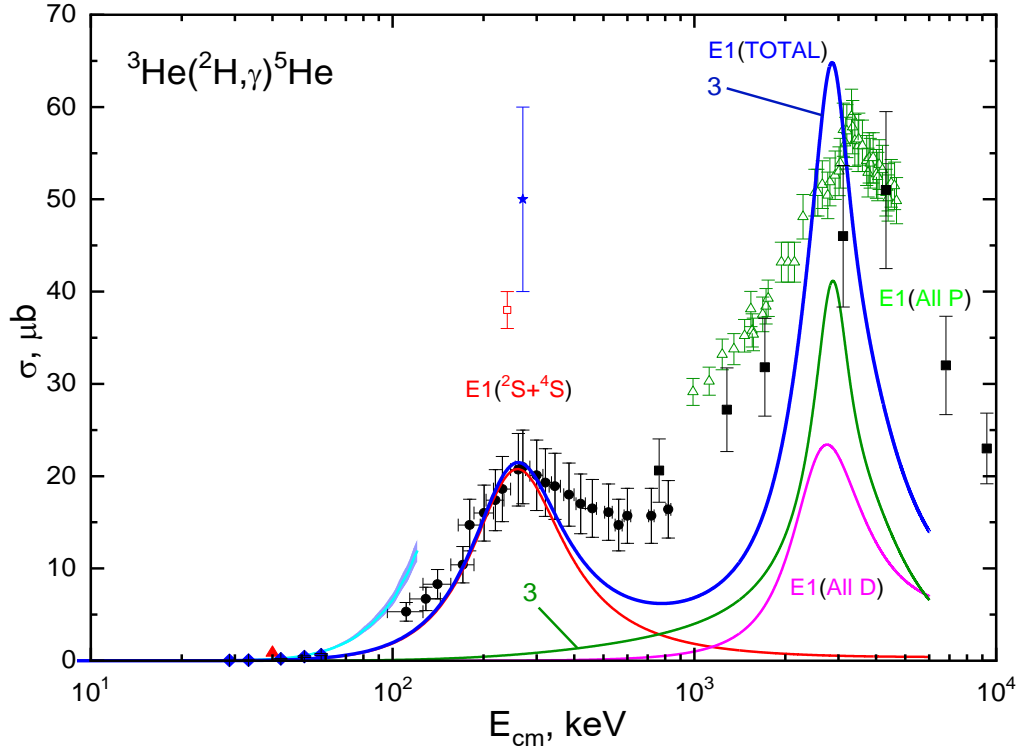
Experimental data: ● are from [30, p. 56-58], ▲ is from [81, p. 181-183], ♦ – from [88, p. 691-692, 89, p. 796-797], ■ – from [84, p. 344-345], △ – from [31, p. 238-239], ★ – from [27, p. 1023-1029], □ – from [28, p. 593-602], cyan band 5 – results from [34, p. R.63-R64]. Two last black dots (●) are taken from Figure 9 of the work [30, p. 63].

Figure 3.1b – Total cross section for ^{3}He(^{2}H,γ)^{5}Li bellow 5.0 MeV.

Solid curve 2 in Figure 3.1 denotes the cross section for the $E1$ transition to the GS from the resonating $^{2+4}D_{5/2}$ waves calculated with parameters (7) and (9). This result includes all other small in value amplitudes for the non-resonating D waves listed in Table 2 (see Table 4). The main contribution here is given by the $D_{5/2}$ resonance, and the contribution of the $D_{1/2}$ wave is very small [47, p. 62].

Curve 3 in Figure 3.1 shows the contribution of the $M1$ transitions from the resonating $^{2+4}P_{3/2}$ and $^{2+4}P_{5/2}$ waves corresponding to potentials (6) and (10) and non-resonance set for P potentials from Table 2. Figure 3.1 clearly shows the $P_{3/2}$ resonance at 2.89 MeV in c.m., the value of which is even larger than the resonance for the $E1$ transition, since the additional contribution is given by the $P_{5/2}$ resonance.

The total cross section included all $E1$ and $M1$ transitions listed above is shown by the curve 4 in Figure 3.1 [47, p. 63].

In Figure 3.1 one can see that at energies above 400 keV the results of our calculation are much lower than the available experimental data [30, p. 56-58], and at energies less than 2 MeV they lie below the results obtained in [31, p. 238-239]. This difference in the cross sections can be due to two reasons: i. in our calculations, we considered 12 different electromagnetic transitions, but perhaps some additional relevant processes were not taken into account; ii. in Refs. [30, p. 56-58] and [31, p. 238-239] in the energy range from 0.4 to 2 MeV the effect of capture on the FES is not entirely excluded. In addition, the

maximum of the calculated cross section in the 3 MeV region is lower than the data given by the reference [31, p. 238-239], which can be explained by the inaccuracy of the spectra [83, p. 16-18] known for the authors of [31, p. 238-239], but used by us today [82, p. 27-29]. In both cases, the results of [30, p. 56-58] and [31, p. 238-239] require refinement on the basis of modern methods of experimental measurements [47, p. 63-64].

We note that the experimental error of the cross sections given in Figure 3.1 was taken to be 19%, as indicated by [30, p. 56-63] for an energy of 450 keV in l.s. or 270 MeV in c.m. and the cross section 21(4) µb with an error of 15 keV for the center-of-mass energy. The data given as a function of laboratory energy in [30, p. 56-58] were recalculated to the c.m. energy with integer particle masses.

The data given as a function of the excitation energy in the research [31, p. 238-243] were also recalculated to the c.m. energy with the binding energy of the ^{2}H^{3}He channel of 16.4 MeV, which is given by [31, p. 238-243]. The data from [27, p. 1023-1029] are given for the c.m. energy of 0.27(3) MeV, at which the maximum values of the cross sections are observed in this work. The data from [28, p. 593-602] are given for an energy of 240 keV in the c.m [47, p. 64].

3.1.2 Astrophysical S-factor
The astrophysical S-factors that characterize the behavior of the total cross section of the nuclear reaction at an energy tending to zero are determined as follows [123]

$$S(NJ, J_f) = \sigma(NJ, J_f) E_{cm} \exp\left(\frac{31.335 Z_1 Z_2 \sqrt{\mu}}{\sqrt{E_{cm}}} \right),$$ (3.1)

where σ is the total cross section of the radiative capture process in barn, E_{cm} is the particle energy usually measured in keV in the center-of-mass system, μ is the reduced mass of the particles in the initial channel in amu, Z_1 and Z_2 are the charges of particles in units of elementary charge and N are the E or M transitions of the J-th multipolarity to a finite J_f state of the nucleus. The value of the numerical coefficient 31.335 is obtained on the basis of the modern values of the fundamental constants [124].

Now the results obtained for the astrophysical S-factor for d^3He process are performed. Figure 3.2 displays the total astrophysical S-factor (the solid curve) for the transitions to the GS due to the E1 and M1 processes in direct correspondence with the cross sections shown in Figure 3.1 [47, p. 64].

S-factor at the energy of 6-30 keV in c.m. is still relatively stable but equal to 0.125(2) keV·b, which is still less comparing the experimental data reported in [30, p. 56-58]. The error of the calculated S-factor shown here is obtained by averaging it over the indicated energy interval.

The value of the calculated S-factor is 0.125 keV·b at the energy of 6 keV. At a maximum energy of 230 keV in c.m. the S-factor equals to 0.43 keV·b. If one uses for the $^4S_{3/2}$ scattering wave the resonance potential (2.9) obtained on the basis of the characteristics of the first resonance level, instead of its parameters from Table 2.2, it does not significantly change the magnitude and shape of the calculated S-factor.

We recalculated data [30, p. 56-58] for the cross sections into *S*-factor and presented them as points in Figure 3.2. As we defined at minimal energies 100–200 keV its value is near 0.39 keV·b. This value in the indicated energy range can be approximated by a trivial constant energy dependence $S(E) = S_0$ with $S_0 = 0.386$ keV·b and a mean value for $\chi^2 = 0.21$. Experimental 19% errors were assumed for the *S*-factor and the result is shown by the dashed curve 1 in Figure 3.2 [47, p. 64].
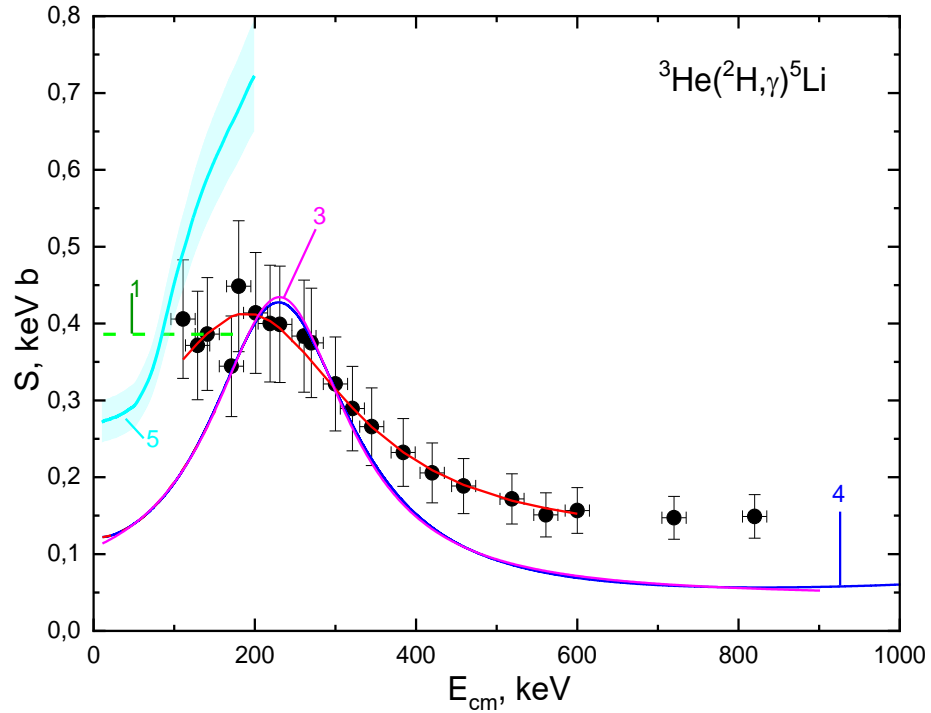
Data are the same as in Figure 3.1a. Cyan band 5 – results from [34, p. R63-R64].

Figure 3.2a – *S*-factor data from [30, p. 56-58] and calculations with potentials from Tables 2 and bellow 1.0 MeV

To improve the description of the experimental data we tried the following approximating function [80, p. 4]

$$S(E \text{ in keV}) = S_0 + S_1 E + S_2 E^2 \tag{3.2}$$

but did not succeed at this very low energy region.

In what follows we implement the parametrization of the calculated *S*-factor according to the expression (3.2) with $S_0 = 0.12133E00$ keV·b, $S_1 = -0.12718E - 04$ b, $S_2 = 0.73463E - 05$ b×keV^{-1} for the energy range up to 150 keV in c.m. We found the value χ^2 to be 0.31 within 1% precision of the theoretical *S*-factor.
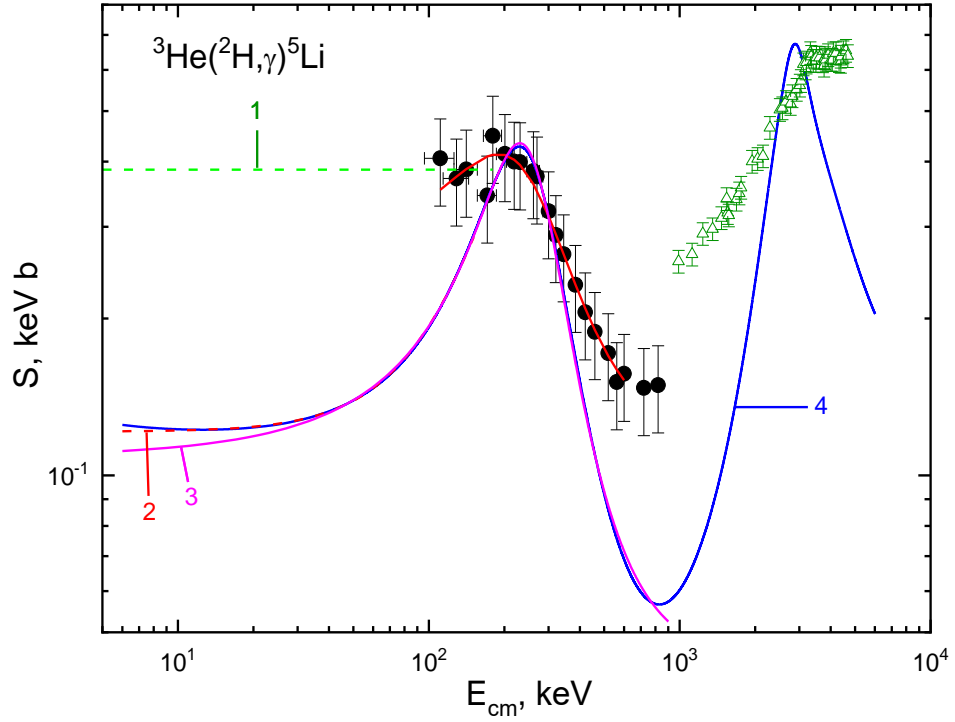
Data are the same as in Figure 3.1b.

Figure 3.2b – Same as in Figure 3.2a, but at the energy bellow 5.0 MeV

The result is shown by the dashed curve 2 in Figure 3.2 and is consistent with experimental data in the previously mentioned energy region [47, p. 65].

Experimental data shown by dots in Figure 3.2 can be approximated by the Breit-Wigner type function

$$S(E) = a_1 + \frac{a_2}{(E - a_3)^2 + a_4^2 / 4} \tag{3.3}$$

with the following parameters $a_1 = 0.11413$, $a_2 = 7370.5$, $a_3 = 189.78$, $a_4 = 313.92$ (the energy is given in keV in c.m.). The results of this parametrization is shown by the solid curve 3 in Figure 3.2, χ^2 is equal to 0.1 at 19% of experimental errors. At zero energy, this parametrization gives $S(0) = 0.236$ keV·b [47, p. 66]. This form of parametrization at a resonance energy of 190 keV leads to a width of 314 keV, which almost coincides with the $3/2^+$ resonance parameters [82, p. 27-29].

We apply the ordinary χ^2 statistics as usually was done in [22, 23] and defined as

$$\chi^2 = \frac{1}{N} \sum_{i=1}^{N} \left[\frac{S^a(E_i) - S^c(E_i)}{\Delta S^c(E_i)} \right]^2 = \frac{1}{N} \sum_{i=1}^{N} \chi_i^2 \tag{3.4}$$

Here S^c is the original, *i.e.* calculated and S^a is an approximate S-factor for the i-th energy, ΔS^c is the error of the original S-factor, which was usually taken equal to 1%,

and N is the number of points in the summation in the expression. As the original S-factor its experimental or calculated values shown in points or the solid curve 4 in Figure 3.2 were used, and the approximated S-factor is obtained on the basis of expressions (3.2) and (3.3) [47, p. 66].

We also use parametrization (3.2) for the calculation of the S-factor in the energy range up to 0.9 MeV c.m. and obtained the following parameters: $a_1 = 0.43449E-01$, $a_2 = 0.41439E+04$, $a_3 = 0.23046E+03$, $a_4 = 0.20604E+03$.

Figure 3.2 with curve 3 illustrates the quality of this procedure at $\chi^2 = 7.7$ at 1% error. At 6 keV in the c.m. or zero energy the value of the approximated S-factor (3.2) is 0.11 keV·b. The parametrization leads to a resonant energy of 230 keV at a width of 206 keV, which also in a good agreement with the data reported by [82, p. 27-29, 47, p. 66].

3.1.3 Screening effects

The screening effects in plasma in laboratory as well as astrophysical conditions are discussed in detail in review [125]. Let us focus on the key points that can be applied to the reaction under consideration. The following relations for the cross sections and, accordingly, for the S-factors, are the generally accepted approximation for the estimation of electron screening [47, p. 66]

$$\frac{\sigma_s(E)}{\sigma_b(E)} = \frac{S_s(E)}{S_b(E)} = \frac{E}{E+U_e}\exp(\pi\eta U_e/E) \tag{3.5}$$
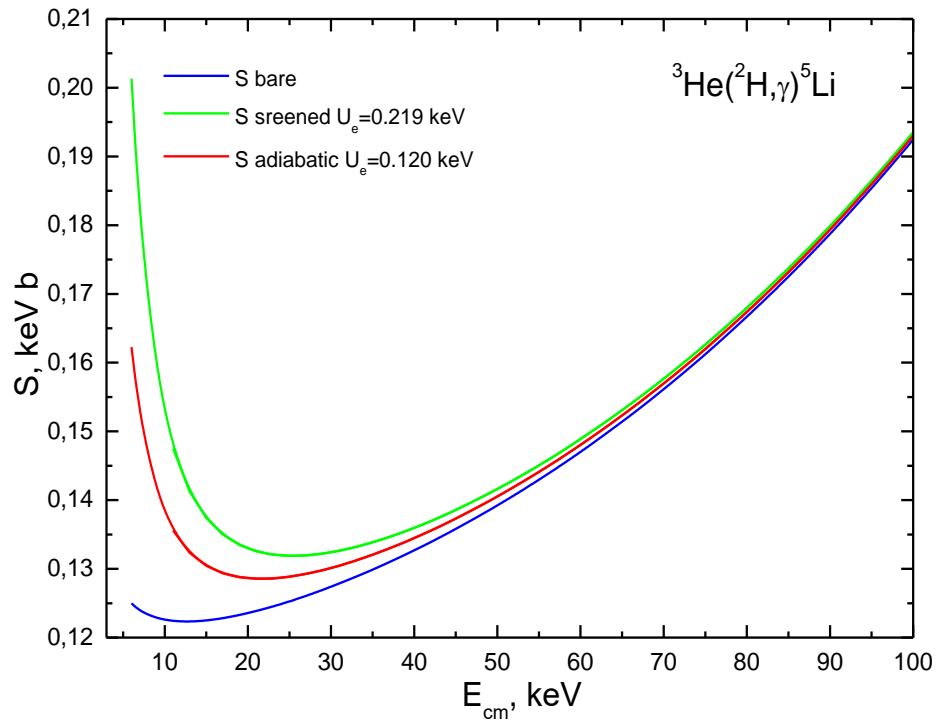
Figure 3.3 – The screening effects for the astrophysical S-factor of the $^3\text{He}(^2\text{H},\gamma)^5\text{Li}$ capture

Here $\sigma_s(E)$ is the electron-screened cross section; $\sigma_b(E)$ is a cross bare nucleus; U_e is a constant electron screening potential energy. The Sommerfeld parameter is

$$\eta = \frac{Z_1 Z_2}{\hbar c} \sqrt{\frac{\mu c^2}{2 E_{cm}}}. \qquad (3.6)$$

The value of U_e can be calculated analytically (*the adiabatic approximation*), or determined experimentally [47, p. 66].

In our case, the ^{3}He(^{2}H, p)^{4}He process is of interest, since it has a common initial channel with the reaction under consideration ^{3}He(^{2}H,γ)^{5}Li. For this initial channel $U_e = 120$ eV is the adiabatic limit value [125, p. 101]. It should be noted that for different experimental conditions U_e has a different value. So in [89, p. 796-798] the direct measurements give the values $U_e = 219\pm7$ eV for ^{3}He(^{2}H, p)^{4}He and $U_e = 109\pm9$ eV for ^{2}H(^{3}He, p)^{4}He. Thus, for the same reaction the difference is almost two fold.

In a later experimental work [126], the screening effect turned out to be negligible. For some reason, the reference [126, p. 1-4] was not included in the review [125, p. 56-100], in which the significance of electron screening for astrophysical plasma is discussed in terms of *pycnonuclear ignition* [47, p. 66-67].

Figure 3.3 illustrates the possible effect of electron screening for the process we are considering. The value of S_b corresponds to the blue curve in Figure 3.3, e.g. $U_e = 0$, and the minimum value for E_{cm} is 6 keV. It is clearly seen from Figure 3.3 that the screening effect strongly depends on the value of U_e, and it varies from 65 to 219 keV in different works [125, p. 99-102]. Obviously, until this value is determined quite accurately, it is also impossible to determine the impact of the screening effect. Therefore, it is not taken into account in calculating the reaction rate [47, p. 67].

3.1.4 Reaction rates
The reaction rate in cm^{3}mol^{-1}s^{-1} units is usually defined as

$$N_A \langle \sigma v \rangle = 3.7313 \cdot 10^4 \, \mu^{-1/2} T_9^{-3/2} \int_0^\infty \sigma(E) E \exp(-11.605 E / T_9) dE, \qquad (3.7)$$

where the energy E is taken in MeV, total cross section $\sigma(E)$ in μb, the reduced mass μ in amu, and temperature T_9 in 10^9 K [127]. To calculate this integral 10^4 points of the theoretical cross section were taken in c.m. energy range from 6 keV to 10 MeV [47, p. 67].

In Figure 3.4 the solid curve shows the results of our calculations for reaction rate of the ^{3}He(^{2}H, γ)^{5}Li capture on the GS at T_9 from 0.003 to 10, which corresponds to the same curve in Figures 3.1 and 3.2. It should be borne in mind that the reaction rate was obtained from the calculated cross section, which slightly differs from the experimental cross section.
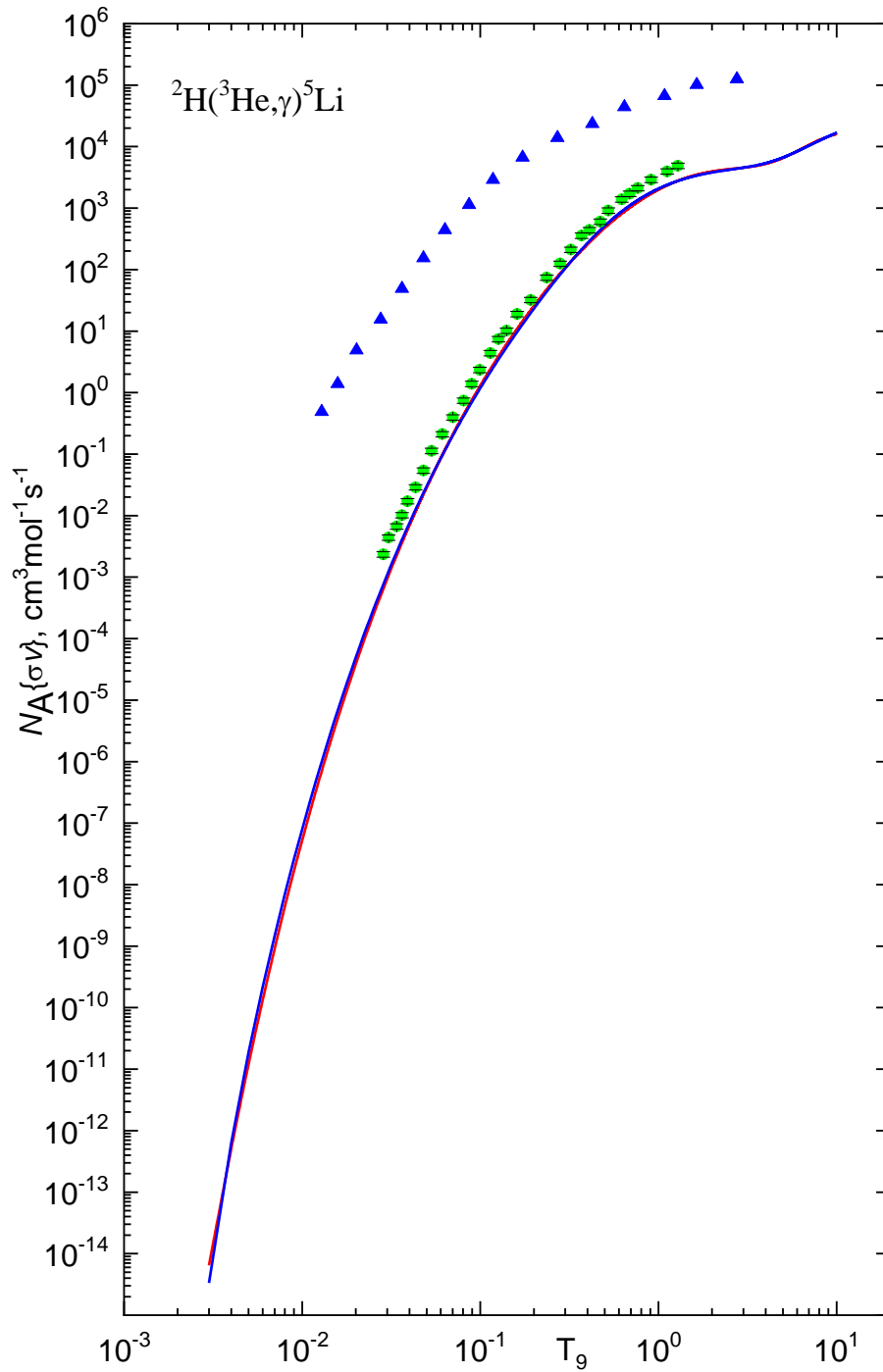
Theoretical curves obtained with potentials from Tables 1 and 3. An explanation of the parameterization functions is given in text. ● are the results from Ref. [87, p. 412-413] for the $^3\mathrm{He}(^2\mathrm{H},\gamma)^5\mathrm{Li}$ capture, ▲ are the results of [87, p. 412-413] for the $^3\mathrm{He}^2(\mathrm{H},\gamma)^5\mathrm{He}$ capture.

Figure 3.4 – Reaction rate of the $^3\mathrm{He}(^2\mathrm{H},\gamma)^5\mathrm{Li}$ radiative capture.

The dots in Figure 3.4 display the results of [87, p. 412-413], which have a larger value of reaction rate. This is due to the strong decrease of our calculated total cross sections in the energy range 0.5 ± 1.0 MeV and insufficiently accurate description of

the cross sections at energies 1-6 MeV. This reaction rate is more than an order of magnitude higher than the rate of the ^{3}He(^{2}H, γ)^{5}Li reaction considered here [47, p. 67].

The calculated reaction rate shown on Figure 3.4 was approximated in the range 0.03–10.0 T_9 as follows [35, p. 294-308]

$$
\begin{aligned}
N_A \langle \sigma v \rangle &= 20986.49 / T_9^{2/3} \cdot \exp(-7.13006 / T_9^{1/3}) \times \\
&\times (1.0 + 126.7438 \cdot T_9^{1/3} - 28.83194 \cdot T_9^{2/3} + 65.13721 \cdot T_9 \\
&+ 47.34928 \cdot T_9^{4/3} - 22.35306 \cdot T_9^{5/3}) - 4.94921 \cdot 10^6 / T_9^{1/2} \times \\
&\times \exp(-8.34422 / T_9^{1/2}).
\end{aligned}
\tag{3.8}
$$

The resulting curve is shown as dashed one in Figure 3.4, χ^2 is equal to 10. In the approximation, the calculated points shown in Figure 3.4 with a solid curve were used. To estimate the χ^2 the error was taken to be 1% [47, p. 68].

3.2 Alternative way of ^{6}Li nuclei formation at the BBN

Furthermore, we consider a possible scenario of thermonuclear astrophysical processes involving a short-lived ^{5}Li isotope, which is formed as a result of the ^{3}He(^{2}H,γ)^{5}Li reaction. In any plasma, when a short-lived ^{5}Li isotope is formed the probability of neutron capture followed by the formation of a stable ^{6}Li is not zero [47, p. 68].

At first, such a chain of two reactions allows us to overcome the mass disruption at $A = 5$, leading to a stable nucleus with $A = 6$. Secondly, the reaction ^{5}Li(n,γ)^{6}Li leads to an additional ^{6}Li formation channel, which can be considered for the explanation of the prevalence ^{6}Li.

We will describe below a possible and, as it seems to us, a new scenario for the synthesis of the ^{6}Li isotope in astrophysical processes and, first of all, at the Big Bang. It is required to find out whether there is a "temperature window" that would allow such an amount of ^{6}Li to be accumulated during the Big Bang, which could change the balance of ^{6}Li, including in the region of a sharp drop in the number of neutrons at $T_9 < 1$ [47, p. 68-69].

The general dynamics of the synthesis of the light and lightest elements within the conditions of the standard Big Bang is represented by a graph of the participating particles fractions, shown in Figure 12 in work [128]. This graph is adapted here for our purposes and shown in Figure 3.5. It displays a sharp drop in the number of neutrons at $T_9 < 1$, which turn out to be bound in heavier nuclei. The number of such nuclei, for example, ^{4}He and ^{3}He, increases strongly at lower temperatures, since the energy of the interaction becomes so small for their breakdown [47, p. 69].

We present below two reactions of radiative capture, which are usually considered as candidates for the role of the ^{6}Li formation processes in the Big Bang and compare their rates with each other. It is believed that the radiative capture reaction

$$
^4\text{He} + {}^2\text{H} \rightarrow {}^6\text{Li} + \gamma
\tag{3.9}
$$

is one of the source of ^{6}Li in the Big Bang, *i.e.*, in the temperature range 50–400 keV [125, p. 99-102]. The relationship between temperature and energy is assumed to be 1.0 T_9 = 86.17 keV [47, p. 69].
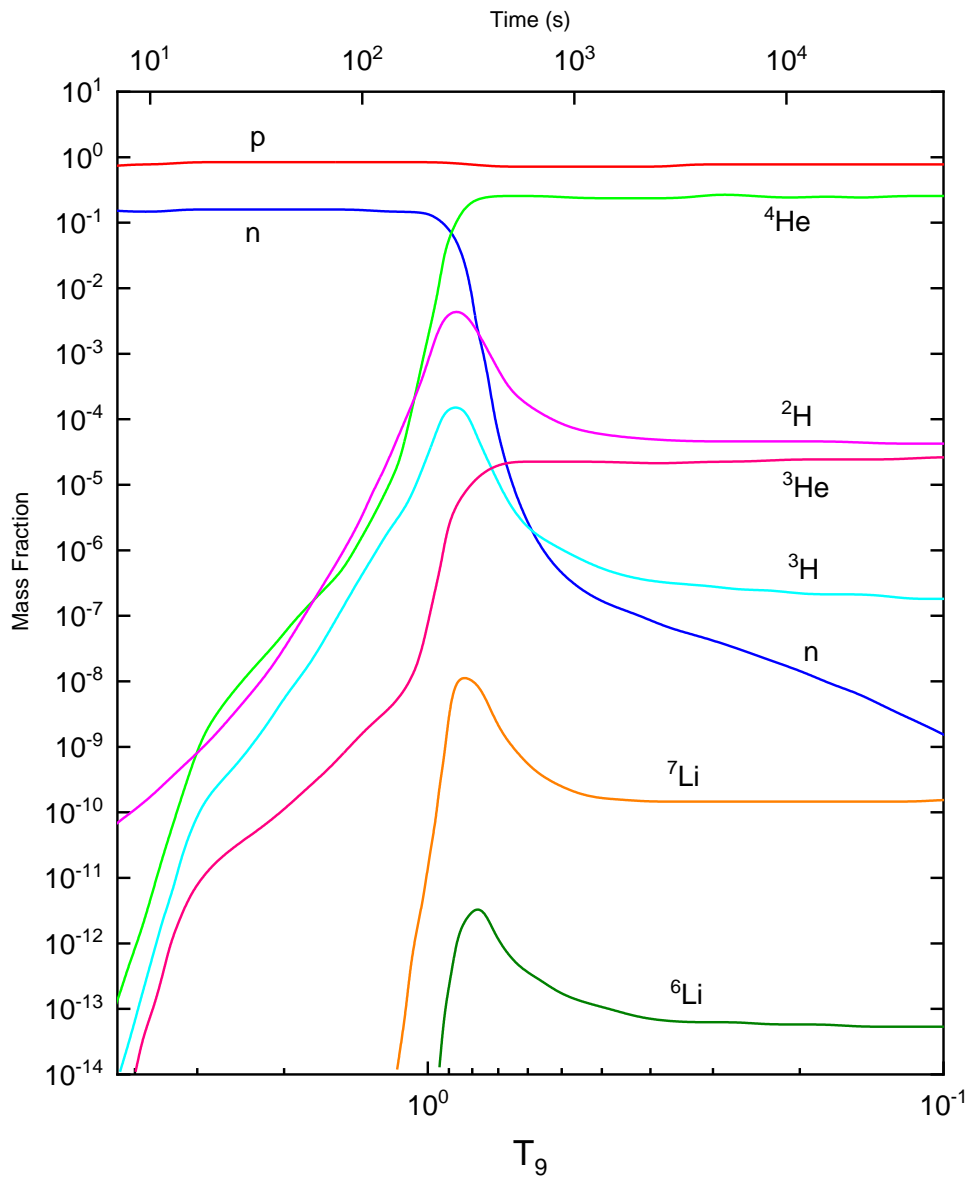
Figure 3.4 – Nuclei formation mass fractions in the Big Bang thermonuclear processes

Therefore, the energy range from 50 up to 400 keV corresponds approximately to the temperature range 0.6–4.5 T_9. A feature of this process is the forbiddance of the "strong" dipole $E1$ transition by the selection rules. So the reaction is due to the $E2$ transition, excepting the lowest energies, where the $E1$ process makes an appreciable contribution to the overall picture. As a result, the cross section of reaction (3.9) is only a few nanobarns and sharply decreases with energy decreasing due to the Coulomb barrier. The specified parametrization of this reaction rate is given by Trezzi et al. [129]

$$N_{\mathrm{A}}\langle\sigma v\rangle = 20.07 T_9^{-2/3}\exp(-7.47 T_9^{-1/3})(1.0 - 4.709 T_9^{1/3} +$$
$$+ 17.219 T_9^{2/3} - 23.839 T_9 + 19.27 T_9^{4/3} - 3.752 T_9^{5/3}) + \qquad (3.10)$$
$$+ 65.409 T_9^{-3/2}\exp(-7.565 T_9^{-1}).$$

This parametrization is used for comparison of the rates of radiative capture processes under consideration [47, p. 70]. There are no fundamental differences between (3.10) and similar parametrization from the survey [35, p. 294-308].

Theoretical and experimental aspects of the ^{6}Li formation problem in the ^{4}He + ^{2}H $\rightarrow$ ^{6}Li + γ reaction (Lithium problem) are discussed in detail in one of the most recent publication [130]. The authors believe that despite all the efforts of accurate theoretical calculations, even when the tensor component of the ^{4}He^{2}H forces [131] is taken into account, it is possible to overcome the discrepancy with the experimentally established prevalence of ^{6}Li/H ~ 1.7 10^{-14} only within ~20% [47, p. 70].

Therefore, as an additional source of ^{6}Li formation in the Big Bang, the reaction [132]

$$^3\mathrm{He} + {}^3\mathrm{H} \rightarrow {}^6\mathrm{Li} + \gamma. \qquad (3.11)$$

was considered. However, we could not find the parametrization of the rate of such a reaction or its theoretical calculations. In order to calculate the rate of this reaction, we perform the parametrization of its total cross sections [47, p. 70]. We use polynomial form with the Breit-Wigner term

$$\sigma(E) = a_1 + \frac{a_2}{(E - a_3)^2 + a_4^2/4} + a_5 E^{b_1} + a_6 E^{b_2} + a_7 E^{b_3} +$$
$$+ a_8 / E^{b_4}\exp(-a_9 / E^{b_5}). \qquad (3.12)$$

Basic experimental data were taken from [133, p. 1766]. Here we give 23 points for the total cross sections and we took one more point from [132, p. 4] at 81 keV in c.m. All experimental data are shown in Figure 3.5. The parametrization (3.12) with the parameters given in Table 3.1 leads to $\chi^2 = 0.4$, and the corresponding result is shown in Figure 3.5 with the solid curve 1 [47, p. 70-71].

All parameters given in Table 3.1 are varied independently to obtain a minimum value of χ^2. From Table 3.1 we see that the power of b_4 is 3/2, as is usually assumed in similar calculations [35, p. 294-308], the powers of b_1, b_2 and b_5 are close to 2/3, and the power of b_3 is approximately equal 2. But if we take powers, excepting the one of b_4, to be equal to these integers, this leads to an increase in χ^2 of up to 1.4. Moreover, if we perform additional variation of the remaining parameters a_i, then, despite the small value of $\chi^2 = 0.3$, the approximated cross section becomes negative even at energies below 50 keV, which strongly affects the shape of the reaction rate. Therefore,

in order to calculate the reaction rate, we used the parametrization (3.12) with the parameters given in Table 3.1 [47, p. 71].

Table 3.1 – The parameters of the expression (3.12) for parameterizing the data in Figure 3.5

a_i		b_i	
Coefficient	Value	Coefficient	Value
a_1	-	b_1	0.63402E+00
a_2	0.92167E+03	b_2	0.65888E+00
a_3	0.18011E+01	b_3	0.22340E+01
a_4	0.64950E+01	b_4	0.15001E+01
a_5	-	b_5	0.62889E+00
a_6	-		
a_7	0.16969E+00		
a_8	0.90199E+04		
a_9	0.60666E+01		

This parametrization leads to negative cross sections at energies below 5 keV, therefore the calculation of the cross section is limited by this energy value. In Figure 3.5, the dashed curve 2 shows the cross section obtained from the parameterization (3.12) and calculated in the energy range from 0.005 to 10 MeV, which is directly used later for calculations of the rate of reaction (3.11).

Furthermore, another reaction can be considered. The following process can be estimated as an additional ^{6}Li synthesis channel

$$n + {}^5\text{Li} \rightarrow {}^6\text{Li} + \gamma. \tag{3.13}$$

Obviously, a direct measurement of the cross section of this process is impossible. However, according to detailed balance, this cross section can be estimated from data for the photodisintegration reaction ^{6}Li(γ,n)^{5}Li with binding energy $E_{51} = 5.67$ MeV. The arguments in favor of the fact that the cross section of the reaction (3.13) can be significant is the absence of a Coulomb barrier, and also a centrifugal barrier, since a "strong" dipole $E1$ transition is realized from scattering S-waves [47, p. 71].

For further analytical calculations of the reaction (3.13) rate two variants of the cross section parameterization were obtained. In Figure 3.6a the solid curve shows the following version of the parameterization

$$\sigma(E) = a_1 + \frac{a_2}{(E - a_3)^2 + a_4^2 / 4} + a_5 E \tag{3.14}$$

with the parameters $a_1 = -0.62090\text{E}{-}01$, $a_2 = 0.10927\text{E}{+}03$, $a_3 = 0.64065\text{E}{+}01$, $a_4 = 0.79845\text{E}{+}01$, $a_5 = 0.27650\text{E}{+}00$ with $\chi^2 = 0.023$.
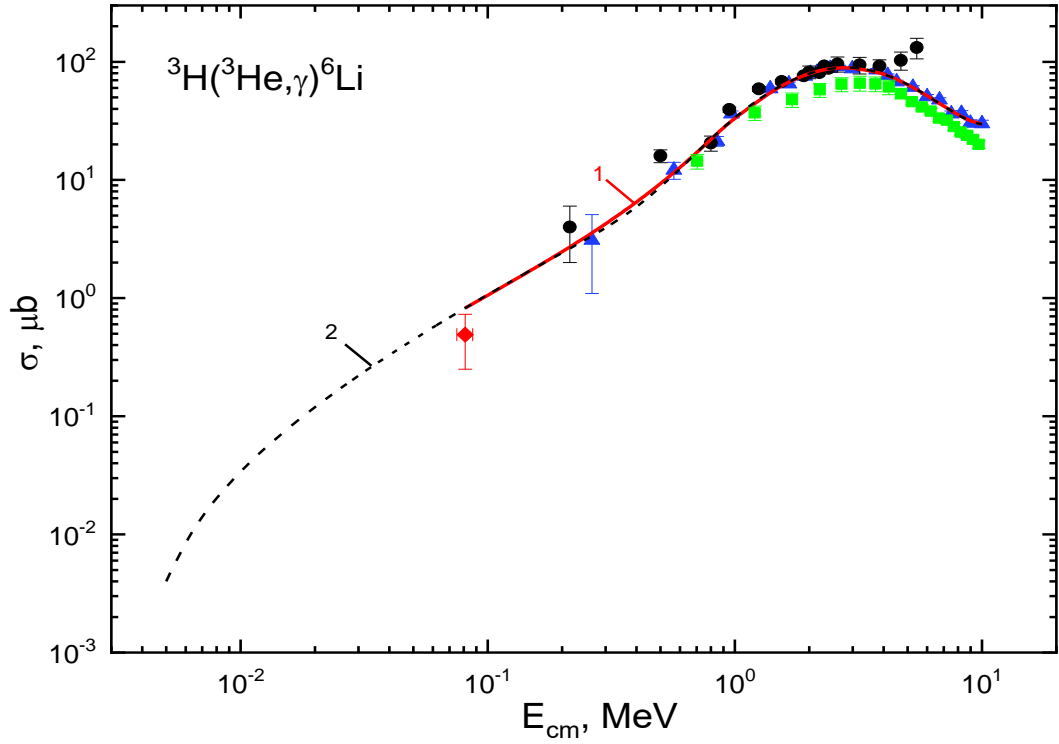
The experimental data are as follows: [134] – •, [133, p. 1766] – ▲, [132, p. 4] – ♦. For comparison, the results of [135] are given (■). Solid curves show different parameterizations (3.12).

Figure 3.5 – Radiative ^{3}H(^{3}He,γ)^{6}Li capture cross sections

These parameters were obtained as a parametrization of the data of [135] taken from [136] and shown with the dots in Figure 3.6. However, this parameterization does not properly describe the behavior of the cross section at thermal energy. The cross section reaches a plateau with a value of 1.9 microbars for any, arbitrarily low energy [47, p. 71].

Since the thermal cross section for this reaction was not measured by anyone, we can assume for it the value of 40 mb, as for ^{7}Li [137]. The use of this data on thermal neutrons for ^{7}Li is completely justified, because in the ground state this nucleus has the same quantum numbers $J^\pi = 3/2^-$ as ^{5}Li, while it is reasonable, for the first estimate, to assume that they have similar rms sizes.

For a correct description of the thermal cross sections, it is required to change the form of the parametrization (3.14) as

$$\sigma(E) = a_1 + \frac{a_2}{(E - a_3)^2 + a_4^2/4} + a_5 E + a_6/\sqrt{E} + a_7/E \qquad (3.15)$$

with parameters $a_1 = -0.62090E\text{-}01$; $a_2 = 0.10823E\text{+}03$; $a_3 = 0.63957E\text{+}01$; $a_4 = 0.79517E\text{+}01$; $a_5 = 0.27950E\text{+}00$; $a_6 = -0.14339E\text{-}01$; $a_7 = 0.10142E\text{-}02$ and $\chi^2 = 0.0216$ [47, p. 71].

74
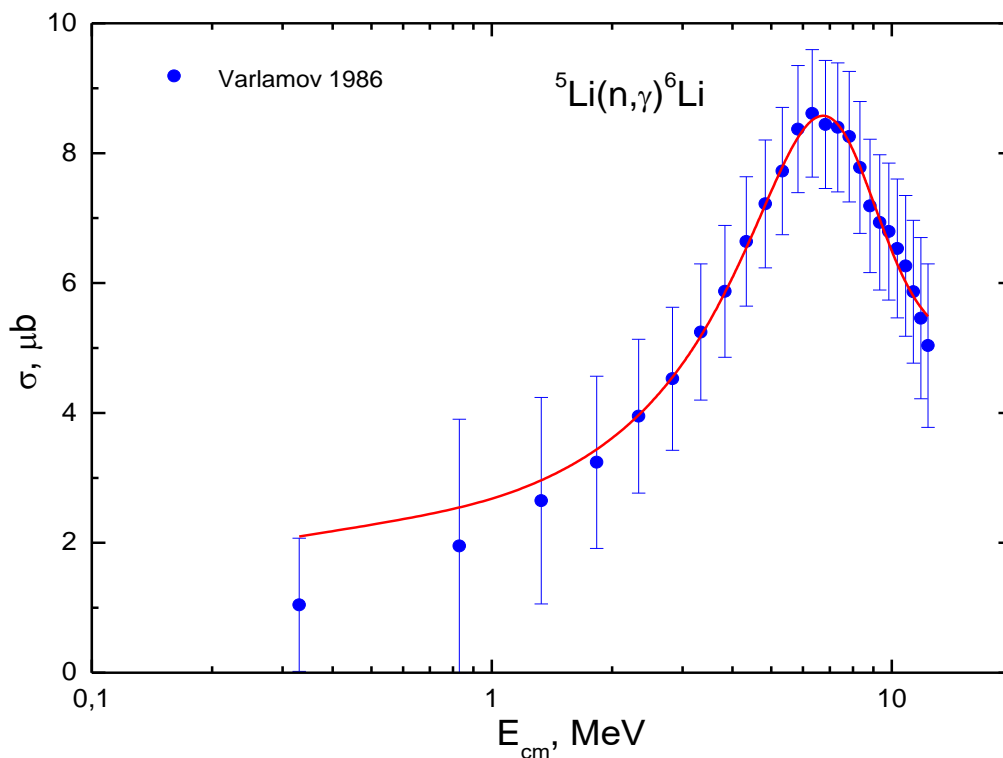
The experimental data from [135].

Figure 3.6a – The cross section for the radiative ^{5}Li$(n,\gamma)^6$Li capture based on the data for ^{6}Li$(\gamma,n)^5$Li photodisintegration [135] without reference to thermal cross sections σ_{th}

The green curve in Figure 3.6b is obtained from the parametrization (3.15), taking into account the reference to the thermal neutron capture cross section. Hence one can see that the parametrized cross section well conveys the results from [135] and describes the data at the thermal energy. However, one must bear in mind that at medium energies below the data given in [135], there is a "plateau", which is not characteristic of such cross sections [47, p. 72].

Furthermore, in Figure 3.7 one can see the reaction rates of some radiative capture processes which can lead to synthesis of ^{6}Li or can be an intermediate stage for its synthesis. The solid curve 1 shows the results for the capture reaction rate of ^{3}H$(^3$He$,\gamma)^6$Li obtained on the basis of our the parameterization (3.12) [47, p. 72].

Let us once again pay attention to the fact that such a parametrization leads to negative cross sections at energies below 5 keV. Therefore, the cross sections are cut off at this energy, which apparently leads to a more rapid decrease in the reaction rates at low temperatures. The solid curve 2' shows the rate of the neutron capture on ^{5}Li for the case of the parametrization (3.14), and the curve 2 – for the parameterization (3.15), which makes it possible to describe the cross sections at thermal energies.
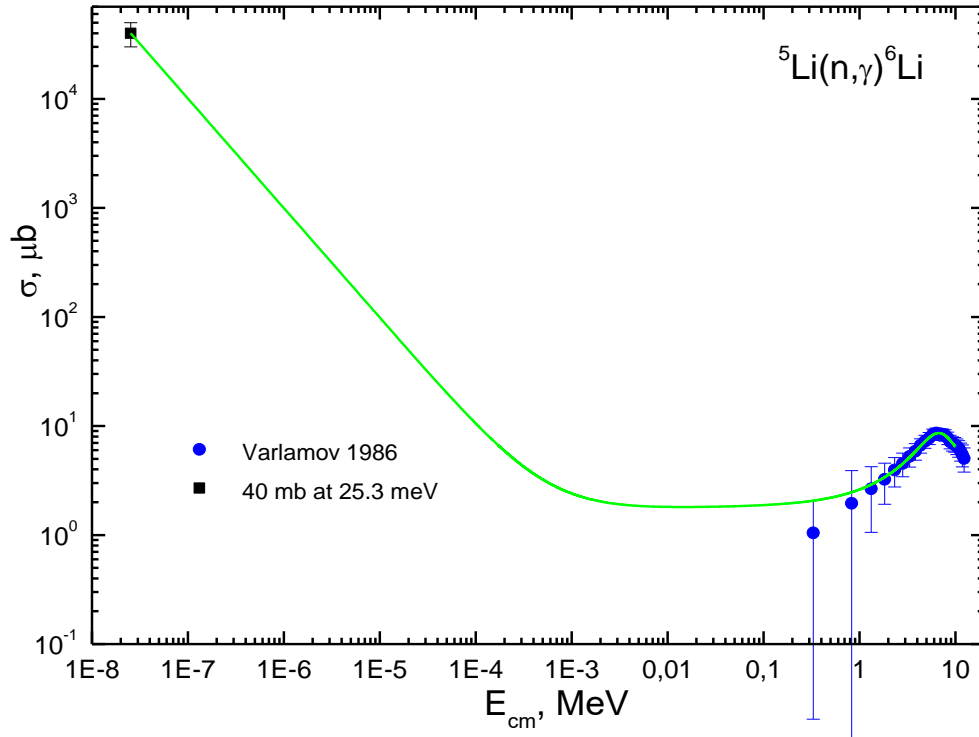
The experimental data from [135].

Figure 3.6b – The cross section for the radiative ^{5}Li$(n,\gamma)^6$Li capture based on the data for ^{6}Li$(\gamma,n)^5$Li photodisintegration [64, p. 193-197] with reference to σ_{th} for ^{7}Li

It is easy to see an increase in the reaction rate at low temperatures if we take into account the thermal cross sections for the ^{5}Li$(n,\gamma)^6$Li capture. The curve 3 is the rate of the capture ^{4}He$(^2$H$,\gamma)^6$Li reaction, obtained from the parametrization (9) of [129, p. 8]. The curve 4 shows our calculations of the rate of the ^{3}He$(^2$H$,\gamma)^5$Li capture reaction, which can be parametrized with the expression (3.3) [47, p. 72].

As follows from Figure 3.7, the rate of the "priority" reaction ^{4}He + ^{2}H $\rightarrow$ ^{6}Li + γ is less than all the others. Therefore, the question about the role of the ^{3}He + ^{3}H $\rightarrow$ ^{6}Li + γ process, as a possible candidate for amplifying the ^{6}Li yield arose [47, p. 72-73].

The answer is contained in the comparison of the reaction rates presented in Figure 3.7 and particles fractions in the process of BBN in Figure 3.4. Against the background of a large fraction of alpha particles, the deuterium fraction decreases with decreasing temperature. The synthesis of ^{3}He is accelerated and to some extent compared with the amount of ^{2}H, starting from $T_9 \sim 1$. In the same region, a maximum is observed for tritium ^{3}H, the fraction of which, however, sharply decreases with time. As a result, the conclusions of [132, p. 5] on the minor contribution of this reaction in comparison with (3.9) are understandable [47, p. 73].
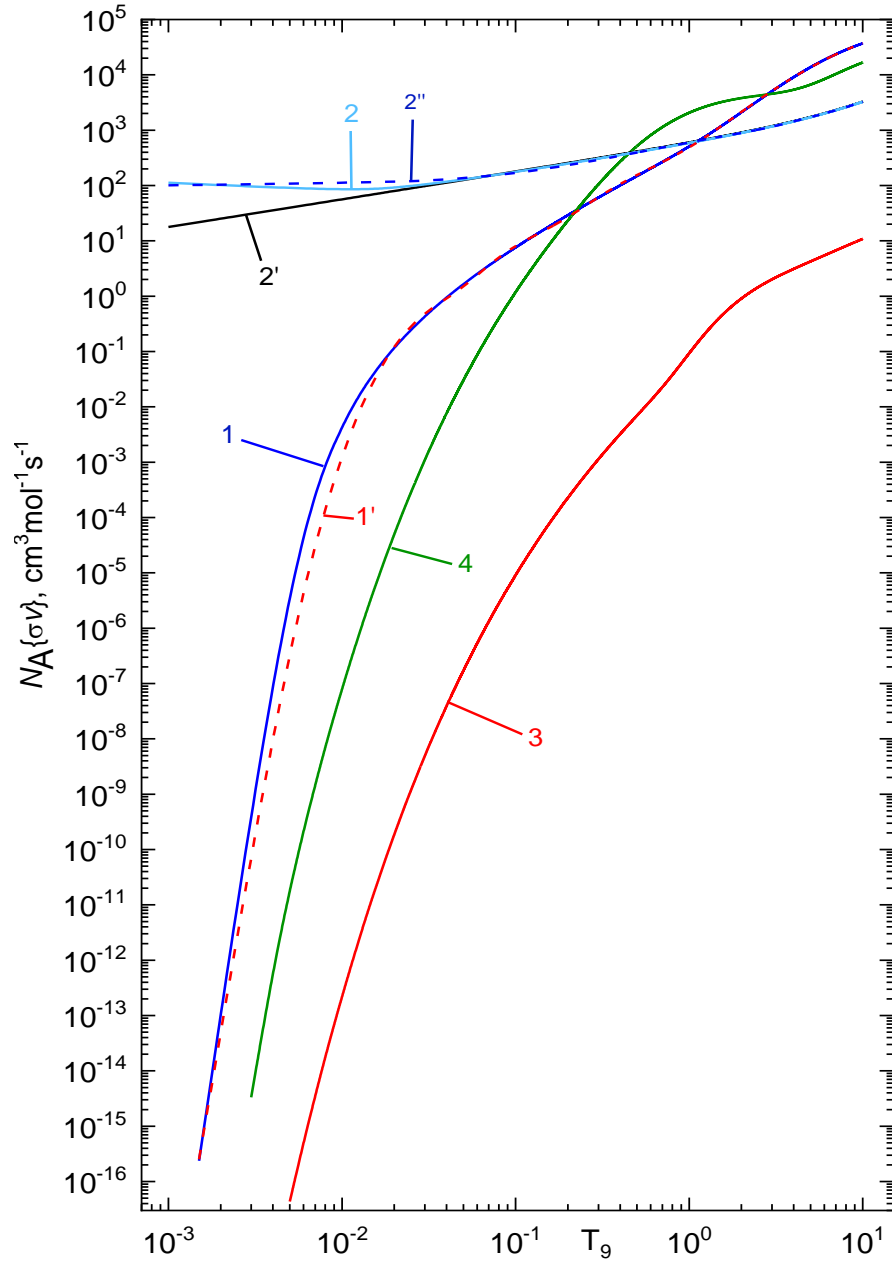
Figure 3.7 – Different radiative capture reactions rates

It follows from Figure 3.7 that the reaction rate of the ^{5}Li synthesis (curve 4) with the participation of deuterium and ^{3}He at $T_9 \sim 1$ is comparable and even greater than the process (3.9), and the deuterium fraction exceeds the tritium fraction by one order. In Figure 3.7 it is clearly shown that the rate of reaction ^{5}Li$(n,\gamma)^6$Li is greater than for ^{3}H$(^3$He$,\gamma)^6$Li and ^{3}He$(^2$H$,\gamma)^5$Li, and even greater than for ^{4}He$(^2$H$,\gamma)^6$Li reactions. Therefore, it can be assumed that in the $T_9 \sim 1$ region, which corresponds to a large neutron concentration, we can expect the real contribution of the reaction $n + {}^5$Li $\rightarrow$ ^{6}Li $+ \gamma$ to the ^{6}Li synthesis [47, p. 73].

Now we give the parametrizations of ^{5}Li$(n,\gamma)^6$Li and ^{3}H$(^3$He$,\gamma)^6$Li capture reactions rates. In the first case, it was possible to find only a polynomial form of the parametrization

$$N_A \langle \sigma v \rangle = \sum_{i=1}^{N} a_i E^{i-1} \tag{3.16}$$

with the parameters from Table 3.2. This form at $N = 7$ leads to $\chi^2 = 3.0$. Here and below, for calculations of χ^2, the error was assumed to be 1%. The results of the approximation are shown in Figure 3.7 with the dashed curve 2" [47, p. 73-74].

Table 3.2 – The parameters for expression (3.16)

Coefficient	Value	Coefficient	Value
a_1	100.2674	a_5	-15.13806
a_2	717.7027	a_6	1.2058
a_3	-296.7566	a_7	-0.0374
a_4	93.84265		

To parameterize the rate of the second reaction, another form

$$N_A \langle \sigma v \rangle = a_1 / T_9^{a_2} \exp(-a_3 / T_9^{a_4})(1.0 + a_5 T_9^{a_6} + a_7 T_9^{a_8} +$$
$$+ a_9 T_9^{a_{10}} + a_{11} T_9^{a_{12}}) + a_{13} / T_9^{a_{14}} \exp(-a_{15} / T_9^{a_{16}}) \tag{3.17}$$

was used which leads to $\chi^2 = 32.4$. The results of the approximation are shown in Figure 3.7 with the dashed curve 1' with parameters given in Table 3.3.

As seen from Figure 3.7, the rate of the ^{3}H(^{3}He,γ)^{6}Li capture reaction has an unusual form. Perhaps this is a consequence of the overestimated cross section obtained from the parametrization (3.12) in the low-energy region. Therefore, in expression (3.17), it is required to vary not only the coefficients of the T_9 powers, but also the values of the powers themselves [47, p. 74].

Based on the obtained results, a more consistent evaluation of the role of the $n + {}^5\text{Li} \rightarrow {}^6\text{Li} + \gamma$ process in the BBN and in stars is desirable in the future. For this purpose, all necessary cross section parameterizations and reaction rates are obtained in this research. In addition, simple estimates based on the mass fraction distribution shows qualitatively that the role of the $n + {}^5\text{Li} \rightarrow {}^6\text{Li} + \gamma$ reaction requires a further study for astrophysical processes in conditions of high neutron concentration, which have a different temperature regime compared to the BBN [47, p. 74].

We present calculations for the total cross sections, astrophysical S-factor, and reaction rates for ^{3}He(^{2}H,γ)^{5}Li radiative capture in the framework of the potential cluster model with forbidden states using a single channel approach. We show that the integral characteristics of ^{3}He(^{2}H,γ)^{5}Li radiative capture can be reproduced with very high accuracy [47, p. 74].

Our results are promising and pave the way for further microscopic analyses of this process. However, it is well known that the ^{3}He(^{2}H,p)^{4}He and ^{3}H(^{2}H,n)^{4}He) reactions are strongly dominant. We are well aware of the classical works within the method of resonating groups on the investigation of the $\alpha + N$ scattering channels

taking into account the coupled-channels for five-nucleon systems. This formalism found wide acceptance following its application to calculations of various polarization characteristics [138]. Indeed, there are indications of very subtle effects associated with channels coupling for polarization characteristics [47, p. 74].

Table 3.3 – The parameters for expression (3.17)

Coefficient	Value	Coefficient	Value
a_1	74.07273	a_9	907.838
a_2	1.8375	a_{10}	3.00098
a_3	4.95476	a_{11}	–
a_4	0.4065	a_{12}	3.31375
a_5	2183.953	a_{13}	11793.31
a_6	–	a_{14}	2.28774
a_7	–	a_{15}	2.48388
a_8	-1.56543	a_{16}	0.53456

Today the Gaussian expansion method to accurately solve the Schrödinger equations, which includes heavy calculations for bound, resonant and scattering states of three- to five-body systems (see review: [139] and references) is used for coupled-channels calculations. Our calculations can be further improved by including additional $\alpha + N$ channels by performing coupled-channels calculations. The description of the five-nucleon system using the potential model within the Schrödinger equations with modern nucleon-nucleon potentials is a challenging issue and beyond the scope of the present research.

One can see that the experimental data can be reproduced within a single-channel approach. In our opinion the coupled-channels calculations will not dramatically change the resulting pattern [47, p. 75].

4 Astrophysical n^{10}Be process at low energies

In this the results obtained with the potentials from Section 2 for the total cross section, the astrophysical S-factor, the S-factor screening effects, and the rate of the ^{3}He(^{2}H,γ)^{5}Li radiative capture reaction.

4.1 Processing of experimental data

In the current section we present the formalities of the Coulomb dissociation data recalculation into the radiative capture total cross-sections, since we were faced with a problem of some differences in numerical results, caused by that different authors use the different initial data, for instance, the binding energy in the n^{10}Be channel, ^{11}Be Coulomb dissociation measuring results, etc [48, p. 92].

We considered the total cross-section of $A(\gamma,n)B$ direct photodisintegration process, where $B = A$-1 expressed in terms of the reduced transition probability of Coulomb dissociation, can be written as

$$\sigma_{\gamma n} = \frac{16\pi^3}{9\hbar c} E_\gamma \cdot \frac{dB(E1)}{dE_\gamma}. \tag{4.1}$$

Here the excitation energy is equal to $E^* \equiv E_\gamma$, $E_{cm} = E_\gamma - E_b$, where E_b is the binding energy of a neutron, and the constant $e^2 / \hbar c = 0.007297$ [140]. The neutron radiative capture cross-section is connected with the photodisintegration cross-section by the detailed equilibrium [106, p. 67-119]

$$\sigma_{n\gamma}(E_{c.m.}) = \frac{2J_A + 1}{2J_{A-1} + 1} \cdot \frac{E_\gamma^2}{2\mu c^2 E_{c.m.}} \cdot \sigma_{\gamma n}(E_\gamma), \tag{4.2}$$

where μc^2 is the reduces mass in MeV, which is equal to 853.590 MeV for the reaction under consideration at $m(^{10}$Be$) = 9327.546$ MeV [141] and $m_n = 939.573$ MeV, $J_A = 1/2$, $J_{A-1} = 0$, $E_b = 0.507$ MeV [105, p. 4-10] or $E_b = 0.504$ MeV [104, p. 298-300, 106, p. 67-119]. It is obvious, the binding energy value has a strong influence on E_{cm} particles energy at low energies, and in the different works the different values of this energy have been used [48, p. 92].

In order to test the used by us calculation methods and computer programs we have considered ^{14}C(n,γ)^{15}C reaction detailed in [106, p. 67-119]. Figure 2.10 of [106, p. 67-119] illustrates the Coulomb dissociation probabilities data, and Figure 2.11 shows the results of their recalculation into the total cross-sections of the neutron radiative capture on ^{10}Be. We have digitized the data presented in Figure 2.10 and recalculated them into the total cross-sections. The results of present recalculation and data from Figure 2.11 [106, p. 67-119] are presented here in Figure 4.1. For this recalculation we used the mass $m(^{14}$C$) = 13043.936$ MeV, and the neutron mass given above [48, p. 92].

As we can see from Figure 4.1 the difference between the present results and data [106, p. 67-119] for the neutron capture on ^{14}C total cross-sections is small enough and

caused by accuracy of digitization of data for the Coulomb dissociation probability from the figures presented in [106, p. 67-119].
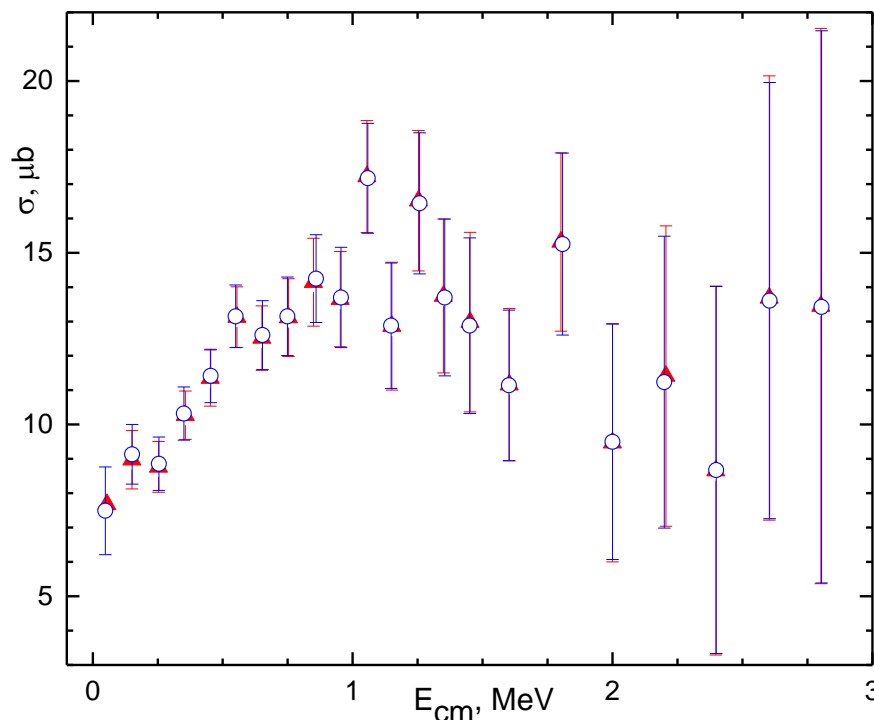
Figure 4.1 – Comparison of the $^{14}C(n,\gamma)^{15}C$ capture total cross-sections obtained by using the Coulomb dissociation data (▲ , the present calculation) and results for these cross-sections (◌) presented in [106, p. 67-119]

The following is the recalculation of data for ^{11}Be Coulomb dissociation probability from [104, p. 298-300, 106, p. 67-119], presented in Figure 4.2, into $^{10}Be(n,\gamma)^{11}$Be radiative capture total cross-sections. This recalculation results are shown in Figure 4.3, but another ones for the Coulomb dissociation data [105, p. 9-10] provided by Professor T. Aumann are given in Table 4.1 [48, p. 93].

The similar recalculation of data for $^{10}Be(n,\gamma)^{11}$Be reaction, provided by Professor T. Nakamura [106, p. 67-119], is presented in Table 4.2.

In Figure 4.2 the energy 0.5 MeV is shown by the vertical red line. Red points illustrate the results [105, p. 9-10], blue squares correspond to data [104, p. 298-300], and green triangles show the results [106, p. 67-119]. One can see from Figure 4.2 that there is a great difference between the data [104, p. 298-300], [105, p. 9-10], and [106, p. 67-119]. Data [105, p. 9-10] are substantially less than results [104, p. 298-300, 106, p. 67-119], and this difference can reach 50%.

In Figure 4.3 the black points show the recalculation results for data [104, p. 298-300]. It seen they differ substantially from the present recalculation of the same data [104, p. 298-300], shown in Figure 4.3 by the blue squares [48, p. 92].

81

Table 4.1 – The reduced probabilities of the Coulomb dissociation, the total cross-sections of ^{11}Be(γ,n)^{10}Be photodisintegration and ^{10}Be(n,γ)^{11}Be radiative capture

E_γ	dB/dE_γ	$\delta[dB/dE\gamma]$	E_n	$\sigma(\gamma,n)$	$\delta[\sigma(\gamma,n)]$	$\sigma(n,\gamma)$	$\delta[\sigma(n,\gamma)]$
0.52500E+00	0.13430E+00	0.23950E-01	0.19813E-01	0.28368E+03	0.50589E+02	0.50889E+01	0.90751E+00
0.57500E+00	0.26770E+00	0.32620E-01	0.74850E-01	0.61931E+03	0.75464E+02	0.35276E+01	0.42985E+00
0.62500E+00	0.41420E+00	0.41430E-01	0.12989E+00	0.10416E+04	0.10418E+03	0.40393E+01	0.40403E+00
0.67500E+00	0.36680E+00	0.44020E-01	0.18492E+00	0.99615E+03	0.11955E+03	0.31650E+01	0.37983E+00
0.72500E+00	0.45310E+00	0.49170E-01	0.23996E+00	0.13217E+04	0.14343E+03	0.37333E+01	0.40513E+00
0.77500E+00	0.48750E+00	0.48250E-01	0.29500E+00	0.15201E+04	0.15045E+03	0.39910E+01	0.39501E+00
0.82500E+00	0.57460E+00	0.50710E-01	0.35003E+00	0.19073E+04	0.16832E+03	0.47824E+01	0.42206E+00
0.87500E+00	0.48410E+00	0.51430E-01	0.40507E+00	0.17043E+04	0.18106E+03	0.41539E+01	0.44130E+00
0.95000E+00	0.59000E+00	0.37860E-01	0.48762E+00	0.22551E+04	0.14471E+03	0.53822E+01	0.34537E+00
0.10500E+01	0.57530E+00	0.38790E-01	0.59770E+00	0.24304E+04	0.16387E+03	0.57810E+01	0.38979E+00
0.11500E+01	0.53680E+00	0.41580E-01	0.70777E+00	0.24837E+04	0.19239E+03	0.59846E+01	0.46356E+00
0.12500E+01	0.47300E+00	0.39440E-01	0.81784E+00	0.23788E+04	0.19835E+03	0.58606E+01	0.48867E+00
0.13500E+01	0.40120E+00	0.38150E-01	0.92792E+00	0.21791E+04	0.20721E+03	0.55192E+01	0.52482E+00
0.14500E+01	0.37890E+00	0.39470E-01	0.10380E+01	0.22105E+04	0.23026E+03	0.57738E+01	0.60145E+00
0.16000E+01	0.32110E+00	0.29730E-01	0.12031E+01	0.20670E+04	0.19138E+03	0.56718E+01	0.52514E+00
0.18000E+01	0.27860E+00	0.27970E-01	0.14232E+01	0.20176E+04	0.20256E+03	0.59230E+01	0.59464E+00
0.20000E+01	0.25270E+00	0.28770E-01	0.16434E+01	0.20334E+04	0.23150E+03	0.63823E+01	0.72663E+00
0.22000E+01	0.20650E+00	0.29800E-01	0.18635E+01	0.18278E+04	0.26377E+03	0.61217E+01	0.88342E+00
0.24000E+01	0.17000E+00	0.29390E-01	0.20837E+01	0.16415E+04	0.28379E+03	0.58516E+01	0.10116E+01
0.26000E+01	0.14130E+00	0.25010E-01	0.23038E+01	0.14781E+04	0.26162E+03	0.55929E+01	0.98993E+00
0.28000E+01	0.10960E+00	0.27320E-01	0.25240E+01	0.12347E+04	0.30777E+03	0.49456E+01	0.12328E+01
0.30000E+01	0.12030E+00	0.26590E-01	0.27441E+01	0.14520E+04	0.32094E+03	0.61411E+01	0.13574E+01
0.32000E+01	0.65070E-01	0.26880E-01	0.29643E+01	0.83776E+03	0.34607E+03	0.37319E+01	0.15416E+01
0.34000E+01	0.95910E-01	0.26130E-01	0.31844E+01	0.13120E+04	0.35744E+03	0.61418E+01	0.16733E+01
0.36000E+01	0.30730E-01	0.28190E-01	0.34046E+01	0.44510E+03	0.40831E+03	0.21849E+01	0.20043E+01
0.38000E+01	0.34140E-01	0.23230E-01	0.36247E+01	0.52196E+03	0.35516E+03	0.26814E+01	0.18245E+01
0.40000E+01	0.45360E-01	0.23380E-01	0.38449E+01	0.73000E+03	0.37627E+03	0.39174E+01	0.20191E+01
0.42000E+01	0.52790E-01	0.24560E-01	0.40650E+01	0.89205E+03	0.41502E+03	0.49918E+01	0.23224E+01
0.44000E+01	0.64780E-01	0.22730E-01	0.42851E+01	0.11468E+04	0.40239E+03	0.66812E+01	0.23443E+01
0.46000E+01	0.12210E-01	0.23220E-01	0.45053E+01	0.22598E+03	0.42974E+03	0.13686E+01	0.26028E+01
0.48000E+01	-0.99970E-02	0.20930E-01	0.47254E+01	-0.19306E+03	0.40420E+03	-0.12139E+01	0.25414E+01
0.50000E+01	0.25010E-01	0.21770E-01	0.49456E+01	0.50312E+03	0.43794E+03	0.32797E+01	0.28548E+01
0.52000E+01	0.15750E-01	0.18990E-01	0.51657E+01	0.32951E+03	0.39730E+03	0.22242E+01	0.26818E+01
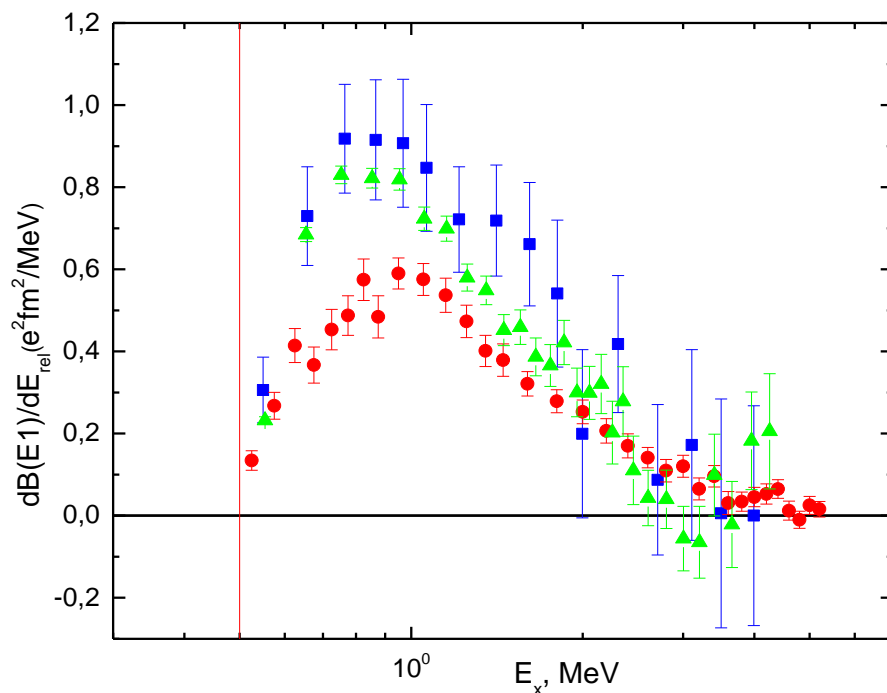
Experimental data: ■ are from [104, p. 298-300], ● from [105, p. 9], and ▲ from [106, p. 67-119].

Figure 4.2 – The Coulomb dissociation probabilities
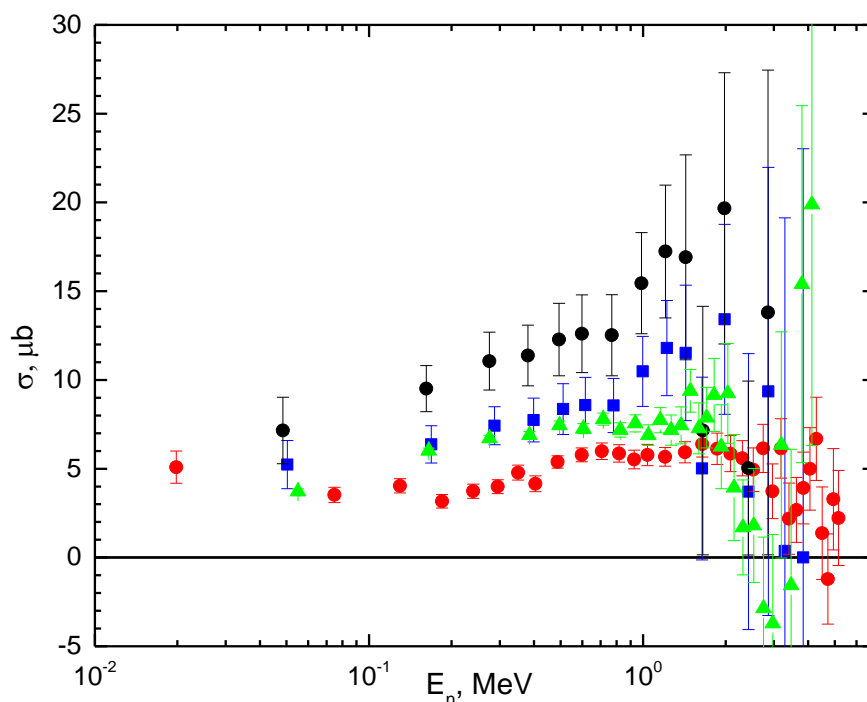
Data: ■ from [104, p. 298-300], ● from [105, p. 4-10], and ▲ from [106, p. 67-119]. ● show the recalculation results for data [104, p. 298-300].

Figure 4.3 – The obtained by us ^{10}Be$(n,\gamma)^{11}$Be radiative capture total cross-sections based on the Coulomb dissociation probability

Table 4.2 – The reduced probabilities of the Coulomb dissociation, the total cross-sections of ^{11}Be$(\gamma,n)^{10}$Be photodisintegration and ^{10}Be$(n,\gamma)^{11}$Be radiative capture

| E_γ	dB/dE_γ	$\delta[dB/dE_\gamma]$	E_n	$\sigma(\gamma,n)$	$\delta[\sigma(\gamma,n)]$	$\sigma(n,\gamma)$	$\delta[\sigma(n,\gamma)]$
0.55400E+00	0.23220E+00	0.88112E-02	0.55037E-01	0.51755E+03	0.19640E+02	0.37218E+01	0.14123E+00
0.65400E+00	0.68446E+00	0.16999E-01	0.16511E+00	0.18010E+04	0.44728E+02	0.60163E+01	0.14942E+00
0.75400E+00	0.82996E+00	0.21356E-01	0.27518E+00	0.25178E+04	0.64787E+02	0.67077E+01	0.17260E+00
0.85400E+00	0.82182E+00	0.23971E-01	0.38526E+00	0.28238E+04	0.82363E+02	0.68933E+01	0.20106E+00
0.95400E+00	0.81894E+00	0.26301E-01	0.49533E+00	0.31433E+04	0.10095E+03	0.74478E+01	0.23919E+00
0.10540E+01	0.72331E+00	0.28438E-01	0.60540E+00	0.30673E+04	0.12060E+03	0.72581E+01	0.28537E+00
0.11540E+01	0.69900E+00	0.30684E-01	0.71548E+00	0.32454E+04	0.14247E+03	0.77897E+01	0.34195E+00
0.12540E+01	0.57986E+00	0.32868E-01	0.82555E+00	0.29256E+04	0.16583E+03	0.71861E+01	0.40733E+00
0.13540E+01	0.54881E+00	0.34808E-01	0.93562E+00	0.29897E+04	0.18962E+03	0.75543E+01	0.47914E+00
0.14540E+01	0.45194E+00	0.37923E-01	0.10457E+01	0.26438E+04	0.22185E+03	0.68927E+01	0.57838E+00
0.15540E+01	0.45915E+00	0.41971E-01	0.11558E+01	0.28708E+04	0.26242E+03	0.77350E+01	0.70705E+00
0.16540E+01	0.38684E+00	0.46088E-01	0.12658E+01	0.25743E+04	0.30670E+03	0.71743E+01	0.85475E+00
0.17540E+01	0.36575E+00	0.51044E-01	0.13759E+01	0.25811E+04	0.36022E+03	0.74422E+01	0.10386E+01
0.18540E+01	0.42178E+00	0.54085E-01	0.14860E+01	0.31462E+04	0.40344E+03	0.93847E+01	0.12034E+01
0.19540E+01	0.30008E+00	0.59193E-01	0.15961E+01	0.23591E+04	0.46536E+03	0.72775E+01	0.14356E+01
0.20540E+01	0.29910E+00	0.64603E-01	0.17061E+01	0.24718E+04	0.53388E+03	0.78819E+01	0.17024E+01
0.21540E+01	0.32079E+00	0.72091E-01	0.18162E+01	0.27801E+04	0.62476E+03	0.91584E+01	0.20581E+01
0.22540E+01	0.20229E+00	0.76464E-01	0.19263E+01	0.18345E+04	0.69343E+03	0.62392E+01	0.23584E+01
0.23540E+01	0.27806E+00	0.84503E-01	0.20364E+01	0.26335E+04	0.80033E+03	0.92412E+01	0.28084E+01
0.24540E+01	0.11028E+00	0.83553E-01	0.21464E+01	0.10889E+04	0.82495E+03	0.39395E+01	0.29846E+01
0.26040E+01	0.42889E-01	0.67467E-01	0.23115E+01	0.44935E+03	0.70685E+03	0.16998E+01	0.26739E+01
0.28040E+01	0.39987E-01	0.71057E-01	0.25317E+01	0.45111E+03	0.80163E+03	0.18066E+01	0.32103E+01
0.30040E+01	-0.56019E-01	0.78597E-01	0.27518E+01	-	0.94994E+03	-	0.40171E+01
0.32040E+01	-0.64728E-01	0.87340E-01	0.29720E+01	-	0.11259E+04	-	0.50150E+01
0.34040E+01	0.98931E-01	0.99400E-01	0.31921E+01	0.13549E+04	0.13613E+04	0.63423E+01	0.63723E+01
0.36540E+01	-0.21345E-01	0.10489E+00	0.34673E+01	-	0.15420E+04	-	0.76568E+01
0.39540E+01	0.18232E+00	0.11905E+00	0.37975E+01	0.29005E+04	0.18939E+04	0.15398E+02	0.10055E+02
0.42540E+01	0.20553E+00	0.14036E+00	0.41277E+01	0.35177E+04	0.24023E+04	0.19887E+02	0.13581E+02

4.2 Classification for the E1 transition capture

On the basis of the data given above in Section 2 it can be assumed that the E1 capture of a neutron is allowed from ^2P scattering waves without the bound FSs or ASs to the $^2S_{1/2}$ GS of ^{11}Be with the bound FSs or ASs.

$$
\begin{aligned}
{}^2P_{1/2} &\to {}^2S_{1/2}, \\
{}^2P_{3/2} &\to {}^2S_{1/2}.
\end{aligned}
\tag{4.3}
$$

For the radiative capture to the FES the analogous E1 transition from $^2S_{1/2}$ and $^2D_{3/2}$ scattering waves with the bound FSs, but without bound ASs to $^2P_{1/2}$ BS with the bound AS, but without bound FS, is allowed [48, p. 96].

$$^2 S_{1/2} \rightarrow {}^2 P_{1/2},$$
$$^2 D_{3/2} \rightarrow {}^2 P_{1/2}. \tag{4.4}$$

The potentials of the GS and FES are constructed so that to describe correctly the channel binding energy, ^{11}Be charge radius and its asymptotic constant C_w in the n^{10}Be channel [48, p. 97].

Data for the asymptotic normalizing coefficients A_{NC} are given, for example, in [37, p. 108]. In further calculations we have used ^{10}Be GS radius equal to 2.357(18) fm from [141], and ^{11}Be GS radius value given in [110, p. 99] is equal to 2.463(15) fm. The charge radius of the neutron is equal to zero and its mass radius equal to 0.8775(51) fm agrees with the known radius of a proton [140].

Furthermore, the estimated value of the charge radius of ^{11}Be FES presented in [35, p. 283-294] is equal to 2.43(10) fm, and the value of ^{11}Be GS obtained in the same work is equal to 2.42(10) fm [48, p. 97].

The value of radius of the neutron in ^{11}Be, given in [142], is equal to 5.6(6) fm. At the same time the value of the neutron radius in the GS, presented in [143], is equal to 7.60(25) fm, and another one for the FES, given in the same work, is equal to 4.58(25) fm. In all further calculations we have used the exact values of ^{10}Be and neutron masses: $m(^{10}$Be$) = 10.01134$ amu [141], and $m_n = 1.008665$ amu [140, 141].

4.3 Calculation of the n^{10}Be reaction characteristics

Now let us discuss the results for the total cross-sections and this reaction rate of the neutron radiative capture on ^{10}Be. These characteristics were obtained on the basis of the described in Subsection 2 nuclear model using the potentials given above.

4.3.1 ^{10}Be$(n,\gamma)^{11}$Be reaction total cross section

As it was already mentioned we assume that the radiative $E1$ capture (4.3) occurs from the ^2P scattering waves to the $^2S_{1/2}$ GS of ^{11}Be in the n^{10}Be channel. The present calculation of such capture cross-sections for the GS potential (2.20) leads to the results shown in Figure 4.4 by the blue solid line. In all these calculations for $^2P_{1/2}$ elastic scattering potentials we used the potential of zero width, and for $^2P_{3/2}$ scattering potentials the potential with parameters (2.22) was used [48, p. 98].

The experimental data for the neutron radiative capture on ^{10}Be, shown in Figure 4.4, were recalculated by us from [104, p. 298-300, 106, p. 67-119]. As it can be seen from these results the calculated cross-sections on the whole describe the recalculated by us experimental data [104, p. 298-300, 106, p. 67-119] in the considered energy region. Seemingly, they are in the best agreement with the results [106, p. 67-119] and do not practically exceed the limits of available experimental varieties of this research.

The results of other works and our previous results of calculation are given below for comparison. Particularly, the blue dashed line in Figure 4.4 shows the results from [103, p. 326c], the black dashed-dotted line is the result [36, p. 1546]. The green dashed line present results from [122, p. 10], and here one should keep in mind that these results have been obtained with zero potentials for both P waves, i.e. the resonance in $^2P_{3/2}$ scattering wave was not taken into account [48, p. 98-99].

The black solid line shows the present calculation results obtained by using the potentials from [122, p. 10] while the *ME* integrating up to 150 fm. These results in contrast to another one obtained in [122, p. 10] reproduce well data [103, p. 326c] at all energies [48, p. 99].

As it can be seen from Figure 4.4 the calculated cross-section (the blue solid line) is decreased slowly at the energies of the order of 10 keV and less, that does not enable to describe its value at the thermal energy equal to 290(90) μb, presented in [36, p. 1546]. Therefore, let us consider further the *E*1 transitions from $^2S_{1/2}$ and $^2D_{3/2}$ scattering waves to $^2P_{1/2}$ FES, which were given above as transition (4.4).

The blue dashed line in Figure 4.5 presents the results for the *E*1 transition (4.3) to the GS with potentials (2.20), (2.22), and zero potential of $^2P_{1/2}$ scattering, these results were shown in Figure 4.4 by the blue solid line. The black dotted line corresponds to *E*1 transition (4.4) from $^2S_{1/2}$ and $^2D_{3/2}$ scattering waves with potential (2.20) and the moment *L* equal to 0 and 2 to $^2P_{1/2}$ FES with potential (2.23) [48, p. 99].

The blue solid line shows the total cross-section of these two *E*1 processes and on the whole correctly reproduces the general trend of available experimental data in the whole energy region under consideration from the thermal energy equal to 25.3 meV to the energy about 5.0 MeV. The calculated cross-section at the thermal energy takes on a value equal to 302 μb [48, p. 99].

The cross-section of the allowed *M*1 transition from the $^2S_{1/2}$ scattering wave to the $^2S_{1/2}$ GS of ^{11}Be in the n^{10}Be channel with the same potential (2.20) in both states will tend to zero due to orthogonality of the discrete and continuous spectra wave functions in one potential. The real numerical calculation of such cross-sections leads to the value that is less than 10^{-2} μb in the energy region from 1 keV to 3.0 MeV. At the energy equal to 25.3 meV such cross-section is less than 1% from the cross-section of transition to the FES, shown in Figure 4.5 by the black dotted line [48, p. 99].

If we consider further *M*1 transitions from ^2P scattering waves with zero potential for the $^2P_{1/2}$ wave and potential (2.22) for the $^2P_{3/2}$ waves to the $^2P_{1/2}$ FES with potential (2.23), then the cross-sections do not exceed the value equal to 0.15 μb in all energy ranges. For the *E*2 transitions from the $^2D_{3/2}$ wave with potential (2.20) at $L = 2$ and the $^2D_{5/2}$ wave with potential (2.21) to the GS with $^2S_{1/2}$ the cross-sections value does not exceed 10^{-3} μb even at the resonance energies. It can be seen from these results that such transitions do not make noticeable contribution to the total cross-sections of the process under consideration [48, p. 99].

Figure 4.5 demonstrates the difference between the total cross-sections at the thermal energy, in [36, p. 1546] the value 290(90) μb was obtained, and in [144, p. 1-19] the upper value is equal to 1 mb, i.e. three times more, was given. Therefore, other potential of the FES may be proposed, for example, with the following parameters

$$V_{P1/2} = 42.112565 \text{ MeV and } \gamma_{1/2} = 0.15 \text{ fm}^{-2}. \tag{4.5}$$

^{10}Be(n,γ)^{11}Be
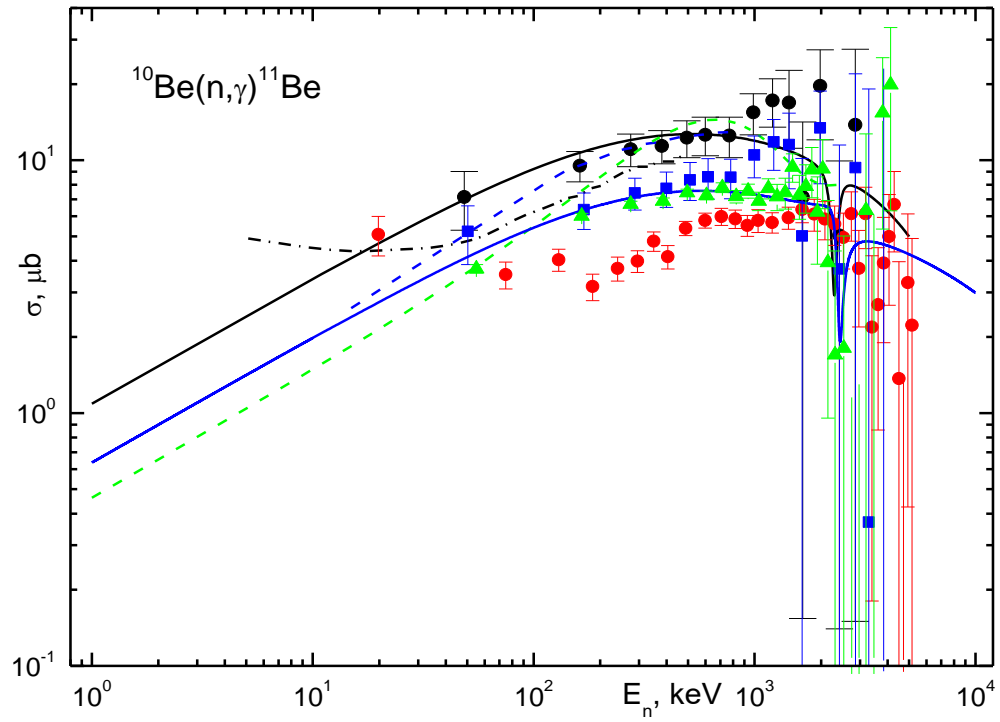
• correspond to data from [103, p. 326c], based on the results [104, p. 298-300]; •
show the present recalculation of data [105, p. 4-10]; ▲ show the recalculation of data
[106, p. 67-119], ■ are the present recalculation of data [104, p. 298-300]. The blue
dashed line shows the results [103, p. 326c]; the black dotted-dashed line is the result
from [36, p. 1546]; the green dashed line shows results from [122, p. 10]; the black
solid line shows the results of present calculation with potentials from [122, p. 10]; the
blue solid line shows the results of present calculations with potentials (2.20), (2.22),
and zero potential of the $^2P_{1/2}$ scattering.

Figure 4.4 – The total cross-sections of ^{10}Be(n,γ)^{11}Be radiative $E1$ capture to the GS

The potential (4.5) leads to the binding energy equal to -0.181560 MeV at the
FDM accuracy equal to 10^{-6} MeV, the AC is equal to 0.40(1) in the range of 7–30 fm,
the mass radius is equal to 2.90 fm, and the charge radius is equal to 2.43 fm. Such
potential phase shift is shown in Figure 2.5 by the blue dotted-dashed line, and the AC
value is in the range of possible values from 0.29 to 0.81 [48, p. 99].

The total cross-sections with such potential are shown in Figure 4.5 by the red
dotted line, and at the thermal energy it leads to the cross-sections equal to 809 μb.
Thus, it is seen that significant ambiguity of the thermal cross-sections and wide range
of the AC possible values do not enable to fix uniquely the FES potential parameters.

Since, at the energies from 25.3 meV to about 10 eV the calculated cross-section
is the straight line (the blue solid line in Figure 4.5), it can be approximated by the
function of energy of the following form

$$\sigma_{ap}(\mu b) = \frac{A}{\sqrt{E(keV)}}.$$ (4.6)

87

The constant value $A = 1.5218$ μb·keV$^{1/2}$ was determined by one point in the calculated cross-sections at the minimum energy equal to 25.3 meV. The modulus of relative deviation

$$M(E) = \left\| [\sigma_{ap}(E) - \sigma_{theor}(E)] / \sigma_{theor}(E) \right\| \qquad (4.7)$$

of the calculated theoretical cross-section (σ_{theor}) and approximation (σ_{ap}) of this cross-section by the function (4.6) given above in the energy region up to 10 eV is at the level of 0.2% [48, p. 99-100].

It is quite real to assume that this form of the total cross-section dependence on the energy will be the same also at lower energies. Therefore, on the basis of the given expression for cross-section (4.6) approximation one can evaluate the cross-section at the energy equal, for example, to 1 μeV (1 μeV = 10^{-6} eV = 10^{-9} keV) that gives the value of the order of 48.1 mb.
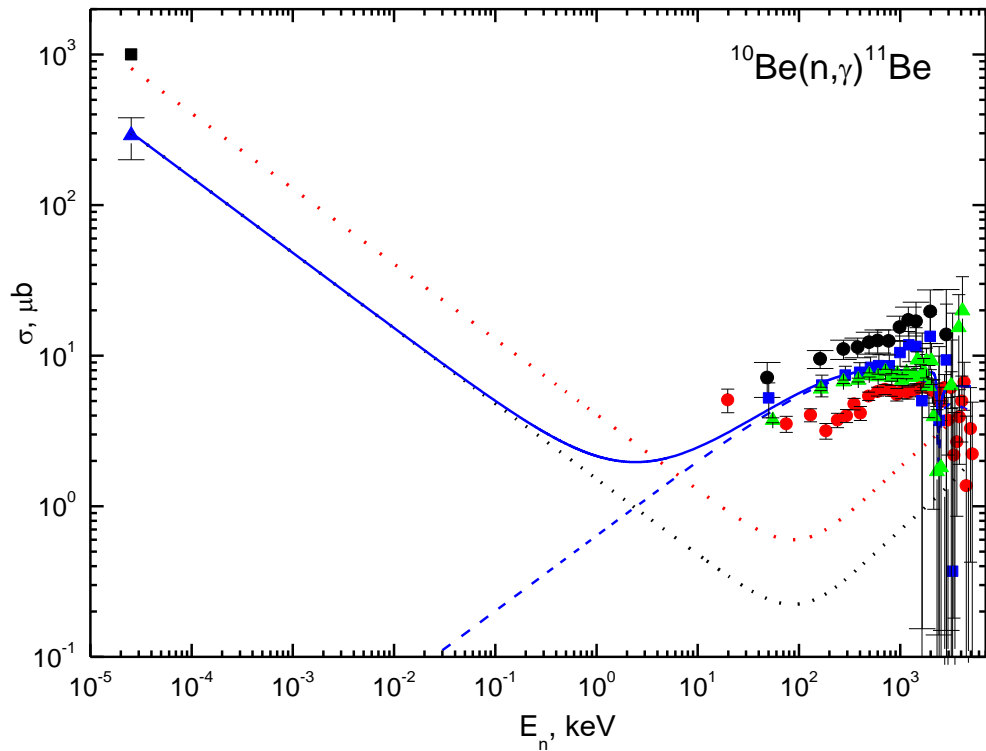
● are data from [103, p. 326c] based on results [104, p. 298-300], ● correspond to the recalculation of data from [105, p. 4-10], ▲ show the recalculation of data [106, p. 67-119], ■ correspond to the present recalculation of data [104, p. 298-300], ▲ is our recalculation of data [36, p. 1546], and ■ is the present recalculation of data [144, p. 1-19]. The blue solid line is the present calculation; the black dotted line shows the cross-sections of the transition to the first excited state (the present calculation); the red dotted line shows the present calculation with potential (4.5); the blue dashed line shows the present calculations with potentials (2.20), (2.22), and zero potential of the $^2P_{1/2}$ scattering [48, p. 100].

Figure 4.5 – The total cross-sections of the ^{10}Be(n,γ)^{11}Be radiative capture

4.3.2 ^{10}Be$(n,\gamma)^{11}$Be reaction rate

Next in Figure 4.6 the reaction rate N_A<σv> of the neutron radiative capture on ^{10}Be (the red solid line) in the region 0.01–10.0 T_9 is shown. It corresponds to the blue solid line in Figure 4.5 and is presented in the usual form [67, p. 6]

$$N_A\left\langle\sigma v\right\rangle = 3.7313\cdot10^4\mu^{-1/2}T_9^{-3/2}\int_0^\infty \sigma(E)E\exp(-11.605E/T_9)dE, \qquad (4.8)$$

where E is given in MeV, the cross-section σ(E) is measured in μb, μ is the reduced mass in amu, T_9 is the temperature in 10^9 K [48, p. 100].

To calculate this rate, the total cross-section shown in Figure 4.5 was computed in the region from 10.0 meV to 10.0 MeV. The blue doted-dashed line in Figure 4.6 shows the reaction rate of capture to the GS, and the red dotted-dashed line does the rate of capture to the FES [48, p. 100].

The black solid line presents the results of approximation of the calculated rate of the reaction under consideration from [36, p. 1546]. This curve is appreciably higher than the present results at the temperatures less than 1.0 T_9. It is explained by using in [36, p. 1546] the cross-sections agreed with data [103, p. 326c].

Next in Figure 4.6 the green solid line shows the results of the reaction rate from [145] which were also agreed with the results for the cross-sections from [103, p. 326c]. The reaction rate from [41, p. 511] is shown by the blue solid line, and it has absolutely different form and is in the worst agreement with all results given above.

The red solid line in Figure 4.6 in the region 0.01–10.0 T_9 can be approximated by the expression of the form

$$N_A\left\langle\sigma v\right\rangle = \sum_{k=1}^{6} a_k T_9^{k-1} \qquad (4.9)$$

with parameters from Table 4.3.

The results of approximation with such parameters are shown in Figure 4.6 by the blue dashed line at the average value $\chi^2 = 0.4$ and 1% varieties of the theoretical reaction rate. Also another form of approximation of the calculated reaction rate [146] can be used

$$N_A\left\langle\sigma v\right\rangle = 5.9688/T_9^{2/3}\cdot\exp(-0.34181/T_9^{1/3})\cdot(1.0+0.01441\cdot T_9^{1/3} +$$
$$+55.30271\cdot T_9^{2/3} - 287.1127\cdot T_9 + 883.6600\cdot T_9^{4/3} - 227.0900\cdot T_9^{5/3}) \qquad (4.10)$$

with $T_9 = 10^9$ K, that also leads to $\chi^2 = 0.3$ at 1% varieties of the calculated reaction rate. The results of such approximation are shown in Figure 4.6 by the green dotted line [48, p. 100].
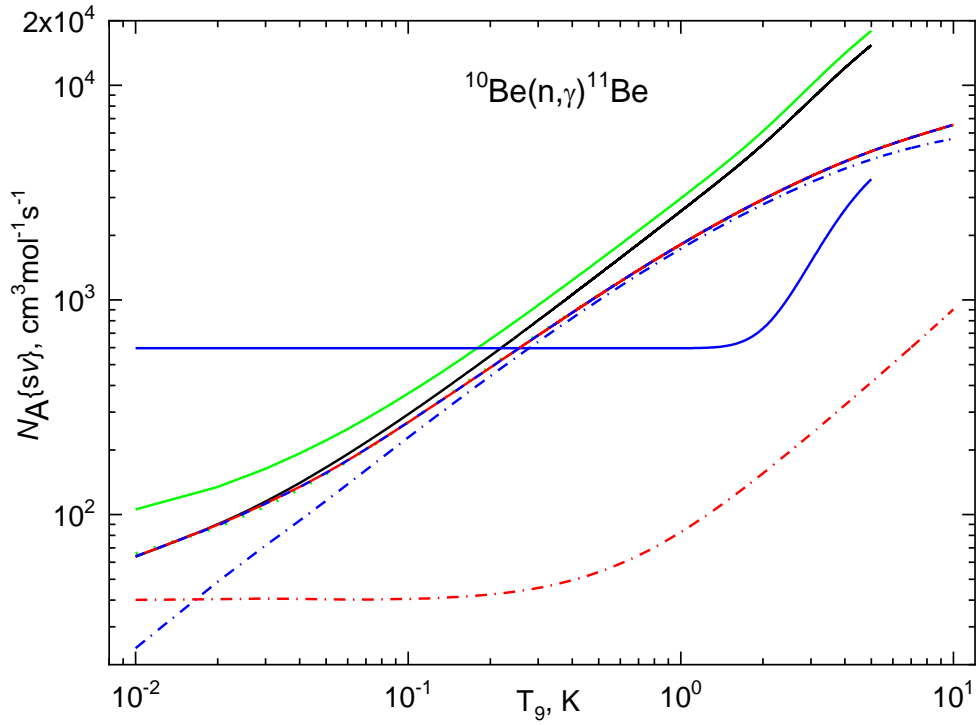
The blue dotted-dashed line is the reaction rate for capture to the ground state (present calculation); the red dotted-dashed line is the reaction rate for capture to the first excited state (present calculation); the red solid line shows the total reaction rate (present calculation); the blue dashed line shows the approximation of the calculated reaction rate at $\chi^2 = 0{,}4$ (4.9); the green dotted line shows the approximation of the calculated reaction rate at $\chi^2 = 0{,}3$ (4.10); the green solid line shows the results from [145, p. 323-326]; the blue solid line shows the results from [41, p. 511]; the black solid line shows the results of approximation of the calculated reaction rate from [36, p. 1546].

Figure 4.6 – The reaction rate of the neutron capture on ^{10}Be

Table 4.3 – Extrapolation parameters from Expression (4.9)

k	1	2	3	4	5	6
a_k	44.23061	2271.351	-580.9702	105.1334	-9.97608	0.36633

Thus, in the framework of the MPCM with the classification of states according to the Young diagrams we quite succeeded in constructing the potentials of n^{10}Be interaction, which enables on the whole to reproduce correctly the general trend of available experimental data for the total cross-sections of the neutron radiative capture on ^{10}Be at low and ultralow energies. The theoretical cross-sections have been calculated from the thermal energy 10.0 meV up to 10.0 MeV and approximated by the function of energy (4.6) which can be used for calculation of the cross-sections at energies less than 10 eV. The reaction rate has been calculated, and two forms of its

approximation have been presented at temperatures from 0.01 to 10.0 T_9 with small value of χ^2 [48, p. 100].

The results of calculation are in quite good agreement with the present determinations of the radiative capture total cross-sections from data [104, p. 298-300, 106, p. 67-119] for [11]Be Coulomb dissociation probability. On the basis of the results obtained above we recommend form (4.10) for the reaction rate approximation shown in Figure 4.6, which is seemingly the best for such rate description at the minimal χ^2 [48, p. 100].

CONCLUSION

The practical development of the scattering phase shift formalism for the high-spin nuclear processes is presented and examples of its application for the relevant astrophysical processes are threated.

While the lack of experimental data on the elastic scattering differential cross sections, we involved the MPCM, that allows to obtain scattering phase shifts indirectly. The MPCM is based on experimental data: binding energy E_b for discreet spectra and excitation energy E_{cm}, level widths Γ, quantum characteristics J^{π}, and ANC.

Based on the phase shifts obtained, the binary interaction potentials within the cluster model approach were constructed and the total cross sections, astrophysical S-factor and reaction rates for the radiative capture reactions $^3\mathrm{He}(^2\mathrm{H},\gamma)^5\mathrm{Li}$ and $^{10}\mathrm{Be}(n,\gamma)^{11}\mathrm{Be}$ were calculated.

As a result of the research, the following conclusions were formulated.

1. The analytical expressions obtained for the differential cross sections for elastic scattering can be applied for channels with an integer $(S=1, 2)$ and half-integer $(S=3/2, 5/2)$ spin value. The total differential cross sections are expressed in terms of the corresponding independent partial amplitudes for each channel spin. These expressions are presented for arbitrary orbital angular momentum ℓ and taking into account spin-orbit splitting. It should be noted that due to this, these expressions can be used for any arbitrary number of partial waves ℓ.

Obviously, as the channel spin value and the number of waves ℓ increase, the complexity of the problem to be solved increases as well. For example, for the description of the half-integer doublet $S=1/2$ channel spin state only 2 independent partial amplitudes $D^{1/2}{}^{\nu}_{\nu'}$ are required, while for the quartet state with the channel spin $S=3/2$ number of independent amplitudes $Q^{3/2}{}^{\nu}_{\nu'}$ equals 8. There are 18 independent partial amplitudes $S^{5/2}{}^{\nu}_{\nu'}$ for the sextet state with the channel spin $S=5/2$. To describe the triplet state with the channel spin $S=1$, 5 independent amplitudes $T^{1\nu}_{\nu'}$ are required. To describe the quintet with $S=2$, the number of independent amplitudes $Q^{2\nu}_{\nu'}$ increases to 13.

Obviously, with an increase of the channel spin, the number of required independent amplitudes for a correct description of scattering processes increases. For low energy processes, whose description requires a small number of partial waves, general expressions for the partial amplitudes can be reduced to simple algebraic expressions.

The obtained expressions for the differential cross sections in the terms of independent partial amplitudes enable phase shift analyses for different integer and half-integer channel spins and allow one to find corresponding phase shifts using experimental data for a nucleon-nucleus and nuclear-nuclear reaction cross sections.

Formula (1.18) for the differential cross section has a universal form and can be applied to any processes of elastic scattering, regardless of whether the channel spins are integer or half-integer.

2. Comparatively simple single-cannel model representations (namely, the use of MPCM in this work) succeeded to obtain the theoretical results in general agreement with the available experimental data for the S-factor or total cross section of the radiative ^{3}He(^{2}H,γ)^{5}Li capture. This model is much simpler than the known RGM and its modifications, but in many cases it allows one to obtain quite reliable numerical results for many reactions such as radiative capture.

It should be noted, that in order to make a detailed phase shift analysis the measurements of differential cross sections in the energy region of interest in steps of 0.3–0.5 MeV is required. In order to properly depict the phase shift resonance, it is necessary to have a step of measuring cross sections in the resonance region of not less than $\Gamma/5$. In other words, within the width of the resonance there must be at least five points of the cross sections measurement. Only in this case the resonance form of the phase shift appears quite accurately.

From the point of view of further application of the results obtained here in astrophysical problems, we can indicate the following:

−   Analytical parametrizations of the considered radiative ^{5}Li(n,γ)^{6}Li and ^{3}H(^{3}He,γ)^{6}Li capture reactions cross sections and their rates are obtained.

−   The rates of these two processes and the rate of the ^{3}He(^{2}H,γ)^{5}Li capture reaction considered here are compared.

−   The possible contribution of the neutron capture on ^{5}Li to the formation of a stable ^{6}Li is considered.

−   It has been shown qualitatively that the neutron capture on ^{5}Li formed at ^{3}He(^{2}H,γ)^{5}Li capture in the temperature range of the order of $1.0T_9$ at the BBN, can make a significant contribution to the processes of primary accumulation of a stable ^{6}Li.

In this research piece we make the assumption related to the existence of the two step mechanism ^{3}He(^{2}H,γ)^{5}Li $\rightarrow$ ^{5}Li (n,γ)^{6}Li in formation of ^{6}Li as one of the options to address the lithium abundance within the BBN model. The role of short-lived isotopes in astrophysical thermonuclear processes is quickly becoming a popular subject of experimental and theoretical research, so in this pioneering work, we tried to identify some problematic aspects of these calculations regarding the lack of information in the literature for the considered processes.

In addition, a role of two-step processes, which are extremely difficult to study in laboratory conditions, but which, nevertheless, occur in natural plasma, requires clarification. These processes either make a certain contribution to the scenario of stellar plasma evolution as a whole, or their role should be considered insignificant. This question is open, and we have demonstrated one of ways to address its solution [47, p. 75].

On the basis of all results obtained here it is clear that now it is required to make quantitative calculations of the contribution of such reactions to the accumulation of the ^{6}Li nucleus at BBN in stars and other astrophysical processes.

3. In the framework of MPCM, experimental data are reproduced properly for the process of radiative capture of neutrons on a ^{10}Be nucleus in the energy range from 25.3 meV to 10.0 MeV. This should be considered as evidence of reliability and justification of the quasiqualitative models, such as MPCM, applications. Sometimes the necessary experimental data on scattering cross sections required for a sequential phase shift analysis are not available. For the constructing of the interaction potentials in these cases MPCM, that relies on experimental data on ANC, the position and width of the corresponding resonances in the continuous spectrum, and binding energies, is applicable.

In the framework of MPCM the potentials of n^{10}Be interaction were constructed. These potentials reproduce correctly the general trend of experimental data for the total cross-sections of the neutron radiative capture on ^{10}Be nucleus at low and ultralow energies.

The theoretical cross-sections have been calculated from the thermal energy 10.0 meV up to 10.0 MeV and approximated by the simple function of energy (4.6) which can be used for calculation of the cross-sections at energies less than 10 eV. The reaction rate has been calculated, and two forms of its approximation have been presented at temperatures from 0.01 to 10.0 T_9 with small value of χ^2 [48, p. 100].

The scattering phase shifts obtained within the framework of the calculated in Subsection 2.3.2 interaction potentials are presented in the Figure 2.5. MPCM application for the radiative neutron capture reaction $^{10}\text{Be}(n,\gamma)^{11}\text{Be}$ was so successful that the phase shifts obtained may be regarded as a benchmark for future consistent phase shift analysis, further reconstruction and refinement of interaction potentials, programs debugging.

REFERENCES

1   Weinberg S. The First Three Minutes A modem view of the origin of the universe. – NY: Basic Books, 1993. – 224 p.

2   The Universe. Leading Scientists Explore the Origin, Mysteries, and the Future of the Cosmos / Edited by John Brockman. – USA: Harper Perennial, 2014. – 400 p.

3   Keshe M.T. The Origin of the Universe. – 2-nd edition. – Stichting The Keshe Foundation, 2019. – 193 p.

4   Gorbunov D.S., Rubakov V.A. Introduction to the theory of the early universe. Hot Big Bang theory. – World Scientific, 2018. – 584 p.

5   Descouvemont P. Theoretical Models for Nuclear Astrophysics. – Nova Science Publishers, 1981. – 94 p.

6   Nuclear astrophysics: proceedings / Edited by D. Wilkinson. – Oxford: Pergamon Press, 1981. – 345 p.

7   Thompson I., Nunes F. Nuclear reactions for Astrophysics. – Cambridge University Press, 2009. – 466 p.

8   Dubovichenko, S. B. Properties of light nuclei in potential cluster model. Chapter 6. – 1-st Russian edition. – Almaty: Daneker, 2004. – 247 p.

9   Wildermuth. K., Tang, Y. C. A unified theory of the nucleus. – Branschweig: Vieweg, 1977. – 389 p.

10   Mertelmeir T., Hofmann H. M. Consistent cluster model description of the electromagnetic properties of lithium and beryllium nuclei // Nucl. Phys. A. – 1986. – V.459. – P. 387-416.

11   Dohet-Eraly J. Microscopic cluster model of elastic scattering and bremsstrahlung of light nuclei. – Brussels: Université Libre De Bruxelles, 2013. – 120 p.

12   Descouvemont P., Dufour, M. Microscopic cluster model // In: Clusters in Nuclei, V.2 / Edited by C. Beck. – Berlin-Heidelberg: Springer-Verlag, 2012. – P. 1-66.

13   Nesterov, A., Arickx F., Broeckhove J., Vasilevsky V.S. Three-cluster description of properties of light neutron- and proton-rich nuclei in the framework of the algebraic version of the resonating group method // Phys. Part. Nuclei. – 2010. – Vol. 41. – P. 716-765.

14   Dubovichenko, S. B., Dzhazairov-Kakhramanov, A.V. Thermonuclear processes for three body system in the potential cluster model // Nucl. Phys. A. – 2015. – Vol. 941. – P. 335-363.

15   Neudatchin V.G., Kukulin V.I., Pomerantsev V.N., and Sakharuk A.A. Generalized potential-model description of mutual scattering of the lightest $p+d$, $d+{}^3$He nuclei and the corresponding photonuclear reactions // Phys. Rev. C. – 1992. – Vol. 45. – P. 1512-1527.

16   Dubovichenko, S. B., Dzhazairov-Kakhramanov, A.V. The Reaction

^{8}Li$(n,\gamma)^9$Li at Astrophysical Energies and Its Role in Primordial Nucleosynthesis // Astrophys. Journ. – 2016. – Vol. 819. – P. 78 (8 p.).

17   Dubovichenko, S. B. & Dzhazairov-Kakhramanov, A.V. Study of the Nucleon Radiative Captures ^{8}Li(n,γ), ^{9}Be(p,γ), ^{10}Be(n,γ), ^{10}B(p,γ), and ^{16}O(p,γ) at Thermal and Astrophysical Energies // Int. Jour. Mod. Phys. – 2017. – Vol. E25. – P. 1630009 (1-56).

18   Dubovichenko S. B., Burkova, N. A. n^{11}B capture at astrophysical energies // Mod. Phys. Lett. – 2014. – Vol. A 29. – P. 1450036 (1-14).

19   Dubovichenko S. B. Neutron capture by light nuclei at astrophysical energies // Phys. Part. Nuclei. – 2013. – Vol. 44. – P. 803-847.

20   Dubovichenko S.B., Dzhazairov-Kakhramanov A.V. Radiative n^7Li capture at astrophysical energies // An. der Physik. – 2012. – Vol. 524, № 12. – P. 850-861.

21   Dubovichenko S. B., Dzhazairov-Kakhramanov A.V. Astrophysical S-factor of the radiative p^2H capture // Euro. Phys. Journ. – 2009. – Vol. A 39. – P. 139-143.

22   Dubovichenko S.B. Thermonuclear processes in Stars and Universe. – 2-nd English edition of the book «Thermonuclear processes of the Universe». – Germany, Saarbrucken: Scholar's Press, 2015. – 332 p.

23   Dubovichenko S.B. Radiative neutron capture and primordial nucleosynthesis in the Universe. – 5-th Russian edition of the book «Selected Methods for nuclear astrophysics», revised and expanded. – Germany, Saarbrucken: Lambert Academy Publ. GmbH&Co. KG., 2016. – 293 p.

24   Barnes C.A., Clayton D.D., Schramm D.N. Essays in Nuclear Astrophysics / Presented to William A. Fowler. – Campridge: Cambridge University Press, 1982. – 562 p.

25   Lierrer J.R., et al. A proton activation diagnostic to measure D-^{3}He reaction yields // Rev. Sci. Instrum. – 1992. – Vol. 63. – P. 4847-4849.

26   Sharapov S.E., Hellsten T., Kiptily V.G. Fusion product studies via fast ion D–D and D–^{3}He fusion on JET // Nucl. Fusion. – 2016. – Vol. 56. – P. 112021 (10 p).

27   Blair J.M., et al. Radiative capture of deuterons by ^{3}He // Phys. Rev. – 1954. – Vol. 96. – P. 1023-1029.

28   Kraus L., et al. Etude de la reaction ^{2}H$(^3$He$,\gamma)^5$Li a E$_{3\text{He}}$ ≤ 5.5 MeV // Nucl. Phys. A. – 1968. – Vol. 109. – P. 593-602.

29   Del Bianco W., et al. D$(^3$He$,\gamma)^5$Li reaction from 2 to 11 MeV // Can. J. Phys. – 1968. – Vol. 46. – P. 1585-1587.

30   Buss W., et al. Deuteron capture in ^{3}He // Nucl. Phys. A. – 1968. – Vol. 112. – P. 47-64.

31   Schroder H., Mausberg W. Study of ^{5}Li around 20 MeV Excitation Energy by a Radiative Capture Reaction // Z. Phys. – 1970. – Vol. 235. – P. 234-243.

32   Weller H.R., Balbes M.J. Polarized deuteron capture on ^{3}He in the fusion resonance region // Nucl. Instrum. and Methods in Phys. Research A. – 1998. – Vol. 402. – P. 428-432.

33   Balbes M.J., et al. Polarized deuteron capture by ^{3}He and ^{3}H at and above the fusion resonance region // Phys. Rev. C. – 1994. – Vol. 49. – P. 912-925.

34   Kiptily V.G., Cecil F.E., Medley S.S. Gamma ray diagnostics of high temperature magnetically confined fusion plasmas // Plasma Phys. Control. Fusion. –

2006. – Vol. 48. – P. R59-82.

35   Caughlan G.R., Fowler W.A. Thermonuclear reaction rates V // Atom Data and Nucl. Data Tab. – 1988. – Vol. 40. – P. 283-334.

36   Zu-Hua L., Hong-Yu Zh. Nuclear halo effect on nucleon capture reaction rate at stellar energies // Chinese Phys. – 2015. – Vol. 14. – P. 1544-1548.

37   Guimaraes V., et al. Investigation of nucleosynthesis neutron capture reactions using transfer reactions induced by ^{8}Li beam // Proceedings of the International Symposium on Nuclear Astrophysics – Nuclei in the Cosmos. – CERN, Geneva, Switzerland, 2006. – P. 108.

38   Terasawa M. New nuclear reaction flow during r-process nucleosynthesis in supernovae: critical role of light, neutron-rich nuclei // Astrophys. J. – 2001. – Vol. 562. – P. 470-479.

39   Kajino, T. *et al*. Fusion Reactions in Supernovae and the Early Universe // Prog. Theor. Phys. Supp. – 2004. – Vol. 154. – P. 301-308.

40   Sasaqui T., Kajino T., Mathews G.J., Otsuki K., Nakamura T. Sensitivity of r-process nucleosynthesis to light-element nuclear reactions // Astrophys. J. – 2005. – Vol. 634. – P. 1173-1189.

41   Rauscher T., *et al*. Production of heavy elements in inhomogeneous cosmologies // Astrophys. J. – 1994. – Vol. 429. – P. 499-530.

42   Burkova N.A., Tkachenko A.S. Algebraic basics for high spin elastic scattering // International Journal of Mathematics and Physics. – 2016. – №1. P. 141-146.

43   Tkachenko A.S., Burkova N.A., Dubovichenko S.B. Analytical expressions for the differential elastic scattering cross sections of nonidentical nuclear particles with channel spins 3/2 and 5/2 // Russian Physics Journal. – 2019. – Vol. 62, № 2. – P. 232-241.

44   Tkachenko A.S., Burkova N.A., Dubovichenko S.B. Analytical expressions for the differential elastic scattering cross sections of nonidentical nuclear particles with channel spin 1 and 2 // Russian Physics Journal. – 2019. – Vol. 62, № 6. – P. 1-7.

45   Dubovichenko S.B, Dzhazairov-Kahramanov A.V., Burkova N.A., Tkachenko A.S. Radiacionnyj ^{2}H^{3}He zahvat pri astrofizicheskih energiyah // Izv. NAN RK. Ser. fiz.-mat.– 2016. – Vol. 309, №5. – P. 41-49.

46   Tkachenko A.S., Kezerashvili R.Ya., Burkova N.A., Dubovichenko S.B. Integer and half-integer channel spins for elastic scattering cross sections // Nuclear Physics A. – 2019 – Vol. 991 – P. 121609 (33 p.).

47   Dubovichenko S.B., Burkova N.A., Dzhazairov-Kakhramanov A.V., Kezerashvili R.Ya., Omarov Ch.T., Tkachenko A.S., Zazulin D.M. Radiative ^{3}He(^{2}H,γ)^{5}Li capture at astrophysical energy and its role in accumulation of ^{6}Li at the BBN // Nuclear Physics A. – 2019. – Vol. 987. – P. 46-78.

48   Dubovichenko S.B., Burkova N.A., Afanasyeva N.V., Dzhazairov-Kakhramanov A.V., Tkachenko A.S. New results for neutron radiative capture on ^{10}Be at energies between 25.3 meV and 10.0 MeV // Astroparticle Physics. – 2019. – Vol. 104. – P. 91–101.

49   Burkova N.A., Tkachenko A.S. Cross section parametrization for the high spin elastic scattering // Book of Abstracts of the 9th International Scientific Conference

«Modern Achievements of Physics and Fundamental Physical Education». – Kazakhstan, Almaty, 2016. – P. 38.

50   Tkachenko A.S., Beisenov B.U. Non-diogonal elements of scattering matrix with spin structure 1/2+3/2 and 1/2+1 and interference effects // Book of Abstracts of the international scientific conference for students and young scientists «Farabi Alemi». – Kazakhstan, Almaty, 2017. – P. 6.

51   Tkachenko A.S., Mukaeva A.R. Background for phase shift analysis in channels with spin structure 1+1 // Book of Abstracts of the international scientific conference for students and young scientists «Farabi Alemi». – Kazakhstan, Almaty, 2017. – P. 11.

52   Tkachenko A.S., Mukanova A.S. The screening effects of $a(b,\gamma)A$ reactions // Book of Abstracts of the international scientific conference for students and young scientists «Farabi Alemi». – Kazakhstan, Almaty, 2018. – P. 11.

53   Tkachenko A.S., Bodenbaeva M., Eleusheva B. The screening effects of $^3He(^2H,\gamma)^5Li$ reaction // Book of Abstracts of the international scientific conference for students and young scientists «Farabi Alemi». – Kazakhstan, Almaty, 2018. – P. 67.

54   Burkova N.A., Tkachenko A.S., Mukaeva A.R., Beisenov B.U. Algebraic methods for describing the elastic scattering processes with high-spin states // Book of Abstracts of the international scientific forum «Nuclear science and tecnologies». – Kazakhstan, Almaty, 2017. – P. 154.

55   Dubovichenko S.B., Burkova N.A., Dzhazairov-Kakhramanov A.V., Tkachenko A.S., Kezerashvili R.Ya. Radiative $^3He(^2H,\gamma)^5Li$ capture at astrophysical energy and its role in accumulation of ^6Li at the BBN // Proceedings of the 22-nd International Conference on Few-Body Problems in Physics (FB22) «Recent Progress in Few-Body Physics». – France, Caen, 2018. – P. 227-230.

56   Nichitiu F. Phase Shifts Analysis in Physics. – Romania: Acad. Publ. – 1980. – 416 p.

57   Dubovichenko S.B. Phase Shifts Analysis in Nuclear Astrophysics. – Germany: Lambert Academy Publ. GmbH & Co. – 2015. – 368 p.

58   Satchler G.R. Direct Nuclear Reactions. – UK: Oxford University Press. – 2009. – 833 p.

59   Hodgson P.E. The Optical Model of Elastic Scattering. – Oxford: Clarendon Press. – 1963. – 211 p.

60   Seyler R.G. Polarization from scattering polarized spin-1/2 on unpolarized spin-1 particles // Nucl. Phys. A. – 1969. – Vol. 124. – P. 253-272.

61   Brown L., Stainer E., Arnold L.G., Seyler R.G. Polarization and phase shifts in $^7Li(p,p)^7Li$ from 0.4 to 2.5 MeV and the structure of ^8Be // Nucl. Phys. A. – 1973. – Vol. 206. – P. 353-373.

62   Lane A.M., Thomas R.G. R-Matrix Theory of Nuclear Reactions // Rev. Mod. Phys. – 1958. – Vol. 30. – P. 257.

63   Varshalovich D.A., Moskalev A.N., Khersonskii V.K. Quantum Theory of Angular Momentum and Its Applications, Vol. 1. – M.: Fizmatlit. – 2017. – 568 p.

64   Davydov A.S. Teoriya atomnogo yadra. – Moskva: Fizmatlit, 1958. – 612 p.

65   Dubovichenko S.B. Methods of calculation of nuclear characteristics: Nuclear and thermonuclear processes. – Germany: Lambert Acad. Publ. GmbH & Co, 2012. – 432 p.

66   Dubovichenko S.B. Radiative Neutron Capture. – Berlin: Walter de Gruyter GmbH, 2019. – 296 p.

67   Angulo C., et al. A compilation of charged-particle induced thermonuclear reaction rates // Nucl. Phys. A. – 1999. – Vol. 656. – P. 3-183.

68   Nemets O.F., Neudatchin V.G., Rudchik A.T., Smirnov Y.F., Tchuvil'sky Yu.M. Nucleon association in atomic nuclei and nuclear reactions of many nucleons transfers. – Kiev: Naukova dumka, 1988. – 488 p.

69   Dubovichenko S.B., Dzhazairov-Kakhramanov A.V. The reaction ^{8}Li$(n,\gamma)^9$Li at astrophysical energies and its role in primordial nucleosynthesis // Astrophys. J. – 2016. – Vol. 819, №1. – P. 78 (8 p.).

70   Dubovichenko S.B., Dzhazairov-Kakhramanov A.V. Study of the nucleon radiative captures ^{8}Li(n,γ), ^{9}Be(p,γ), ^{10}Be(n,γ), ^{10}B(p,γ), and ^{16}O(p,γ) at thermal and astrophysical energies // Int. Jour. Mod. Phys. – 2017. – Vol. E 26. – P. 1630009(56 p.).

71   Adelberger E.G., et al. Solar fusion cross sections II. The pp chain and CNO cycles // Rev. Mod. Phys. – 2011. – Vol. 83. – P. 195-245.

72   Kukulin V.I., Neudatchin V.G., Obukhovsky I.T., Smirnov Yu.F. Clusters as subsystems in light nuclei // In: Clustering Phenomena in Nuclei; Edited by K. Wildermuth and P. Kramer. – Branschweig: Vieweg, 1983. – V.3. – P. 1-155.

73   Dubovichenko S.B., Uzikov Yu.N. Astrophysical S-factors of reactions with light nuclei // Phys. Part. Nucl. – 2011. – Vol. 42. – P. 251-301.

74   Mukhamedzhanov A.M., Tribble R.E. Connection between asymptotic normalization coefficients, sub threshold bound states, and resonances // Phys. Rev. C. – 1999. – Vol. 59. – P. 3418-3424.

75   Blokhintsev L.D., Borbey I., Dolinsky E.I. Nuclear vertex constants // Phys. Part. Nucl. – 1977. – Vol. 8. – P. 1189-1245.

76   Plattner G.R., Viollier R.D. Coupling constants of commonly used nuclear probes // Nucl. Phys. A. – 1981. – Vol. 365. – P. 8-12.

77   EXFOR data base. https://www-nds.iaea.org/exfor/exfor.htm. 02.06.2020

78   Casella C., et al. First measurement of the $d(p,\gamma)^3$He cross section down to the solar Gamow peak // Nucl. Phys. A. – 2002. – Vol. 706. – P. 203-216.

79   Schimd G.J., et al. The ^{2}H$(p,\gamma)^3$He and ^{1}H$(d,\gamma)^3$He reactions below 80 keV // Phys. Rev. C. – 1997. – Vol. 56. – P. 2565-2681.

80   Canon R., et al. ^{3}H$(p,\gamma)^4$He reaction below $E_p = 80$ keV // Phys. Rev. C. – 2002. – Vol. 65. – P. 044008 (7 p.).

81   Cecil F.E., Liu H., Yan J.S. Recent measurements of nuclear reaction cross sections with ion beams at very low energies // Vacuum. – 1993. – Vol. 44. – P. 181-183.

82   Tilley D.R., et al. Energy level of light nuclei A = 5,6,7 // Nucl. Phys. A. – 2002. – Vol. 708. – P. 3-163.

83   Ajzenberg-Selove F. Energy level of light nuclei A = 5-10 // Nucl. Phys. A. – 1988. – Vol. 490. – P. 1-225.

84   King H.T., Meyerhof W.E., Hirko R.G. The ^{2}H(^{3}He,γ)^{5}Li reaction from 2-26 MeV // Nucl. Phys. A. – 1972. – Vol. 178. – P. 337-349.

85   NIST. http://physics.nist.gov/cgi-bin/cuu/Value?mud|search_for=atomnuc!. 28.05.2020

86   Map of atomic nuclei. http://cdfe.sinp.msu.ru/services/ground/ NuclChart_release.html. 05.06.2020

87   Cecil F.E., Cole D.M., Wilkinson F.J. Measurement and application of DDγ, DTγ and D^{3}Heγ reactions at low energy // Nucl. Instr. and Meth. in Phys. Research B. – 1985. – Vol. 10/11. – P. 411-414.

88   Cecil F.E., Cole D.M., Philbin R. Reaction ^{2}H(^{3}He,γ)^{5}Li at center-of-mass energies between 25 and 60 keV // Phys. Rev. C. – 1985. – Vol. 32. – P. 690-693.

89   Aliotta M.A., et al. Electron screening effect in the reactions ^{3}He(d,p)^{4}He and d(^{3}He,p)^{4}He // Nucl. Phys. A. – 2001. – Vol. 690. – P. 790-800.

90   Chwieroth F.S., et al. Study of d+^{3}H and d+^{3}He Systems with the Resonating-Group Method // Phys. Rev. C. – 1973. – Vol. 8. – P. 938-950.

91   Kurath D. Fusion resonance in ^{5}He, ^{5}Li // Phys. Rev. C. – 1993. – Vol. 47. – P. 1306.

92   Tanifuji M., Kameyama H. Analyzing power formulae for nuclear reactions in the low-energy limit and applications to the ^{2}H(d,p)^{3}H, ^{3}He(d,γ)^{5}Li and ^{7}Li(p,γ)^{8}Be // Nucl. Phys. A. – 1996. – Vol. 602. – P. 1-20.

93   Wagner R.F., Werntz C. Even-Parity States of the Five-Nucleon System and Deuteron-Triton Photocapture // Phys. Rev. C. – 1971. – Vol. 4. – P. 2-9.

94   Navratil P., Quaglioni S. Ab Initio Many-Body Calculations of the ^{3}H(d,n)^{4}He and ^{3}He(d,p)^{4}He Fusion Reactions // Phys. Rev. Lett. – 2012. – Vol. 108. – P. 042503.

95   Mertelmeir T., Hofmann H.M. Consistent cluster model description of the electromagnetic properties of lithium and beryllium nuclei // Nucl. Phys. A. – 1986. – Vol. 459. – P. 387-416.

96   Descouvemont P., et al. Few-body models for nuclear astrophysics // AIP Advances. – 2014. – Vol. 4. – P. 041011.

97   Descouvemont P., et al. Nuclear reactions in stars: theoretical and experimental aspects // In: The Universe Evolution. Astrophysical and Nuclear Aspects. – NY: NOVA Sci. Publ, 2013. – P. 1-48.

98   Neudatchin V.G., et al. Generalized potential model description of mutual scattering of the lightest p^2H, ^{2}H^{3}He nuclei and the corresponding photonuclear reactions // Phys. Rev. C. – 1992. – Vol. 45. – P. 1512-1527.

99   Dubovichenko S.B., Dzhazairov-Kakhramanov A.V. Electromagnetic effects in light nuclei and the cluster potential model // Phys. Part. Nucl. – 1997. – Vol. 28. – P. 615-641.

100   Itzykson C., Nauenberg M. Unitary groups: Representations and decompositions // Rev. Mod. Phys. – 1966. – Vol. 38. – P. 95-101.

101   Jenny B. et al. Phase shift analysis of ^{3}He(d,d)^{3}He scattering // Nucl. Phys. A. – 1980. – Vol. 337. – P. 77-106.

102   Plattner G.R., Viollier R.D. Coupling constants of commonly used nuclear probes // Nucl. Phys. A. – 1981. – Vol. 365. – Vol. 8-12.

103 Mengoni A., Otsuka T., Nakamura T. and Ishihara M. Exotic structure of light nuclei and their neutron capture reaction rates // Nuclear Physics A. – 1997. – Vol. 621. – P. 323c-326c.

104 Nakamura T., et al. Coulomb dissociation of a halo nucleus ^{11}Be at 72 MeV // Phys. Lett. B. – 1994. – Vol. 331. – P. 296-301.

105 Palit R., et al. Exclusive measurement of breakup reactions with the one-neutron halo nucleus ^{11}Be // Phys. Rev. C. – 2003. – Vol. 68. – P. 034318(1-14).

106 Nakamura S., Kondo Y. Neutron Halo and Breakup Reactions, Clusters in Nuclei / In: Lecture Notes in Physics; Edited by C. Beck, Vol. 2, 2012. – Vol. 848. – P. 67-119.

107 Neudatchin V.G., Smirnov Yu.F. Nucleon associations in light nuclei. – Moscow: Nauka, 1969. – 414 p.

108 Itzykson C. Nauenberg M. Unitary groups: Representations and decompositions // Rev. Mod. Phys. – 1966. – Vol. 38. – P. 95-101.

109 Tilley D.R., et al. Energy level of light nuclei. A = 8,9,10 // Nucl. Phys. A. – 2004. – Vol. 745. – P. 155-363.

110 Kelley J.H., et al. Energy level of light nuclei A = 11 // Nucl. Phys. A. – 2012. – Vol. 880. – P. 88-195.

111 Dubovichenko S.B., Dzhazairov-Kakhramanov A.V. Thermonuclear processes for three body system in the potential cluster model // Nucl. Phys. A. – 2015. – Vol. 941. – P. 335-363.

112 Dubovichenko S.B., Dzhazairov-Kakhramanov A.V. Neutron radiative capture on ^{10}B, ^{11}B and proton radiative capture on ^{11}B, ^{14}C and ^{15}N at thermal and astrophysical energies // Int. Jour. Mod. Phys. E. – 2014. – Vol. 23. – P. 1430012(1-55).

113 Dubovichenko S.B., Dzhazairov-Kakhramanov A.V., Afanasyeva N.V. New Results for Reaction Rate of the Proton Radiative Capture on ^{3}H // Nucl. Phys. A. – 2017. – Vol. 963. – P. 52-67.

114 Neudatchin V.G., et al. Generalized potential model description of mutual scattering of the lightest p^{2}H, ^{2}H^{3}He nuclei and the corresponding photonuclear reactions // Phys. Rev. C. – 1992. – Vol. 45. – P. 1512-1527.

115 Aumann T., et al. One-Neutron Knockout from Individual Single-Particle States of ^{11}Be // Phys. Rev. Lett. – 2000. – Vol. 84. – P. 35-38.

116 Fukuda N., et al. Coulomb and nuclear breakup of a halo nucleus ^{11}Be // Phys. Rev. C. – 2004. – Vol. 70. – P. 054606(1-12).

117 Sukhoruchkin S.I., Soroko Z.N. Excited nuclear states // In: Sub.G. Suppl. I/25 A-F, USA: Springer, 2016. – 641 p.

118 Auton D.L. Direct reactions on ^{10}Be // Nucl. Phys. A. – 1970. – Vol. 157. – P. 305-322;

119 Zwieglinski B., et al. Study of the ^{10}Be$(d, p)^{11}$Be reaction at 25 MeV // Nucl. Phys. A. – 1979. – Vol. 315. – P. 124-132.

120 Dubovichenko S.B. Calculation method of the nuclear characteristics. – Almaty: Complex, 2006. – 311 p.

121 Quaglioni S., Navrátil P. Ab initio many-body calculations of nucleon-nucleus scattering // Phys. Rev. C. – 2009. – Vol. 79. – P. 044606(1-28).

122 Dubovichenko S.B., Dzhazairov-Kakhramanov A.V. The radiative ^{10}Be(n,γ)^{11}Be capture at thermal and astrophysical energies // J. Phys. G. – 2016. – Vol. 43. – P. 095201 (14 p.).

123 Fowler W.A., Caughlan G.R., Zimmerman B.A. Thermonuclear reaction rates. II // Ann. Rev. Astr. Astrophys. – 1975. – Vol. 13. – P. 69-112.

124 Mohr P.J., Taylor B.N. CODATA recommended values of the fundamental physical constants: 2002 // Rev. Mod. Phys. – 2005. – Vol. 77, №1. – P. 1-107.

125 Bertulani C.A., Kajino T. Frontiers in Nuclear Astrophysics // Prog. in Part. and Nucl. Phys. – 2016. – Vol. 89. – P. 56-100.

126 Barbui M., Bang W., Bonasera A. Measurement of the Plasma Astrophysical S Factor for the ^{3}He(d,p)^{4}He Reaction in Exploding Molecular Clusters // Phys. Rev. Lett. – 2013. – Vol. 111. – P. 082502 (4 p.).

127 Angulo C., *et al.* A compilation of charged-particle induced thermonuclear reaction rates // Nucl. Phys. A. – 1999. – Vol. 656. – P. 3-183.

128 Coc A., et al. Standard BIG bang nucleosynthesis up to CNO with an improved extended nuclear network // Astrophys. J. – 2012. – Vol. 744. – P. 158 (18 p.).

129 Trezzi D., *et al*. Big Bang ^{6}Li nucleosynthesis studied deep underground // Astropart. Phys. – 2017. – Vol. 89. – P. 57-65.

130 Grassi A., Mangano G., Marcucci L.E., Pisanti O. The $\alpha + d \rightarrow {}^6$Li $+ \gamma$ astrophysical S-factor and its implications for Big Bang Nucleosynthesis // Phys. Rev. C. – 2017. – Vol. 96. – P. 045807.

131 Dubovichenko S.B. Tensor ^{2}H^{4}He interactions in the potential cluster model infolving forbidden states // Phys. Atom. Nucl. – 1998. – Vol. 61. – P. 162-168.

132 Zylstra A.B., Herrmann H.W., Johnson M.G., et al. Using Inertial Fusion Implosions to Measure the T + ^{3}He Fusion Cross Section at Nucleosynthesis-Relevant Energies // Phys. Rev. Lett. – 2016. – Vol. 117. – P. 035002 (5 p.).

133 Young A.M., Blatt S.L., Seyler R.G. Direct Radiative Capture of ^{3}He by Tritons and $t + {}^3$He Cluster States in ^{6}Li // Phys. Rev. Lett. – 1970. – Vol. 25. – P. 1764-1767.

134 Blatt S.L., et al. Reaction T(^{3}He,γ)^{6}Li in the Energy Range 0.5-11 MeV // Phys. Rev. – 1968. – Vol. 176. – P. 1147-1153.

135 Photonuclear data. Photodisintegration of lithium. Evaluated cross sections of channels and reactions. http://cdfe.sinp.msu.ru. 15.06.2020

136 Center for photonuclear experiments data. http://cdfe.sinp.msu.ru/exfor/index.php. 16.06.2020

137 Firestone R.B., Revay Zs. Thermal neutron radiative cross sections for ^{6,7}Li, ^{9}Be, ^{10,11}B, ^{12,13}C and ^{14,15}N // Phys. Rev. C. – 2016. – Vol. 93. – P. 054306 (12 p.).

138 Wildermuth K., Tang Y.C. Unified Theory of the Nucleus. – Braunschweig: Vieweg, 1977. – 389 p.

139 Hiyama E., Kamimura M. Study of various few-body systems using Gaussian expansion method (GEM) // Front. Phys. – 2018. – V.18. – P. 132106.

140 Atomic and nuclear constants. https://physics.nist.gov/cgi-bin/cuu/Value?alph|search_for=atomnuc! 30.06.2020

141 Nortershauser W., et al. Nuclear Charge Radii of ^{7,9,10}Be and the One-

Neutron Halo Nucleus ^{11}Be // Phys. Rev. Lett. – 2009. – Vol. 102. – P. 062503.

142 Hammer H.W., Phillips D.R. Electric properties of the Beryllium-11 system in Halo EFT // Nucl. Phys. A. – 2011. – Vol. 865. – P. 17-42.

143 Belyaeva T.L., *et al*. Neutron asymptotic normalization coefficients and halo radii of the first excited states of ^{12}C and ^{11}Be // EPJ Web of Conferences. – 2014. – Vol. 66. – P. 03009.

144 Mughabghab S.F. Atlas of neutron resonances. – USA: National Nuclear Data Center, Brookhaven, National Laboratory, 2006. – 1008 p.

145 Mengoni A., et al. Exotic structure of light nuclei and their neutron capture reaction rates // Nucl. Phys. A. – 1997. – Vol. 621. – P. 323-326.

146 Caughlan G.R., Fowler W.A // Atom. Data Nucl. Data Tab. – 1988. – Vol. 40. – P. 283-334.

147 Dubovichenko S.B. Selected Methods of Nuclear Astrophysics. In series Kazakhstan Space Research, V. 9. – Almaty: Kazak universitety, 2011. – 311 p.

APPENDIX A

Spin-mixing $M-$matrix elements

Spin-mixing M$-$matrix elements, integer spin channel values $S = 1$ and $S = 2$:

$$
\begin{aligned}
\mathfrak{M}_{22}^{11} = \frac{i}{2k} \sum_l \Bigg[& \frac{l+2}{\sqrt{8l\,(2l+1)}} \exp\left(i\left(\omega_l + \omega_{l-1}\right)\right) U_{2(l-1)1l}^{l+1} P_{l-1}^1 \\
& - \sqrt{\frac{l+2}{4l}} \exp\left(2i\omega_l\right) U_{2l1l}^{l+1} P_l^1 - \\
& + \sqrt{\frac{(l+2)(l+3)}{2\,(2l+1)\,(2l+5)}} \exp\left(i\left(\omega_l + \omega_{l+1}\right)\right) U_{2(l+1)1l}^{l+1} P_{l+1}^1 \\
& - \sqrt{\frac{l+2}{4\,(l+3)}} \exp\left(i\left(\omega_l + \omega_{l+2}\right)\right) U_{2(l+2)1l}^{l+1} P_{l+2}^1 \\
& + \sqrt{\frac{(l+2)(l+1)}{8\,(l+3)\,(2l+5)}} \exp\left(i\left(\omega_l + \omega_{l+3}\right)\right) U_{2(l+3)1l}^{l+1} P_{l+3}^1 \\
& - \sqrt{\frac{(2l+1)(l+1)}{8\,(l-1)\,(2l-1)}} \exp\left(i\left(\omega_l + \omega_{l-2}\right)\right) U_{2(l-2)1l}^{l} P_{l-2}^1 \\
& + \sqrt{\frac{2l+1}{4\,(l-1)}} \exp\left(i\left(\omega_l + \omega_{l-1}\right)\right) U_{2(l-1)1l}^{l} P_{l-1}^1 \\
& - \sqrt{\frac{2l+1}{4\,(2l-1)\,(2l+3)}} \exp\left(2i\omega_l\right) U_{2l1l}^{l} P_l^1 \\
& + \sqrt{\frac{2l+1}{4\,(l+2)}} \exp\left(i\left(\omega_l + \omega_{l+1}\right)\right) U_{2(l+1)1l}^{l} P_{l+1}^1 \\
& - \sqrt{\frac{l\,(2l+1)}{8\,(l+2)\,(2l+3)}} \exp\left(i\left(\omega_l + \omega_{l+2}\right)\right) U_{2(l+2)1l}^{l} P_{l+2}^1 \\
& + \sqrt{\frac{l\,(l-1)}{8\,(2l-3)\,(l-2)}} \exp\left(i\left(\omega_l + \omega_{l-3}\right)\right) U_{2(l-3)1l}^{l-1} P_{l-3}^1 \\
& - \sqrt{\frac{l-1}{4\,(l-2)}} \exp\left(i\left(\omega_l + \omega_{l-2}\right)\right) U_{2(l-2)1l}^{l-1} P_{l-2}^1
\end{aligned}
\tag{A.1}
$$

$$+\sqrt{\frac{(l-1)(2l-1)}{4(2l-3)(2l+1)}}\exp\left(i\left(\omega_l+\omega_{l-1}\right)\right)U^{l-1}_{2(l-1)1l}P^1_{l-1}$$

$$-\sqrt{\frac{l-1}{4(l+1)}}\exp\left(2i\omega_l\right)U^{l-1}_{2l1l}P^1_l$$

$$+\frac{l-1}{\sqrt{8(l+1)(2l+1)}}\exp\left(i\left(\omega_l+\omega_{l+1}\right)\right)U^{l-1}_{2(l+1)1l}P^1_{l+1}\Bigg],$$

$$\mathfrak{M}^{10}_{22}=\frac{i}{2k}\sum_l\Bigg[\frac{1}{2\sqrt{l(2l+1)}}\exp\left(i\left(\omega_l+\omega_{l-1}\right)\right)U^{l+1}_{2(l-1)1l}P^2_{l-1}$$

$$-\frac{1}{\sqrt{2l(l+2)}}\exp\left(2i\omega_l\right)U^{l+1}_{2l1l}P^2_l$$

$$+\sqrt{\frac{3(2l+3)}{2(2l+1)(2l+5)(l+2)}}\exp\left(i\left(\omega_l+\omega_{l+1}\right)\right)U^{l+1}_{2(l+1)1l}P^2_{l+1}$$

$$-\frac{1}{\sqrt{2(l+2)(l+3)}}\exp\left(i\left(\omega_l+\omega_{l+2}\right)\right)U^{l+1}_{2(l+2)1l}P^2_{l+2}$$

$$+\sqrt{\frac{l+1}{4(l+3)(l+2)(2l+5)}}\exp\left(i\left(\omega_l+\omega_{l+3}\right)\right)U^{l+1}_{2(l+3)1l}P^2_{l+3}$$

$$-\sqrt{\frac{l}{4(2l-3)(l-1)(l-2)}}\exp\left(i\left(\omega_l+\omega_{l-3}\right)\right)U^{l-1}_{2(l-3)1l}P^2_{l-3}$$

$$+\frac{1}{\sqrt{2(l-1)(l-2)}}\exp\left(i\left(\omega_l+\omega_{l-2}\right)\right)U^{l-1}_{2(l-2)1l}P^2_{l-2}$$

$$-\sqrt{\frac{3(2l-1)}{2(2l-3)(2l+1)(l-1)}}\exp\left(i\left(\omega_l+\omega_{l-1}\right)\right)U^{l-1}_{2(l-1)1l}P^2_{l-1}$$

$$+\frac{1}{\sqrt{2(l-1)(l+1)}}\exp\left(2i\omega_l\right)U^{l-1}_{2l1l}P^2_l$$

$$+\frac{1}{\sqrt{4(2l+1)(l+1)}}\exp\left(i\left(\omega_l+\omega_{l+1}\right)\right)U^{l-1}_{2(l+1)1l}P^2_{l+1}\Bigg],$$

(A.2)

$$\mathfrak{M}_2^{1-1} = \frac{i}{2k} \sum_l \left[\sqrt{\frac{(l+2)(l-2)(l-3)}{8l(2l+1)(l+1)}} \exp\left(i\left(\omega_l + \omega_{l-1}\right)\right) U_{2(l-1)1l}^{l+1} P_{l-1}^1 \right.$$

$$+ \frac{\sqrt{(l+2)(l+3)(l-2)(l-1)}}{2l(l+1)} \exp\left(2i\omega_l\right) U_{2l1l}^{l+1} P_l^1$$

$$+ \sqrt{\frac{3l(l+3)(l+4)(2l+3)(l-1)}{2(l+1)^2(l+2)(2l+1)(2l+5)}} \exp\left(i\left(\omega_l + \omega_{l+1}\right)\right) U_{2(l+1)1l}^{l+1} P_{l+1}^1$$

$$- \sqrt{\frac{l(l+5)(l+4)}{4(l+1)(l+2)(l+3)}} \exp\left(i\left(\omega_l + \omega_{l+2}\right)\right) U_{2(l+2)1l}^{l+1} P_{l+2}^1$$

$$- \sqrt{\frac{(l+5)(l+6)}{8(l+3)(2l+5)}} \exp\left(i\left(\omega_l + \omega_{l+3}\right)\right) U_{2(l+3)1l}^{l+1} P_{l+3}^1$$

$$- \sqrt{\frac{(2l+1)(l-3)(l-4)}{8l(l-1)(2l-1)}} \exp\left(i\left(\omega_l + \omega_{l-2}\right)\right) U_{2(l-2)1l}^{l} P_{l-2}^1$$

$$+ \frac{\sqrt{(2l+1)(l+2)(l-2)(l-3)}}{2l(l-1)} \exp\left(i\left(\omega_l + \omega_{l-1}\right)\right) U_{2(l-1)1l}^{l} P_{l-1}^1$$

$$- \sqrt{\frac{2l+1}{2}} \exp\left(2i\omega_l\right) U_{2l1l}^{l} P_l^1$$

$$+ \sqrt{\frac{(2l+1)(l+3)(l+4)(l-1)}{2l(l+1)^2(l+2)}} \exp\left(i\left(\omega_l + \omega_{l+1}\right)\right) U_{2(l+1)1l}^{l} P_{l+1}^1$$

$$- \sqrt{\frac{(2l+1)(l+4)(l+5)}{8(l+1)(l+2)(2l+3)}} \exp\left(i\left(\omega_l + \omega_{l+2}\right)\right) U_{2(l+2)1l}^{l} P_{l+2}^1$$

$$+ \sqrt{\frac{(l-4)(l-5)}{8(2l-3)(l-2)}} \exp\left(i\left(\omega_l + \omega_{l-3}\right)\right) U_{2(l-3)1l}^{l-1} P_{l-3}^1$$

$$+ \sqrt{\frac{(l+1)(l-3)(l-4)}{4(l-2)^2(l-1)}} \exp\left(i\left(\omega_l + \omega_{l-2}\right)\right) U_{2(l-2)1l}^{l-1} P_{l-2}^1$$

$$+ \sqrt{\frac{3(l-1)(l-2)(l-3)(2l-1)(l+1)(l+2)}{4(2l-3)(2l+1)}}$$

$$\times \exp\left(i\left(\omega_l + \omega_{l-1}\right)\right) U_{2(l-1)1l}^{l-1} P_{l-1}^1$$

$$- \sqrt{\frac{(l+3)(l+2)(l-2)}{4l^2(l+1)}} \exp\left(2i\omega_l\right) U_{2l1l}^{l-1} P_l^1$$

$$\left. + \sqrt{\frac{(l+3)(l+4)(l-1)}{8l(l+1)(2l+1)}} \exp\left(i\left(\omega_l + \omega_{l+1}\right)\right) U_{2(l+1)1l}^{l-1} P_{l+1}^1 \right],$$

<div align="right">(A.3)</div>

$$
\begin{aligned}
\mathfrak{M}_{21}^{11} = \frac{i}{2k} \sum_{l} \Bigg[& \frac{l+2}{\sqrt{2\,(2l+1)\,(l-1)}} \exp\left(i\left(\omega_l + \omega_{l-1'}\right)\right) U_{2(l-1)1l}^{l+1} P_{l-1}^{1} \\
& - \sqrt{\frac{(l+2)}{4\,(l+1)}} \exp\left(2i\,\omega_l\right) U_{2l1l}^{l+1} P_{l}^{1} \\
& - \sqrt{\frac{3\,(2l+3)}{4\,(l+1)\,(2l+1)\,(2l+5)}} \exp\left(i\left(\omega_l + \omega_{l+1}\right)\right) U_{2(l+1)1l}^{l+1} P_{l+1}^{1} \\
& + \frac{1}{2} \exp\left(i\left(\omega_l + \omega_{l+2}\right)\right) U_{2(l+2)1l}^{l+1} P_{l+2}^{1} \\
& - \sqrt{\frac{(l+2)\,(l+1)}{2\,(l+4)\,(2l+5)}} \exp\left(i\left(\omega_l + \omega_{l+3}\right)\right) U_{2(l+3)1l}^{l+1} P_{l+3}^{1} \\
& - \sqrt{\frac{(2l+1)\,(l+1)}{2\,(l-2)\,(2l-1)}} \exp\left(i\left(\omega_l + \omega_{l-2}\right)\right) U_{2(l-2)1l}^{l} P_{l-2}^{1} \\
& + \sqrt{\frac{2l+1}{4l}} \exp\left(i\left(\omega_l + \omega_{l-1}\right)\right) U_{2(l-1)1l}^{l} P_{l-1}^{1} \\
& + \frac{\sqrt{3}\,(2l+1)}{\sqrt{4l\,(2l-1)\,(2l+3)\,(l+1)}} \exp\left(2i\,\omega_l\right) U_{2l1l}^{l} P_{l}^{1} \\
& - \sqrt{\frac{2l+1}{4\,(l+1)}} \exp\left(i\left(\omega_l + \omega_{l+1}\right)\right) U_{2(l+1)1l}^{l} P_{l+1}^{1} \\
& + \sqrt{\frac{l\,(2l+1)}{2\,(l+3)\,(2l+3)}} \exp\left(i\left(\omega_l + \omega_{l+2}\right)\right) U_{2(l+2)1l}^{l} P_{l+2}^{1} \\
& + \sqrt{\frac{l\,(l-1)}{2\,(2l-3)\,(l-3)}} \exp\left(i\left(\omega_l + \omega_{l-3}\right)\right) U_{2(l-3)1l}^{l-1} P_{l-3}^{1} \\
& - \frac{1}{2} \exp\left(i\left(\omega_l + \omega_{l-2}\right)\right) U_{2(l-2)1l}^{l-1} P_{l-2}^{1} \\
& - \sqrt{\frac{3\,(2l-1)}{4l\,(2l-3)\,(2l+1)}} \exp\left(i\left(\omega_l + \omega_{l-1}\right)\right) U_{2(l-1)1l}^{l-1} P_{l-1}^{1} \\
& + \sqrt{\frac{l-1}{4l}} \exp\left(2i\,\omega_l\right) U_{2l1l}^{l-1} P_{l}^{1} \\
& - \frac{l-1}{\sqrt{2\,(l+2)\,(2l+1)}} \exp\left(i\left(\omega_l + \omega_{l+1}\right)\right) U_{2(l+1)1l}^{l-1} P_{l+1}^{1} \Bigg],
\end{aligned}
\tag{A.4}
$$

$$\mathfrak{M}_{21}^{10} = \frac{i}{2k} \sum_l \left[\frac{l+1}{\sqrt{l\,(2l+1)}} \exp\left(i\left(\omega_l + \omega_{l-1}\right)\right) U_{2(l-1)1l}^{l+1} P_{l-1}^1 \right.$$

$$- \sqrt{\frac{l+2}{2l}} \exp\left(2i\omega_l\right) U_{2l1l}^{l+1} P_l^1$$

$$+ \sqrt{\frac{3\,(2l+3)}{2\,(l+2)\,(2l+1)\,(2l+5)}} \exp\left(i\left(\omega_l + \omega_{l+1}\right)\right) U_{2(l+1)1l}^{l+1} P_{l+1}^1$$

$$+ \frac{l+1}{\sqrt{2\,(l+2)\,(l+3)}} \exp\left(i\left(\omega_l + \omega_{l+2}\right)\right) U_{2(l+2)1l}^{l+1} P_{l+2}^1$$

$$- \sqrt{\frac{(l+2)\,(l+1)}{(l+3)\,(2l+5)}} \exp\left(i\left(\omega_l + \omega_{l+3}\right)\right) U_{2(l+3)1l}^{l+1} P_{l+3}^1$$

$$\text{(A.5)}$$

$$- \sqrt{\frac{l\,(l-1)}{(2l-3)\,(l-2)}} \exp\left(i\left(\omega_l + \omega_{l-3}\right)\right) U_{2(l-3)1l}^{l-1} P_{l-3}^1$$

$$+ \frac{l}{\sqrt{2\,(l-1)\,(l-2)}} \exp\left(i\left(\omega_l + \omega_{l-2}\right)\right) U_{2(l-2)1l}^{l-1} P_{l-2}^1$$

$$- \sqrt{\frac{3\,(2l-1)}{2\,(2l-3)\,(2l+1)\,(l-1)}} \exp\left(i\left(\omega_l + \omega_{l-1}\right)\right) U_{2(l-1)1l}^{l-1} P_{l-1}^1$$

$$- \sqrt{\frac{l-1}{2\,(l+1)}} \exp\left(2i\omega_l\right) U_{2l1l}^{l-1} P_l^1$$

$$\left. - \frac{l}{\sqrt{(l+1)\,(2l+1)}} \exp\left(i\left(\omega_l + \omega_{l+1}\right)\right) U_{2(l+1)1l}^{l-1} P_{l+1}^1 \right],$$

$$
\begin{aligned}
\mathfrak{M}_2^{1\,-1} = -\frac{i}{2k}\sum_l \Bigg[& \frac{(l+2)\sqrt{l-2}}{\sqrt{2l\,(2l+1)\,(l+1)}}\exp\left(i\left(\omega_l+\omega_{l-1'}\right)\right)U^{l+1}_{2(l-1)1l}P^1_{l-1} \\
& +\frac{(l+4)\sqrt{l-1}}{4\,(l+1)\sqrt{l}}\exp\left(2i\omega_l\right)U^{l+1}_{2l1l}P^1_l \\
& +3\sqrt{\frac{3l\,(l+3)\,(2l+3)}{2\,(l+1)^2\,(l+2)\,(2l+1)\,(2l+5)}}\exp\left(i\left(\omega_l+\omega_{l+1}\right)\right)U^{l+1}_{2(l+1)1l}P^1_{l+1} \\
& -\frac{(l-1)\sqrt{l+4}}{\sqrt{2\,(l+1)\,(l+2)\,(l+3)}}\exp\left(i\left(\omega_l+\omega_{l+2}\right)\right)U^{l+1}_{2(l+2)1l}P^1_{l+2} \\
& -\sqrt{\frac{(l+1)\,(l+5)}{2\,(l+3)\,(2l+5)}}\exp\left(i\left(\omega_l+\omega_{l+3}\right)\right)U^{l+1}_{2(l+3)1l}P^1_{l+3} \\
& -\sqrt{\frac{(2l+1)\,(l+1)\,(l-3)}{2l\,(l-1)\,(2l-1)}}\exp\left(i\left(\omega_l+\omega_{l-2}\right)\right)U^{l}_{2(l-2)1l}P^1_{l-2} \\
& -\frac{(l+3)\sqrt{(2l+1)\,(l-2)}}{2l\sqrt{(l-1)\,(l+1)}}\exp\left(i\left(\omega_l+\omega_{l-1}\right)\right)U^{l}_{2(l-1)1l}P^1_{l-1} \\
& -\frac{3\,(2l+1)\sqrt{3\,(l+2)\,(l-1)}}{l\,(l+1)\sqrt{2\,(2l-1)\,(2l+3)}}\exp\left(2i\omega_l\right)U^{l}_{2l1l}P^1_l \\
& -\frac{(l-2)\sqrt{(2l+1)\,(l+3)}}{2\,(l+1)\sqrt{l\,(l+2)}}\exp\left(i\left(\omega_l+\omega_{l+1}\right)\right)U^{l}_{2(l+1)1l}P^1_{l+1} \\
& +\sqrt{\frac{l\,(l+4)\,(2l+1)}{2\,(l+1)\,(l+2)\,(2l+3)}}\exp\left(i\left(\omega_l+\omega_{l+2}\right)\right)U^{l}_{2(l+2)1l}P^1_{l+2} \\
& +\sqrt{\frac{l\,(l-4)}{2\,(2l-3)\,(l-2)}}\exp\left(i\left(\omega_l+\omega_{l-3}\right)\right)U^{l-1}_{2(l-3)1l}P^1_{l-3} \\
& +\frac{(l+2)\sqrt{l-3}}{2\sqrt{l\,(l-1)\,(l-2)}}\exp\left(i\left(\omega_l+\omega_{l-2}\right)\right)U^{l-1}_{2(l-2)1l}P^1_{l-2} \\
& +\frac{3\sqrt{3\,(l+1)\,(l-2)\,(2l-1)}}{2l\sqrt{(l-1)\,(l-2)}}\exp\left(i\left(\omega_l+\omega_{l-1}\right)\right)U^{l-1}_{2(l-1)1l}P^1_{l-1} \\
& -\frac{(l-3)\sqrt{(l+2)}}{2l\sqrt{(l+1)}}\exp\left(2i\omega_l\right)U^{l-1}_{2l1l}P^1_l \\
& -\frac{(l-1)\sqrt{l+3}}{\sqrt{2l\,(l+1)\,(2l+1)}}\exp\left(i\left(\omega_l+\omega_{l+1}\right)\right)U^{l-1}_{2(l+1)1l}P^1_{l+1} \Bigg],
\end{aligned}
$$

(A.6)

$$
\begin{aligned}
\mathfrak{M}^{11}_{20} = \frac{i}{2k} \sum_l \Bigg[& \frac{l+2}{\sqrt{4l\,(2l+1)}} \exp\left(i\left(\omega_l + \omega_{l-1^l}\right)\right) U^{l+1}_{2(l-1)1l} P^1_{l-1} \\
& + \sqrt{\frac{3\,(l+2)}{2l\,(l+1)^2}} \exp\left(2i\omega_l\right) U^{l+1}_{2l1l} P^1_l \\
& + \frac{\sqrt{(l+2)\,(2l+3)}\,(3-(l+1)\,(l+2))}{\sqrt{2}\,(2l+1)\,(2l+5)} \exp\left(i\left(\omega_l + \omega_{l+1}\right)\right) U^{l+1}_{2(l+1)1l} P^1_{l+1} \\
& - \frac{1}{\sqrt{2}\,(l+2)\,(l+3)} \exp\left(i\left(\omega_l + \omega_{l+2}\right)\right) U^{l+1}_{2(l+2)1l} P^1_{l+2} \\
& + \sqrt{\frac{3\,(l+2)\,(l+1)}{4\,(l+3)\,(2l+5)}} \exp\left(i\left(\omega_l + \omega_{l+3}\right)\right) U^{l+1}_{2(l+3)1l} P^1_{l+3} \\
& - \sqrt{\frac{(2l+1)\,(l+1)}{4\,(2l-1)\,(l-1)}} \exp\left(i\left(\omega_l + \omega_{l-2}\right)\right) U^{l}_{2(l-2)1l} P^1_{l-2} \\
& - \sqrt{\frac{3\,(2l+1)}{2l^2\,(l-1)}} \exp\left(i\left(\omega_l + \omega_{l-1}\right)\right) U^{l}_{2(l-1)1l} P^1_{l-1} \\
& - \frac{(2l+1)\,(3-l\,(l+1))}{l\,(l+1)\,\sqrt{2\,(2l+3)\,(2l-1)}} \exp\left(2i\omega_l\right) U^{l}_{2l1l} P^1_l \\
& - \sqrt{\frac{3\,(2l+1)}{2\,(l+1)^2\,(l+2)}} \exp\left(i\left(\omega_l + \omega_{l+1}\right)\right) U^{l}_{2(l+1)1l} P^1_{l+1} \\
& - \sqrt{\frac{3l\,(2l+1)}{4l+2\,(2l+3)}} \exp\left(i\left(\omega_l + \omega_{l+2}\right)\right) U^{l}_{2(l+2)1l} P^1_{l+2} \\
& + \sqrt{\frac{l\,(l-1)}{4\,(l-2)\,(2l-3)}} \exp\left(i\left(\omega_l + \omega_{l-3}\right)\right) U^{l-1}_{2(l-3)1l} P^1_{l-3} \\
& + \sqrt{\frac{3}{2\,(l-1)\,(l-2)}} \exp\left(i\left(\omega_l + \omega_{l-2}\right)\right) U^{l-1}_{2(l-2)1l} P^1_{l-2} \\
& + \frac{\sqrt{(2l-1)}\,(3-l\,(l-1))}{l\,\sqrt{2\,(l-1)\,(2l+1)\,(2l-3)}} \exp\left(i\left(\omega_l + \omega_{l-1}\right)\right) U^{l-1}_{2(l-1)1l} P^1_{l-1} \\
& + \sqrt{\frac{3\,(l-1)}{2l^2\,(l+1)}} \exp\left(2i\omega_l\right) U^{l-1}_{2l1l} P^1_l \\
& + \frac{\sqrt{3}\,(l-1)}{2\,\sqrt{(2l+1)\,(l+1)}} \exp\left(i\left(\omega_l + \omega_{l+1}\right)\right) U^{l-1}_{2(l+1)1l} P^1_{l+1} \Bigg],
\end{aligned}
$$

(A.7)

$$\mathfrak{M}_{11}^{22} = -\frac{i}{2k} \sum_l \left[\frac{(l+3)(l+4)}{2(l+2)\sqrt{2(2l+3)(l+1)}} \exp\left(i\left(\omega_l+\omega_{l+1}\right)\right) U_{1(l+1)2l}^{l+2} P_{l+1}^1 \right.$$

$$-\frac{(l+4)\sqrt{(l+1)(2l+5)}}{2(l+2)\sqrt{2(2l+3)(l+1)}} \exp\left(i\left(\omega_l+\omega_{l+2}\right)\right) U_{1(l+2)2l}^{l+2} P_{l+2}^1$$

$$+\sqrt{\frac{(l+1)(l+2)}{8(2l+3)(l+3)}} \exp\left(i\left(\omega_l+\omega_{l+3}\right)\right) U_{1(l+3)2l}^{l+2} P_{l+3}^1$$

$$-\frac{(l+3)\sqrt{l+2}}{(l+1)\sqrt{2l}} \exp\left(2i\omega_l\right) U_{1l2l}^{l+1} P_l^1$$

$$+\frac{(l+3)\sqrt{l(2l+3)}}{4(l+1)(l+2)} \exp\left(i\left(\omega_l+\omega_{l+1}\right)\right) U_{1(l+1)2l}^{l+1} P_{l+1}^1$$

$$-\frac{\sqrt{l(l+1)}}{2(l+2)} \exp\left(i\left(\omega_l+\omega_{l+2}\right)\right) U_{1(l+2)2l}^{l+1} P_{l+2}^1$$

$$+\sqrt{\frac{3(l+1)(l+2)(2l+1)}{4l^2(2l+3)(2l-1)}} \exp\left(i\left(\omega_l+\omega_{l-1}\right)\right) U_{1(l-1)2l}^{l} P_{l-1}^1$$

$$-\frac{3(l+2)(l-1)(2l+1)}{l(l+1)\sqrt{(2l+3)(2l-1)}} \exp\left(2i\omega_l\right) U_{1l2l}^{l} P_l^1$$

$$+\frac{(l-1)\sqrt{3l(2l+1)}}{2(l+1)\sqrt{(2l+3)(2l-1)}} \exp\left(i\left(\omega_l+\omega_{l+1}\right)\right) U_{1(l+1)2l}^{l} P_{l+1}^1$$

$$-\frac{\sqrt{l(l+1)}}{2(l-1)} \exp\left(i\left(\omega_l+\omega_{l-2}\right)\right) U_{1(l-2)2l}^{l-1} P_{l-2}^1$$

$$+\frac{\sqrt{(l+1)(l-2)(2l-1)}}{2(l-1)\sqrt{l}} \exp\left(i\left(\omega_l+\omega_{l-1}\right)\right) U_{1(l-1)2l}^{l-1} P_{l-1}^1$$

$$-\frac{(l-2)\sqrt{l-1}}{2l\sqrt{l+1}} \exp\left(2i\omega_l\right) U_{1l2l}^{l-1} P_l^1$$

$$+\sqrt{\frac{l(l-1)}{8(l-2)(2l-1)}} \exp\left(i\left(\omega_l+\omega_{l-3}\right)\right) U_{1(l-3)2l}^{l-2} P_{l-3}^1$$

$$-\frac{(l-3)\sqrt{l(2l-3)}}{2(l-1)\sqrt{(l-2)(2l-1)}} \exp\left(i\left(\omega_l+\omega_{l-2}\right)\right) U_{1(l-2)2l}^{l-2} P_{l-2}^1$$

$$\left. +\frac{(l-3)(l-2)}{2(l-1)\sqrt{2l(2l-1)}} \exp\left(i\left(\omega_l+\omega_{l-1}\right)\right) U_{1(l-1)2l}^{l-2} P_{l-1}^1 \right],$$

(A.8)

$$
\begin{aligned}
\mathfrak{M}_{11}^{21} = -\frac{i}{2k} \sum_{l} \Bigg[& \frac{(l+3)\sqrt{(l+1)}}{\sqrt{2(2l+3)}} \exp\left(i\left(\omega_l + \omega_{l+1}\right)\right) U_{1(l+1)2l}^{l+2} P_{l+1}^{1} \\
& - \sqrt{\frac{(l+1)(l+3)(2l+5)}{2(2l+3)}} \exp\left(i\left(\omega_l + \omega_{l+2}\right)\right) U_{1(l+2)2l}^{l+2} P_{l+2}^{1} \\
& + \sqrt{\frac{(l+1)(l+2)(l+3)}{2(2l+3)}} \exp\left(i\left(\omega_l + \omega_{l+3}\right)\right) U_{1(l+3)2l}^{l+2} P_{l+3}^{1} \\
& - \frac{\sqrt{l(l+2)}}{2} \exp\left(2i\omega_l\right) U_{1l2l}^{l+1} P_{l}^{1} \\
& + \frac{\sqrt{l(2l+3)}}{2} \exp\left(i\left(\omega_l + \omega_{l+1}\right)\right) U_{1(l+1)2l}^{l+1} P_{l+1}^{1} \\
& - \frac{\sqrt{l(l+1)}}{2} \exp\left(i\left(\omega_l + \omega_{l+2}\right)\right) U_{1(l+2)2l}^{l+1} P_{l+2}^{1} \\
& - \sqrt{\frac{3(l+1)(2l+1)}{4(2l+3)(2l-1)}} \exp\left(i\left(\omega_l + \omega_{l-1}\right)\right) U_{1(l-1)2l}^{l} P_{l-1}^{1} \\
& + \frac{\sqrt{3}(2l+1)}{2\sqrt{(2l+3)(2l-1)}} \exp\left(2i\omega_l\right) U_{1l2l}^{l} P_{l}^{1} \\
& - \sqrt{\frac{3l(2l+1)}{4(2l+3)(2l-1)}} \exp\left(i\left(\omega_l + \omega_{l+1}\right)\right) U_{1(l+1)2l}^{l} P_{l+1}^{1} \\
& + \frac{\sqrt{l(l+1)}}{2} \exp\left(i\left(\omega_l + \omega_{l-2}\right)\right) U_{1(l-2)2l}^{l-1} P_{l-2}^{1} \\
& - \frac{\sqrt{(l+1)(2l-1)}}{2} \exp\left(i\left(\omega_l + \omega_{l-1}\right)\right) U_{1(l-1)2l}^{l-1} P_{l-1}^{1} \\
& + \frac{\sqrt{(l-1)(l+1)}}{2} \exp\left(2i\omega_l\right) U_{1l2l}^{l-1} P_{l}^{1} \\
& - \sqrt{\frac{l(l-2)(l-1)}{2(2l-1)}} \exp\left(i\left(\omega_l + \omega_{l-3}\right)\right) U_{1(l-3)2l}^{l-2} P_{l-3}^{1} \\
& + \frac{\sqrt{l(l-2)(2l-3)}}{\sqrt{2(2l-1)}} \exp\left(i\left(\omega_l + \omega_{l-2}\right)\right) U_{1(l-2)2l}^{l-2} P_{l-2}^{1} \\
& - \frac{(l-2)\sqrt{l}}{\sqrt{2(2l-1)}} \exp\left(i\left(\omega_l + \omega_{l-1}\right)\right) U_{1(l-1)2l}^{l-2} P_{l-1}^{1} \Bigg],
\end{aligned}
\tag{A.9}
$$

$$\mathfrak{M}_{11}^{20} = \frac{i}{2k} \sum_l \left[\sqrt{\frac{3(l+1)}{4(2l+3)}} \exp\left(i\left(\omega_l + \omega_{l+1}\right)\right) U_{1(l+1)2l}^{l+2} P_{l+1}^1 \right.$$

$$- \sqrt{\frac{3(l+1)(2l+5)}{4(2l+3)(l+3)}} \exp\left(i\left(\omega_l + \omega_{l+2}\right)\right) U_{1(l+2)2l}^{l+2} P_{l+2}^1$$

$$+ \sqrt{\frac{3(l+1)(l+2)}{4(l+3)(2l+3)}} \exp\left(i\left(\omega_l + \omega_{l+3}\right)\right) U_{1(l+3)2l}^{l+2} P_{l+3}^1$$

$$- \sqrt{\frac{(2l+1)(l+1)}{2(2l+3)(2l-1)}} \exp\left(i\left(\omega_l + \omega_{l-1}\right)\right) U_{1(l-1)2l}^{l} P_{l-1}^1$$

$$+ \frac{2l+1}{\sqrt{(2l+3)(2l-1)}} \exp\left(2i\omega_l\right) U_{1l2l}^{l} P_{l}^1 \tag{A.10}$$

$$- \sqrt{\frac{l(2l+1)}{(2l+3)(2l-1)}} \exp\left(i\left(\omega_l + \omega_{l+1}\right)\right) U_{1(l+1)2l}^{l} P_{l+1}^1$$

$$+ \sqrt{\frac{3l(l-1)}{4(l-2)(2l-1)}} \exp\left(i\left(\omega_l + \omega_{l-3}\right)\right) U_{1(l-3)2l}^{l-2} P_{l-3}^1$$

$$- \sqrt{\frac{3l(2l-3)}{2(l-2)(2l-1)}} \exp\left(i\left(\omega_l + \omega_{l-2}\right)\right) U_{1(l-2)2l}^{l-2} P_{l-2}^1$$

$$\left. + \sqrt{\frac{3l}{2(2l-1)}} \exp\left(i\left(\omega_l + \omega_{l-1}\right)\right) U_{1(l-1)2l}^{l-2} P_{l-1}^1 \right],$$

$$
\mathfrak{M}_1^{2\,-1} = \frac{i}{2k} \sum_l \left[\frac{\sqrt{l+1}}{(l+2)\sqrt{2(2l+3)}} \exp\left(i\left(\omega_l + \omega_{l+1}\right)\right) U_{1(l+1)2l}^{l+2} P_{l+1}^2 \right.
$$

$$
+ \frac{\sqrt{(l+1)(2l+5)}}{(l+2)\sqrt{2(2l+3)(l+3)}} \exp\left(i\left(\omega_l + \omega_{l+2}\right)\right) U_{1(l+2)2l}^{l+2} P_{l+2}^2
$$

$$
+ \sqrt{\frac{l+1}{2(l+3)(l+2)(2l+3)}} \exp\left(i\left(\omega_l + \omega_{l+3}\right)\right) U_{1(l+3)2l}^{l+2} P_{l+3}^2
$$

$$
- \frac{\sqrt{l}}{2(l+1)\sqrt{(l+2)}} \exp\left(2i\omega_l\right) U_{1l2l}^{l+1} P_l^2
$$

$$
- \frac{\sqrt{l(2l+3)}}{2(l+1)(l+2)} \exp\left(i\left(\omega_l + \omega_{l+1}\right)\right) U_{1(l+1)2l}^{l+1} P_{l+1}^2
$$

$$
- \frac{\sqrt{l}}{2\left(l+2\sqrt{l+1}\right)} \exp\left(i\left(\omega_l + \omega_{l+2}\right)\right) U_{1(l+2)2l}^{l+1} P_{l+2}^2
$$

$$
- \frac{\sqrt{3(2l+1)}}{2l\sqrt{(2l+3)(2l-1)(l+1)}} \exp\left(i\left(\omega_l + \omega_{l-1}\right)\right) U_{1(l-1)2l}^{l} P_{l-1}^2
$$

$$
- \frac{\sqrt{3(2l+1)}}{2l\sqrt{(2l+3)(2l-1)(l+1)}} \exp\left(2i\omega_l\right) U_{1l2l}^{l} P_l^2 \tag{A11}
$$

$$
- \frac{\sqrt{3(2l+1)}}{2(l+1)\sqrt{l(2l+3)(2l-1)}} \exp\left(i\left(\omega_l + \omega_{l+1}\right)\right) U_{1(l+1)2l}^{l} P_{l+1}^2
$$

$$
+ \frac{\sqrt{l+1}}{2(l-1)\sqrt{l}} \exp\left(i\left(\omega_l + \omega_{l-2}\right)\right) U_{1(l-2)2l}^{l-1} P_{l-2}^2
$$

$$
+ \frac{\sqrt{(l+1)(2l-1)}}{2l(l-1)} \exp\left(i\left(\omega_l + \omega_{l-1}\right)\right) U_{1(l-1)2l}^{l-1} P_{l-1}^2
$$

$$
+ \frac{\sqrt{l+1}}{2l\sqrt{l-1}} \exp\left(2i\omega_l\right) U_{1l2l}^{l-1} P_l^2
$$

$$
- \sqrt{\frac{l}{2(2l-1)(l-1)(l-2)}} \exp\left(i\left(\omega_l + \omega_{l-3}\right)\right) U_{1(l-3)2l}^{l-2} P_{l-3}^2
$$

$$
- \frac{\sqrt{l(2l-3)}}{(l-1)\sqrt{2(2l-1)(l-2)}} \exp\left(i\left(\omega_l + \omega_{l-2}\right)\right) U_{1(l-2)2l}^{l-2} P_{l-2}^2
$$

$$
\left. - \frac{\sqrt{l}}{(l-1)\sqrt{2(2l-1)}} \exp\left(i\left(\omega_l + \omega_{l-1}\right)\right) U_{1(l-1)2l}^{l-2} P_{l-1}^2 \right],
$$

$$\mathfrak{M}_1^{2-2}{}_1 = \frac{i}{2k} \sum_l \left[\frac{1}{2(l+2)\sqrt{2(2l+3)(l+1)}} \exp\left(i\left(\omega_l + \omega_{l+1}\right)\right) U^{l+2}_{1(l+1)2l} P^3_{l+1} \right.$$

$$+ \frac{1}{2(l+2)\sqrt{(2l+3)(l+1)(l+3)}} \exp\left(i\left(\omega_l + \omega_{l+2}\right)\right) U^{l+2}_{1(l+2)2l} P^3_{l+2}$$

$$+ \frac{1}{\sqrt{8(l+3)(l+2)(l+1)(2l+3)}} \exp\left(i\left(\omega_l + \omega_{l+3}\right)\right) U^{l+2}_{1(l+3)2l} P^3_{l+3}$$

$$- \frac{1}{2(l+1)\sqrt{l(l+2)}} \exp\left(2i\omega_l\right) U^{l+1}_{1l2l} P^3_{l}$$

$$- \frac{\sqrt{(2l+3)}}{2(l+1)(l+2)\sqrt{l}} \exp\left(i\left(\omega_l + \omega_{l+1}\right)\right) U^{l+1}_{1(l+1)2l} P^3_{l+1}$$

$$- \frac{1}{2(l+2)\sqrt{l(l+1)}} \exp\left(i\left(\omega_l + \omega_{l+2}\right)\right) U^{l+1}_{1(l+2)2l} P^3_{l+2}$$

$$+ \frac{\sqrt{3(2l+1)}}{2l\sqrt{(2l+3)(2l-1)(l+1)}} \exp\left(i\left(\omega_l + \omega_{l-1}\right)\right) U^{l}_{1(l-1)2l} P^3_{l-1}$$

$$+ \frac{(2l+1)\sqrt{3}}{2l(l+1)\sqrt{(2l+3)(2l-1)}} \exp\left(2i\omega_l\right) U^{l}_{1l2l} P^3_{l} \tag{A.12}$$

$$+ \frac{\sqrt{3(2l+1)}}{2(l+1)\sqrt{l(2l+3)(2l-1)}} \exp\left(i\left(\omega_l + \omega_{l+1}\right)\right) U^{l}_{1(l+1)2l} P^3_{l+1}$$

$$- \frac{1}{2(l-1)\sqrt{l(l+1)}} \exp\left(i\left(\omega_l + \omega_{l-2}\right)\right) U^{l-1}_{1(l-2)2l} P^3_{l-2}$$

$$- \frac{\sqrt{(2l-1)}}{2(l-1)l(l+1)} \exp\left(i\left(\omega_l + \omega_{l-1}\right)\right) U^{l-1}_{1(l-1)2l} P^3_{l-1}$$

$$+ \frac{1}{2l\sqrt{(l-1)(l+1)}} \exp\left(2i\omega_l\right) U^{l-1}_{1l2l} P^3_{l}$$

$$+ \frac{1}{\sqrt{8(2l-1)l(l-1)(l-2)}} \exp\left(i\left(\omega_l + \omega_{l-3}\right)\right) U^{l-2}_{1(l-3)2l} P^3_{l-3}$$

$$+ \frac{\sqrt{(2l-3)}}{2(l-1)\sqrt{l(2l-1)(l-2)}} \exp\left(i\left(\omega_l + \omega_{l-2}\right)\right) U^{l-2}_{1(l-2)2l} P^3_{l-2}$$

$$+ \left. \frac{1}{2(l-1)\sqrt{2l(2l-1)}} \exp\left(i\left(\omega_l + \omega_{l-1}\right)\right) U^{l-2}_{1(l-1)2l} P^3_{l-1} \right],$$

$$
\mathfrak{M}_{10}^{22} = -\frac{i}{2k} \sum_l \left[\frac{l+4}{2\left(l+2\right)\sqrt{\left(l+1\right)\left(2l+3\right)}} \exp\left(i\left(\omega_l + \omega_{l+1}\right)\right) U_{1(l+1)2l}^{l+2} P_{l+1}^2 \right.
$$

$$
+ \frac{\sqrt{\left(2l+5\right)}}{\left(l+2\right)\sqrt{\left(2l+3\right)\left(l+3\right)\left(l+1\right)}} \exp\left(i\left(\omega_l + \omega_{l+2}\right)\right) U_{1(l+2)2l}^{l+2} P_{l+2}^2
$$

$$
+ \sqrt{\frac{\left(l+1\right)\left(l+3\right)}{4\left(l+2\right)\left(2l+3\right)}} \exp\left(i\left(\omega_l + \omega_{l+3}\right)\right) U_{1(l+3)2l}^{l+2} P_{l+3}^2
$$

$$
- \frac{l+3}{\sqrt{2}l\left(l+2\right)\left(l-1\right)} \exp\left(2i\omega_l\right) U_{1l2l}^{l+1} P_l^2
$$

$$
- \frac{\sqrt{2\left(2l+3\right)}}{\left(l+1\right)\left(l+2\right)\sqrt{l}} \exp\left(i\left(\omega_l + \omega_{l+1}\right)\right) U_{1(l+1)2l}^{l+1} P_{l+1}^2
$$

$$
- \frac{\sqrt{l}}{\left(l+2\right)\sqrt{2\left(l+1\right)}} \exp\left(i\left(\omega_l + \omega_{l+2}\right)\right) U_{1(l+2)2l}^{l+1} P_{l+2}^2
$$

$$
- \frac{\left(l+2\right)\sqrt{3\left(2l+1\right)}}{l\sqrt{2\left(2l+3\right)\left(2l-1\right)\left(l-1\right)}} \exp\left(i\left(\omega_l + \omega_{l-1}\right)\right) U_{1(l-1)2l}^{l} P_{l-1}^2
$$

$$
\text{(A.13)}
$$

$$
+ \frac{\sqrt{6\left(2l+1\right)}}{l\left(l+1\right)\sqrt{\left(2l+3\right)\left(2l-1\right)}} \exp\left(2i\omega_l\right) U_{1l2l}^{l} P_l^2
$$

$$
- \frac{\left(l-1\right)\sqrt{3\left(2l+1\right)}}{\left(l+1\right)\sqrt{2l\left(2l+3\right)\left(2l-1\right)}} \exp\left(i\left(\omega_l + \omega_{l+1}\right)\right) U_{1(l+1)2l}^{l} P_{l+1}^2
$$

$$
- \frac{\sqrt{l+1}}{\left(l-1\right)\sqrt{2l}} \exp\left(i\left(\omega_l + \omega_{l-2}\right)\right) U_{1(l-2)2l}^{l-1} P_{l-2}^2
$$

$$
- \frac{\sqrt{2\left(2l-1\right)}}{l\left(l-1\right)\sqrt{l+1}} \exp\left(i\left(\omega_l + \omega_{l-1}\right)\right) U_{1(l-1)2l}^{l-1} P_{l-1}^2
$$

$$
+ \frac{l-2}{l\sqrt{2\left(l+1\right)\left(l-1\right)}} \exp\left(2i\omega_l\right) U_{1l2l}^{l-1} P_l^2
$$

$$
+ \sqrt{\frac{l}{4\left(2l-1\right)\left(l-1\right)\left(l-2\right)\left(l-4\right)}} \exp\left(i\left(\omega_l + \omega_{l-3}\right)\right) U_{1(l-3)2l}^{l-2} P_{l-3}^2
$$

$$
+ \frac{\sqrt{2l-3}}{\left(l-1\right)\sqrt{l\left(2l-1\right)\left(l-2\right)}} \exp\left(i\left(\omega_l + \omega_{l-2}\right)\right) U_{1(l-2)2l}^{l-2} P_{l-2}^2
$$

$$
\left. - \frac{l-3}{2l\left(l-1\right)\sqrt{2l-1}} \exp\left(i\left(\omega_l + \omega_{l-1}\right)\right) U_{1(l-1)2l}^{l-2} P_{l-1}^2 \right],
$$

$$
\begin{aligned}
\mathfrak{M}_{10}^{21} = -\frac{i}{2k} \sum_l \Bigg[& \frac{(l+3)\sqrt{l+1}}{(l+2)\sqrt{2l+3}} \exp\left(i\left(\omega_l + \omega_{l+1}\right)\right) U_{1(l+1)2l}^{l+2} P_{l+1}^1 \\
& + \frac{\sqrt{(l+1)(2l+5)}}{(l+2)\sqrt{(l+3)(2l+3)}} \exp\left(i\left(\omega_l + \omega_{l+2}\right)\right) U_{1(l+2)2l}^{l+2} P_{l+2}^1 \\
& - \sqrt{\frac{(l+1)(l+2)}{(l+3)(2l+3)}} \exp\left(i\left(\omega_l + \omega_{l+3}\right)\right) U_{1(l+3)2l}^{l+2} P_{l+3}^1 \\
& - \frac{\sqrt{l(l+2)}}{\sqrt{2}(l+1)} \exp\left(2i\omega_l\right) U_{1l2l}^{l+1} P_l^1 \\
& - \frac{\sqrt{l(2l+3)}}{\sqrt{2}(l+1)(l+2)} \exp\left(i\left(\omega_l + \omega_{l+1}\right)\right) U_{1(l+1)2l}^{l+1} P_{l+1}^1 \\
& - \frac{\sqrt{l(l+1)}}{\sqrt{2}(l+2)} \exp\left(i\left(\omega_l + \omega_{l+2}\right)\right) U_{1(l+2)2l}^{l+1} P_{l+2}^1 \\
& - \sqrt{\frac{3(l+1)(2l+1)}{2l^2(2l+3)(2l-1)}} \exp\left(i\left(\omega_l + \omega_{l-1}\right)\right) U_{1(l-1)2l}^{l} P_{l-1}^1 \\
& - \frac{\sqrt{3}(2l+1)}{l(l+1)\sqrt{2(2l+3)(2l-1)}} \exp\left(2i\omega_l\right) U_{1l2l}^{l} P_l^1 \\
& + \frac{\sqrt{3l}(2l+1)}{(l+1)\sqrt{2(2l+3)(2l-1)}} \exp\left(i\left(\omega_l + \omega_{l+1}\right)\right) U_{1(l+1)2l}^{l} P_{l+1}^1 \\
& + \frac{\sqrt{l(l+1)}}{\sqrt{2}(l-1)} \exp\left(i\left(\omega_l + \omega_{l-2}\right)\right) U_{1(l-2)2l}^{l-1} P_{l-2}^1 \\
& + \frac{\sqrt{(l+1)(2l-1)}}{\sqrt{2}l(l-1)} \exp\left(i\left(\omega_l + \omega_{l-1}\right)\right) U_{1(l-1)2l}^{l-1} P_{l-1}^1 \\
& - \frac{\sqrt{(l-1)(l+1)}}{\sqrt{2}l} \exp\left(2i\omega_l\right) U_{1l2l}^{l-1} P_l^1 \\
& - \sqrt{\frac{l(l-1)}{(2l-1)(l-2)}} \exp\left(i\left(\omega_l + \omega_{l-3}\right)\right) U_{1(l-3)2l}^{l-2} P_{l-3}^1 \\
& - \frac{\sqrt{l(2l-3)}}{(l-1)\sqrt{(2l-1)(l-2)}} \exp\left(i\left(\omega_l + \omega_{l-2}\right)\right) U_{1(l-2)2l}^{l-2} P_{l-2}^1 \\
& + \frac{(l-2)\sqrt{l}}{(l-1)\sqrt{2(2l-1)}} \exp\left(i\left(\omega_l + \omega_{l-1}\right)\right) U_{1(l-1)2l}^{l-2} P_{l-1}^1 \Bigg].
\end{aligned}
$$

(A.14)

Spin-mixing M−matrix elements for half-integer channel spin S = 1/2 and S = 3/2:

$$
\mathfrak{M}^{1/2\,1/2}_{3/2\,3/2} = \frac{i}{2k}\sum_l \Bigg[\frac{l+1}{\sqrt{2l\,(2l+1)}} \exp\left(i\,(\omega_l + \omega_{l-1})\right) U^{l+1/2}_{3/2(l-1)1/2l} P^1_{l-1}
$$

$$
- \frac{\sqrt{3}\,(l+1)}{\sqrt{2l\,(2l+3)}} \exp\left(2i\omega_l\right) U^{l+1/2}_{3/2l1/2l} P^1_l
$$

$$
- \frac{\sqrt{3}\,(l+1)}{\sqrt{2\,(l+2)\,(2l+3)}} \exp\left(i\,(\omega_l + \omega_{l+1})\right) U^{l+1/2}_{3/2(l+1)1/2l} P^1_{l+1}
$$

$$
- \frac{l+1}{\sqrt{2\,(l+2)\,(2l+3)}} \exp\left(i\,(\omega_l + \omega_{l+2})\right) U^{l+1/2}_{3/2(l+2)1/2l} P^1_{l+2}
$$

$$
- \frac{l}{\sqrt{2\,(l-1)\,(2l-1)}} \exp\left(i\,(\omega_l + \omega_{l-2})\right) U^{l-1/2}_{3/2(l-2)1/2l} P^1_{l-2} \tag{A.15}
$$

$$
+ \frac{\sqrt{3l}}{\sqrt{2\,(l-1)\,(2l+1)}} \exp\left(i\,(\omega_l + \omega_{l-1})\right) U^{l-1/2}_{3/2(l-1)1/2l} P^1_{l-1}
$$

$$
- \frac{\sqrt{3l}}{\sqrt{2\,(l+1)\,(2l-1)}} \exp\left(2i\omega_l\right) U^{l-1/2}_{3/2l1/2l} P^1_l
$$

$$
+ \frac{l}{\sqrt{2\,(l+1)\,(2l+1)}} \exp\left(i\,(\omega_l + \omega_{l+1})\right) U^{l-1/2}_{3/2(l+1)1/2l} P^1_{l+1} \Bigg]
$$

$$
\mathfrak{M}^{1/2\,-1/2}_{3/2\,3/2} = \frac{i}{2k}\sum_l \Bigg[\frac{1}{\sqrt{2l\,(2l+1)}} \exp\left(i\,(\omega_l + \omega_{l-1})\right) U^{l+1/2}_{3/2(l-1)1/2l} P^2_{l-1}
$$

$$
+ \sqrt{\frac{3\,(l+1)}{2l\,(2l+3)\,(l-1)}} \exp\left(2i\omega_l\right) U^{l+1/2}_{3/2l1/2l} P^2_l
$$

$$
+ \sqrt{\frac{3}{(2l+1)\,(l+2)}} \exp\left(i\,(\omega_l + \omega_{l+1})\right) U^{l+1/2}_{3/2(l+1)1/2l} P^2_{l+1}
$$

$$
+ \frac{1}{\sqrt{2\,(l+2)\,(2l-1)}} \exp\left(i\,(\omega_l + \omega_{l+2})\right) U^{l+1/2}_{3/2(l+2)1/2l} P^2_{l+2}
$$

$$
- \frac{1}{\sqrt{2\,(l-1)\,(2l-1)}} \exp\left(i\,(\omega_l + \omega_{l-2})\right) U^{l-1/2}_{3/2(l-2)1/2l} P^2_{l-2} \tag{A.16}
$$

$$
- \sqrt{\frac{3l}{2\,(2l+3)\,(l-1)\,(l-2)}} \exp\left(i\,(\omega_l + \omega_{l-1})\right) U^{l-1/2}_{3/2(l-1)1/2l} P^2_{l-1}
$$

$$
- \sqrt{\frac{3}{2\,(2l-1)\,(l+1)}} \exp\left(2i\omega_l\right) U^{l-1/2}_{3/2l1/2l} P^2_l
$$

$$
- \frac{1}{\sqrt{2\,(l+1)\,(2l+1)}} \exp\left(i\,(\omega_l + \omega_{l+1})\right) U^{l-1/2}_{3/2(l+1)1/2l} P^2_{l+1} \Bigg]
$$

$$\mathfrak{M}_{3/2\ 1/2}^{1/2\ 1/2} = -\frac{i}{2k}\sum_l \left[\frac{\sqrt{3l}\,(l+1)}{\sqrt{2\,(2l+1)}} \exp\left(i\,(\omega_l + \omega_{l-1})\right) U_{3/2(l-1)1/2l}^{l+1/2} P_{l-1}^0 \right.$$

$$-\frac{(l+1)\,\sqrt{l}}{\sqrt{2\,(2l+3)}} \exp\left(2i\omega_l\right) U_{3/2l1/2l}^{l-1/2} P_l^0$$

$$-\frac{(l+1)\,\sqrt{l+2}}{\sqrt{2\,(2l+1)}} \exp\left(i\,(\omega_l + \omega_{l+1})\right) U_{3/2(l+1)1/2l}^{l+1/2} P_{l+1}^0$$

$$+\frac{(l+1)\,\sqrt{3\,(l+2)}}{\sqrt{2\,(2l+3)}} \exp\left(i\,(\omega_l + \omega_{l+2})\right) U_{3/2(l+2)1/2l}^{l+1/2} P_{l+2}^0 \tag{A.17}$$

$$-\frac{l\sqrt{3\,(l-1)}}{\sqrt{2\,(2l-1)}} \exp\left(i\,(\omega_l + \omega_{l-2})\right) U_{3/2(l-2)1/2l}^{l-1/2} P_{l-2}^0$$

$$+\frac{l\sqrt{l-1}}{\sqrt{2\,(2l+1)}} \exp\left(i\,(\omega_l + \omega_{l-1})\right) U_{3/2(l-1)1/2l}^{l-1/2} P_{l-1}^0$$

$$+\frac{l\sqrt{l+1}}{\sqrt{2\,(2l-1)}} \exp\left(2i\omega_l\right) U_{3/2l1/2l}^{l-1/2} P_l^0$$

$$\left. -\frac{l\sqrt{3\,(l+1)}}{\sqrt{2\,(2l+1)}} \exp\left(i\,(\omega_l + \omega_{l+1})\right) U_{3/2(l+1)1/2l}^{l-1/2} P_{l+1}^0 \right]$$

$$\mathfrak{M}_{3/2\ 1/2}^{1/2-1/2} = -\frac{i}{2k}\sum_l \left[\frac{\sqrt{3l\,(l-1)}\,(l+1)}{\sqrt{2\,(2l+1)}} \exp\left(i\,(\omega_l + \omega_{l-1})\right) U_{3/2(l-1)1/2l}^{l+1/2} P_{l-1}^0 \right.$$

$$+\frac{(l+1)\,\sqrt{l+3}}{\sqrt{2\,(2l+3)}} \exp\left(2i\omega_l\right) U_{3/2l1/2l}^{l+1/2} P_l^0$$

$$-\frac{(l-1)\,\sqrt{l+1}}{\sqrt{2\,(2l+3)}} \exp\left(i\,(\omega_l + \omega_{l+1})\right) U_{3/2(l+1)1/2l}^{l+1/2} P_{l+1}^0$$

$$-\frac{(l+1)\,\sqrt{3\,(l+3)}}{\sqrt{2\,(2l+3)}} \exp\left(i\,(\omega_l + \omega_{l+2})\right) U_{3/2(l+2)1/2l}^{l+1/2} P_{l+2}^0 \tag{A.18}$$

$$-\frac{l\sqrt{3\,(l-2)}}{\sqrt{2\,(2l-1)}} \exp\left(i\,(\omega_l + \omega_{l-2})\right) U_{3/2(l-2)1/2l}^{l-1/2} P_{l-2}^0$$

$$-\frac{(l+1)\,\sqrt{l}}{\sqrt{2\,(2l+1)}} \exp\left(i\,(\omega_l + \omega_{l-1})\right) U_{3/2(l-1)1/2l}^{l-1/2} P_{l-1}^0$$

$$+\frac{(l-2)\,\sqrt{l}}{\sqrt{2\,(2l-1)}} \exp\left(2i\omega_l\right) U_{3/2(l-1)1/2l}^{l-1/2} P_{l-1}^0$$

$$\left. +\frac{l\sqrt{3\,(l+2)}}{\sqrt{2\,(2l+1)}} \exp\left(i\,(\omega_l + \omega_{l+1})\right) U_{3/2(l+1)1/2l}^{l-1/2} P_{l+1}^0 \right]$$

$$\mathfrak{M}_{1/2\ 1/2}^{3/2\ 3/2} = -\frac{i}{2k} \sum_l \left[\frac{l+3}{\sqrt{2\,(2l+3)\,(l+1)}} \exp\left(i\,(\omega_l + \omega_{l+1})\right) U_{1/2(l+1)3/2l}^{l+3/2} P_{l+1}^1 \right.$$

$$- \sqrt{\frac{l+1}{2\,(2l+3)}} \exp\left(i\,(\omega_l + \omega_{l+2})\right) U_{1/2(l+2)3/2l}^{l+3/2} P_{l+2}^1$$

$$- \frac{l+2}{\sqrt{2l\,(2l+3)}} \exp\left(2i\omega_l\right) U_{1/2l3/2l}^{l+1/2} P_l^1$$

$$+ \sqrt{\frac{3l}{2\,(2l+3)}} \exp\left(i\,(\omega_l + \omega_{l+1})\right) U_{1/2(l+1)3/2l}^{l+1/2} P_{l+1}^1$$

$$+ \sqrt{\frac{l+1}{2\,(2l-1)}} \exp\left(i\,(\omega_l + \omega_{l-1})\right) U_{1/2(l-1)3/2l}^{l-1/2} P_{l-1}^1$$

$$- \frac{l-1}{\sqrt{2\,(l+1)\,(2l-1)}} \exp\left(2i\omega_l\right) U_{1/2l3/2l}^{l-1/2} P_l^1$$

$$- \sqrt{\frac{l}{2\,(2l-1)}} \exp\left(i\,(\omega_l + \omega_{l-2})\right) U_{1/2(l-2)3/2l}^{l-3/2} P_{l-2}^1$$

$$\left. + \frac{l-2}{\sqrt{2l\,(2l-1)}} \exp\left(i\,(\omega_l + \omega_{l-1})\right) U_{1/2(l-1)3/2l}^{l-3/2} P_l^1 \right] \tag{A.19}$$

$$\mathfrak{M}_{1/2\ 1/2}^{3/2\ 1/2} = -\frac{i}{2k} \sum_l \left[\frac{(l+2)\sqrt{l+3}}{\sqrt{2\,(2l+3)}} \exp\left(i\,(\omega_l + \omega_{l+1})\right) U_{1/2(l+1)3/2l}^{l+3/2} P_{l+1}^0 \right.$$

$$- \frac{(l+2)\sqrt{l+3}}{\sqrt{2\,(2l+3)}} \exp\left(i\,(\omega_l + \omega_{l+2})\right) U_{1/2(l+2)3/2l}^{l+3/2} P_{l+2}^0$$

$$- \frac{(l+1)\sqrt{3\,(l+2)}}{\sqrt{2\,(2l+3)}} \exp\left(2i\omega_l\right) U_{1/2(l)3/2l}^{l+1/2} P_l^0$$

$$+ \frac{(l+1)\sqrt{3\,(l+2)}}{\sqrt{2\,(2l+3)}} \exp\left(i\,(\omega_l + \omega_{l+1})\right) U_{1/2(l+1)3/2l}^{l+1/2} P_{l+1}^0 \tag{A.20}$$

$$+ \frac{l\sqrt{3\,(l-1)}}{\sqrt{2\,(2l-1)}} \exp\left(i\,(\omega_l + \omega_{l-1})\right) U_{1/2(l-1)3/2l}^{l-1/2} P_{l-1}^0$$

$$+ \frac{l\sqrt{3\,(l-1)}}{\sqrt{2\,(2l-1)}} \exp\left(2i\omega_l\right) U_{1/2l)3/2l}^{l-1/2} P_l^0$$

$$- \frac{(l-1)\sqrt{(l-2)}}{\sqrt{2\,(2l-1)}} \exp\left(i\,(\omega_l + \omega_{l-2})\right) U_{1/2(l-2)3/2l}^{l-3/2} P_{l-2}^0$$

$$\left. + \frac{(l-1)\sqrt{(l-2)}}{\sqrt{2\,(2l-1)}} \exp\left(i\,(\omega_l + \omega_{l-1})\right) U_{1/2(l-1)3/2l}^{l-3/2} P_{l-1}^0 \right]$$

$$\mathfrak{M}^{3/2\;-1/2}_{1/2\;\;1/2} = -\frac{i}{2k}\sum_l \left[\sqrt{\frac{l+3}{2\,(2l+3)}}\exp\left(i\left(\omega_l + \omega_{l+1}\right)\right) U^{l+3/2}_{1/2(l+1)3/2l}\,P^1_{l+1} \right.$$

$$+\sqrt{\frac{l+3}{2\,(2l+3)}}\exp\left(i\left(\omega_l + \omega_{l+2}\right)\right) U^{l+3/2}_{1/2(l+2)3/2l}\,P^1_{l+2}$$

$$-\sqrt{\frac{3\,(l+2)}{2\,(2l+3)}}\exp\left(2i\omega_l\right) U^{l+1/2}_{1/2(l)3/2l}\,P^1_l$$

$$-\sqrt{\frac{3\,(l+2)}{2\,(2l+3)}}\exp\left(i\left(\omega_l + \omega_{l+1}\right)\right) U^{l+1/2}_{1/2(l+1)3/2l}\,P^1_{l+1}$$

$$+\frac{\sqrt{3\,(l-1)}}{\sqrt{2\,(2l-1)}}\exp\left(i\left(\omega_l + \omega_{l-1}\right)\right) U^{l-1/2}_{1/2(l-1)3/2l}\,P^1_{l-1} \qquad \text{(A.21)}$$

$$+\sqrt{\frac{3\,(l-1)}{2\,(2l-1)}}\exp\left(2i\omega_l\right) U^{l-1/2}_{1/2l)3/2l}\,P^1_l$$

$$-\sqrt{\frac{(l-2)}{2\,(2l-1)}}\exp\left(i\left(\omega_l + \omega_{l-2}\right)\right) U^{l-3/2}_{1/2(l-2)3/2l}\,P^1_{l-2}$$

$$\left. +\sqrt{\frac{(l-2)}{2\,(2l-1)}}\exp\left(i\left(\omega_l + \omega_{l-1}\right)\right) U^{l-3/2}_{1/2(l-1)3/2l}\,P^1_{l-1} \right]$$

$$\mathfrak{M}^{3/2\;-3/2}_{1/2\;\;1/2} = \frac{i}{2k}\sum_l \left[\frac{1}{\sqrt{2l\,(2l+3)\,(l+1)}}\exp\left(i\left(\omega_l + \omega_{l+1}\right)\right) U^{l+3/2}_{1/2(l+1)3/2l}\,P^2_{l+1} \right.$$

$$+\frac{1}{\sqrt{2l\,(2l+3)\,(l+1)}}\exp\left(i\left(\omega_l + \omega_{l+2}\right)\right) U^{l+3/2}_{1/2(l+2)3/2l}\,P^2_{l+2}$$

$$-\sqrt{\frac{3}{2l\,(2l+3)}}\exp\left(2i\omega_l\right) U^{l+1/2}_{1/2(l)3/2l}\,P^2_l$$

$$-\sqrt{\frac{3}{2l\,(2l+3)}}\exp\left(i\left(\omega_l + \omega_{l+1}\right)\right) U^{l+1/2}_{1/2(l+1)3/2l}\,P^2_{l+1} \qquad \text{(A.22)}$$

$$+\sqrt{\frac{3}{2\,(2l-1)\,(l+1)}}\exp\left(i\left(\omega_l + \omega_{l-1}\right)\right) U^{l-1/2}_{1/2(l-1)3/2l}\,P^2_{l-1}$$

$$+\sqrt{\frac{3}{2\,(2l-1)\,(l+1)}}\exp\left(2i\omega_l\right) U^{l-1/2}_{1/2l)3/2l}\,P^2_l$$

$$-\frac{1}{\sqrt{2l\,(2l-1)}}\exp\left(i\left(\omega_l + \omega_{l-2}\right)\right) U^{l-3/2}_{1/2(l-2)3/2l}\,P^2_{l-2}$$

$$\left. -\frac{1}{\sqrt{2l\,(2l-1)}}\exp\left(i\left(\omega_l + \omega_{l-1}\right)\right) U^{l-3/2}_{1/2(l-1)3/2l}\,P^2_{l-1} \right]$$

Computing test program for the phase shift analysis for the *pd*-system

This program is based on the formalism, presented in Section 1. It is developed on the basis of the works and research of S.B. Dubovichenko, Head of the Laboratory of Nuclear Astrophysics of the Fessenkov Astrophysical Institute, and in collaboration with him. A similar code is presented, for example, in his monograph [147].

```
PROGRAM FAZ_AN_N2H
IMPLICIT REAL(8) (A-Z)
INTEGER I,L,LMA,NI,NV,NT,NP,NPP,K,J
CHARACTER(34) AA,BB
CHARACTER(15) CC
COMMON /A1/
SE(0:100),DS(0:100),DE(0:100),DS1(0:100),ST(0:100),TT(0:100),CULKV(0:100),NT
,NP,LMA
COMMON /A2/ GG,SS
COMMON /A5/ PI
COMMON /BB/ NPP
DIMENSION XP(0:100)
COMMON FP12D(0:50),FM12D(0:50),  FP32Q(0:50),FM32Q(0:50),
FP12Q(0:50),FM12Q(0:50)
!  ************** INITIAL VALUES ********************************
PI=4.0D0*DATAN(1.0D0)
Z1=1.0D0
Z2=1.0D0
AM1=1.0D0 ! N
AM2=2.0D0 ! 2H
G=AM1/AM2
AM=AM1+AM2
A1=41.46860D0
!A1=41.80158990D0
PM=AM1*AM2/AM
B1=2.0D0*PM/A1
!*************************************************************************
!AA="400.dat"; NT=20; BB="p2H-400.DAT"; EP=0.400D0; ECM=AM2/AM*EP; LMA=3;
CC="FAZ-400.DAT"
!AA="647.dat"; NT=19; BB="p2H-647.DAT"; EP=0.647D0; ECM=AM2/AM*EP; LMA=2;
CC="FAZ-647.DAT"
AA="1000.dat"; NT=56; BB="p2H-1000.DAT"; EP=1.0D0; ECM=AM2/AM*EP; LMA=2;
CC="FAZ-1000.DAT"
!AA="2000.dat"; NT=32; BB="p2H-2000.DAT"; EP=2.0D0; ECM=AM2/AM*EP; LMA=10;
CC="FAZ-2000.DAT"
!AA="3000.dat"; NT=36; BB="p2H-3000.DAT"; EP=3.0D0; ECM=AM2/AM*EP; LMA=10;
CC="FAZ-3000.DAT"
!AA="4000.dat"; NT=28; BB="p2H-4000.DAT"; EP=4.0D0; ECM=AM2/AM*EP; LMA=6;
CC="FAZ-4000.DAT"
!AA="5000.dat"; NT=28; BB="p2H-5000.DAT"; EP=5.0D0; ECM=AM2/AM*EP; LMA=10;
CC="FAZ-5000.DAT"
!AA="6000.dat"; NT=28; BB="p2H-6000.DAT"; EP=6.0D0; ECM=AM2/AM*EP; LMA=4;
CC="FAZ-6000.DAT"
!AA="8000.dat"; NT=28; BB="p2H-8000.DAT"; EP=8.0D0; ECM=AM2/AM*EP; LMA=5;
CC="FAZ-8000.DAT"
!AA="10000.dat"; NT=27; BB="p2H-10000.DAT"; EP=10.0D0; ECM=AM2/AM*EP; LMA=4;
CC="FAZ-10000.DAT"
SK=ECM*B1; SS=DSQRT(SK); GG=3.4495312D-2*Z1*Z2*PM/SS ! КУЛОНОВСКИЙ ПАРАМЕТР
```

```
EP=1.0D-015; NP=2*LMA; NPP=6*LMA+6
OPEN (1,FILE=AA)
DO L=1,NT
READ(1,*) EP,TT(L),SE(L),DE(L)
!PRINT *,  EP,TT(L),SE(L),DE(L)
ENDDO
CLOSE(1)


!PHASE SHIFTS FOR L FROM 0 TO LMA
IF(ECM<1.0) THEN

IF(ECM>0.5D0) THEN
FP12D(0)=-10.53D0  ! 2S12
FM12D(0)= 0.0D0     ! 2S-12 = 0
FP12D(1)=-3.42D0    ! 2P32
FM12D(1)=-2.91D0    ! 2P12


FP32Q(0)=-36.81D0 ! 4S32
FP12Q(0)=0.0D0        ! 4S12 =  0
FM12Q(0)=0.0D0        ! 4S-12 = 0
FM32Q(0)=0.0D0        ! 4S-32 = 0


FP32Q(1)=10.14D0    ! 4P52
FP12Q(1)=10.62D0    ! 4P32
FM12Q(1)=9.18D0     ! 4P12
FM32Q(1)=0.0D0      ! 4P-12 = 0
ELSE
FP12D(0)=-7.64D0    ! 2S12
FM12D(0)= 0.0D0     ! 2S-12 = 0
FP12D(1)=-1.61D0    ! 2P32
FM12D(1)=-2.17D0    ! 2P12


FP32Q(0)=-27.48D0 ! 4S32
FP12Q(0)=0.0D0        ! 4S12 =  0
FM12Q(0)=0.0D0        ! 4S-12 = 0
FM32Q(0)=0.0D0        ! 4S-32 = 0


FP32Q(1)=5.69D0     ! 4P52
FP12Q(1)=6.19D0     ! 4P32
FM12Q(1)=5.06D0     ! 4P12
FM32Q(1)=0.0D0      ! 4P-12 = 0
ENDIF
ELSE
FP12D(0)=-23.69D0   ! 2S12
FM12D(0)= 0.0D0      ! 2S-12 = 0
FP12D(1)=-2.18D0     ! 2P32
FM12D(1)=-3.39D0     ! 2P12


FP12D(2)=-1.67D0    ! 2D32
FM12D(2)= 0.7D0     ! 2D12
FP12D(3)=-1.65D0    ! 2F72
FM12D(3)=-1.65D0    ! 2F52
FP12D(4)=0.39D0     ! 2G92
FM12D(4)=0.39D0     ! 2G72


FP32Q(0)=-68.57D0 ! 4S32
FP12Q(0)=0.0D0        ! 4S12 =  0
FM12Q(0)=0.0D0        ! 4S-12 = 0
FM32Q(0)=0.0D0        ! 4S-32 = 0
```

```
FP32Q(1)=24.26D0    ! 4P52
FP12Q(1)=22.98D0    ! 4P32
FM12Q(1)=22.70D0    ! 4P12
FM32Q(1)=0.0D0      ! 4P-12 = 0

FP32Q(2)=-4.51D0    ! 4D72
FP12Q(2)=-5.47D0    ! 4D52
FM12Q(2)=-4.68D0    ! 4D32
FM32Q(2)=-4.26D0    ! 4D12

FP32Q(3)=0.85D0     ! 4F92
FP12Q(3)=0.85D0     ! 4F72
FM12Q(3)=0.85D0     ! 4F52
FM32Q(3)=0.85D0     ! 4F32

FP32Q(4)=-0.34D0    ! 4G112
FP12Q(4)=-0.34D0    ! 4G92
FM12Q(4)=-0.34D0    ! 4G72
FM32Q(4)=-0.34D0    ! 4G52
ENDIF

NV=1;
FH=0.123D0
NI=1;


K=1
IF(K==1) THEN
OPEN (1,FILE=CC)
DO I=0,LMA
READ(1,*) FP12D(I),FM12D(I),FP12Q(I),FM12Q(I),FP32Q(I),FM32Q(I)
!PRINT*,   FP12D(I),FM12D(I),FP12Q(I),FM12Q(I),FP32Q(I),FM32Q(I)
ENDDO
CLOSE(1)
!STOP
ENDIF
! ****************** ENERGY IN LAB. SYSTEM **************************

DO L=0,LMA
FP12D(L)=FP12D(L)*PI/180.0D0
FM12D(L)=FM12D(L)*PI/180.0D0
FP32Q(L)=FP32Q(L)*PI/180.0D0
FP12Q(L)=FP12Q(L)*PI/180.0D0
FM12Q(L)=FM12Q(L)*PI/180.0D0
FM32Q(L)=FM32Q(L)*PI/180.0D0
ENDDO
FH=FH*PI/180.0D0

DO J=0,LMA
XP(J*6)=  FP12D(J)
XP(J*6+1)=FP12Q(J)
XP(J*6+2)=FP32Q(J)
XP(J*6+3)=FM12D(J)
XP(J*6+4)=FM12Q(J)
XP(J*6+5)=FM32Q(J)
ENDDO

!    **************** TRANSFORM TO C.M. **************************

CALL VAR(XP,FH,NI,EP,XI,NV)

! ****************** TOTAL CROSSS SECTION ***********************
```

```
DO J=0,LMA
FP12D(J)=XP(J*6)
FP12Q(J)=XP(J*6+1)
FP32Q(J)=XP(J*6+2)
FM12D(J)=XP(J*6+3)
FM12Q(J)=XP(J*6+4)
FM32Q(J)=XP(J*6+5)
ENDDO

DO L=0,LMA
FP12D(L)=FP12D(L)/PI*180.0D0
FM12D(L)=FM12D(L)/PI*180.0D0
FP32Q(L)=FP32Q(L)/PI*180.0D0
FP12Q(L)=FP12Q(L)/PI*180.0D0
FM12Q(L)=FM12Q(L)/PI*180.0D0
FM32Q(L)=FM32Q(L)/PI*180.0D0
ENDDO

PRINT*, "----------------------------------------------------------"
!PRINT *,"      T           SE          ST           XI"
DO I=1,NT
!WRITE(*,100) TT(I),SE(I),ST(I),DS(I),CULKV(i)
ENDDO

PRINT *
PRINT *,"   XI=     ",XI
PRINT *

OPEN (1,FILE=BB)
WRITE(1,*) " ECM=  ",ECM
WRITE(1,*) " XI=    ",XI

WRITE(1,*) "         T               SE               DSE                 ST
XI"
DO I=1,NT
WRITE(1,200) TT(I),SE(I),DE(I),ST(I),DS(I),CULKV(i)
ENDDO

WRITE(1,*) ''
WRITE(1,*) "           FP12D                  FM12D                 FP12Q
FM12Q        FP32Q        FM32Q"
DO I=0,LMA
WRITE(1,*) FP12D(I),FM12D(I),FP12Q(I),FM12Q(I),FP32Q(I),FM32Q(I)
ENDDO

OPEN (1,FILE=CC)
DO I=0,LMA
WRITE(1,*) FP12D(I),FM12D(I),FP12Q(I),FM12Q(I),FP32Q(I),FM32Q(I)
ENDDO
CLOSE(1)

DO I=0,LMA
!WRITE(*,*) FP12D(I),FM12D(I),FP12Q(I),FM12Q(I),FP32Q(I),FM32Q(I)
ENDDO
PRINT*, "----------------------------------------------------------"
100 FORMAT(10E12.4)
200 FORMAT(10E12.4)
END

SUBROUTINE VAR(XP,PHN,NI,EP,AMIN,NV)
```

```fortran
      IMPLICIT REAL(8) (A-Z)
      INTEGER I,NI,NT,NV,NP,NN,INE,IIN,NPP
      COMMON /A1/
     SE(0:100),DS(0:100),DE(0:100),DS1(0:100),ST(0:100),TT(0:100),CULKV(0:100),NT
     ,NPP,LMA
      COMMON /A5/ PI
      COMMON /BB/ NP
      DIMENSION XPN(0:100),XP(0:100)
! ***************** DETERMINATING THE MINIMUM *************************
      DO I=0,NP
      XPN(I)=XP(I)
      ENDDO

      NN=0
      PH=PHN
      CALL SEC(XPN,ALA)
      B=ALA
      IF (NV==0) GOTO 3012

!print *,'N=',nn,XPN(nn)*180./PI,ALA
!PRINT *,"--------------------------------------------------------------"
      DO IIN=1,NI
      NN=-1
!PRINT *,'FF=',ALA,IIN
1119  NN=NN+1
      INE=0
2229  A=B
      XPN(NN)=XPN(NN)+PH*xp(nn)
      INE=INE+1
! ------------------------------------------------------------------
      CALL SEC(XPN,ALA)
      B=ALA
! ------------------------------------------------------------------
      IF (B<A) GOTO 2229
      C=A
      XPN(NN)=XPN(NN)-PH*xp(nn)
      IF (INE>1) GOTO 3339
      PH=-PH
      GOTO 5559

3339  IF (ABS((C-B)/(B))<EP) GOTO 4449
      PH=PH/2.0D-000
5559  B=C
      GOTO 2229

4449  PH=PHN
      B=C
      IF (NN<NP) GOTO 1119
      AMIN=B
      PH=PHN
      ENDDO
3012  AMIN=B

      DO I=0,NP
      XP(I)=XPN(I)
      ENDDO

      END

      SUBROUTINE SEC(XP,XI)
      IMPLICIT DOUBLE COMPLEX(8) (A-Z)
```

```
REAL(8) GG,SS,PI,X,T,SCU,SECD,SECQ,SQ1,SQ2,SDA,SDB,SD,SQ,CULKV
REAL(8) SE,DS,DE,DS1,TT,ST,XI,S
REAL(8)
FP12D(0:100),FM12D(0:100),FP32Q(0:100),FM32Q(0:100),FP12Q(0:100),FM12Q(0:100
)
REAL(8) P0(0:100),P1(0:100),P2(0:100),P3(0:100),AL(0:100),XP(0:100)
INTEGER NT,LMA,L,NP,N,J,NPP
COMMON /A1/
SE(0:100),DS(0:100),DE(0:100),DS1(0:100),ST(0:100),TT(0:100),CULKV(0:100),NT
,NP,LMA
COMMON /A2/ GG,SS
COMMON /A5/ PI
COMMON /BB/ NPP
DIMENSION SCUL(0:100),SP12D(0:100),SM12D(0:100),  SP32Q(0:100),SM32Q(0:100),
SP12Q(0:100),SM12Q(0:100)
I=(0,1)

DO J=0,LMA
FP12D(J)=XP(J*6)
FP12Q(J)=XP(J*6+1)
FP32Q(J)=XP(J*6+2)
FM12D(J)=XP(J*6+3)
FM12Q(J)=XP(J*6+4)
FM32Q(J)=XP(J*6+5)
ENDDO

CCD=-0.5D0/SS*I; CCQ=-0.25D0/SS*I

DO J=1,NT

AA2=(0,0);BB2=(0,0);CC4=(0,0);DD4=(0,0);EE4=(0,0);FF4=(0,0);GG4=(0,0);HH4=(0
,0);II4=(0,0);JJ4=(0,0)
T=TT(J)*PI/180.0D0; X=COS(T)
CALL FUNLEG0(X,LMA,P0); CALL FUNLEG1(X,LMA,P1); CALL FUNLEG2(X,LMA,P2); CALL
FUNLEG3(X,LMA,P3)

AL(0)=0.0D0
DO N=1,LMA
AL(N)=AL(N-1)+ATAN(GG/N)
ENDDO

SCU=1.0D0/SIN(T/2.0D0)**2;
CUL=-GG/(2.0D0*SS)*SCU*EXP( I*GG*LOG(SCU))
CULKV(J)=ABS(CUL)**2*10.0D0;

DO L=0,LMA
SP12D(L)=EXP(2.0D0*I*FP12D(L))-1.0;SM12D(L)=EXP(2.0D0*I*FM12D(L))-
1.0;SCUL(L)=EXP(2.0D0*I*AL(L))
AA2=AA2+((L+1.0)*SP12D(L)+L*SM12D(L))*P0(L)*SCUL(L)
BB2=BB2+(SP12D(L)-SM12D(L))*P1(L)*SCUL(L)
ENDDO
AA2CUL=CCD*AA2+CUL;

DO L=0,LMA
SP12Q(L)=EXP(2.0D0*I*FP12Q(L))-1.0; SM12Q(L)=EXP(2.0D0*I*FM12Q(L))-1.0
SP32Q(L)=EXP(2.0D0*I*FP32Q(L))-1.0; SM32Q(L)=EXP(2.0D0*I*FM32Q(L))-1.0
!LL1=L+1.0; LL2=L+2.0;LL3=L+3.0;LM1=L-
1.0;DL1=2.0*L+1.0;DL2=2.0*L+2.0;DL3=2.0*L+3.0;DLM1=2.0*L-1.0;
!CC4=CC4+(3.0*LL1*LL2/DL3*SP32Q(L)+L*LL1/DL3*SP12Q(L)+L*LL1/DLM1*SM12Q(L)+3.
0*L*LM1/DLM1*SM32Q(L))*P0(L)*SCUL(L)
```

```
!DD4=DD4+(LL2*LL3/DL3*SP32Q(L)+3.0*LL1*LL2/DL3*SP12Q(L)+3.0*L*LM1/DLM1*SM12Q
(L)+LM1*LL2/DL2*SM32Q(L))*P0(L)*SCUL(L)

CC4=CC4+(
3.0*(L+1.0)*(L+2.0)/(2.0*L+3.0)*SP32Q(L)+L*(L+1.0)/(2.0*L+3.0)*SP12Q(L)+L*(L
+1.0)/(2.0*L-1.0)*SM12Q(L)+&
3.0*L*(L-1.0)/(2.0*L-1.0)*SM32Q(L)  )*P0(L)*SCUL(L)
DD4=DD4+(
(L+2.0)*(L+3.0)/(2.0*L+3.0)*SP32Q(L)+3.0*(L+1.0)*(L+2.0)/(2.0*L+3.0)*SP12Q(L
)+3.0*L*(L-1.0)/(2.0*L-1.0)*SM12Q(L)+&
(L-1.0)*(L-2.0)/(2.0*L-1.0)*SM32Q(L)  )*P0(L)*SCUL(L)
ENDDO
CC4CUL=CCQ*CC4+CUL;  DD4CUL=CCQ*DD4+CUL

DO L=1,LMA
EE4=EE4+(3.0*(L+2.0)/(2.0*L+3.0)*SP32Q(L)-(L+3.0)/(2.0*L+3.0)*SP12Q(L)+(L-
2.0)/(2.0*L-1.0)*SM12Q(L)-3.0*(L-1.0)/(2.0*L-1.0)*&
SM32Q(L))*P1(L)*SCUL(L)
FF4=FF4+sqrt(3.0)*(
(L+2.0)/(2.0*L+3.0)*SP32Q(L)+(L+1.0)/(2.0*L+3.0)*SP12Q(L)-L/(2.0*L-
1.0)*SM12Q(L)-(L-1.0)/(2.0*L-1.0)&
*SM32Q(L)  )*P1(L)*SCUL(L)
GG4=GG4+sqrt(3.0)*(
(L+3.0)*(L+2.0)/((L+1.0)*(2.0*L+3.0))*SP32Q(L)+(L+2.0)*(L-
3.0)/(L*(2.0*L+3.0))*SP12Q(L)-&
(L+4.0)*(L-1.0)/((L+1.0)*(2.0*L-1.0))*SM12Q(L)-(L-1.0)*(L-2.0)/(L*(2.0*L-
1.0))*SM32Q(L)  )*P1(L)*SCUL(L)
ENDDO
EE4=-EE4;  FF4=-FF4;  GG4=-GG4

DO L=2,LMA
HH4=HH4+sqrt(3.0)*((1.0/(2.0*L+3.0)*SP32Q(L)-1.0/(2.0*L+3.0)*SP12Q(L)-
1.0/(2.0*L-1.0)*SM12Q(L)+&
1.0/(2.0*L-1.0)*SM32Q(L))*P2(L))*SCUL(L)
II4=II4+sqrt(3.0)*(((L+3.0)/((L+1.0)*(2.0*L+3.0))*SP32Q(L)-
(L+6.0)/(L*(2.0*L+3.0))*SP12Q(L)-&
(L-5)/((L+1.0)*(2.0*L-1.0))*SM12Q(L)+(L-2.0)/(L*(2.0*L-1.0))&
*SM32Q(L))*P2(L))*SCUL(L)
ENDDO

DO L=3,LMA
JJ4=JJ4-(1.0/((L+1.0)*(2.0*L+3.0))*SP32Q(L)-
3.0/(L*(2.0*L+3.0))*SP12Q(L)+3.0/((L+1.0)*(2.0*L-1.0))*SM12Q(L)-&
1.0/(L*(2.0*L-1.0))*SM32Q(L))*P3(L)*SCUL(L)
ENDDO

SDA=ABS(AA2CUL)**2;  SDB=ABS(CCD*BB2)**2
SD=(SDA+SDB)*10.0D0
SQ1=ABS(CC4CUL)**2+ABS(DD4CUL)**2;
SQ2=ABS(CCQ*EE4)**2+ABS(CCQ*FF4)**2+ABS(CCQ*GG4)**2+ABS(CCQ*HH4)**2+ABS(CCQ*
II4)**2+&
ABS(CCQ*JJ4)**2
SQ=(SQ1+SQ2)*10.0D0

SECD=1.0D0/3.0D0*SD
SECQ=2.0D0/3.0D0*SQ/2.0D0
ST(J)=SECD+SECQ

ENDDO

S=0.0D0
```

```fortran
DO J=1,NT
DS(J)=((ST(J)-SE(J))/DE(J))**2
S=S+DS(J)
ENDDO
XI=S/NT

END

SUBROUTINE FUNLEG0(X,L,P0)
IMPLICIT REAL(8) (A-Z)
INTEGER I,L
DIMENSION P0(0:50)
P0(0)=1.0D0; P0(1)=X
DO I=2,L
P0(I)=(2.0D0*I-1.0D0)*X/I*P0(I-1)-(I-1.0D0)/I*P0(I-2)
ENDDO
END

SUBROUTINE FUNLEG1(X,L,P1)
IMPLICIT REAL(8) (A-Z)
INTEGER I,L
DIMENSION P1(0:50)
P1(0)=0.0D0; P1(1)=(1.0D0-X**2)**0.5; P1(2)=3.0D0*X*P1(1)
!IF (L>=3) THEN
DO I=2,L
P1(I+1)=(2.0D0*I+1.0D0)*X/I*P1(I)-(I+1.0D0)/I*P1(I-1)
ENDDO
!ENDIF
END

SUBROUTINE FUNLEG2(X,L,P2)
IMPLICIT REAL(8) (A-Z)
INTEGER I,L
DIMENSION P2(0:50)
P2(0)=0.0D0; P2(1)=0.0D0; P2(2)=3.0D0*(1.0D0-X**2)
DO I=2,L
P2(I+1)=(2.0D0*I+1.0D0)*X/I*P2(I)-(I+1.0D0)/I*P2(I-1)
ENDDO
END

SUBROUTINE FUNLEG3(X,L,P3)
IMPLICIT REAL(8) (A-Z)
INTEGER I,L
DIMENSION P3(0:50)
P3(0)=0.0D0; P3(1)=0.0D0; P3(2)=0.0D0; P3(3)=15.0D0*(1.0D0-X**2)**1.5
DO I=3,L
P3(I+1)=(2.0D0*I+1.0D0)*X/I*P3(I)-(I+1.0D0)/I*P3(I-1)
ENDDO
END
```